# Development of novel photocatalytic materials by magnetron sputtering for photoelectrochemical hydrogen production via solar activated water splitting

Thomas Pomone

A THESIS SUBMITTED IN PARTIAL FULFILMENT OF THE
REQUIREMENTS OF MANCHESTER METROPOLITAN UNIVERSITY
FOR THE DEGREE OF DOCTOR OF PHILOSOPHY

Manchester Metropolitan University

Faculty of Science and Engineering, Department of Engineering

Surface Engineering group

2024

# Declaration

This is to certify that the material contained in this thesis has been produced by author and has not been accepted in substance for any other degree and is not currently submitted in candidature for any other academic award.

# Acknowledgments

The writing of this thesis would not have been possible without the help and support of many people over the last few years. I would like to express my sincere gratitude to all of them.

I would first like to express my deepest thanks to my Director of Studies, Dr. Marina Ratova, for her help, her support and her patience during all these years. From my first internship in the Surface Engineering Department in 2018 to the end of writing this thesis, her mentorship, her advice and her expertise in photocatalysis have been invaluable resources in bringing this project to its conclusion. For that, I am sincerely grateful.

I would like to express my sincere gratitude to all of my supervisors who helped me during this project. I would like to thank Dr. Glen West, for his advice, for sharing his knowledge about magnetron sputtering, for always bringing new ideas for the project and for his continuous help during the writing of the thesis. I would like to express my sincere gratitude to Prof. Peter Kelly, Head of the Surface Engineering group, for his guidance and his help, and for providing to the students an excellent work environment within the Surface Engineering Group. Finally, I would like to express my sincere gratitude to Dr. Tiziana Denaro, for her help and advice. I especially thank her for bringing her expertise about electrochemistry to the project.

I would like to thank the technical services and especially Gary Miller and Hayley Andrews, for teaching me many things about the different characterisation techniques. I would also like to thank Leeds EPSRC Nanoscience and Nanotechnology Facility (accessed through Henry Royce access scheme) for performing TEM experiments.

I would also like to thank every person I met during my time in the Surface Engineering Group. From my first day of internship in 2018, I've always felt welcomed and supported by the group, and for that I am sincerely grateful. I would like to thank Justyna, Laurie, Yagya, Robert (my fellow Arsenal FC supporter) and Adele for their availability when I needed help or advice in the laboratory. I would like to sincerely thank the postgraduate students with whom I shared this crazy PhD adventure, for the amazing moments in and out of the lab. I really would like to thank Matthieu, Sam, Isabella, Hadi, Thaïs, Katharina, Deb, Khalid, Gwyn and James.

I would have like to have a special though for my housemates Francisco and Emmanuel, for making the Covid period so much more enjoyable. I would like to thank Miguel for teaching me so many things about the Brazilian culture (and especially food). I would like to thank Julie for being such a good friend over the last 15 years. And I would like to thank my group of

friends from Limoges for their support and friendship: Fabien “Bob Graou”, Grégoire “Furet”, Cassandre, Dimitri, Jacky, Axel, Corentin, Kevin, Thomas and Nicolas. I would like to express special thanks to the table tennis club of Beauvais, and to all of its members, for allowing me to restart this sport I loved so much during my childhood. Enfin, je souhaiterais écrire ces quelques mots en français pour remercier l’ensemble de ma famille : mes grands-parents, Simone et Denis Paillard ainsi qu’André et Marie-Thérèse Pomone ; mes oncles et tantes ; mon cher neveux Vixen, mes cousins et cousines qui m’ont énormément encouragé. J’ai une pensée toute spéciale pour ma maman, Céline, mon beau-père, Judicaël, et mes deux sœurs, Lucie et Jade. Votre soutien quotidien m’aura permis d’aller jusqu’au bout de ce projet.

*Je dédie enfin ce travail à la mémoire de mon papa, Jean-Yves Pomone.*

# Abstract

Hydrogen is a promising green source of energy, and its use could be one of the solutions against the global threats such as global warming. However, its current production ways mainly use fossil fuels in different processes, releasing a high amount of greenhouse gases. There is then a need to turn to renewable and sustainable ways to produce hydrogen. Among those methods, photoelectrochemical water splitting appears to be an interesting alternative, as it relies on the use of the most renewable and abundant source of energy on Earth (solar energy) to produce hydrogen from the water molecule $H_2O$, the most abundant source of hydrogen on Earth. To use photoelectrochemical water splitting, photocatalyst semiconductors must be produced. The most common and studied photocatalyst is titanium dioxide ($TiO_2$), but it is rather limited by its bandgap, reducing its absorption properties to the UV part of the solar spectrum. Novel photocatalysts, such as $BiVO_4$ and $CuBi_2O_4$, are more and more studied as candidates to be used as photoelectrodes. In this work, both $BiVO_4$ and $CuBi_2O_4$ photocatalysts were produced using pulsed direct current reactive magnetron co-sputtering to be studied as visible light active photoelectrodes in a PEC tandem cell. Then, the produced materials were studied by several analytical techniques to determine their crystallinity (XRD, Raman Spectroscopy), their morphology (SEM, 3D Optical profilometry, AFM) or their chemical composition (EDX, XPS). Their photocatalytic abilities under UV irradiation were successfully assessed by methylene blue dye degradation tests. Their photoelectrochemical properties were assessed in a PEC cell to study the oxygen evolution reaction, the proton reduction reaction and the overall water splitting reaction. Monoclinic scheelite $BiVO_4$ was identified by XRD and Raman analysis, with impressive performances regarding MB dye degradation and photocurrent production. Tetragonal $CuBi_2O_4$ was also successfully produced as an efficient photocathode. Both materials present similar behaviour regarding their efficiencies, due to the presence of oxygen vacancies implemented in the lattice during the production process. It results in increasing their charge transport efficiency but does not enable them to have a good charge transfer efficiency. This piece of work describes the use of reactive magnetron co-sputtering to deposit efficient photocatalytic coatings for photoelectrochemical purposes, with a study of the production parameters to determine the optimised deposition conditions. The photoelectrodes produced were used to study a first approach for a PEC tandem cell to study the production of hydrogen via solar activated water splitting. The results of this work address the viability and the challenges faced by this process.

# Table of Figures

# List of Tables

# Content

# I. Introduction and Literature Review

## 1. Introduction

*The primary goal of this research was to develop novel photocatalytic materials for visible-light photocatalytic water splitting for the production of green hydrogen. The magnetron sputtering technique was chosen for its potential to produce efficient photocatalytic thin films on an industrial scale. In this chapter, the background information is provided about hydrogen gas production, the environmental issues related to its current production methods and the new approaches to produce hydrogen in a renewable and sustainable way. A description of the main research and thesis layout is also provided.*

*The chapter is structured as follows: Section 1 is dedicated to the background and motivation for this research work, the research aims are described in Section 2, and Section 3 presents the thesis structure*

### 1.1 Background and motivation

In 2015, the United Nations Climate Change Conference (or COP 21) held in Paris was concluded by a common agreement to decrease the global carbon emissions by 43% in 2030, with the objective of the Net Zero Carbon emissions by the year 2050 [1]. According to the International Energy Agency (IEA), the main source of $CO_2$ emissions in 2021 was the energy sector, due to the global production of electricity and heat, with over 1000 Mt more $CO_2$ produced compared to 2020 [2]. The main reason is the use of fossil fuels (such as oil, coal, or natural gas), a major source of carbon emissions, that account for 80% of the energy production around the globe and are responsible for global threats such as climate change or ocean acidification [3, 4]. Moreover, according to predictions, the global energy demand will continue to increase due to population growth and economic development [5]. For example, between 1950 and 2022, the global primary energy consumption increased from 30.000 TWh to 180.000 TWh, with a need of more than 250.000 TWh predicted for 2050 [6, 7]. Finally, the current fossil fuels stocks are depleting, with a prediction of 57 years remaining for global oil stocks [8]. Hence, there is a need to turn to new energy resources in order to establish a sustainable society for the future generations

In response to this environmental emergency, research and industry focused their interest in recent years on renewable energy sources that produce little to no greenhouse gas emissions, such as solar, wind and hydroelectric power [9]. The development of technologies related to the energy production, storage and distribution is also a key factor, to ensure the growth of global renewable capacity: to meet the Net Zero Carbon scenario, the renewable capacity should increase by 3750 GW between 2022 and 2027, whereas the current growth is around 2250 GW [10]. Hydrogen gas ($H_2$) has attracted considerable interest over the past decades. It is not considered as an energy source by itself but as an energy carrier of high energy density that can be used in many key sectors, from industry to transportation and energy production [11]. Currently, the main use of $H_2$ is within industrial processes for the production of various chemicals, such as ammonia, methanol or hydrogen peroxide [12]. However, its use for heat production (via $H_2$ combustion) and electricity generation (when used with a fuel cell technologies) makes this gas an environmental-friendly fuel, as does not directly produce carbon emissions [13]. It can then be considered as a promising solution for a low-carbon future and for a global transition to a sustainable society.

However, the main issue with hydrogen today is its current production methods, mainly relying on fossil fuels as a feedstock: the vast majority of $H_2$ is produced from natural gas via steam reforming (76%) and coal via gasification (22%) [14]. These processes are associated with high carbon emissions, resulting in the hydrogen being classified as “black” or “grey”. The goal of research today is to turn to “new colours” of hydrogen, such as blue or green [15]. “Blue hydrogen” regroups all processes associated with reduced-carbon emissions. For example, it can be accomplished by integrating carbon capture and storage (CCS) technologies with thermochemical processes to decrease the carbon emissions released in the atmosphere [16]. Based on that, new $H_2$ classification systems are developed, based on the intensity of $CO_2$ released [16]. Nevertheless, the goal of Net Zero Carbon is to suppress $CO_2$ emission by 2050, so research should focus on the development of “green $H_2$”, grouping the technologies with low to net-zero carbon emissions. Those technologies rely mainly on the use of a sustainable energy source to produce $H_2$ from an abundant source of hydrogen [17].

Among the different “green $H_2$” processes, water splitting utilises the most abundant source of hydrogen on Earth, $H_2O$. This process is already in use via different electrolyser technologies, using the energy provided by electricity to force the separation of H and O to produce $H_2$ and $O_2$ gases. However, only 4% of global $H_2$ is produced using electrolysis and the different electricity production pathways do not necessarily make electrochemical water splitting a low-carbon emission process [18]. For example, depending on the country, the electricity can be either produced mainly with nuclear power (as it's the case in France [19]), by thermal power plant (such as in Germany [19]) or by renewable energies (as in the UK [19]). To ensure the production of "green $H_2$", water splitting needs a renewable energy source to be powered. Solar energy represents the most abundant source of energy, with a more than 170.000 TWh delivered to the Earth's surface per hour, equivalent to current global energy needs for one year [20]. Today, different technologies are under investigation to achieve solar activated water splitting to produce "green $H_2$", such as photoelectrochemical water splitting.

## 1.2 Aim and objectives

The objectives and research goals of this project are summarised in this section. Here, the aim of this work is to produce efficient photocatalysts to perform the complete water splitting reaction in a laboratory scale photoelectrochemical water splitting cell. The photocatalysts are produced as thin films by reactive magnetron sputtering. The main objectives of this research are:

1. The study of deposition parameters for the production of efficient bismuth vanadate photocatalyst used as photoanode to study the oxygen evolution reaction.

2. To produce a novel copper bismuth oxide photocatalyst via magnetron sputtering to be used as a photocathode for the study of the hydrogen evolution reaction.
3. The optimisation of the deposition parameters to maximise the efficiency of the photoelectrodes and identify the main limits of the produced materials.
4. The integration of both photocatalysts into a lab scale photoelectrochemical water splitting cell for the study of the overall water splitting reaction.

In this thesis, both materials were then tested in lab scale water splitting cell to prove their ability to perform the reactions under visible light illumination.

## 1.3 Thesis structure

The thesis is divided into four parts with a total of 9 chapters plus annexes. The first part of the thesis is dedicated to the scientific background of the work, with a comprehensive literature review on the different topics related to the research. Part II describes the analytical and experimental techniques used in the thesis for the thin films production, characterisation and testing. Part III provides a description of the results obtained during this investigation and a discussion of their meaning with respect to the application. Finally, Part IV provides an overview of the main results obtained and develops possible future research suggestions.

**The thesis chapters are structured as follows:**

**Chapter 1** Background and motivations, where the research aims and objectives of the thesis are discussed.

**Chapter 2** Overview of solar activated water splitting, with a focus on the basics of water splitting, the development of photocatalysis for water splitting and one specific configuration (Photoelectrochemical water splitting).

**Chapter 3** Discussion of the main photocatalytic materials used for photoelectrochemical water splitting, with details of the specific requirements of oxide semiconductors.

**Chapter 4** Overview of thin films, their applications and production methods, with a specific focus on PVD and magnetron sputtering.

**Chapter 5** Description of the different analytical and experimental techniques used to produce, test and characterise the materials produced during this project.

**Chapter 6** Presentation of the work done for the reactive magnetron co-deposition of $BiVO_4$ thin films to study the oxygen evolution reaction of the overall water splitting reaction.

**Chapter 7** Describes the development of photocathode material $CuBi_2O_4$ for the hydrogen evolution reaction in a PEC water splitting cell.

**Chapter 8** Discusses the photoelectrochemical measurements performed with both photocathode and photoanode in a tandem PEC cell, their intrinsic limitations and how to overcome the latter.

**Chapter 9** Conclusion of work done and suggestions for future work.

# 2. From electrolysis to Photoelectrochemical water splitting

*In this chapter, the application of photocatalysis for water splitting is discussed. The requirements, configurations and limitations associated with photocatalytic water splitting are presented. Photoelectrochemical water splitting is also reviewed, as photocatalytic water splitting may exhibit several drawbacks discussed below.*

*This chapter is divided into several sections. Section 2.1 describes the thermodynamic and kinetic basics of the overall water splitting reaction, followed by a description of the different technologies (electrolysers) currently used in industrial hydrogen production. Section 2.2 is dedicated to the description of photocatalysis and how photocatalysis can be applied to water splitting. Section 2.3 describes the photoelectrochemical water splitting process, its associated efficiencies and the different configurations possible for the use of this process.*

## 2.1 Hydrogen production by electrolysis

### 2.1.1. Basics of water splitting

J.R. Rudolph and A.P. van Troostwijk first reported an experiment in 1789, where gold electrode wires, connected to an electrostatic generator based on friction, were used to electrochemically split water into two different gases [21]. Then, several experiments were performed during the 19th century to understand the water splitting mechanism (W. Nicholson and A. Carlisle in 1800 [22]), allowing the development of the water electrolysis industry for hydrogen generation.

The decomposition of the water molecule $H_2O$ into its elemental components O and H is not a spontaneous reaction. The overall water splitting reaction in standard conditions ($T^0$ = 98 K, $P^0$ = 1 bar) is described in Equation (1):

$$H_2O_{(l)} \rightarrow H_{2(g)} + \frac{1}{2}O_{2(g)};\ \Delta G^0 = -237\ \mathrm{kJ.mol^{-1}} \qquad (1)$$

where $\Delta G^0$ is the Gibbs free energy of the reaction. Here, $\Delta G^0$ is negative, showing the endothermic nature of the reaction and then an energy input is required to cleave the bonds between hydrogen and oxygen.

This energy can be provided by temperature via the use of heat sources (thermal decomposition of water), but the high temperatures needed, and the low efficiency of the process limits its applications [23]. Today, the most standard method to achieve water splitting is to perform the electrolysis of water. In electrolysis, non-spontaneous chemical reactions are driven by electrical current flowing between two electrodes, electrically connected by an ionic conductor (such as an aqueous electrolyte) and an external circuit. To initiate the electrical flow, a potential difference is implemented between a cathode, site of a reduction reaction, and an anode, site of an oxidation reaction. The devices used to perform electrolysis are called electrolysers (described in 2.1.2.). The overall water splitting reaction (1) is a redox reaction, where an exchange of electrons happens between a reducing agent and an oxidizing agent. It can be then divided into two half reactions (Equations 2 and (3)) [24].

$$2H_2O_{(l)} \rightarrow O_{2(g)} + 4H^+ + 4e^- \; ; \; E^0{}_{O_2/H_2O} = 1.23\, V\ vs\ RHE \tag{2}$$

$$2H^+ + 2e^- \rightarrow H_{2(g)}; \;\; E^0{}_{H^+/H_2} = 0.00\, V\ vs\ RHE \tag{3}$$

It must be noted that those equations are valid in acidic environment, whereas in alkaline solutions, the redox couples involved are different. Both redox couples ($H^+/H_2$ and $O_2/H_2O$) possess specific standard potentials, respectively 0.00 V vs RHE and 1.23 V vs RHE. The hydrogen evolution reaction (HER) is a multi-step process where a transfer of two electrons occurs at the cathode surface to produce the hydrogen molecule $H_2$. The equation (3), corresponding to a reduction reaction, involves different mechanisms which can be described by several models. The Volmer-Heyrovsky model describes how a proton is captured by an electron from the surface catalyst to form an adsorbed hydrogen intermediate ($H^*$) [25]. This attracts a proton and an electron simultaneously to generate a hydrogen molecule. Depending on the pH of the electrolyte, the reactive species involved differ, as shown in Equations (4) to (7). Additionally, a Tafel reaction can take place, where two adsorbed hydrogen intermediates are joined together chemically to generate a hydrogen molecule at the cathode surface , as shown by Equation (8) [25].

- Volmer reaction:

$$H_2O + e^- + * \rightarrow H^* + OH^- \text{, in alkaline electrolyte} \tag{4}$$

$$H_3O^+ + e^- + * \rightarrow H^* + H_2O \text{ , in acidic electrolyte} \tag{5}$$

- Heyrovsky reaction:

$$H^* + H_3O^+ + e^- \rightarrow H_2 + H_2 \text{ , in acidic electrolyte} \tag{6}$$

$$H^* + H_2O + e^- \rightarrow H_2 + OH^- \text{ , in alkaline electrolyte} \tag{7}$$

- Tafel reaction:

$$H^* + H^* \rightarrow H_2 \tag{8}$$

Regarding the oxygen evolution reaction (OER), a transfer of 4 electrons occurs at the anode surface to produce the oxygen molecule $O_2$. Due to different kinetics, the OER involves more complex mechanisms and reaction pathways, but most of the models proposed agree on the presence of three main intermediates during the OER steps ($OH^*$, $O^*$ and $HOO^*$) [25]. Such as HER, the different species involved in the OER depends on the pH of the electrolyte used. The acidic reactions are described in Equations (9) to (12) and the alkaline ones are described in Equations (13) to (16).

- OER in the acidic electrolyte:

$$H_2O + * \rightarrow HO^* + H^+ + e^- \tag{9}$$

$$HO^* \rightarrow O^* + H^+ + e^- \tag{10}$$

$$O^* + H_2O \rightarrow HOO^* + H^+ + e^- \tag{11}$$

$$HOO^* \rightarrow * + O_2 + H^+ + e^- \tag{12}$$

- OER in the alkaline electrolyte:

$$OH^- + * \rightarrow HO^* + e^- \tag{13}$$

$$HO^* + OH^- \rightarrow O^* + H_2O + e^- \tag{14}$$

$$O^* + OH^- \rightarrow HOO^* + e^- \tag{15}$$

$$HOO^* \rightarrow * + O_2 + H_2O + e^- \tag{16}$$

To fulfil the thermodynamic requirement of the overall water splitting reaction during an electrolysis, a minimum voltage should be applied between the electrodes. This minimum voltage needed for the hydrolysis can be calculated via Equation (17) [26]:

$$\Delta G^0 = nFE \tag{17}$$

with $\Delta G^0$ is the Gibbs free energy, n is the number of electrons exchanged (in this case $n = 2$), F is the Faraday constant ($F = 96\ 500\ C.mol^{-1}$), and E is the applied voltage. The theoretical voltage to apply for water electrolysis is then equal to 1.23 V. However, higher voltage is usually needed in industrial electrolysers due to several kinetic barriers [24]. This additional potential required $\eta$ is called overpotential and can be caused by several factors (activation barriers on both cathode and anode, ohmic resistance of electrolytes and electrolysers components etc). In practice, voltages from 1.8 to 2 V are used to achieve water splitting.

### 1.1.2.1. Technologies for electrochemical water splitting

The first generation of hydrogen from the principle of electrolysis was done by Troostwijk and Diemann in 1789, by using an electrostatic generator as a direct source of current [21]. Since then, more and more water electrolysers were developed, especially in the 20th century, to produce hydrogen used in the synthesis of ammonia fertilizers. Different types of technologies have been developed to perform water electrolysis, starting with the development of alkaline water electrolysers, followed by Proton Exchange Membrane (PEM) and solid oxide electrolysers in the 1980s. To understand the operating principles and the configuration of the electrolysis technologies, an example is shown in Figure 2.1 with the example of alkaline water electrolysis. The electrolyte is transported to the cathode through a Gas Diffusion Layer (GDL). Two moles of alkaline solution are then reduced to produce one mole of $H_2$ and two moles of hydroxyl ions ($OH^-$). The $H_2$ gas travels through the GDL and is evacuated, whereas the hydroxyl ions are transferred to the anode side through a porous diaphragm. $OH^-$ are discharged to produce ½ mole of oxygen, one mole of $H_2O$ and two moles of electrons. The electrons are sent to the cathode via an external circuit to sustain the electrochemical reactions, whereas the $O_2$ and $H_2O$ are evacuated through a Porous Transport Layer (PTL).

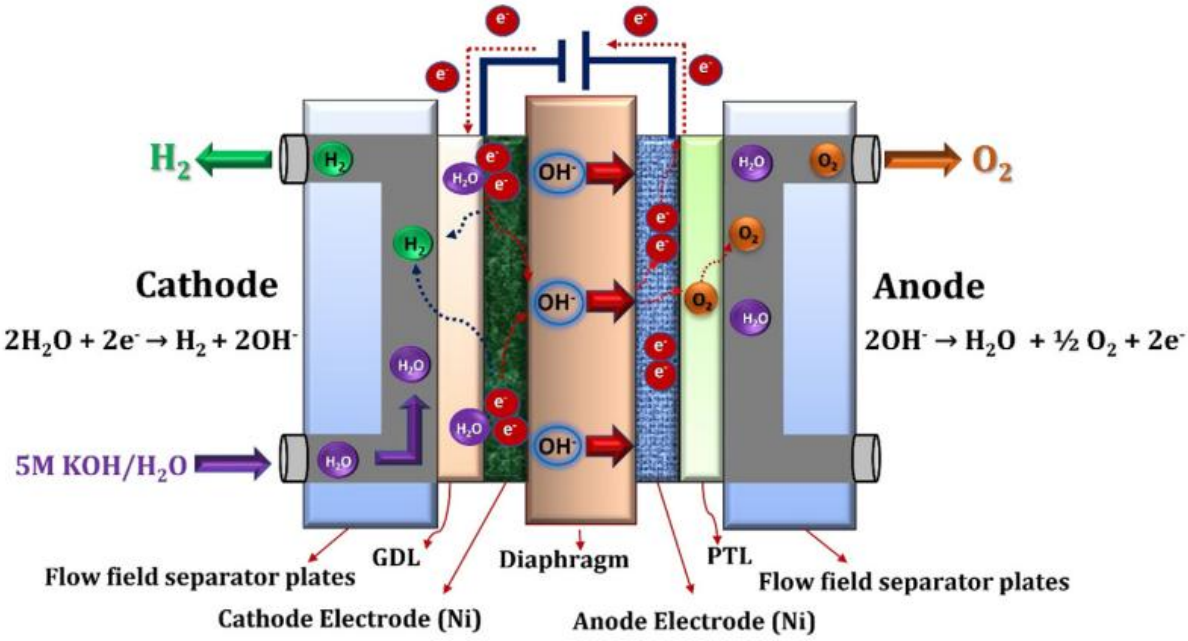

Figure 2.1: Schematic illustration of alkaline water electrolysis working principle (reproduced from [27])

All electrolysis technologies rely on the same operating principles. Today, four main technologies are used in water electrolysis for hydrogen production:

- The alkaline water electrolysis phenomenon was first studied by Troostwijk and Diemann and was then developed during the 19th century. The principle is described above, and it is considered as a well-established technology with a relatively low cost and long-term stability. However, several drawbacks limit the efficiency of this technology, such as the low current densities produced. Moreover, there is a high crossover of the gases produced [28].
- The Anion Exchange Membrane (AEM) water electrolysis was first reported by We and Scott in 2011 as a green hydrogen production technology [27]. This technology is similar to the alkaline electrolyser, but the conventional separation diaphragm is here replaced with an anion exchange membrane. This enables a reduction in the concentration of the alkaline electrolyte, from 5M KOH to 1M KOH. AEM then relies on the same working principle, producing higher current densities. However, the limited stability (35,000 h of use with a goal of 100,000 h) limits the current capability to scale-up this technology.
- Proton exchange membrane (PEM) water electrolysis was developed by General Electric Co. in 1966 to overcome the drawbacks of alkaline water electrolysis [29]. In the case of PEM, the electrolyte is brought to the anode side, where one mole of $H_2O$ is dissociated into 2 moles of $H^+$, 2 moles of electrons and ½ moles of $O_2$. The electrons are sent to the cathode via an external circuit and the $O_2$ gas is evacuated from the anode surface. The protons arrive at the cathode through a proton-conducting membrane, where they recombine with the electrons to produce $H_2$. The high current densities and high purity gas produced make this technology interesting for commercial applications, but research is still ongoing to reduce the costs of the components used. In particular, the electrodes are made of noble metal-based electrocatalysts, such as $IrO_2$ or carbon-supported Pt, making the hydrogen produced expensive.
- Solid-Oxide water Electrolysis Cells (SOEC) were developed in 1970s by General Electric Co. and Brookhaven National Laboratory. Contrary to the other technologies, SOEC operates with water in the form of steam at high temperatures (between 500°C and 850°C), resulting in favourable thermodynamics and reaction kinetics for the overall water splitting reaction. The power consumption is drastically reduced, increasing the energy efficiency during the process. Here, the water molecule is split on

the cathode side into $H_2$ and oxide ions $O^{2-}$. The oxide ions are transported to the anode side via a dense ceramic diaphragm to produce $O_2$ and electrons. As AEM technologies, the main drawback of SOECs is their limited stability, despite their high efficiencies [27].

Table 2-1 summarises the different advantages and disadvantages of electrolysis technologies. Although the technologies for electrochemical hydrogen production seem well understood and developed, currently only 4 to 5% of global hydrogen is produced using electrolysers, due to the amount of electrical energy needed to overcome the thermodynamic and kinetic requirements for the overall water splitting reaction, resulting in high costs [29]. Moreover, the source of electrical power does not ensure the process produces green hydrogen, as carbon can be emitted during the production of electricity (such as with coal factory). Green hydrogen production requires the direct use of renewable energies to produce hydrogen, and so photocatalysis appears to be a promising solution.

Table 2-1: Advantages and disadvantages of different water electrolysis technologies [27]

| Electrolysis technology | Advantages | Disadvantages |
|---|---|---|
| Alkaline water electrolysis | • Well established Technology<br>• Commercialised for industrial applications<br>• Noble metal-free electrocatalysts<br>• Relatively low cost<br>• Long-term stability | • Limited current densities<br>• Crossover of the gases<br>• High concentrated (5M KOH) liquid electrolyte |
| AEM water electrolysis | • Noble metal-free electrocatalysts<br>• Low concentrated (1M KOH) liquid electrolyte | • Limited stability<br>• Under development |
| PEM water electrolysis | • Commercialised technology<br>• Operates higher current densities<br>• High purity of the gases<br>• Compact system design<br>• Quick response | • Cost of the cell components<br>• Noble metal electrocatalysts<br>• Acidic electrolyte |
| Solid oxide water electrolysis | • High working temperature<br>• High efficiency | • Limited stability<br>• Under development |

## 2.2 Photocatalysis

The photocatalytic phenomenon was established by the pioneer work of Fujishima and Honda in 1972 [30]. In their work, a single crystal $TiO_2$ electrode irradiated by a UV light source was used in a three-electrode electrolysis cell operating under an applied bias to achieve water splitting. Since then, photocatalysis has been studied for many applications, such as pollutant degradation, self-cleaning coatings or antimicrobial purposes [31 – 33].

### 2.2.1. Principle of photocatalysis

A photocatalyst can be defined as a material able to drive chemical reactions thanks to the absorption of light energy. Photocatalysts are usually semiconductors, known for their particular electronic structure, composed of a valence band ($E_{VB}$) and a conduction band ($E_{CB}$). The difference of energy between the valence band and the conduction band is called the band gap ($E_g$) [34]. When a photocatalyst is illuminated by a light source, photons with an energy greater than the band gap value ($E \geq E_g$) are absorbed and their energy is transferred to the electrons located in the valence band. Those latter are then promoted to the conduction band, leaving in the valence band a positive space charge called “hole”. These electron-hole pairs are mobile and can migrate to the reaction sites on the photocatalyst’s surface, to initiate a charge transfer with adsorbed molecules, through redox reactions. In the case of the overall water splitting reaction, the adsorbed molecules are dissolved $O_2$ and $H_2O$, used to drive both oxygen evolution reaction and hydrogen evolution reaction. However, spontaneous recombination events between electrons and holes can happen in the bulk of the material or at its surface, lowering the efficiency of the photocatalytic process. The photocatalytic process can be then divided into 4 different steps, as shown in Figure 2.2: (1) Absorption of the photon’s energy by the photocatalysts, (2) Separation of charge carriers in the respective bands, (3) Migration of the charge carriers to the photocatalyst surface, (4) Redox reactions with the adsorbed molecules [34]. As photocatalysis only requires a photocatalyst, water and an illumination source to provide energy, it is then theoretically possible to drive the overall water splitting reaction with an abundant source of hydrogen ($H_2O$) and with a renewable source of energy (sunlight).

### 2.2.2. Photocatalytic water splitting

When photocatalysis is applied to water splitting, the holes and electrons produced (see Equation 18), respectively in the valence band and conduction band, can drive the oxygen evolution reaction (Equation 19) and the hydrogen evolution reaction (Equation 20) to perform the overall water splitting reaction (see Figure 2.2).

$$Photocatalyst + h\nu \rightarrow {h^+}_{VB} + {e^-}_{CB} \tag{18}$$

$$ {h^+}_{VB} + 2H_2O \rightarrow\ 4H^+ + O_2 + 4e^- \tag{19}$$

$$2{e^-}_{CB} + 2H^+ \rightarrow\ H_2 \tag{20}$$

As mentioned above, there is a competition between charge transfer from redox reaction and recombination events within the material (bulk or surface), reducing the overall efficiency of the photocatalytic process [34]. In addition, several requirements specific to the water splitting reaction need to be fulfilled. Firstly, the energies of the valence band and conduction band should match the thermodynamic standard potentials of both half-reactions. To perform the oxygen evolution reaction, the valence band should be more positive than the standard potential of the reaction, (${E^0}_{H_2O/O_2} = 1.23$ V vs RHE ), whereas the conduction band should be more negative than the standard potential of the hydrogen evolution reaction (${E^0}_{H^+/H_2} =\ 0.00$ V vs RHE ). Consequently, as both half-reactions are performed by the same photocatalyst, the band gap of the photocatalyst should be at least 1.23 eV, to fulfil these energetic requirements [34].

In terms of hydrogen production, the use of a single photocatalyst is not the ideal configuration for the overall water splitting reaction as both $H_2$ and $O_2$ gases are produced on the same reactive sites. And yet, the surface recombination reactions of $H_2$ and $O_2$ to form $H_2O$ is thermodynamically more favourable than the water splitting reaction (see Figure 2.3) [35 - 38]. Hence, photocatalysis is drastically limited by the surface recombination reactions (e.g. oxygen reduction and hydrogen oxidation). The process can be enhanced using nanoparticles dispersed in solution; however, it causes additional issues relating to the disposal of photocatalyst nanoparticles [36]. Charge scavengers can also be used to enhance the photocatalytic water splitting process [37]. Another way to apply photocatalysis to water splitting is to use the photoelectrochemical configuration.

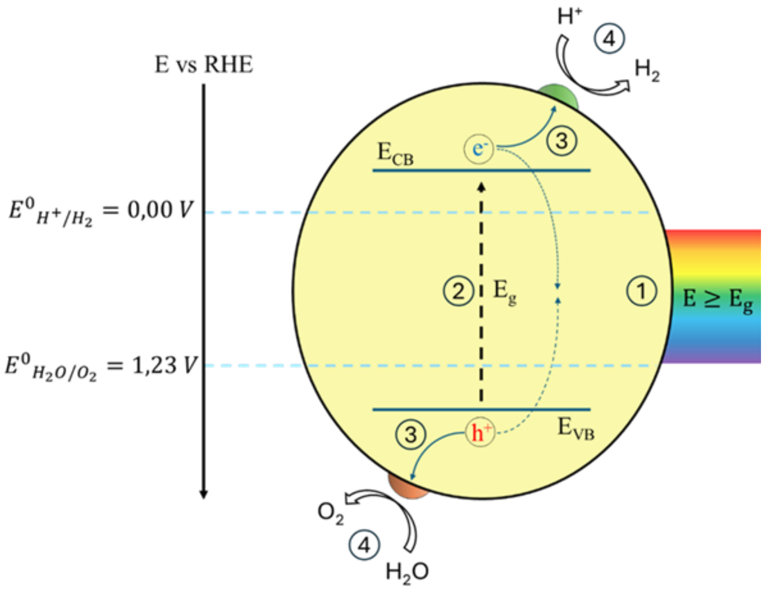

Figure 2.2: Schematic of photocatalysis applied to the overall water splitting reaction; (1) Photons absorption; (2) charge carriers separation; (3) charge carriers migration; (4) redox reactions at photocatalysts surface reaction sites

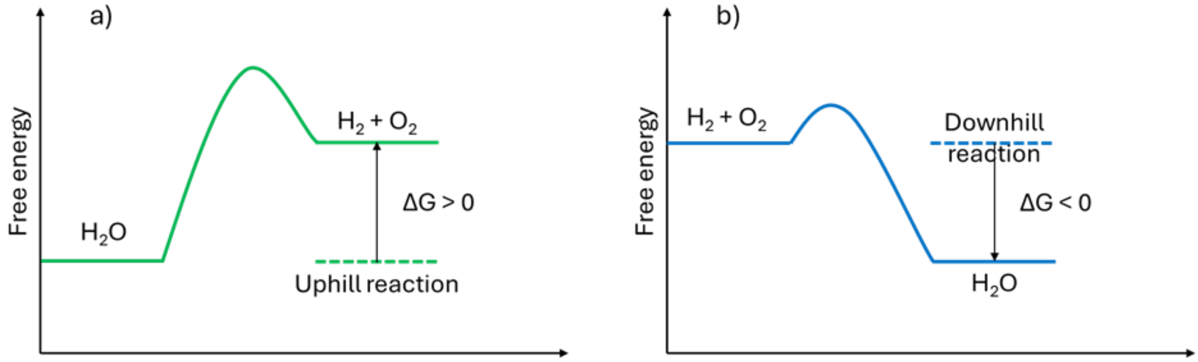

Figure 2.3: Thermodynamic Gibbs free energy for overall water splitting (lef) and recombination between $H_2$ and $O_2$ (right) (adapted from [39])

As seen in section 2.2.1, the photocatalytic phenomenon can be divided into several steps: the light absorption and the production of electron-hole pairs, the migration of the charge carriers from the bulk of the material to the surface of the photocatalyst, and a charge transfer between the photocatalyst and the electrolyte to drive the redox reactions. Each step influences the overall efficiency of the water splitting process, with losses mainly due to charge carrier recombination. All efficiencies attributed to photon absorption, charge transport and charge transfer will be described in Chapter 3.

## 2.3 Photoelectrochemical water splitting

### 2.3.1. Principle

In photoelectrochemical water splitting, the photocatalysts are used in a form of thin films in an electrolysis configuration: typically, two electrodes (a cathode and an anode) are immersed in a conductive electrolyte containing the chemical species on interest. Both electrodes are connected to each other via an external circuit to permit the circulation of electrons between the electrodes. In this configuration, the electrodes are made of a thin layer of photocatalysts deposited on a transparent conductive substrate, to create photoelectrodes [40]. Each photoelectrode is then responsible for one half-reaction, with the photoanode being the reaction site of the oxygen evolution reaction and the photocathode being the reaction site of the hydrogen evolution reaction. The usual configuration of photoelectrochemical water splitting is the use of one photoelectrode combined with a counter-electrode, as shown in Figure 2.4. When the photoelectrode is illuminated by a light source, the photocatalytic process described in section 2.2. happens, allowing the production of electron-hole pairs. When a photoanode is used, the holes migrate to the photoanode's surface, driving the oxygen evolution reaction, while the electrons from the photoanode are attracted to the counter-electrode through the external circuit. When the photoelectrode is a photocathode, the electrons produced drive the hydrogen evolution reaction, while the anode is responsible for the oxygen evolution reaction [40]. Compared to photocatalytic water splitting, photoelectrochemical water splitting presents several advantages. The separation of reactive sites for both half-reactions drastically prevent the recombination of $H_2$ and $O_2$ gases during the reaction, increasing the efficiency of the process [41, 42]. Also, as one photocatalyst is only responsible for one half-reaction in photoelectrochemical water splitting, the band energies should match with just one of the standard potentials ($E_{VB} > E^0{}_{H_2O/O_2}$ for the photoanode and $E_{CB} < E^0{}_{H^+/H_2}$ for the photocathode). It opens then more possibilities for materials to be studied as photoelectrodes, which will be described in chapter 3.

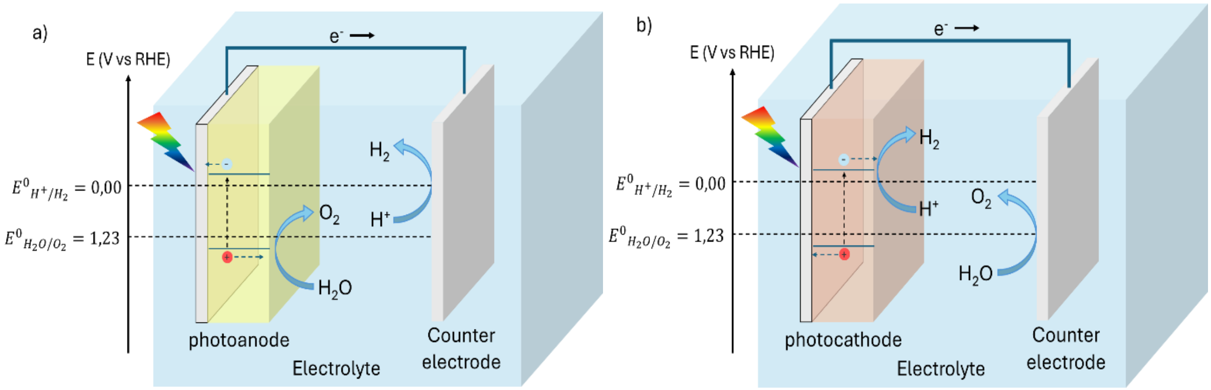

Figure 2.4: Schematic of PEC water splitting with (a) single photoanode, (b) single photocathode

To ensure to operate the photoelectrochemical measurements in standardized conditions, the power intensity of the light source is calibrated to correspond to the air mass coefficient (AM) 1.5 reference spectra. The air mass (AM) coefficient is used to characterize the solar spectrum after traveling through the Earth's atmosphere and corresponds to the ratio between the direct optical path length through the atmosphere and optical path length at the zenith. As the sunlight passes through the atmosphere, its intensity is attenuated (due to phenomena such as scattering, absorption, reflection …). The AM coefficient is then usually followed by a number, corresponding to the atmosphere thickness travelled by the sunlight. This number is determined by the angle of the incident solar radiation: for the AM 1.5 spectra, the angle corresponding to 1.5 atmosphere thickness is 48.2 °, and was chosen in 1970 as a standard, as it corresponds to temperate latitudes where many of the world's major population centre are located (China, Europe, Japan, USA …). This norm is usually referred as ASTM G-173 (see Figure 2.5) [166].

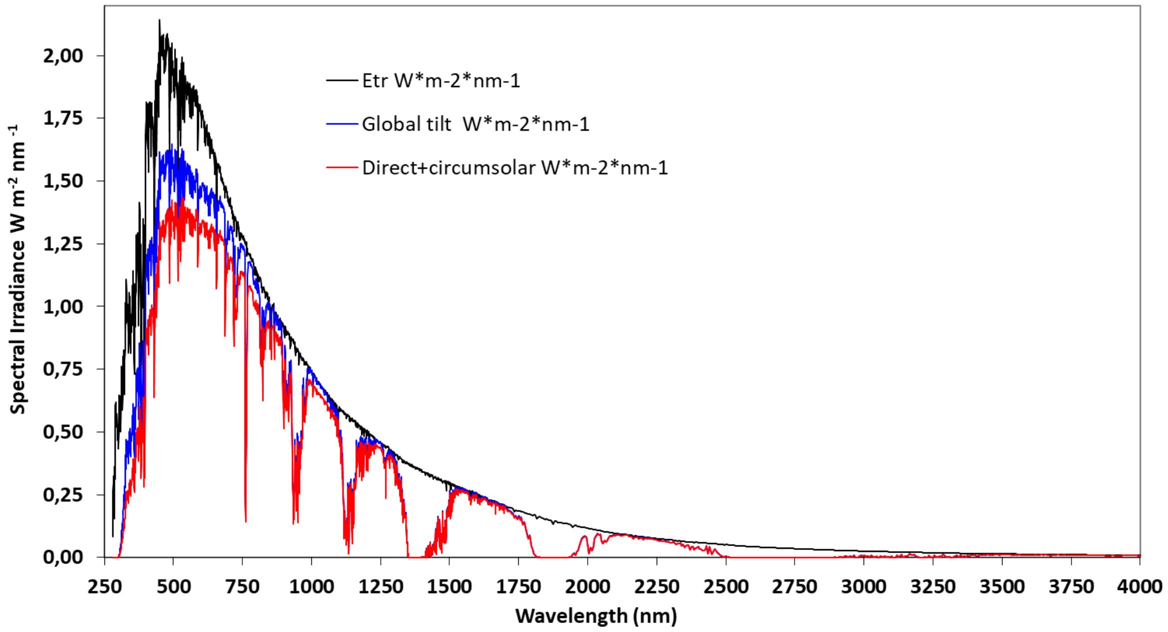

Figure 2.5: ASTM G173-03 Reference spectra [166]

### 2.3.2. Efficiencies for the evaluation of PEC performances

The ability of a photoelectrochemical water splitting cell to produce hydrogen can be characterised by several efficiency measures. There are two main efficiencies that characterise a PEC device: the incident photon-to-current efficiency (IPCE) and the solar-to-hydrogen (STH) efficiency. Each of those measurements should be performed with the same energy input, usually provided by the photons from a calibrated light source reproducing the solar spectrum. The incident photon-to-current efficiency (IPCE) measures the ability of a photoelectrode to convert the energy from the incident photons into electrons used by the PEC cell. As the energy of a photon is related to its frequency, the IPCE measurement is dependent on the wavelength of the illuminating light. The IPCE can be measured using the following Equation (21) [43]:

$$IPCE(\lambda) = \frac{electrons\ produced\ (cm^{-2}.s^{-1})}{incident\ photons\ (cm^{-2}.s^{-1})} = \frac{J_{ph}(\lambda)/e}{P(\lambda)(\frac{hc}{\lambda})} = \frac{J_{ph}(\lambda)\times 1239.8}{P(\lambda)\times\lambda} \qquad (21)$$

The flow of electrons produced is calculated by multiplying the photocurrent density produced under monochromatic irradiation at wavelength λ, $J_{ph}(\lambda)$ (in $mA.cm^{-2}$), by hc/e (with e the charge of one electron, c the speed of light and h the Planck's constant). The incident photons are calculated by multiplying the power intensity of the incident monochromatic light P(λ) (in $mW.cm^{-2}$) by the wavelength λ. By measuring the IPCE of a photoelectrode, it is then possible to determine at which wavelength the PEC cell is the most efficient. As the IPCE measures the converted incident photons into electrons, all the steps associated with the photocatalytic phenomenon have an impact on the IPCE. Then, IPCE can be expressed with the following Equation (22) [43]:

$$IPCE(\lambda) = \eta_{abs} \times \eta_{transport} \times \eta_{transfer} \tag{22}$$

with $\eta_{abs}$ the light absorption efficiency (or light harvesting efficiency), $\eta_{transport}$ the charge transport efficiency and $\eta_{transfer}$ the charge transfer efficiency. An example of IPCE measurement is shown in Figure 2.6.

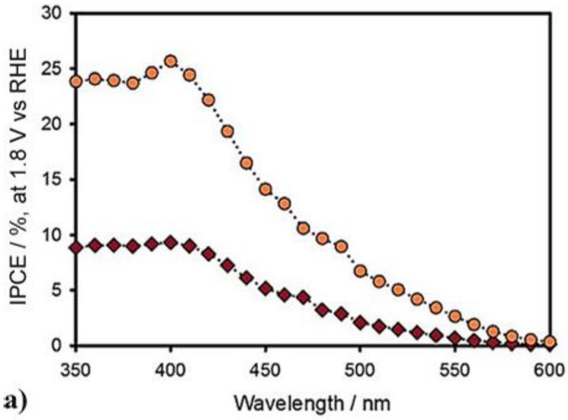

Figure 2.6: IPCE plots for undoped and 6.25% Ti doped hematite electrode measured at 1.8 $V_{RHE}$ (pH = 1, 1 sun illumination) [44]

The solar-to-hydrogen efficiency (STH) is used to measure how efficiently a PEC device can convert the solar energy input into chemical energy stored in $H_2$ gas. This measurement is performed when the device is exposed to broadband solar light to produce $H_2$ and $O_2$ gases at the photocathode and photoanode, respectively [43]. The mathematical expression of STH efficiency is given by the following Equation (23):

$$STH = \frac{mmol\ H_2 s^{-1} \times 237\ kJ.mol^{-1}}{P_{total}(mW.cm^{-2}) \times area\ (cm^2)} \tag{23}$$

where the numerator corresponds to the chemical energy and the denominator is the solar energy input. The chemical energy is calculated by multiplying the amount of $H_2$ produced (in mmol $H_2.s^{-1}$) by the change in the Gibbs free energy per mole of $H_2$ produced, associated with the reaction from $H_2O$ to $H_2$ and $O_2$ (at 25°C, $\Delta G = 237\ 000\ J.mol^{-1}$). The solar energy input is calculated by multiplying the power density of the incident light (in $mW.cm^{-2}$) by the illuminated electrode area (in $cm^2$). The STH efficiency is usually measured in a two-electrode configuration when no external bias is applied. Yet, when only one photoelectrode is measured, the driving force produced by the photovoltage is usually not high enough to run an unassisted PEC water splitting cell. In this case, an applied bias is provided by a power supply. Then, the STH efficiency is called the applied bias photon-to-current efficiency (ABPE), which takes into account the applied bias. STH efficiency depends on the irradiation source but also on the band gap of the semiconductors used for the PEC cells, as shown in Figure 2.7. A theoretical maximum photocurrent density is then associated with each material but is often lower in practice due to the several limitations of each photocatalytic step.

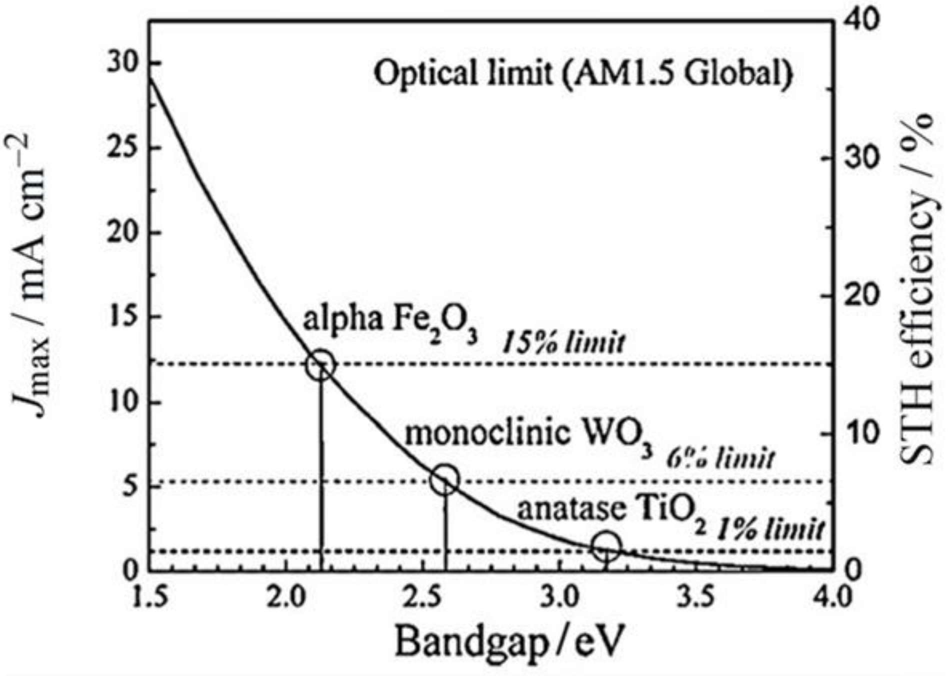

Figure 2.7: The theoretical maximum STH value for a semiconductor according to its bandgap [45]

### 2.3.3. Configurations possible for PEC water splitting

If the configuration with a single photoelectrode represents a first approach of photoelectrochemical water splitting, it still requires the use of an external bias to achieve the overall water splitting reaction, in addition to the use of a light source. Therefore, it is necessary to use different PEC configurations that makes the PEC cell unassisted, as it was first reported by Yoneyama et al. in 1975 [46]. Several parameters should be taken into account when studying a PEC tandem cell configuration. Usually, a STH efficiency of 10% and a stability of 1000 h are generally considered to be the minimum threshold for the commercial application for PEC water splitting cell [47]. The main possible configurations (n-type photoanode/p-type photocathode tandem cell, PEC/PV tandem cell and buried junction cell) all presents theoretical STH superior to 20% [42]. However, the experimental STH efficiency reported for all the configurations are far below the theoretical ones, due to the different limitations of photocatalysis.

One of the main tandem cell configurations studied is the n-type photoanode/p-type photocathode configuration. The n-type photoanode/p-type photocathode tandem device relies on the use of two photocatalysts as photoanode and photocathode, respectively, to perform both half-reactions, as shown in Figure 2.8a. This is the extension of the single-photoelectrode configuration described in section 2.3.1. As the photocurrent and photovoltage produced by photocatalysts can be low, it is possible to engineer multilayer photoelectrodes by adding thin films of photovoltaic materials in order to enhance the PEC power of the photoelectrodes [42]. However, the cost of fabrication increases, and the fabrication becomes more complex, involving several production steps. This configuration offers the possibility to study the combination of many photocatalysts. For example, Chu et al. studied a n-type photoanode/p-type photocathode tandem cell composed of a $TiO_2$ photoanode and a $CuBi_2O_4$ photocathode, with a STH efficiency of 1.23% achieved [48]. The use of smaller band gap materials, such as $Fe_2O_3$, does not necessarily show higher STH (0.15% for a tandem cell composed of $Fe_2O_3$ and $CuBi_2O_4$ photoelectrodes [49]). Examples of n-type photoanode/p-type photocathode tandem cells and their respective efficiencies are provided in Table 2.2.

The PEC/PV tandem cells are obtained by connecting a PV cell to the photoelectrode and counter-electrode used in the single photoelectrode configuration. This configuration exhibits higher STH efficiencies, due to the large photovoltage provided to the device by the additional PV cell. This PV cell can be integrated to the photoelectrode, but it can then suffer from corrosion due to the exposition to the electrolyte. Usually, PV/PEC tandem cells are studied with the PV cell separated from the PEC cell, as shown in Figure 2.8b. This configuration can be studied with a photoanode material, such as $WO_3$, or with a photocathode, such as $Cu_2O$ [50, 51]. Examples of PV/PEC tandem cells and their respective efficiencies are presented in table 3. Finally, the buried junction PEC cell is a compact and integrated structure composed of two photocatalysts, as shown in Figure 2.8c. It presents several advantages, such as a higher light absorption and a diminution of ohmic losses due to smaller distances involved. This configuration is more compact and needs less electrolyte filling. If the configuration brings some advantages, there are also some drawbacks regarding the difficulty of cell assembling or the low efficiencies exhibited by the device. Due to inefficiencies, buried junction PEC tandem cell is not largely studied compared to the two other configurations. Some examples are provided in Table 2.2.

Table 2-2: Examples of water splitting cell configurations with respective STH efficiencies

| Tandem cell | Configurations | Electrodes (anode/cathode) | STH efficiency (%) | References |
|---|---|---|---|---|
| n-type/p-type | All oxide PEC/PEC | $TiO_2/CuBi_2O_4$ | 1.23 | [48] |
| | | $Fe_2O_3/CuBi_2O_4$ | 0.15 | [49] |
| | PV-based PEC/PEC | 3-jn a-Si-$RuO_x$/ 3-jn a-Si-Pt | 1.8 | [52] |
| | | Pt/p-Si-GaAsP | 0.5 | [53] |
| | Oxide photoelectrode-PV hybrid PEC/PV | $\alpha$-$Fe_2O_3$-$NiFeO_x$/a-Si-Pt | 0.91 | [54] |
| | | $WO_3$/a-SiGe:H | 0.7 | [55] |
| PEC/PV | Oxide photoanode/PV | $WO_3$/DSSC | 3.1 | [50] |
| | Oxide photocathode/PV | $Cu_2O$/PSC | 2.5 | [51] |
| Buried junction device | / | Pt/3-jn a-Si/$RuO_x$ | 5 | [56] |
| | | NiMoZn/3-jn a-Si/Co | 2.5 | [57] |
| | | Rh/$TiO_2$/oxide/AlInP-GaInP/GaInAs/GaAs/$RuO_2$ | 19 | [58] |

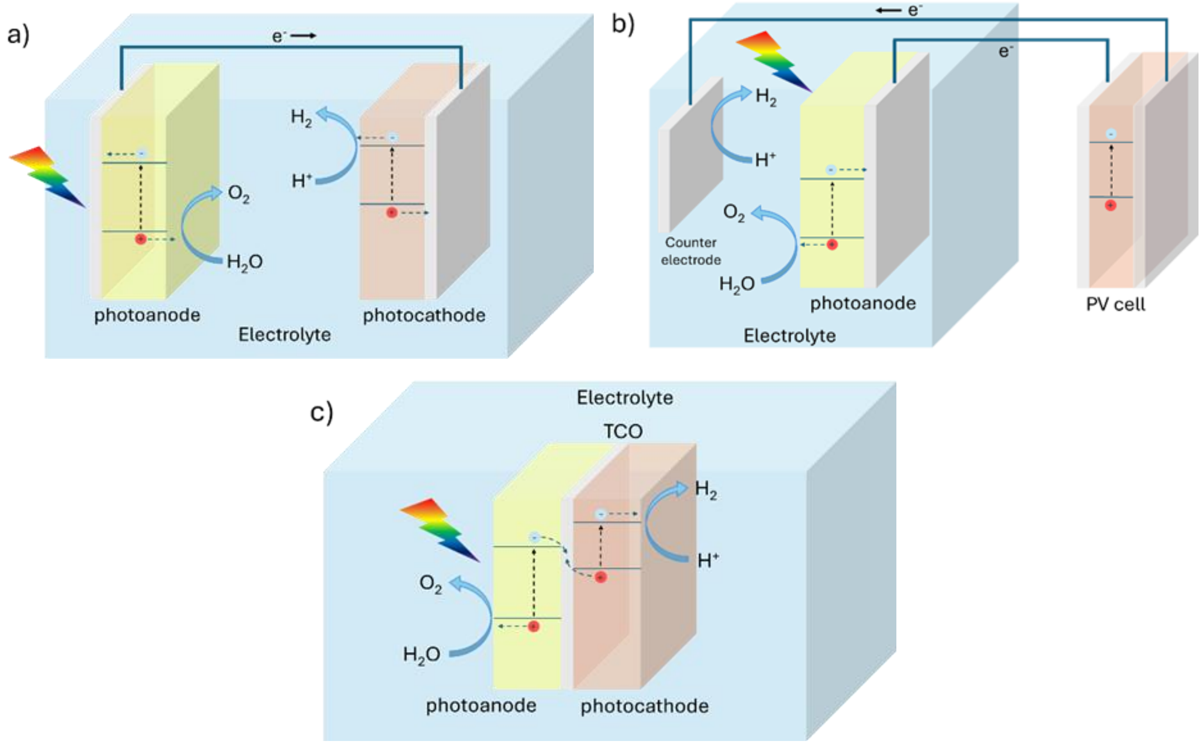

Figure 2.8: Possible configurations for tandem water splitting cell (a) photoanode/photocathode tandem cell, (b) PEC/PV tandem cell, (c) Buried junction tandem cel

# 3. Materials for semiconductor photocatalysts

*In this chapter an overview of the materials used for photoelectrochemical water splitting is provided. Photocatalysis relies on the use of semiconductors and their intrinsic properties. Specific requirements need to be fulfilled for semiconductors to be used either as a photoanode or a photocathode. Ternary metal oxides present a promising type of material for study. Moreover, improvement techniques are developed to enhance the properties of existing semiconductors.*

*This chapter is divided into several sections. Section 3.1 describes the properties of semiconductor photocatalysts, with a focus on their electronic band structure and the interfacial interactions between a semiconductor and an electrolyte. Section 3.2 presents the metal oxide semiconductors, the most studied photocatalysts, with a description of the different types and an overview of the different efficiencies related to metal oxide semiconductors. Finally, Section 3.3 describes the different enhancement strategies proposed to increase the activity of photocatalysts, especially the effect of oxygen vacancies, dopants/co-catalysts and heterostructures.*

## 3.1 Semiconductor photocatalyst

### 3.1.1. Properties of a semiconductor

As discussed in Chapter 2, photocatalysis relies on the use of semiconductor materials, defined by their specific electronic structure. In the band structure theory of solid-state materials, the combination of two atomic orbitals results in the creation of two molecular orbitals of different energies (a bonding orbital and an antibonding orbital). A solid is composed of a large number of atoms, resulting in multiple molecular orbitals produced. As those molecular orbitals are very close in terms of energy (in the order of $10^{-22}$ eV), the adjacent energy levels can be all considered as a continuous level energy called a band [59].

Two specific bands are of interest for semiconductor materials: the valence band, corresponding to the highest occupied molecular orbital (HOMO), and the conduction band, corresponding to the lowest unoccupied molecular orbital (LUMO). The band gap $E_g$ corresponds to the energy difference between the top of the valence band and the bottom of the conduction band. Within the band gap lies the Fermi level $E_{FB}$, a hypothetical energy level which has a 50% chance to be occupied at any temperature [60]. The value of the semiconductor's band gap defines the nature of a solid material: when the band gap is greater than 4 eV, the electrons cannot be promoted to the conduction band, the materials are then considered as insulator. When the valence band and the conduction band overlap, the electrons have the possibility to go to the conduction band, making them highly mobile, the material is then considered as a conductor. Finally, if the band gap is relatively narrow (between 1 and 4 eV [61]), the electrons can be promoted to the conduction band with an energy input, that can be provided by a rise in temperature or from a photon, hence the material can be defined as a semiconductor. For a semiconductor with a Fermi level halfway through the valence band and the conduction band, it is called an intrinsic semiconductor. An extrinsic semiconductor is produced when dopants are added to change nature of the majority charge carriers within the lattice of the materials. For example, a semiconductor with a valency of four (e.g. titanium dioxide) doped with trivalent impurities will provide extra holes, making the semiconductor a p-type (positive). In opposite, a semiconductor doped with pentavalent impurities will provide extra electrons, making the semiconductor an n-type (negative). Both types of doping result in a displacement of the Fermi level close to the conduction band in the case of n-type and close to the valence band in the case of p-type [62]. All electronic structures are shown in Figure 3.1.

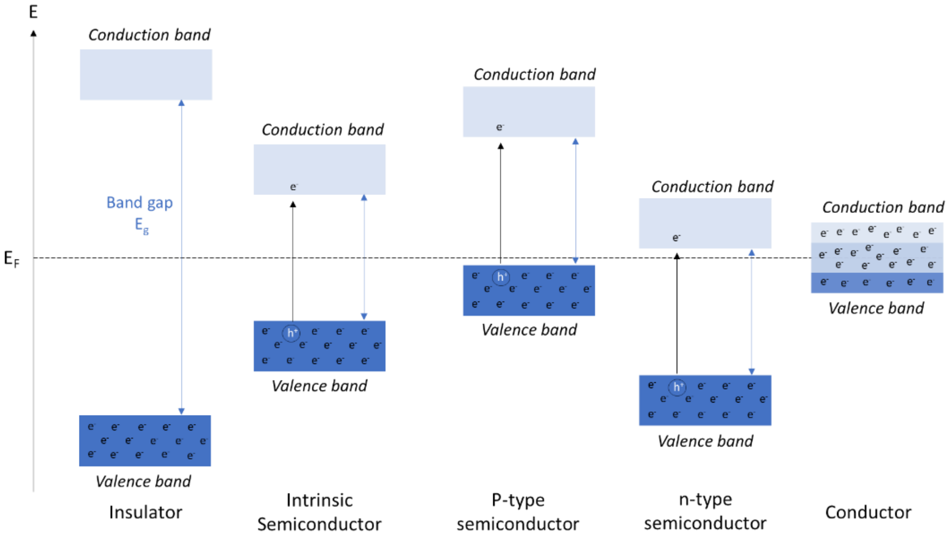

Figure 3.1: Band structure for insulator, semiconductor (intrinsic and extrinsic) and conductor materials

### 3.1.2. Interactions at the semiconductor/electrolyte interface

When a semiconductor photocatalyst is immersed in an electrolyte solution, a potential difference is established at the semiconductor-electrolyte interface, due to the difference of energy between the different Fermi levels (see Figure 3.2a and 3.2b). Both Fermi levels equilibrate via charge transfer through semiconductor/electrolyte junction, leading to several changes [63]. Firstly, the charge transfer induces the formation of a space charge region at the semiconductor side. This region is charged differently depending on the type of semiconductor. In the case of an n-type semiconductor, as the flow of electrons goes from the semiconductor to the electrolyte, the semiconductor loses negative charges, resulting in a depletion layer (positively charged) at the semiconductor side. In the case of a p-type, the space charge region is an enrichment layer, negatively charged due to the flow of electrons, going from the solution to the semiconductor. Depending on the material, this space charge region has a width of the order of 10 to 1000 nm [64]. Also, the conduction band and valence band are both shifted in the space charge region due to the change of charges. The bands are shifted upward in the case of an n-type semiconductor or shifted downward in the case of a p-type semiconductor (see Figure 3.2c and 3.2d). This phenomenon is called band bending and induces a built-in electric field within the space charge region. This electric field is of importance, as it directs the charge carrier flux during charge separation. For example, when holes and electrons are produced within the space charge region of an n-type semiconductor, the holes migrate to the surface of the semiconductor to drive oxidation reactions, whereas the electrons are directed to the bulk of the semiconductor (see Figure 3.2e). The opposite phenomenon happens with a p-type semiconductor, as depicted in Figure 3.2f. Finally, during illumination, the equilibrium reached by the exchange of electrons is broken, altering the charge carrier density and the band bending within the band gap. The Fermi level is then replaced by the concept of quasi-Fermi levels for each band, e.g. a quasi-Fermi level for holes ($E_{f,p}$) and a quasi-Fermi level for electrons ($E_{f,n}$). The electrochemical potential of the illuminated semiconductor/electrolyte interface becomes thus the quasi-Fermi level of its minority carrier (holes for n-type, electrons for p-type). The difference between the two quasi-Fermi levels is called the photovoltage $V_{oc}$. This specific phenomenon related to junctions between semiconductors and liquid phase enables the electrochemical reactions with a different potential than that of conductive electrodes [64]. Hence, a n-type semiconductor can promote oxidation reactions at a lower potential than conductive electrodes, and is called a photoanode, whereas a p-type semiconductor can promote reduction reactions at a higher potential and is called a photocathode.

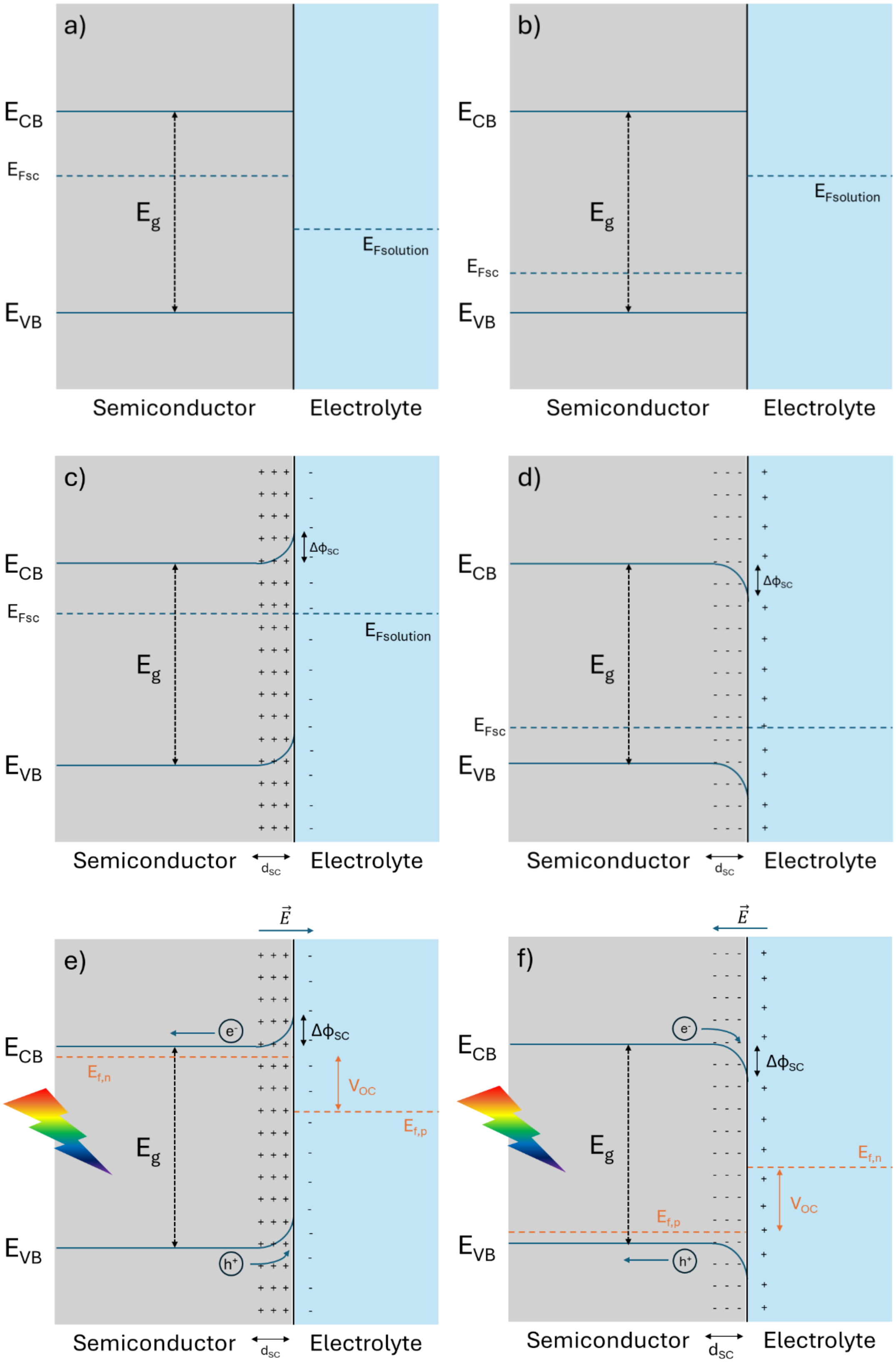

Figure 3.2: (a) Photoanode-electrolyte before equilibrium, (b) Photocathode-electrolyte after equilibrium, (c) Upward band bending, (d) Downward band bending, (e) Photovoltage produced by photoanode,( f) Photovoltage produced by photocathode (adapted from [65])

## 3.2 Metal oxide semiconductors

Several requirements must be fulfilled for a semiconductor to be considered for photoelectrochemical water splitting. Firstly, its conduction band and valence should match the standard potentials of the oxygen evolution reaction or the hydrogen evolution reaction, depending on whether the material is used as photoanode or photocathode. A narrow band-gap should allow it to be visible-light responsive, to harvest the photons from the visible part of the solar spectrum, having a STH efficiency as high as possible. Finally, the material should be stable in aqueous solutions, made of abundant and cheap elements to guarantee the feasibility of photoelectrode production, and should be non-toxic. Over the years, several groups of semiconductors have been studied. The III-V group materials are composed of non-oxide semiconductors, formed from group 13 metal elements and group 15 anion elements. They can be composed of binary compounds, such as InP or GaP, or ternary compounds such as GaInP, GaInN and AlGaAs [66]. These materials present narrow band gaps and exhibit high-photoactivity regarding water splitting, however they are made of expensive elements. Another group of interest is the group II-VI elements, composed of materials formed with group 12 metal elements and group 16 anions elements [67]. These materials (CdS, CdTe) are used for various opto-electronic applications but are composed of elements that have multiple effects on biological organisms and generally considered as toxic. For the purposes of the thesis, the materials that are considered for photoelectrodes are the metal oxide semiconductors.

### 3.2.1. Binary metal oxide semiconductors

The first generation of photocatalysts studied was made of a single transition metal oxide, of formula $A_xO_y$ (with A being a transition metal element). Most examples present the properties required to be used as photocatalysts (non-toxic, made of abundant elements, with simple synthesis routes) [68]. Their nature as semiconductors is determined by the type of defects present in their lattice: a n-type metal oxide semiconductor presents intrinsic oxygen vacancies ($V_O$), acting as electron donors that are the majority charge carriers. Most of transition metal semiconductors are n-type, such as $TiO_2$, $Fe_2O_3$, ZnO or $WO_3$. In the case of a p-type semiconductor, the main defects are metal cation vacancies ($V_M$), acting as positive charge donors [68]. The main p-type metal oxide semiconductors are Cu-based materials ($Cu_2O$ and CuO).

Transition metal oxides exhibit a number of drawbacks that drastically reduce their photocatalytic efficacy. The main disadvantage of those materials is their large band gap that does not allow the absorption of a large part of the solar spectrum. For example, $TiO_2$ presents a band gap comprised between 3.0 eV and 3.2 eV, depending on the crystal phase (for rutile and anatase, respectively) [69]. For a semiconductor, according to the Planck-Einstein Equation (24), the higher the band gap, the lower the maximum wavelength absorbable:

$$E = \frac{h \times c}{\lambda} \tag{24}$$

with h the Planck's constant ($4.135 \times 10^{-15}$ eV.s), c is the speed of light ($3 \times 10^{8}$ m.s$^{-1}$) and λ is the photon's wavelength in nm. Therefore, in the case of $TiO_2$, the maximum wavelength absorbable would be between 380 and 410 nm, which mainly corresponds to the UV part of the solar spectrum. It only represents 4% on the solar radiation on Earth, limiting the ability of $TiO_2$ to perform water splitting under solar illumination [70]. Table 3 presents several transition metal oxides with their band gaps and the respective maximum absorbable wavelengths. It must be noted that some metal oxide semiconductors possess a relatively small band gap allowing them to harvest visible light, such as $Fe_2O_3$ or copper oxides. However, they present another major disadvantage: they all suffer from photo-corrosion when they are used as photoelectrodes [71, 72]. This photo-corrosion behaviour makes them unstable in an aqueous environment and hence less suitable for photoelectrochemical water splitting. To overcome those limitations, ternary metal oxides were investigated.

Table 3-1: Examples of metal oxide photocatalysts and their characteristics

| Metal oxide photocatalyst | SC type | Band gap (eV) | Maximum λ (nm) | References |
|---|---|---|---|---|
| $TiO_2$ | n-type | 3.0 – 3.2 | 387 - 413 | [69] |
| ZnO | n-type | 3.37 | 368 | [73] |
| $WO_3$ | n-type | 2.6 – 3.0 | 413 - 477 | [74] |
| $SnO_2$ | n-type | 3.6 | 345 | [75] |
| $Fe_2O_3$ | n-type | 1.8 – 2.2 | 563 - 689 | [76] |
| $Cu_2O$ | p-type | 2 – 2.17 | 571 - 620 | [77] |
| CuO | p-type | 1.2 – 2.6 | 477 - 1033 | [78] |

## 3.2.2. Ternary metal oxide

Ternary metal oxides have been investigated as a more promising alternative to binary metal oxide. These materials are usually studied for supercapacitor applications [79]. They are represented by $A_xB_yO_z$ chemical composition (with A and B transition metal elements), with three categories depending on the A/B/O ratio: $AB_2O_4$, $ABO_{2/3/4}$ and $A_3B_2O_8$. All these different structures (delafossites, perovskites, spinels …) present a large range of n-type and p-type semiconductors; some example materials are presented in Table 3.2 [80]. Compared to binary metal oxides, the addition of another transition metal element in the lattice brings additional atomic orbital interactions, resulting in a change of the electronic band structure. Usually, the band structure of a ternary metal oxide results from the hybridization of the O 2p orbital with the orbitals from both metal cations. The addition of an additional element in the lattice helps to push the valence band upward, resulting in a decreased band gap compared to binary metal oxides [81]. An example is the comparison between $Bi_2O_3$ and $BiVO_4$, where the band gap of $Bi_2O3$ is 2.7 eV [82] whereas the band gap of monoclinic $BiVO_4$ is around 2.4 eV [80]. Other examples of band gaps of ternary metal oxides are presented in Figure 3.3.

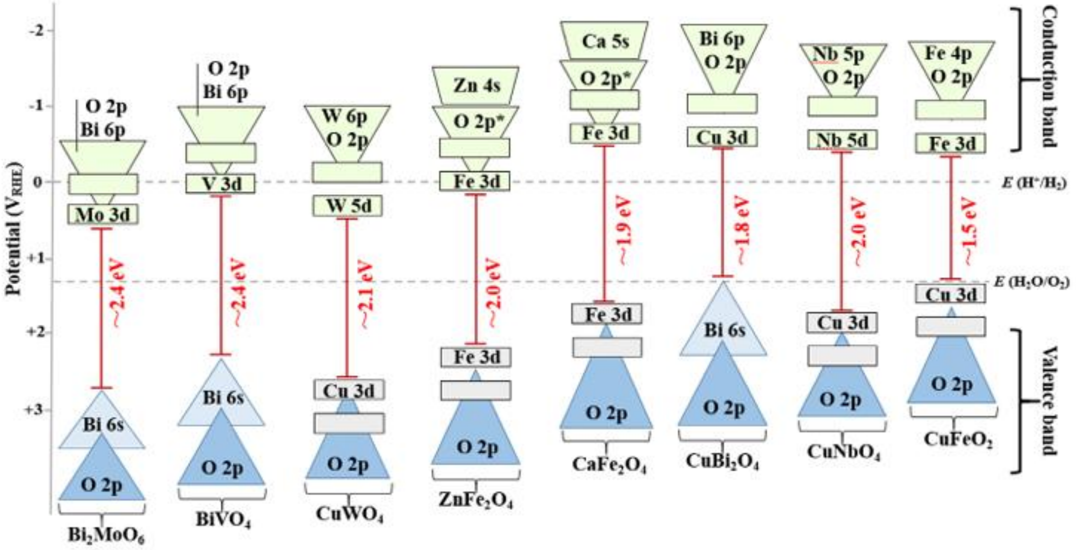

Figure 3.3: Band structures of several typical ternary metal oxide semiconductors [80]

Table 3-2: Examples of ternary metal oxide with band gaps and respective ICPE

| Ternary metal oxide | Structure | Band gap (eV) | IPCE efficiency measured (%) | Reference |
|---|---|---|---|---|
| $ZnRh_2O_4$ | Spinel | 2.0 | 8 | [83] |
| $CaFe_2O_4$ | Spinel | 1.9 | 3 | [84] |
| $CuFe_2O_4$ | Spinel | 1.48 | 18 | [85] |
| $CuFeO_2$ | Delafossite | 1.55 | 1.5 | [86] |
| $CuCrO_2$ | Delafossite | 3.15 | 1 | [87] |
| $CuRhO_2$ | Delafossite | 1.9 | 18 | [88] |
| $CuNbO_3$ | Perovskite | 1.9 | 5 | [89] |
| $BiFeO_3$ | Perovskite | 2.3 | 0.21 | [90] |
| $LaFeO_3$ | Perovskite | 2 – 2.7 | 0.5 | [91] |

### 3.2.3. Efficiencies of ternary metal oxide semiconductors

As discussed in Chapter 2, the photocatalytic phenomenon can be divided into several steps, namely the light absorption for the charge separation, the charge transport for charge carriers' migration to the photocatalyst surface and the charge transfer through the semiconductor/electrolyte interface to drive the redox reactions. Each of those steps can be associated with an efficiency, that allows determination of the IPCE for the photocatalyst, according to Equation (22). It must be noticed that all those efficiencies are intrinsic limits for the photoelectrochemical water splitting process, then they should be all optimised.

The light harvesting efficiency indicates how efficiently the photons are harvested by the photocatalyst. It should be correlated with the band gap value measured for the photocatalyst, as $E_g$ represents the limit for photon harvesting. Nonetheless, light harvesting efficiency gives a useful indication of which range of voltages is more suitable for the photocatalyst to be used. Moreover, as seen in equation (22), its measurement is necessary to estimate the IPCE. An example of the light harvesting efficiency for $BiVO_4$ is provided in Figure 3.4c [92]. Once the electron-hole pairs are created, the charge carriers migrate to the photocatalyst surface to perform the redox reactions, depending on the type of material used. The charge transport efficiency $\eta_{transport}$ estimates the percentage of photogenerated charge carriers that are separated and transported without charge recombination. Ideally, the charge transport efficiency should be as high as possible. However, recombination events within the bulk of a material are caused by intrinsic defects within the lattice (dislocations, grain boundaries …) acting as recombination centres for the charge carriers. The recombination events can also occur at the surface of the material, due to the slow kinetics of the photocatalysts regarding redox reactions. Hence, the surface charge transfer efficiency $\eta_{transfer}$ measures the percentage of charges transferred from the semiconductor to the electrolyte to drive the redox reactions. Examples of the charge transport and charge transfer efficiencies are provided in Figure 3.4a and 3.4b, with $BiVO_4$ thin films produced by Son et al. with a pulsed laser deposition (PLD) method [93]. It was shown that a preferential crystal plane (here (0 1 0) against (0 0 1)) resulted in higher separation and transfer efficiencies. Then, it is possible to optimise the efficiencies by tailoring some parameters of the photocatalysts.

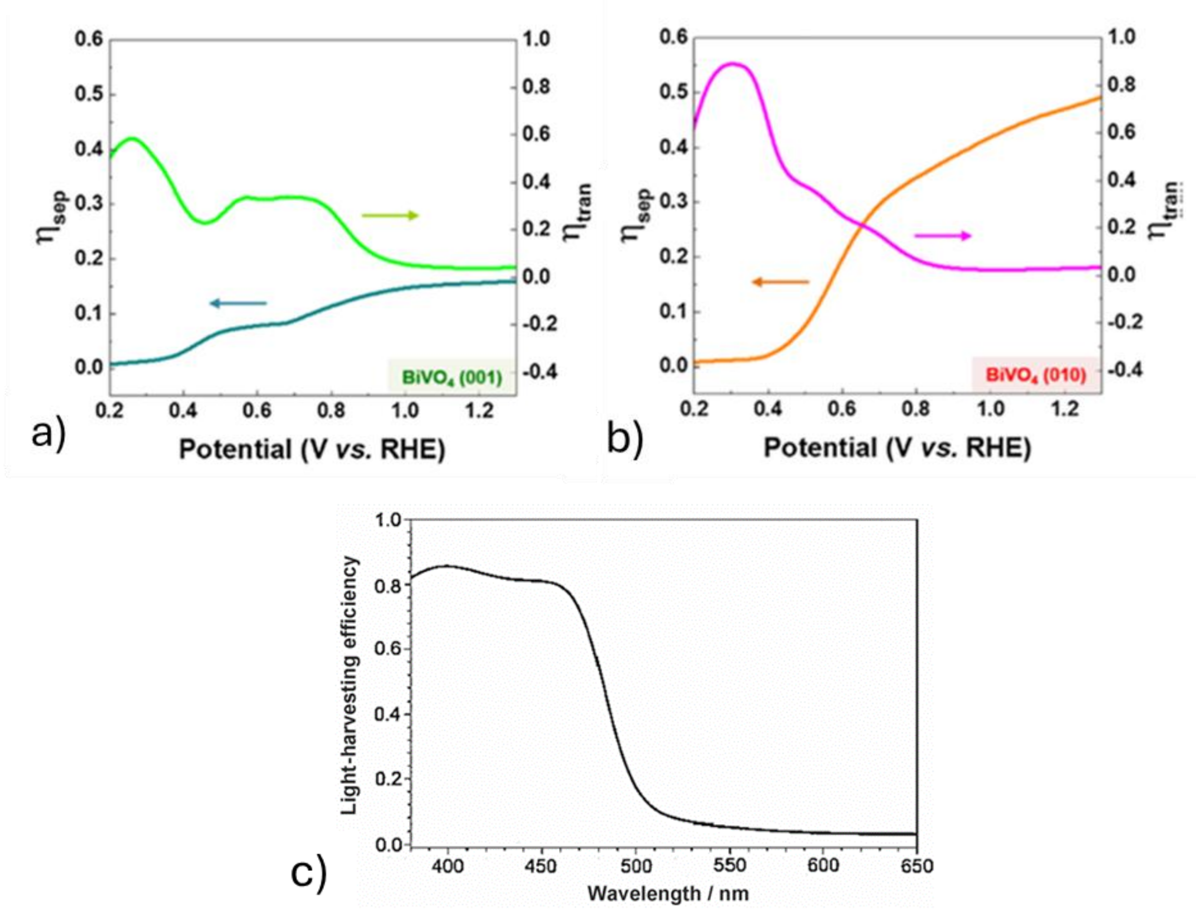

Figure 3.4: Examples of efficiencies for BiVO4 thin films: (a) Charge transport (green) and charge separation (blue) for BiVO4 (001), (b) Charge transfer (pink) and charge separation (orange) for BiVO4 (010) and (c) Light harvesting efficiency [93 , 94]

## 3.3 Enhancement strategies

### 3.3.1. Oxygen vacancies

According to theory, a crystalline material has its constituent atoms perfectly arranged in a periodic lattice. However, different types of defects, such as oxygen vacancies, change this theoretical arrangement of the crystal and hence its physiochemical properties [94]. Oxygen vacancies (VO) are ubiquitous in metal oxide semiconductors and have been first proposed by Tompkins et al. in the 1960s [95]. Since then, VO were found to exist in many photocatalysts, improving their intrinsic properties compared to stoichiometric compounds. VO can act as an active site in (photo)catalytic reactions and enhance the optical characteristics, the electron transport, or the surface kinetics of the material [94]. The electronic structure of the lattice surrounding a vacancy is changed due to the redistribution of charge. One of the main effects of this redistribution if the creation of defect levels in the band gap of the semiconductor, allowing a better absorption of the visible light [96]. Also, these defects levels can act as electron traps, preventing the latter from recombining with holes during charge migration [97]. However, it must be noted that an excess of VO can also reduce the mobility of electrons [98]. This is why the implementation of VO must be controlled.

Several methods for the production of VO in metal oxide compounds have been reported. However, it is rather complicated to control the amount of VO produced during one specific process. Calcination of a sample is one commonly used method to produce VO. Due to the high temperatures, the surface atoms (including surface oxygen atoms) vibrate at high frequencies and surface lattice oxygen can easily diffuse and be lost [94]. This phenomenon has been observed for samples annealed in air [99, 100] or in oxygen-deficit atmosphere [101, 102]. The production of VO by thermal treatment depends then on the production technique and on the compound of study. Chemical reduction is also used, by adding a reductive molecule ($H_2$ or $NH_3$) that adsorbs on the metal oxide surface and captures O atoms to generate VO [94]. Finally, High-Energy Particle Bombardment (HEPB) or ion doping demonstrated their ability to produce OVs in several studies [103, 104].

The most common technique described in literature to establish the presence of oxygen vacancies is X-Ray Photoelectron Spectroscopy (XPS) [105]. This technique is usually used to determine the oxidation state of the surface elements of a sample. In the case of oxygen vacancies, the O 1s high-resolution XPS spectra of a sample can be deconvoluted into several peaks. Specifically, one peak located at around 530.5 – 531.5 eV can be attributed to chemical species adsorbed at oxygen vacant sites [105]. When a defect appears in the lattice, it provides coordinated unsaturated sites for oxygen species chemisorption. As photoelectron spectroscopy relies on the measurement of the kinetic energy of an electron removed from the core or valence level of an atom, no photoelectron signal can originate from a missing oxygen atom in the lattice [106]. Therefore, it is not a direct measurement of the number of oxygen vacancies, but a measurement of the oxygen species chemisorbed on the surface of the sample. This technique is frequently used to assess the presence of oxygen vacancies for many metal oxide semiconductors [107].

### 3.3.2. Dopants and co-catalysts

The introduction of anions and cations into the lattice of a photocatalyst relies on the same phenomenon as the introduction of oxygen vacancies into the lattice, resulting in the formation of distortions in the lattice. This promotes the occurrence of charge carrier trap levels, increasing the charge separation efficiency of the material. Several types of doping are possible, with different effects on the photocatalytic properties:

- Non-metal doping, most frequently with elements having an atomic radius similar to oxygen, such as boron, carbon or nitrogen. Asahi et al. studied the effect of the introduction of non-metal dopants, such as C, N, or S, as substitutional dopants for O in anatase $TiO_2$ [108]. An interaction between non-metal dopants and the O 2p orbital in the valence band was observed. When a non-metal dopant is introduced in the lattice, the 2p orbital from the dopant overlaps with the O 2p, resulting in a mid-gap level close to the valence and then narrowing the value of the band gap. It should be noted that N was used as a dopant with various ternary metal oxides via several methods, usually by using a $NH_3$ treatment at high temperatures [109].
- Noble metals can be used as co-catalysts when added on the surface of photocatalysts to enhance the kinetics of the redox reactions. In the case of noble metal nanoparticles or clusters, the process mainly relies on the surface plasmon resonance (SPR) phenomenon. As seen in section 3.1.1, the electrons are free to move from the valence to the conduction band in conductor nanomaterials. SPR happens when a noble metal nanoparticle is illuminated with light of appropriate wavelength (in the same order as the nanoparticle size), inducing an electron oscillation. When the wavelength of the excited light is higher than the nanoparticle size, called the resonance conditions,

coherent oscillation of all conduction electrons at the metal surface can be generated. Combined with the Schottky junction, an electric field is induced by the contact of metal with semiconductor.

- Incorporation of metal cations in the lattice of semiconductors, which creates additional trap states near the conduction band, acting as electron traps that prevent the recombination with holes. For example, Naing et al. used Co as dopant to enhance the photoelectrochemical performances of $BiVO_4$ photoanode, enhancing the IPCE to more than 40% at 450 nm [110]. The effects of trap states near the conduction band in $BiVO_4$ was also studied by Bakhtaran et al. with the incorporation of Cu in the lattice, increasing the degradation rate of methylene blue [111].

### 3.3.3. Heterostructures

A heterostructure can be defined as an interfacial structure composed of two semiconductor materials with two different energy band structures in contact. These structures enhance several characteristics of semiconductors, such as light absorption or charge separation [112]. It must be noted that the introduction of heterostructures can be combined with other enhancement methods, such as oxygen vacancies to get synergetic effects [113]. Depending on the semiconductors combined, several types of heterostructures can be defined:

- A p-n heterostructure consists of an interfacial region formed by the contact between an n-type and a p-type semiconductor. In this structure, the electrons produced in the CB of the p-type semiconductor are transferred to the n-type semiconductor, while the holes from the VB of the n-type semiconductor migrate to the p-type semiconductor. It then results in the formation of a space-charge region at the interface and a built-in electrical potential, allowing a better separation of the charge carriers. Several photocatalysts have been combined to build p-n heterostructures, such as $GCN/CuBi_2O_4$ or p-NiO/n-ZnO [114, 115].
- In a Z-scheme heterostructure, two photocatalytic systems are put in contact (PS I and PS II), with an electronic medium in between. Under light irradiation, the photogenerated electrons of PS II migrate to the electronic medium, where recombination occurs with the holes from PS I. Meanwhile, the rest of the charge carriers (holes from PS II and electrons from PS I) drive the redox reactions. This type

of heterostructure shows high charge-separation efficiencies and has been studied with several photocatalysts, such as $BiVO_4$/Au/$Cu_2O$ or $CuGaS_2$ /RGO/$TiO_2$ [116, 117].

- It is also possible to combine photocatalyst semiconductors of the same nature to build a heterostructure. Depending on their energy band diagram, heterostructures can be then classified into three categories: straddling gap (type I), staggered gap (type II) and broken gap (type III), as shown in Figure 3.5. Type I or type III heterostructures often exhibit low efficiencies, as they do not possess interleaved energy band structures. In a type II heterostructure configuration, one of the semiconductors has its CB and VB higher than that of the other, establishing a potential difference at the interface between them. This potential difference enhances the charge carrier separation, preventing recombination events. Many photocatalysts can be combined in this way, such as $BiVO_4$/$WO_3$ and $CuBi_2O_4$/CuO [118, 119].

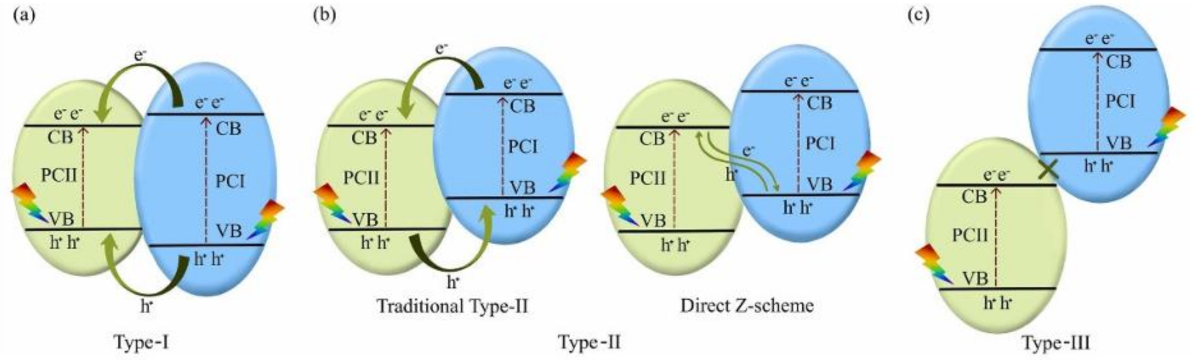

Figure 3.5: Types of heterostructures (a) Type-1, (b) Type-II, (c) Type-III [121]

## 3.4 Examples of materials for photoanode and photocathode

As stated earlier, two different types of photoelectrodes are used in PEC water spliitng: a photoanode, to drive the OER for the production of oxygen, and a photocathode, to drive the HER for the production of hydrogen. Here, two materials are presented as potential photoanode and photocathode

### 3.4.1 Bismuth vanadate as photoanode

Many photocatalysts have been studied to produce an efficient photoanode. In particular, n-type oxide semiconductors fulfil the main requirements to perform the oxygen evolution reaction in a PEC cell. Since the pioneering work of Fujishima and Honda with $TiO_2$ [30], several oxide semiconductors have been studied as n-type photoanode over the past few years, such as $WO_3$ [172], ZnO [173], $Fe_2O_3$ [174] and $BiVO_4$ [175]. All of them are suitable for the oxygen evolution reaction, but they also all have drawbacks that limit their photoelectrochemical properties. For example, $TiO_2$ presents many advantages (easy preparation, low-cost production, stability, non-toxicity), but its absorption efficiency within the solar spectrum is rather limited by its wide bandgap (3.0 – 3.2 eV). Among alternative photocatalysts, bismuth vanadate ($BiVO_4$) attracted a lot of interest in recent years and was first reported by Kudo et al. as a promising visible light photocatalyst [176]. Its narrow bandgap (2.4 eV) makes it a suitable material for harvesting photons from the visible part of the solar spectrum. Moreover, it exhibits good chemical stability. $BiVO_4$ has been studied for many photocatalytic applications, such as dye degradation [177] or antimicrobial activity [178]. Bismuth vanadate compounds present 3 different crystal structures: monoclinic scheelite (m-s), tetragonal scheelite (t-s) and tetragonal zircon (t-z). In both zircon and scheelite structures, the different atoms (V, O and Bi) form 2 different types of units, $VO_4$ tetrahedron and $BiO_8$ octahedron. In the zircon structure, each Bi atom is surrounded by six different $VO_4$ units (eight different $VO_4$ units in the scheelite structure) [179]. This difference induces a change in the band structure between scheelite and zircon $BiVO_4$, as the contribution to the valence band mainly comes from the O 2p orbitals in the zircon structure. The V 3d orbitals contribute to the conduction band, leading to a bandgap of 2.9 eV for the zircon structure. In the scheelite structure, the Bi 6s orbitals overlap the O 2p orbitals, reducing the bandgap value to 2.4 eV. Finally, the V-O and Bi-O bonds do not have the same lengths in m-s and t-s $BiVO_4$. The $VO_4$ tetrahedron and $BiO_8$ octahedron appear to be more distorted in the m-s structure, due to various V-O and Bi-O distances in the units. These distortions promote the transfer and separation of photogenerated charge carriers and then improve the photocatalytic behaviour of bismuth vanadate [179]. For all those reasons, monoclinic scheelite $BiVO_4$ is the main phase of interest for the production of an efficient photoanode. The different crystal structures can be seen in Figure 3.6.

However, as the other n-type oxide semiconductors, $BiVO_4$ photocatalysts present several drawbacks, such as poor conductivity and high charge carrier recombination rates. Several studies have focused on several strategies to improve the photoelectrochemical properties of $BiVO_4$ photoanodes. Among those strategies, introducing heterojunctions [181], co-catalyst coupling [182] and creating oxygen vacancies [183] have shown promising results.

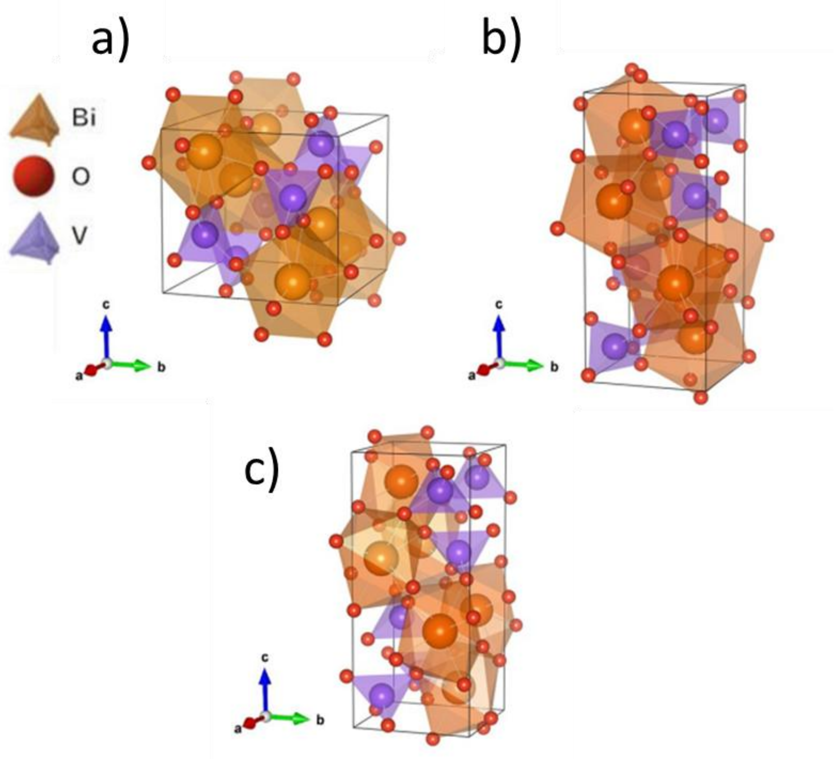

Figure 3.6: Crystal structures of (a) t-z, (b) m-s and (c) t-s $BiVO_4$ [180]

### 3.4.2 Copper bismuth oxide ($CuBi_2O_4$) as photocathode

Similarly to n-type metal oxide semiconductors studied for photoanode production, p-type metal oxide semiconductors are the materials of interest for the study of photocathodes. The latter possess in their lattice several defects due to metal vacancies, acting as electron acceptors and resulting in a production of cathodic photocurrent when illuminated by a light source [218]. Also, their conduction band position is more negative than the standard potential for the proton reduction ($E^0{}_{H^+/H_2} = 0.00\ V\ vs\ RHE$), allowing them to drive the HER. As with n-type semiconductors, materials for the photocathode should be able to harvest visible light (i.e. with a narrow band gap) and should be stable in aqueous environment. Most of those p-type semiconductors are Cu-based oxide materials and are less numerous than n-type metal oxide semiconductors. Binary copper oxides (CuO and $Cu_2O$) are the most common materials for the study of photocathodes, with a p-type behaviour originating from the Cu vacancies in the lattice [218]. On one hand, they show appropriate properties to perform the HER under visible light, with low band gaps (between 1.2 and 1.5 eV for CuO and 2 eV for $Cu_2O$ [219, 220]). On the other hand, their respective redox potentials are located at energetic positions thermodynamically more suitable than HER, making them vulnerable to self-reduction reaction during hydrogen production [221]. Yet, copper oxides possess low onset potentials, meaning they need an applied bias to perform HER, even when illuminated by a light source [221]. To answer those issues, copper bismuth oxide ($CuBi_2O_4$) attracted more and more attention in recent years as a potential photocathode material, with a first study by Sayama et al. in 2007 [222]. $CuBi_2O_4$ have been studied for various photocatalytic applications, from photocatalytic pollutants degradation to synthesis of $H_2O_2$ [223, 224].

Due to its chemical composition, $CuBi_2O_4$ possesses a lower band gap (between 1.6 and 1.9 eV) than copper oxides, allowing it to absorb the visible part of the solar spectrum [225]. DFT calculations were performed to understand the electronic structure of $CuBi_2O_4$. The incorporation of Bi in the lattice results in the hybridization of the O 2p and Bi 6s orbitals, bringing the valence band edge to lower values and thus reducing the band gap. The conduction band results from the interaction between the Cu 2p and O 2p orbitals [226]. This electronic configuration also prevents the material from photocorrosion compared to copper oxides. $CuBi_2O_4$ crystal structure is called kusachiite, which corresponds to a tetragonal crystal structure, with space group P4/ncc (Z = 4). The parameter of the unit cell for $CuBi_2O_4$ are a = 8.4996 Å, b = 8.4996 Å and c = 5.8172 Å. The crystal structure of $CuBi_2O_4$ is shown in Figure 3.7. In the schematic Bi, Cu, and O atoms are represented by blue, orange and red spheres, respectively. It consists of consists of $[CuO_4]^{6-}$ units stacked along the c-axis in a staggered manner, as shown in Fig 3.7a. Bi atoms are incorporated between the stacks of $[CuO_4]^{6-}$ and connected to 6 different O atoms, forming $BiO_6$ complexes with 3 different Bi-O bonds [227].

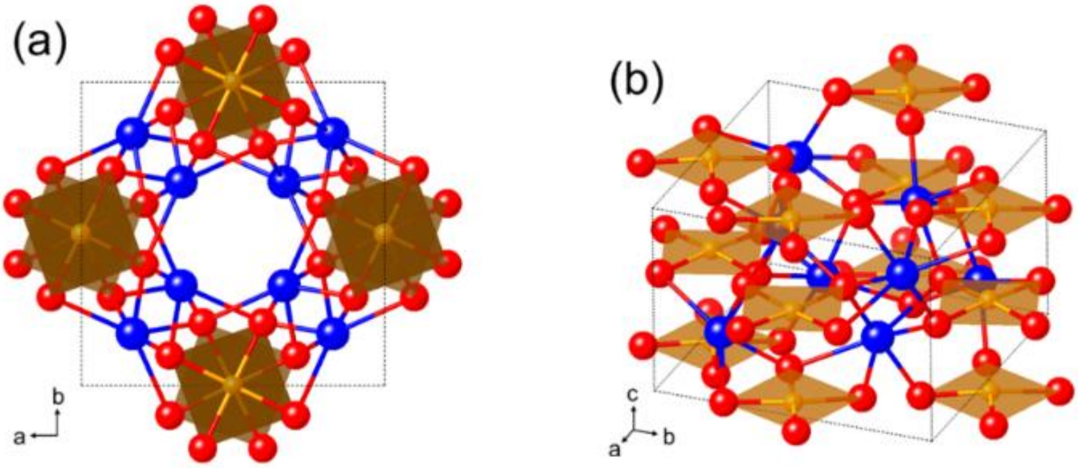

Figure 3.7: a-Drawings of the $CuBi_2O_4$ crystal structure as viewed (a) along the c-axis, (b) at an arbitrary angle (reproduced from [227])

Despite its advantages, $CuBi_2O_4$ suffers from several drawbacks regarding its poor conductivity for charge transportation or poor kinetics regarding the electrochemical reactions of water splitting. The main strategy to enhance the photoelectrochemical properties of $CuBi_2O_4$ is the creation of heterojunction with another semiconductor, such as $CuO/CuBi_2O_4$ for a type II heterojunction or $BiVO_4$/CuBi$_2$O4 for a p-n heterojunction [228, 229].

# 4. Thin film growth and Deposition

*In this chapter, the different techniques used to produce thin films are presented. This chapter focuses on presenting magnetron sputtering as the main technique used in this thesis to produce thin films photocatalysts. The notions of PVD, vacuum, plasma and thin films growth are also presented.*

*The chapter is divided into several sections. Section 4.1 presents an overview of the different industrial techniques used for thin films deposition. Section 4.2 introduces the notion of vacuum and the industrial tools used to implement (pumps) or measure (gauges) vacuum. Physical sputtering is presented in section 4.3, with the notions of industrial plasma and magnetron sputtering. Finally, the thin films growth theory is exposed in section 4.4.*

A thin film can be defined as a layer of material with a thickness ranging from nanometre (monoatomic layer) to several microns. They are used in almost every industrial field, from aeronautic to packaging, as well as electronic or for decorative purposes. The goal of a thin film is to improve the surface properties of a material, which can be mechanical (wear resistance with Diamond-Like Carbon coatings [120]) or chemical resistance (passivation layer with $Al_2O_3$/$Cr_2O3$ protective layers [121]). In the case of this thesis, oxide semiconductors are used as thin films for their photocatalytic properties.

## 4.1 Thin film deposition techniques

Different methods have been used in the industry to produce thin films. In the research field, photocatalyst are produced as thin films mainly by using wet deposition processes, chemical vapour deposition of physical vapour deposition (see Figure 4.1.).

### 4.1.1. Wet chemical methods

Wet chemical methods group all the process used to produce thin films using aqueous chemical precursors. The material of interest is produced by the chemical reactions involving those precursors and is then deposited onto a substrate surface. An annealing step is usually mandatory, to evaporate the solvent or any by-products, and to get a crystalline material. Many wet chemical processes can be used to produce photocatalytic coatings, such as:

- Electrodeposition, where an electric current is used to reduce dissolved metal cations to form the desired compound on the substrate's surface. The main advantage of this technique is the ability to control the thicknesses of the coatings produced [122].
- Spin coating, where the thin film is applied as a solution on a flat substrate, which is spinning at a certain speed to spread the material on its surface. There is a need to synthetise the solution before using soft wet chemical methods, such as sol-gel [123]. The obtained thin film must be then heated to obtain a crystalline photocatalyst.
- Hydrothermal synthesis, where chemical precursors are used to synthetise a suspension of the photocatalyst, which is then heated and filtered for several cycles. This method is very time consuming, as it needs several steps to obtain the crystalline material [124].

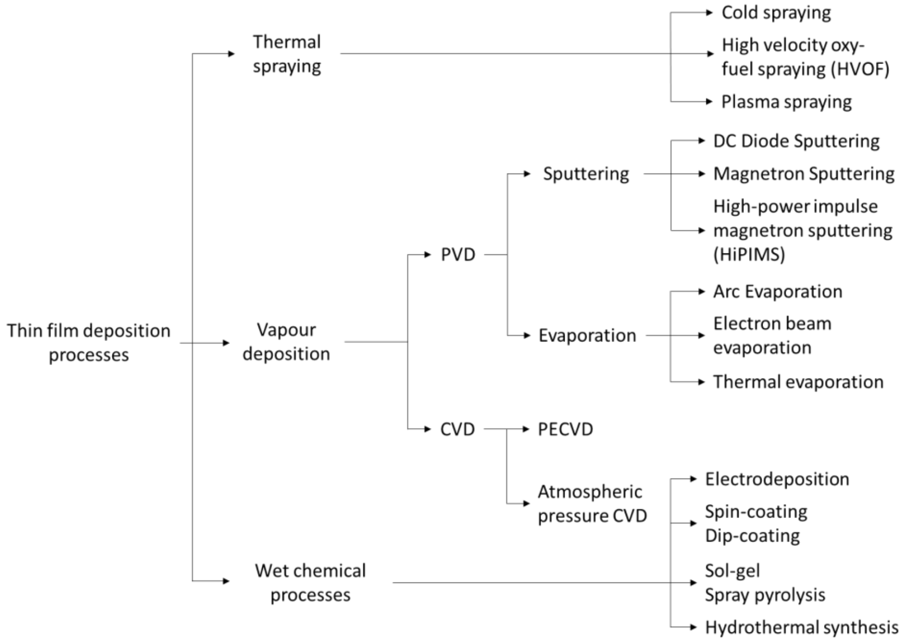

Figure 4.1: Overview of thin film deposition techniques

The main drawback of wet chemical methods is the use of harmful chemicals involved in the processes, that also represents a danger for the environment. In fact, most of those processes need acidic environment to synthetise the photocatalysts.

### 4.1.2. Chemical Vapour Deposition

Chemical vapour deposition (CVD) is a thin film deposition process used in the industry for its versatility and ability to produce coatings on complex geometry substrates. In a chamber, gas phase precursors are introduced with an inert gas carrier (usually argon) and diffuse on the substrate surface. Once adsorbed, the precursors chemically react and diffuse on the substrate surface to form a homogeneous coating. The chemical reactions occurring are various (pyrolysis, reduction, hydrolysis…) and need an important energy input to occur [125]. This energy is usually brought using elevated temperatures (> 900°C), implying high costs and limiting the types of substrates possible. The range of pressure used for CVD processes vary from atmospheric pressure to $10^{-5}$ Pa. Those drawbacks can be avoided by several techniques, such as the use of metalorganic precursors (MOCVD) to lower the temperatures used. Also, the use of plasma enhanced CVD (PECVD) allows to lower the process temperatures around 300 to 500°C [125]. Thanks to a microwave source, a plasma is used to ionise the gas precursors molecules, forming highly reactive species (electrons, ions) that can form the thin film on the substrate surface. The main drawback of CVD processes remains the use of hazardous chemicals as precursors (such as silane $SiH_4$) and produces dangerous by-products that need to be evacuated during the process.

### 4.1.3. Physical Vapour Deposition (PVD)

Physical vapour deposition (PVD) corresponds to the vacuum processes where a vapour made from a solid material condensate onto a substrate surface to form a thin film. PVD requires a medium to high vacuum to operate and vaporise the solid material (from 0.1 to $10^{-5}$ Pa). The vapour can be produced by thermal evaporation, where the source material is heated at elevated temperatures to produce a vapour, or by physical sputtering, where the collision of gas ions with the source material atoms results in the ejection of those latter in a vacuum environment, forming a vapour that condenses on the substrate surface [126]. PVD processes can then be used to deposit a large variety of coatings, from metallic to ceramic, with various thicknesses (from nanometres to microns), on various substrates. However, contrary to CVD, the geometry of the substrates is more limited, due to the directional, line-of-sight, deposition nature of PVD processes. Some examples of evaporation processes are:

- Thermal evaporation, where a material is heated at elevated temperatures and at low pressure. Usually, this technique is used to form a metallic layer onto substrates, but the high temperatures required does not make this evaporation technique cost-effective. [126]

- Cathodic arc evaporation, where a DC arc of high current and low voltage is applied to vaporise a solid material source. The high-density electron cloud resulting ionises the vaporised atoms, producing high reactive species that condensate onto the substrate surface. It is possible to produce ceramic coatings (oxides or nitrides) by introducing a reactive gas in the low-pressure atmosphere. [127]
- Ion plating, where the growing thin films (usually produced with an evaporation technique) is bombarded by a concurrent ion beam directed to the substrate during deposition. This ion bombardment is used to modify the film properties by affecting several growth parameters (changes in the nucleation process, densification of the film microstructure …). However, the technique can suffer from films properties variations due to a lack of the ion bombardment uniformity, or a high substrate heating that limits the type of substrate that can be coated. [127]

One of the main other methods to produce PVD thin films is to use physical sputtering, that is discussed in Section 4.3.

## 4.2 Vacuum

### 4.2.1. Definition of vacuum

In PVD processes, the different physical phenomena used (thermal evaporation, physical sputtering) need a low vacuum environment to work. A vacuum can be defined as a region or a volume that is "empty", where no matter (molecules, particles) can be found. This definition corresponds to the vacuum that exists in the depths of space, where technological vacuum can be defined as a space with a lower pressure than the atmospheric one (101325 Pa) [126]. Usually, vacuum is implemented by mechanically removing the gaseous species from a given volume (for example a deposition chamber) via a pumping system, comprising different types of pumps. Several parameters that define vacuum are important in PVD processes. One of the most important is the mean free path of particles in the chamber. The mean free path of a particle corresponds to the average distance travelled without undergoing collisions. When two particles collide, they lose energy and change directions. PVD processes are considered as directional processes, as the atoms from the solid source are ejected in a preferential direction.

Then, to avoid collisions with other particles, the pressure inside the deposition chamber needs to be as low as possible, to ensure that energetic particles reach the substrate to form the coating. Vacuum pressure is usually measured in Pa and can vary from $10^5$ Pa (atmospheric pressure) to $10^{-7}$ Pa (high vacuum pressure) [128].

### 4.2.2. Positive displacement pumps

To reach the high vacuum needed in PVD processes, a low vacuum needs to be achieved first by removing the air contained in the deposition chamber. In industry, low vacuum is usually implemented using positive displacement pumps. Several types of roughing pumps exist, but the most common positive displacement pumps are the rotary vane pumps. A rotary vane pump is composed of an eccentrically placed rotor and a rotating vane placed in a cylindrical housing (see Figure 4.2). This pump comprises two different chambers, completely isolated one from the other, and both connected to an inlet and an outlet. Firstly, the gas is aspirated through the inlet, thanks to the rotation of the vane, into an expanding space. Due to the position of the rotor and the rotation of the vane, this space and the gas are then compressed and evacuated through an exhaust. This operation is repeated over the time to achieve a low pressure in the deposition chamber. This system is cheap and effective to reach low vacuum pressures but becomes inefficient when it reaches pressure around $10^{-2}$ Pa, as the particle gas density becomes too low [129]. Then, high vacuum pumps are needed to decrease even more the pressure inside the chamber.

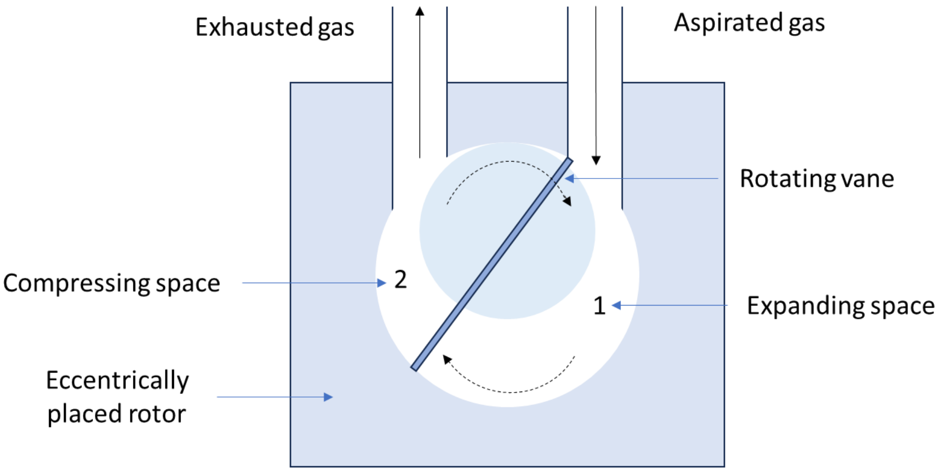

Figure 4.2: Schematic of a rotary vane pump (adapted from [130])

### 4.2.3. High vacuum pumps (turbomolecular and diffusion pumps)

When a gas reaches a low pressure, its behaviour inside the chamber changes from a viscous fluid to a molecular regime flow [129]. A positive displacement pump is then not able to decrease the pressure anymore, and pumps based on momentum transfer are then required to achieve high and ultra-high vacuum. The most common ones are the diffusion pumps and the turbomolecular pumps. In a diffusion pump, a dense, low vapour-pressure liquid (usually oil) is heated until vaporisation. The vapour is then projected at high speed from the centre of the pump to the external body of pump, cooled down with water cooling tubes. The vapour jets collide with the gas particles that enter the diffusion pump, leading them to an exhaust line on the bottom of the pump (see Figure 4.3). The oil vapours are cooled down by the pump walls, condensate and pour down in a reservoir to be evaporated again. This process enables high vacuum until $10^{-8}$ Pa [129]. The main advantage of this type of pump is its high pumping speed, however there is a possibility of oil contamination in the coatings produced. Moreover, the pump cannot be exposed to air due to a risk of oxidising the oil. In a turbomolecular pump, a series of rotor blades are rotating at very high speed (from 20 x $10^3$ to 90 x $10^3$ rpm) and are paired with symmetrical stator blades (see Figure 4.4). This system drags down the remaining gas particles that diffuse into it from the chamber to the bottom of the turbo pumps, toward the roughing pump to be evacuated. Thanks to turbomolecular pumps, high vacuum of $10^{-8}$ Pa can be achieved, and oil contamination can be avoided. However, the specific configuration implies expensive manufacturing costs for turbo pumps [129].

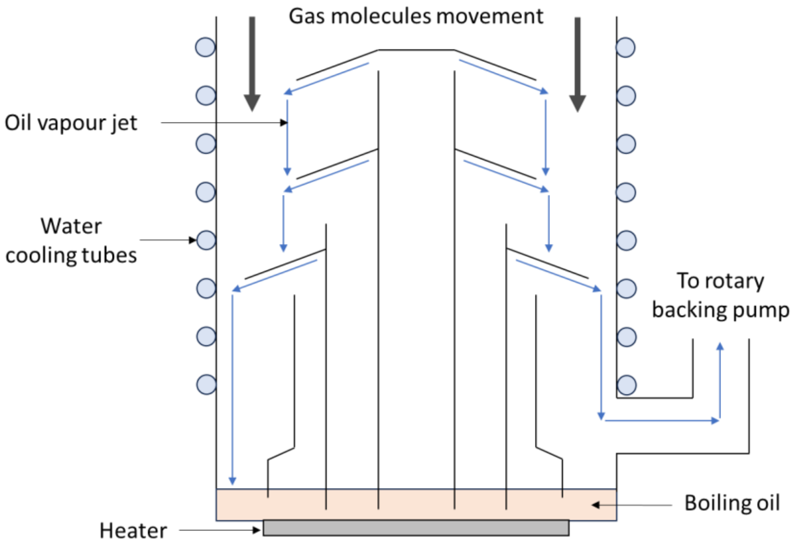

Figure 4.3: Schematic of a diffusion pump system (adapted from [131])

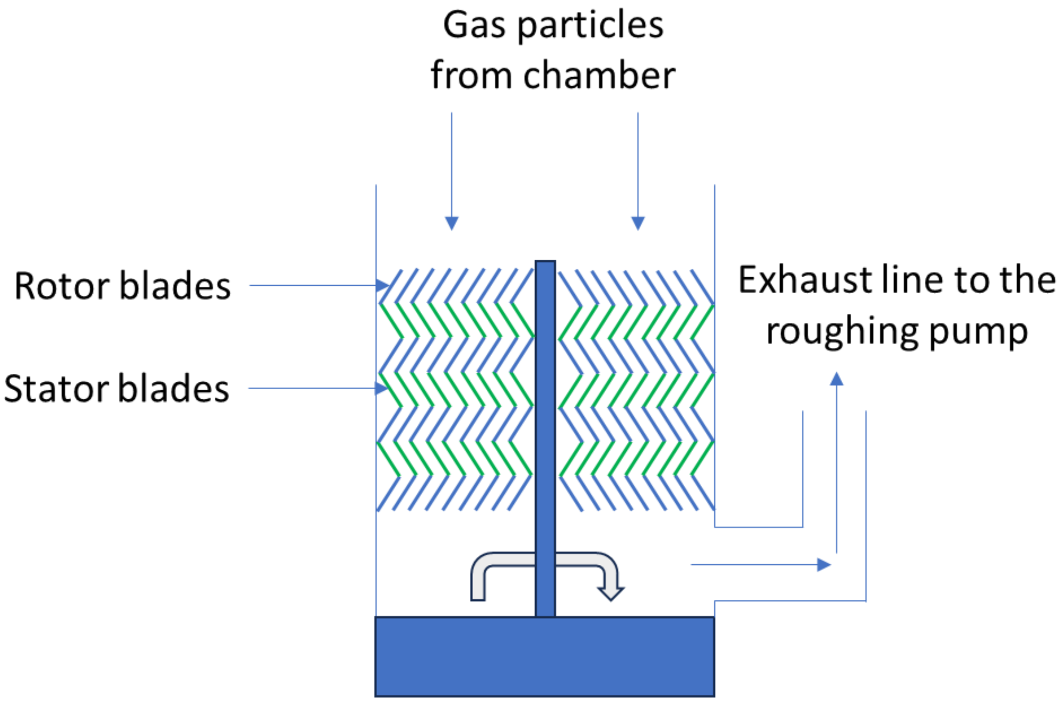

Figure 4.4: Schematic of a turbomolecular pump

### 4.2.4. Vacuum measurement

As a PVD process usually needs high vacuum to be operated, the pressure inside the deposition chamber must be measured to ensure the high vacuum. Different types of gauges can be used to measure the pressure inside a deposition chamber. To measure low vacuum, Pirani gauge is mainly used. A Pirani gauge is made of a metallic wire heated by a current. Due to the gas molecules colliding with the wire, the latter loses heat and its temperature decreases. This temperature loss causes a change in the resistance of the wire, which is measured by a bridge circuit (see Figure 4.5) connected to the heated wire. So, any change of the gas pressure leads to a change of the wire resistance: if the pressure decreases, less gas molecules collide with the wire and its temperature increases. The resulting change of resistance is then converted into a reading of pressure. The masses of the different gases are different and then the heat loss due to the colliding molecules depends on the type of gas. Thus, the Pirani gauge should be calibrated to the type of gas used. It should be noticed that the range of pressures measured varies from 0.13 to 133 Pa [129].

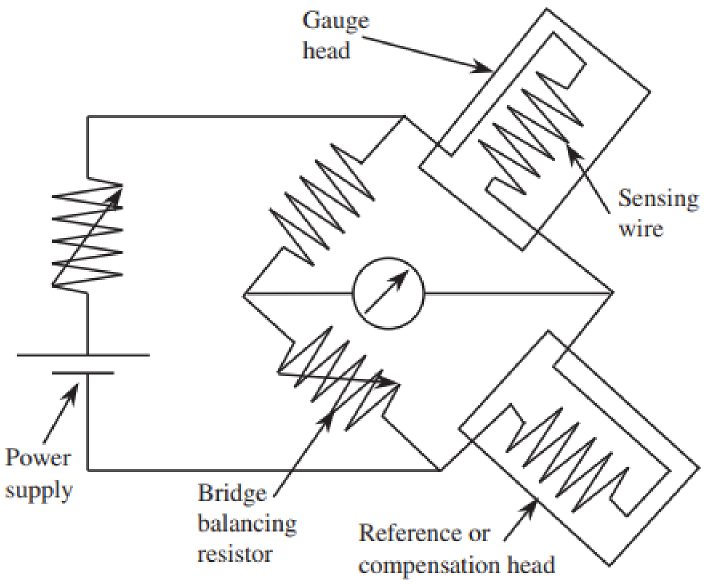

Figure 4.5: Schematic of a Pirani gauge [129]

The Baratron$^{TM}$ gauge (from the name of the manufacturer that first made these gauges available) is a capacitance manometer gauge. It is composed of a tube where a flexible diaphragm separates a reference vacuum from the vacuum of the system studied. Two electrodes are placed on both sides of the diaphragm. When the diaphragm is moved by a change of pressure, the capacitance between the diaphragm and the electrodes changes. This pressure variation can be directly linked to the change of capacitance measured. It does not depend on the type of gas as it only relies on the diaphragm deflection. The Baratron gauge is usually used between 1 Pa and $10^{-3}$ Pa. [129]. A schematic of a Baratron gauge is shown in Figure 4.6. The Penning gauge is a cold cathode ionisation gauge. An anode and a cathode are placed within a magnetic field. An applied potential between the electrodes (around 2 kV) produces a glow discharge. The pressure is indicated by the measurement of the produced ion and electron currents. The higher the pressure, the greater the ion/electron formation. The usual geometry of a Penning gauge is a cylindrical cathode circling an anode, both between the magnets (see Figure 4.7). A Penning gauge only works at a specific range of pressure, as the glow discharge cannot happen if the pressure is too high (too many molecular collisions) or too low (not enough collisions to sustain the glow discharge). The working pressure of a Penning gauge varies from 1.3 Pa to 1.3 mPa [129].

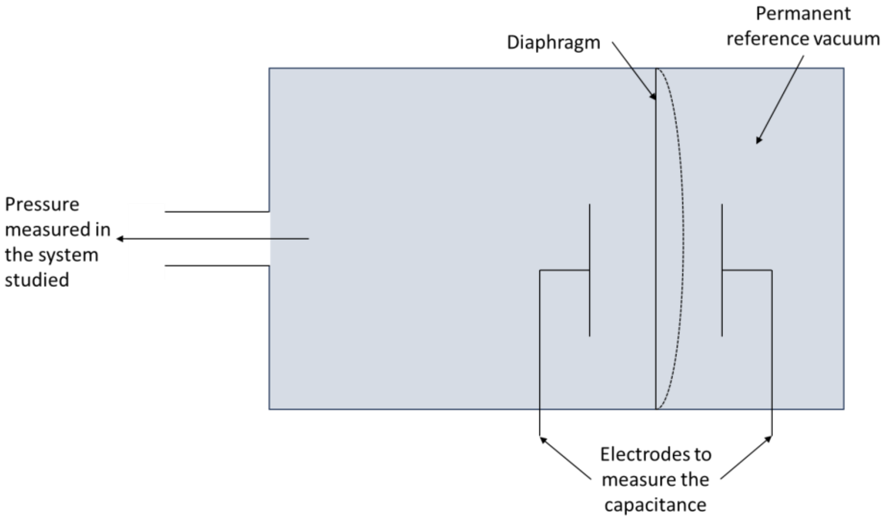

Figure 4.6: Schematic of the Baratron Gauge

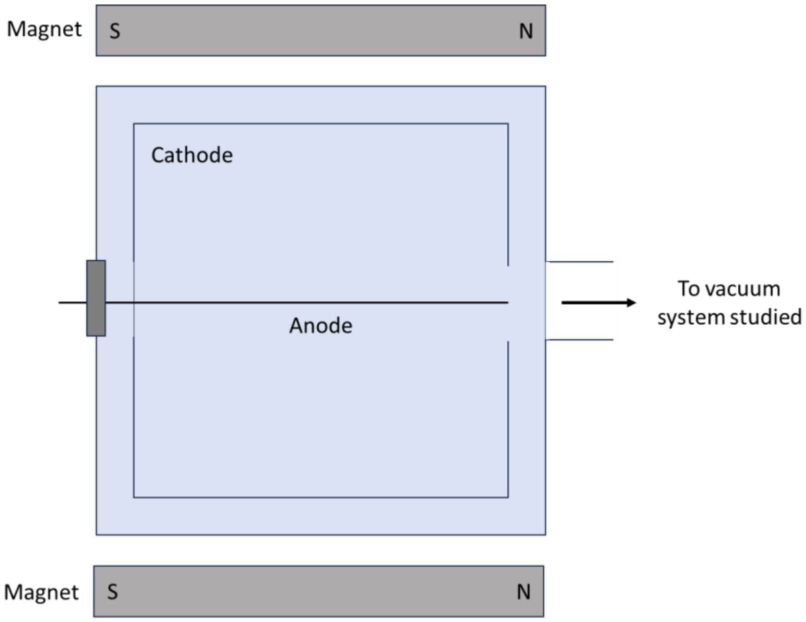

Figure 4.7: Schematic of the Penning Gauge

## 4.3 Physical Sputtering

### 4.3.1. Plasma

Plasma, identified and named by Langmuir in the 20th century, is often defined as the 4th state of matter, after solid, liquid and gas states. The different states of matter can be defined by the way the particles behave within the matter [132]:

- In solid state, the atoms only vibrate, are closely bonded together and cannot move freely within the matter. Their arrangement can be either patterned (crystalline materials) or random (amorphous materials). The shape and volume of solids are clearly defined in space.
- In liquid state, the atoms and molecules take the whole space of its container, while still closely bonded, allowing them to move freely in the container.
- The gas state is a fluid state, where the particles take the whole space of its container and can move freely within without being bounded to each other. Contrary to liquids, gas are compressible fluids.

A plasma is a gas where not only atoms and molecules can be found, but also charged particles, such as electrons, ions, and radical species. It is also called an ionised gas. All those species are moving freely within the plasma, resulting in a conductive behaviour of the plasma (due to the movement of charged particles), despite being a neutral (or quasi neutral) environment [133]. The plasma can be then influenced by magnetic and electric fields. Different parameters can define the temperature of the plasma studied. The average electron energy defines the electrons temperature within the plasma (measured in electron-volts eV) while the electron density (in $cm^{-3}$ or $m^{-3}$) measures the number of electrons for a given volume. The plasma can be then characterised as thermal (hot) or non-thermal (cold). In a hot plasma, the temperature of electrons and the ions are quite similar, whereas a cold plasma possesses electrons with greater temperature than the ions. Examples of hot plasma can be found in space (stars) or in processes that require a huge amount of energy (thermonuclear fusion). Examples of cold plasmas can be found in Figure 4.8, with magnetron discharges or glow discharges. In technological plasmas, a high degree of ionisation of the plasma is required to make the process used efficient. The degree of ionisation can be defined as the ratio between the charged particle density (here the electrons) and the total particle density and can be expressed with Equation (25):

$$\alpha = \frac{n_e}{n_e + n_n} \tag{25}$$

with α the degree of ionisation of a plasma, $n_e$ is the electron density and $n_n$ is the neutral species density [133]. The ionisation process can follow different pathways depending on the way the plasma is produced. In the case of plasma produced in a vacuum environment, the plasma is formed by applying a high electric field between a cathode and an anode, ionising the plasma gas atoms, and generating free electrons. Moreover, a direct ionisation occurs from the inelastic collision between the free electrons produced and gas atoms [134]. The direct ionisation process is described in Equation (26):

$$A + e^- \leftrightarrow A^+ + 2e^- \tag{26}$$

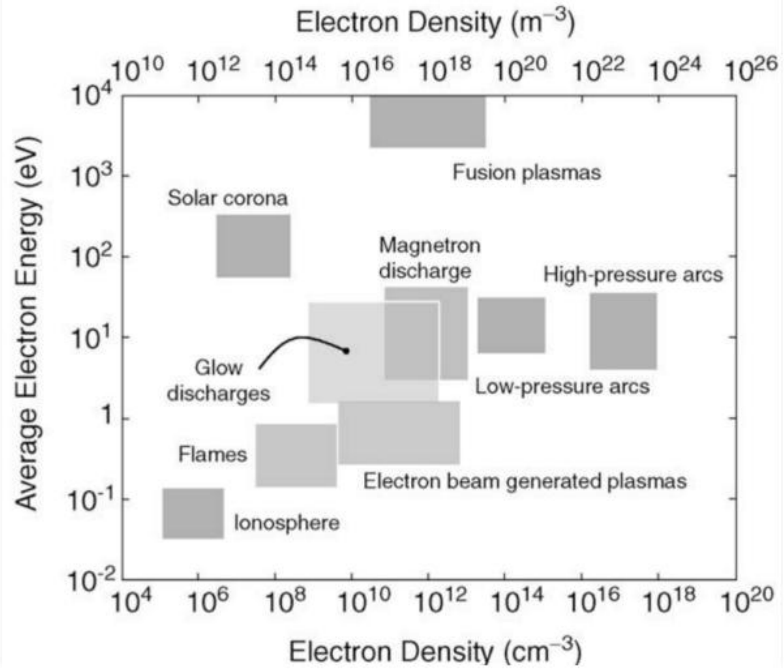

Figure 4.8: Average electron density and energy of various plasma types [132]

### 4.3.2. Sputtering phenomenon

The physical sputtering phenomenon is based on the sublimation of a target material by the bombardment with positive gas ions. It was discovered in 1852 by W.R. Grove [135] and is used for many industrial applications to produce thin coatings. It is usually preferred for industrial applications compared to evaporation for many reasons [136]. The main drawback of evaporation processes is the elevated temperatures used due to the high melting point of several source materials. This requires a huge amount of energy (and so high costs) and limits the type of substrate that can be coated. Moreover, sputtering has demonstrated the ability to produce stoichiometric ceramic thin films on large areas (ex: windows of several square meters) with a high homogeneity.

The principle of sputtering relies on the ejection of the atoms from a solid source material (target) due to the collisions of accelerated gas ions with the target surface. The sputtered atoms then diffuse through the process chamber to condensate on the substrate surface to form a thin film. The process is carried out in a vacuum chamber, and the gas used for sputtering is a noble gas, usually argon. The argon gas is ionised thanks to a negative voltage applied on the cathode (the target material), and the positive ions produced are accelerated toward the target [136]. The collision between the argon ion and the cathode surface atoms results in the transfer of momentum from the ions to the target atoms, ejecting them from the target surface. Moreover, secondary electrons are produced thanks to the collisions, allowing continued ionisation of the argon atoms and then a plasma stability. The number of atoms ejected during sputtering depends on the sputter yield of the material (Y), which corresponds to the number of atoms ejected per incident ions (see Equation 27). Figure 4.9 shows a schematic of the sputtering principle.

$$Y = \frac{\text{removed atoms}}{\text{incident ions}} \tag{27}$$

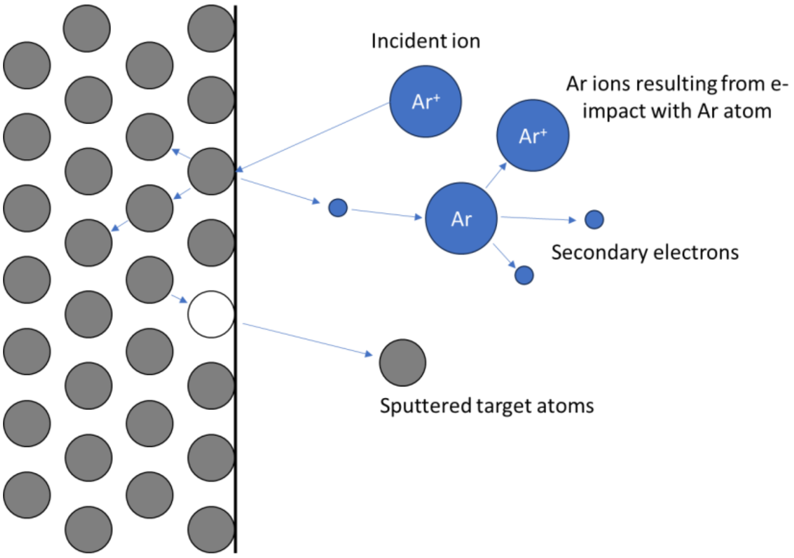

Figure 4.9: Sputtering principle

### 4.3.3. DC Diode Sputtering

DC diode sputtering represents the simplest form of sputtering process and is presented in Figure 4.10. Two plate-electrodes (a cathode and an anode) are placed parallel one to another in a vacuum chamber. The cathode is the target source material, and the anode is the substrate. The plasma forming gas is introduced in the chamber at pressures ranging from 10 to 0.1 Pa. A DC power supply is used to apply a negative potential to the cathode, resulting in a glowing plasma between the electrodes: electrons are removed from the cathode, exciting the argon atoms and ionising them to form a plasma. Then, the same phenomenon describes in the previous paragraph happens: the argon ions are then accelerated toward the cathode, sputtering the atoms from the target to the substrate, forming a coating, with the generation of secondary electrons for the plasma stability [136]. DC diode sputtering is a PVD method that allow the production of thin metallic films. However, several drawbacks can be listed for this technique, such as low deposition rate and low ionisation efficiency. Moreover, the deposition of dielectric materials is very difficult to produce by DC diode sputtering, due to the insulating nature of dielectrics. Radio Frequency (RF) sputtering can be a tool to sputter dielectrics, but the deposition rates remain very low, and the cost of production can be high due to the RF power supply [136]. To enhance the sputtering process, magnetron sputtering has been developed.

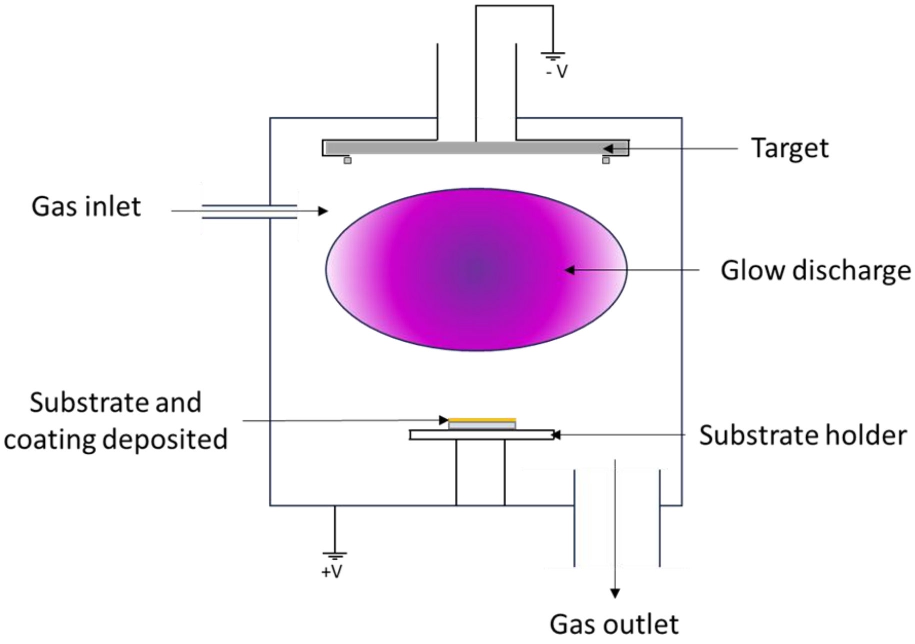

Figure 4.10: DC diode sputtering schematic

### 4.3.4. Magnetron sputtering

As seen before, several drawbacks (low deposition rates and low ionisation efficiency) do not make DC diode sputtering suitable for thin films production at the industrial level. An early study of the influence of magnetic fields onto DC glow discharge by Albert Hull was published in 1921 [137]. In the sputtering processes, a magnetron is a system of magnets placed behind the cathode target during deposition. A centre magnet (or inner magnet), placed behind the centre of the source material target, is circled with magnets of opposite polarity. A permanent magnetic field is then implemented in front of the target and is used to confine the plasma in the target vicinity. A magnetron configuration is illustrated in Figure 4.11. It must be noticed that the magnetic field B implemented is parallel to the target surface [138]. The magnetic field B exerts a force $\vec{F}$ , known as Lorentz Force, onto charged particles in motion described with Equation (28):

$$\vec{F} = q(\vec{v} \wedge \vec{B}) \tag{28}$$

$$\vec{F} = q \times \vec{E} + q(\vec{v} + \vec{B}) \tag{29}$$

with q the electronic charge of the particle, $\vec{v}$ the electron's velocity and $\vec{B}$ the magnetic induction. The electrons are the particles that are governed by this force, as the ions mass is too heavy. An electron subjected to a uniform magnetic field will then have a helical motion, drifting parallel to the magnetic field lines and orbiting around it. During sputtering, an additional electric field $\vec{E}$, perpendicular to the magnetic field, exerts a constant force on the electrons (see Equation (29)). This combination of electric and magnetic fields induces a specific helical motion, known as "E x B drift", where the electrons drift parallel to the cathode surface, but perpendicular to the magnetic field [138]. When using a planar magnetron, this drift path is organised to close on itself, trapping the electrons near the target.

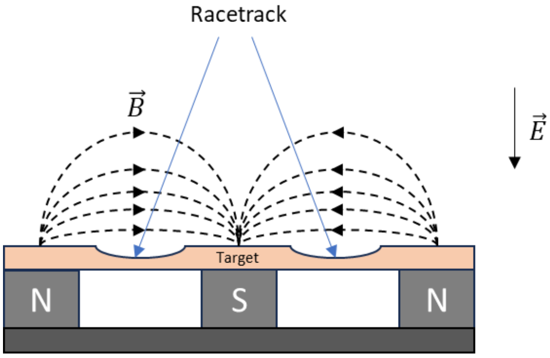

Figure 4.11: Schematic of magnetron configuration used in magnetron sputtering

This electron trap increases the probability of collisions with Ar atoms, leading to a higher degree of ionisation of the plasma in the target vicinity. In addition, the secondary electrons produced by the ion bombardment of the target are also trapped, enhancing the ionisation of the plasma. Magnetron sputtering requires lower Ar pressures comparing to DC diode sputtering, enhancing the mean free path of the ejected atoms and then the deposition rate of the sputtering process. This results in a higher probability to encounter an Ar atom and then to ionise it. The density of $Ar^+$ ions increases in the target vicinity and with it, the ion bombardment on the target surface. The number of ejected atoms is greatly enhanced, allowing higher deposition rates on the substrate. Moreover, more secondary electrons are produced, allowing an efficient ionisation of the argon gas.

The configuration of the magnetron is also a key factor to ensure a higher deposition rate, as the magnets arrangement changes the strength, and directions of the magnetic field lines produces:

- With inner and outer magnets of equal strength, the magnetron is called “balanced”: the magnetic field lines close on themselves, confining the plasma near to the target surface with a high ionisation level. However, this region of dense plasma does not extend more than ten of millimetres from the target, meaning that a substrate out of this region cannot be subjected to ion bombardment (see Figure 4.12a). [139]
- With the inner magnet stronger than the outer ones, the magnetron is a “type-I unbalanced magnetron”: the magnetic field lines are directed toward the walls of the chamber, with a low-density plasma in the substrate vicinity (see Figure 4.12b). [139]
- With the outer magnets stronger than the inner one, the magnetron is called a “type-II magnetron”: the magnetic field lines does not all close on themselves, but some are directed toward the substrate. The plasma is then not just confined in the target vicinity, but is extended towards the substrate, allowing a significant ion current to be transported to the deposited film (see Figure 4.13c). [139, 140]

In industry, the geometry of components to coat varies from simple (flat surfaces for example) to very complex shapes. Therefore, multiple magnetrons are usually used to ensure the production of uniform coatings. Different configurations are then possible in a multiple magnetrons system, where one magnetron is paired with another one of similar or opposite polarity. An example is shown in see Figure 4.11d. When the polarities are the same, the configuration is called “mirrored”: the magnetic field lines are directed toward the walls, resulting in a low plasma density in the substrate vicinity. When the polarities are opposite, the configuration is called “closed-field”: the field lines are linked between the magnetrons, resulting in a high-density plasma in the substrate vicinity and then a high energetic bombardment of argon ions on the growing coating. Their energies are transferred to the adatoms, allowing a higher mobility, and then producing a high quality and dense thin film [141].

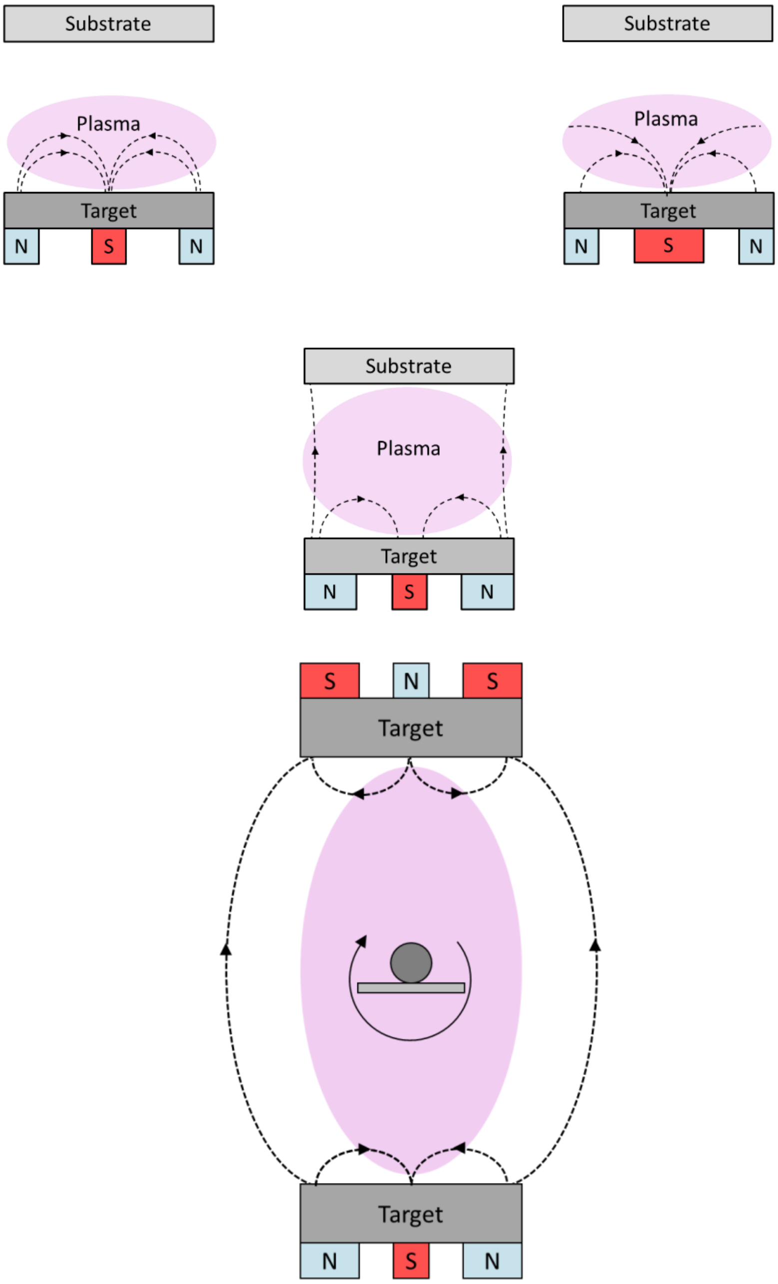

Figure 4.12: Configurations of (top right) balanced, (top left) unbalanced type-I and (top middle) unbalanced type-II magnetrons, (bottom) Closed field configuration with unbalanced type II magnetrons

### 4.3.5. Reactive magnetron Sputtering

Sputtering is not only suitable for the deposition of thin metallic coatings, but also for the deposition of dielectrics and ceramic coatings. Reactive magnetron sputtering consists in the introduction of a reactive gas in the plasma glow discharge to produce the compound of interest ($O_2$ for oxides, $N_2$ for nitrides …). When the reactive gas is introduced, chemical reactions take place onto the surface of the cathode target, forming a compound layer, which acts as an insulator. This phenomenon is called "target poisoning" and affects the usual sputtering conditions for the metallic coatings [142]. The target poisoning can be observed by a hysteresis behaviour of the electrical parameters. An example is given is Figure 4.13, showing the evolution of the voltage applied to a bismuth target as function of the oxygen flow, in an argon/oxygen atmosphere. The hysteresis curve can be divided into several regions, respectively a 'metal mode' and a 'poisoned mode' [142]. The metal mode is characterised by a relatively low reactive gas partial pressure, the compound layer is not built up and the deposition rate stays high. During the poisoned mode, the compound is completely formed onto the target's surface, the electrical parameters completely change, and the deposition rate is drastically reduced. Usually, hysteresis curves exhibit a transition mode, corresponding to a range of reactive gas flow where the hysteresis behaviour occurs. This transition mode corresponds to the deposition of stoichiometric compound at relatively high deposition rates. Optical Emission Monitoring (OEM) systems are usually used to control the reactive gas flow and ensure the deposition of stoichiometric compounds. It must be noticed that the reactive sputtering of ceramic compounds with metallic targets is more convenient that sputtering with dielectric target materials, due to the difficulty to maintain a glow discharge with dielectric cathodes.

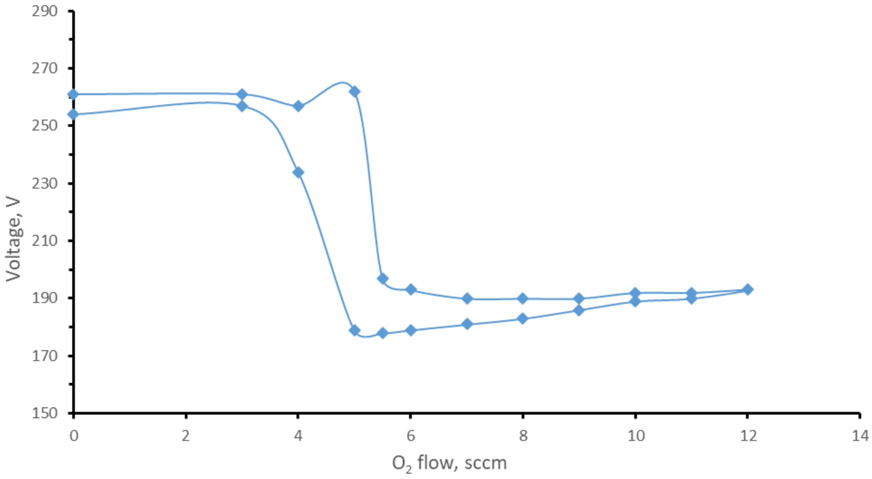

Figure 4.13: Example of hysteresis curve for sputtering process of Bi target in argon/oxygen

### 4.3.6. Pulsed DC magnetron sputtering

The main drawback when using reactive sputtering for the deposition of ceramic layers is the formation of an insulating compound on the surface of the target. Due to their insulating nature, these compound layers act as capacitor, accumulating electrons until they discharge by the formation of electric arcs in the chamber. In the best-case scenario, it can result in the formation of defects in the coatings due to the presence of target ejected. It can also damage the whole device to the formation of electric arcs. Finally, the insulating layer drastically reduces the deposition rate. To overcome these issues, Pulsed DC magnetron sputtering was developed in early 1990s [143]. In DC sputtering, a negative voltage is constantly applied on the target. The idea of pulsed DC sputtering is to periodically switch off the voltage applied on the target (or to switch to a small positive voltage) in order to discharge the compound layer (see Figure 4.14). This period is called "pulse off". To characterise the voltage waveform in pulsed DC sputtering, the duty cycle (corresponding to the ratio between the "pulse on" and the full cycle time) is used. This duty cycle is usually comprised between 50 and 90%, depending on the frequency used (from 0 to 350 kHz) [143]. The combination of pulsed reactive sputtering with the magnetrons closed-field configuration can then be used to obtain defect-free thin oxide layers with a high sputtering rate.

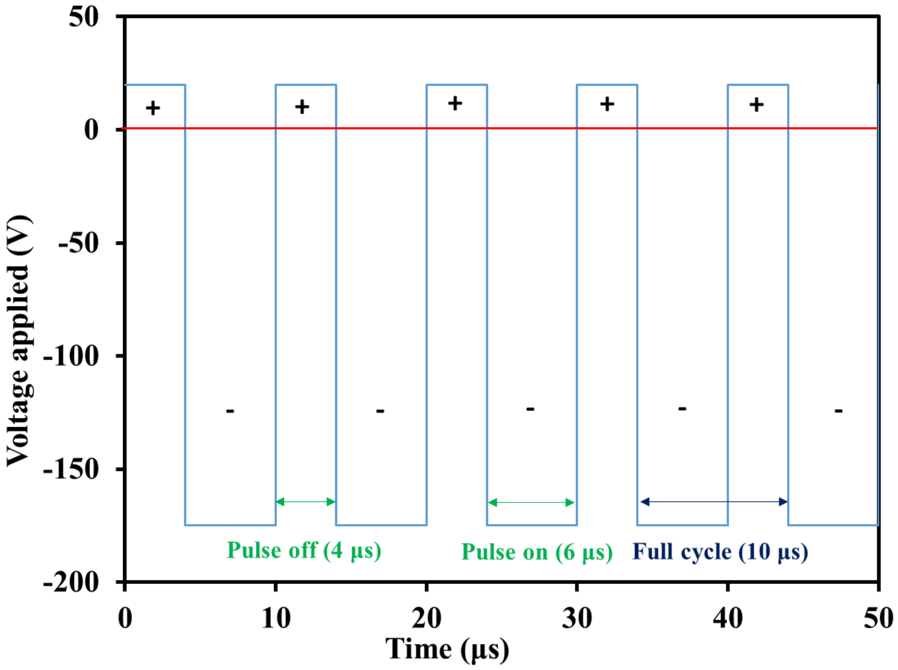

Figure 4.14: Voltage waveform of a power supply operating in asymmetric bipolar pulsed DC mode

## 4.4 Thin films growth

In PVD processes, the ejected particles from the target source material eventually condense onto the substrate to form a thin film. This growth step is a complex process, influenced by several factors, (such as the deposition conditions) and allows the formation of different types of morphology and structures for the thin film.

### 4.4.1. Nucleation-growth

Nucleation growth of thin films with vapor deposition is a typical case of heterogenous nucleation, where atoms from a vapor phase condense onto a substrate made of atoms different than those from the vapor. A basic schematic of atoms condensation in thin film growth is shown in Figure 4.15. Firstly, the evaporated atoms adsorb onto the substrate surface. These atoms (or adatoms) can still have some energy left after the adsorption, allowing them to move around the surface with a certain degree of mobility. This mobility is dependent upon various factors, such as the substrate temperature or the substrate chemistry [144].

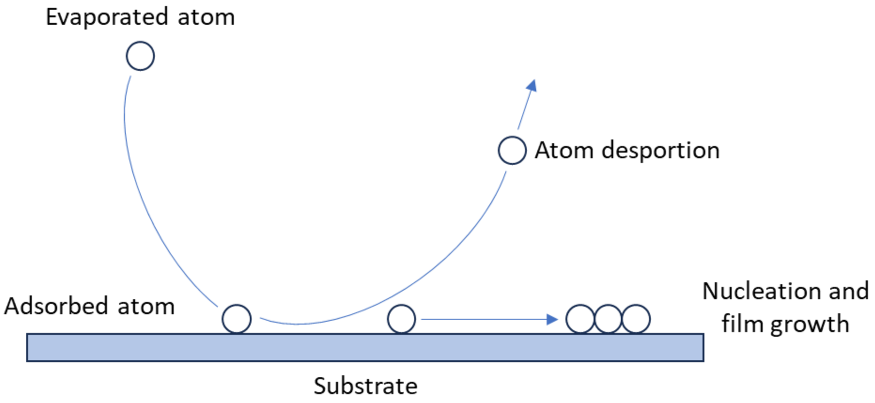

Figure 4.15: Simple schematic of thin film growth on substrate

One of the main factors that influence a thin film growth is the interactions between the substrate and the adatoms. Three main growth modes have been studied (see Figure 4.16) [144, 145]:

- Volmer-Weber growth mode (Island): The binding energies between adatoms are stronger than those between adatoms and the substrate. The adatom-to-substrate interaction is weak, allowing the adatoms to cluster together and to form islands. Those islands represent then preferential nucleation sites for the next adatoms, which eventually coalesce to produce a homogeneous film.

- Frank – van der Merwe growth mode (2D layer): The adatom-to-adatom interactions are stronger than the adatom-to-substrate ones. The adatoms then condensate onto the substrate, forming layers that grow one on top of another.
- Stranski-Krastanov growth mode (2D layer + island): It is a combination of the Volmer-Weber and Frank-van der Merve models. At the beginning of the film growth, and adatom-to-substrate interactions are stronger, leading to the formation of a 2D layer. With the growing thickness of the 2D layer, further layer growth becomes energetically unfavourable and 3D islands start to grow.

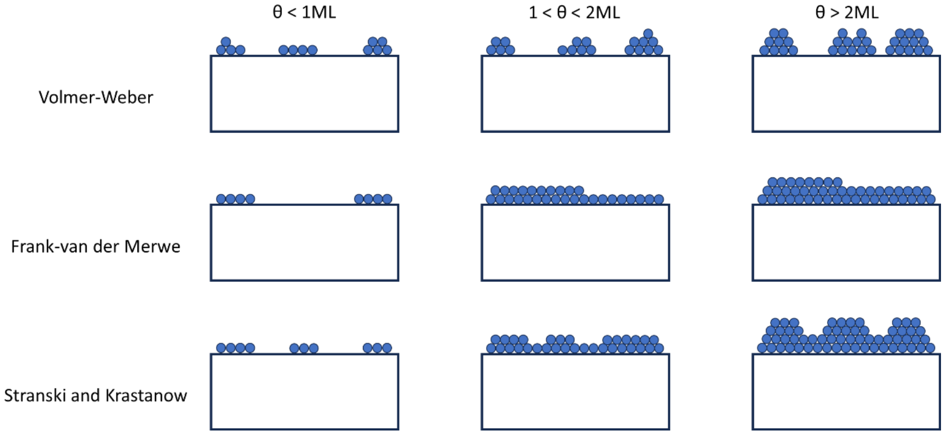

Figure 4.16: Schematic representation of the three possible thin film growth models (ML = monolayer)

It must be noticed that for each growth modes, the interactions between adatoms and the substrate result in surface energies, according to the Young's Equation (30) (see Fig. 4.17) [146]:

$$\gamma_B = \gamma^* + \gamma_A \cos\varphi \qquad (30)$$

where γB is the surface energy of substrate, γA is the surface energy of film material and γ* is the surface energy of film-substrate. Then, it is possible to classify the growth models described above in terms of surface energies. The island growth (φ > 0) mode occurs when $\gamma_B < \gamma^* + \gamma_A \cos\varphi$, whereas the 2D layer growth (φ = 0) is preferred when $\gamma_B > \gamma^* + \gamma_A \cos\varphi$. In a 2D layer + island growth mode, the wetting angle of the adsorbed adatoms tends to increase with the thickness of the monolayer deposited, leading to the formation of 3D islands on top of 2D layers [146].

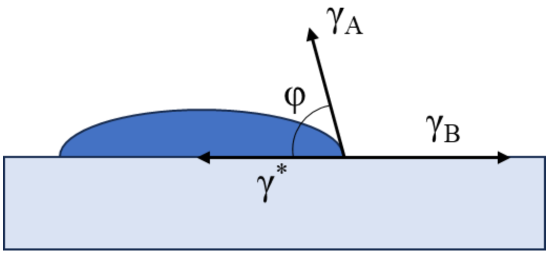

Figure 4.17: Schematic representation of the Young's equation between an adsorb particle and a substrate

### 4.4.2. Microstructure evolution

The evolution of the microstructure of a thin film during the nucleation growth is a parameter of importance, as it defines its final properties. The substrate temperature $T_s$ represent a parameter of importance for the microstructure evolution, as it can provide to the adatoms the energy needed to reach preferential nucleation sites. Different processes related to Ts have been identified [146]:

- Shadowing effect: the adatoms are growing related to the morphology of the surface (roughness). This effect is predominant for low $T_s$.
- Surface diffusion effect: When $T_s$ increases, the adatoms gain more mobility on the surfaces and interfaces (grain boundaries)
- Bulk diffusion effect: The adatoms have a mobility not just on the surface, but also in the bulk of grains.
- Recrystallisation effect: With high Ts, the adatoms can change in crystal orientation and have phase transition.

However, for the deposition of metal and dielectrics, the diffusion of adatoms is also related to the melting temperature of the material $T_m$. In 1969, Movchan and Demchishin proposed a structure zone model (SZM) applicable to the film growth of various metallic coatings [147]. In this model, the morphology of vacuum deposited thin films relies on the homologous temperature, corresponding to the ratio between the substrate's temperature and the source material's melting temperature ($T_s/T_m$). Then, three different growing zones can then be defined (see Figure 4.18):

- Zone I ($T_s/T_m < 0.3$): the adatoms have a low mobility, no diffusion can occur on the substrate surface, the microstructure formed is porous with fine grains.
- Zone II ($0.3 < T_s/T_m < 0.5$): at higher homologous temperatures, some interfacial diffusion can occur, resulting in the formation of columnar structures.
- Zone III ($T_s/T_m > 0.5$): When the homologous temperature is higher than 0.5, bulk diffusion occurs with activation energies above 0.3 eV, resulting in dense films with large grains.

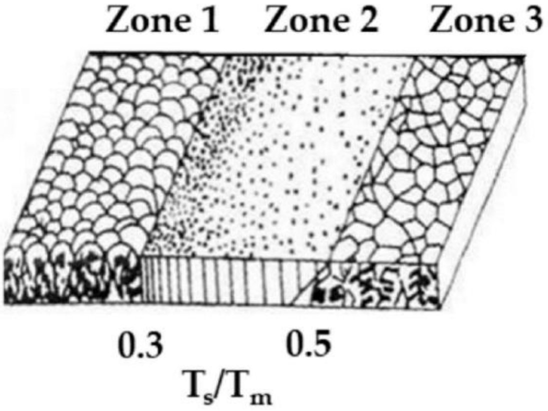

Figure 4.18: Structure zone diagram model from Movchan and Demchishin [147]

The SZM developed by MD was extended several times, to account for the evolution of the PVD technologies and related to their particular operating parameters. For example, Barna and Adamik proposed a model in 1998 related to thin films deposited by thermal evaporation [148]. In 1974, the Thornton SZM describes the crystalline structure of sputtered metal films based on their homologous temperature and the argon gas pressure used during sputtering [149]. In this model (illustrated in Figure 4.19), the previous zones (zone I, zone II and zone III) are still present, with a zone I extended for homologous temperatures higher than 0.3 combined with high argon pressure. However, an additional zone, called transition zone (zone T), is located between zone I and zone II. This transition zone is made of densely packed fibrous microstructure, as the result of the high mobility and diffusion of adatoms, compensating the shadowing effect caused by the low temperature of the substrate.

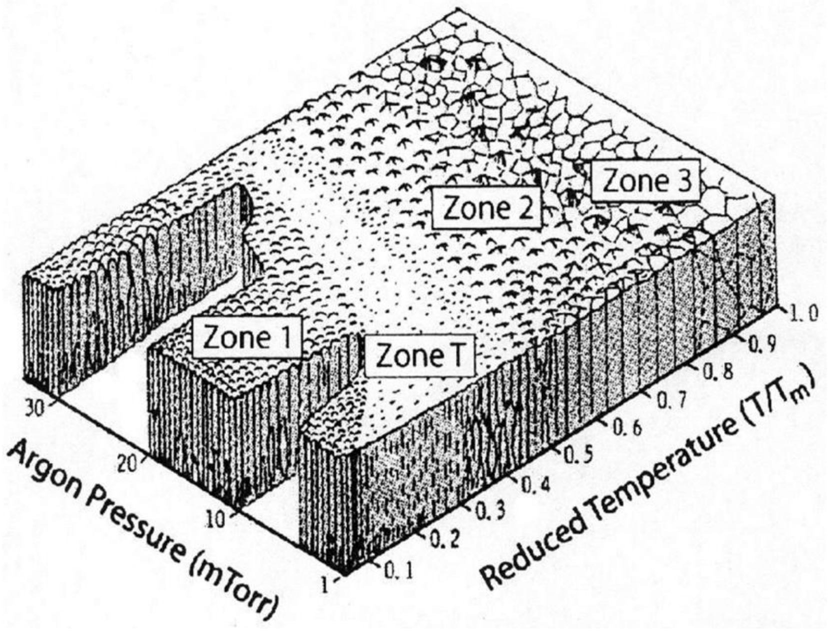

Figure 4.19: Thornton SZM [150]

With the introduction of magnetron sputtering, the plasma produced in sputtering processes becomes denser and more ionised, resulting in energetic ion and atom fluxes that reach the substrate surface. Especially, the energetic ions produced can transfer their energy to the growing thin film, causing rearrangement in the structure of the film, such as adatom displacement or vacancies. The ratio between the ion flux ($J_i$) and the atom flux ($J_a$) then play an important role in the coating's microstructure and can be used to redefine the SZM. In 1998, Kelly et al. studied the microstructure of thin metallic films (Al, Zr and W) produced by closed-field unbalanced magnetron sputtering (CFUBMS) [151]. In this 3-axis model (see Figure 4.20a), the microstructure produced is the result of the homologous temperature, the ratio between the ion and the atom fluxes ($J_i/J_a$) and the bias voltage applied to the substrate. It appears that the formation of porous and voided structures was completely suppressed. The high energetic bombardment of $Ar^+$ ions allowed the formation of dense columnar structures, corresponding to the Zone II and Zone III of the original SZM, but at homologous temperatures far below those required by PVD processes. Moreover, this model allows understanding of the influence of each energy parameter, especially the influence of the ion-to-atom ratio on the coating's microstructure.

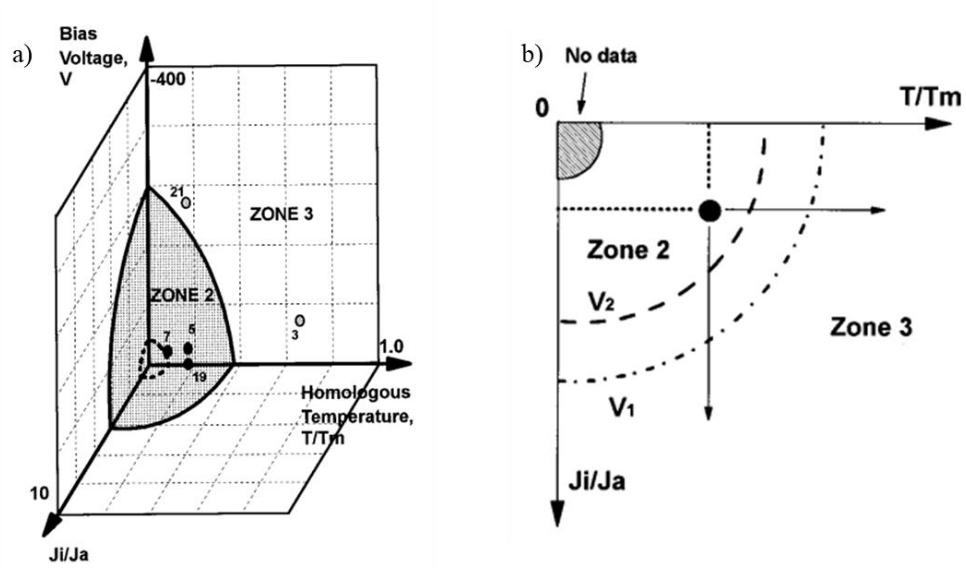

Figure 4.20: (a) Structured zone model proposed by Kelly and Arnell related to the CFUBMS, (b) 2D-slices through SZM at constant bias V1 and V2 (V2 > V1) [152]

# 5. Summary of literature review

The photocatalytic phenomenon appears to be an interesting process to produce green hydrogen from a renewable source of energy (solar energy) with a sustainable source of hydrogen ($H_2O$). The configuration of interest is the photoelectrochemical water splitting, where two photoelectrodes are used to drive the overall water splitting reaction by harvesting the light from an illumination source. Many configurations can be studied, all presenting drawbacks and advantages. However, several factors currently limit the efficiency of binary metal oxides photocatalysts like TiO2, such as their limited light harvesting efficiency, due to their high band gap. Nowadays, the photocatalysts of interest are the ternary metal oxide semiconductors, who presents advantages such as lower band gaps. The main challenges of these photocatalysts remains their poor efficiencies regarding the kinetics of the redox reactions associated to the overall water splitting reaction. Several ternary metal oxide semiconductors have been identified as potential candidates to be used in a tandem PEC water splitting cell. Especially, $BiVO_4$ and $CuBi_2O_4$ appears to be the most interesting photocatalysts to be used as photoanode and photocathode, respectively.

Different techniques for thin films production have been presented in the previous chapter. Despite the fact that all presents some advantages, the technique chosen for the production of photocatalysts coatings used as photoelectrodes is pulsed DC magnetron co-sputtering. Its versatility, scalability for potential upscaling and repeatability makes it a suitable technique for the production photoanodes and photocathodes. In addition, it represents an interesting field of studies, as most of the literature is dedicated to chemical solution deposition for the production of photoelectrochemical thin films. It can then represent one of the novel contributions of the thesis. Moreover, several properties of the photoelectrodes produced can be optimised by pulsed DC magnetron sputtering, such as their thicknesses, compositions or their morphology. All of these parameters are of importance regarding the photocatalytic phenomenon applied to water splitting.

The following part presents the methodology used in this work to produce efficient photocatalyst thin films by pulsed DC reactive magnetron sputtering, the analytical techniques used to characterise them (morphology, crystal structure, composition …) and the analytical techniques used to assess their photoelectrochemical properties.

# II. Methodology

*This chapter presents information about the thin film deposition technique used for the production of coatings discussed in this thesis, including vacuum measurement, reactive gas control and types of power supplies used. The Teer Coatings UDP350 sputtering rig used for the coating production by pulsed magnetron sputtering method. Following, the different analytical techniques used in this thesis are presented, divided in several sections for each characterisation technique.*

## 6. Experimental techniques

### 6.1 Thin film deposition technique

All photocatalysts were deposited using a Teer Coatings Ltd UDP 350 sputtering rig (see Figure 6.1). To achieve a high vacuum, with a base pressure of $2e^{-3}$ Pa, a combination of rotary vane (BOC Edwards 40) and turbo molecular (Leybold TMP1000) pumps were used. The pressure was monitored by using three different gauges: Pirani, Penning and Baratron (capacitance manometer). The coatings were deposited using rectangular metallic targets (300mm x 100mm), vertically placed in a close field configuration with unbalanced type II magnetrons from Teer Coatings Ltd (see Figure 6.2a and b). The substrates were placed on a rotatable substrate holder to ensure the uniformity of the coatings deposited. During the deposition runs, the rotation of the substrate holder and the distance between the targets and the substrates were kept constant (4 rpm and 20 cm, respectively). The argon flow was maintained at 40 sccm, and several oxygen flow rates were used (10 or 20 sccm) depending on the material deposited. The magnetrons were powered in pulsed DC mode using an Advanced Energy Pinnacle Plus power supply, with two channels at a frequency of 100 kHz and 60% duty cycle. Different substrates were used during depositions to be used in different experiments:

- Fluorine-doped tin oxide (FTO) coated glass from Pilkington®, with a resistance sheet comprised between 12 and 14 Ω/sq, to produce photoelectrodes for photoelectrochemical tests.
- Fisherbrand ™ soda-lime glass microscope slides, to study the photocatalytic activity of the samples produced.
- Si wafer for analysis of compositions (EDX).

The substrates were all ultrasonically cleaned in acetone and then isopropanol prior to deposition. All chemicals were purchased from Sigma Aldrich, unless stated otherwise. For the production of bismuth vanadate coatings, metallic bismuth and vanadium targets (300mm x 100 mm, 99.5 % purity) were used simultaneously, as shown in Figure 34. The vanadium target was replaced by a copper target when copper bismuth oxide was produced. The targets were used in a close-field configuration to ensure a high ionic bombardment [152] of the substrates during the deposition and then the formation of dense coatings.

Figure 6.1: Teer Coatings Ltd UDP 350 rig

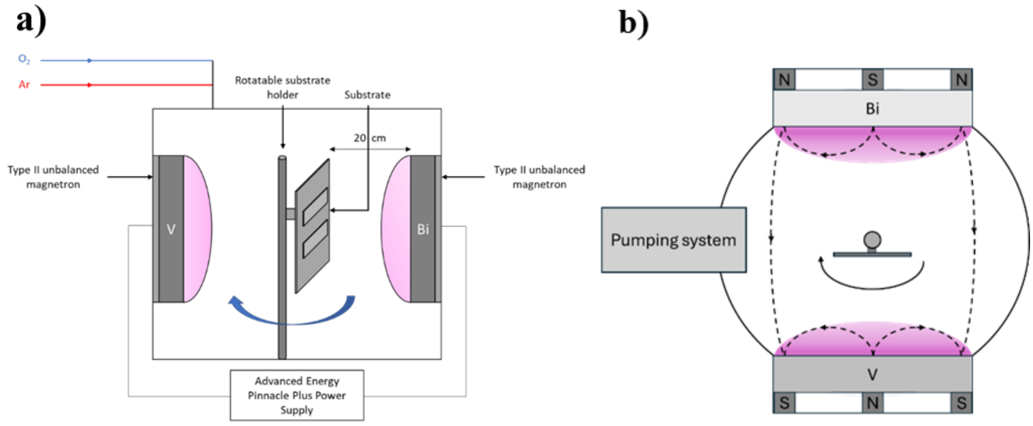

Figure 6.2: (a) Schematic of the UDP 350 sputtering rig configured for $BiVO_4$ thin film production; (b) Close-field magnetrons configuration for the production of $BiVO_4$ thin films

## 6.2 Photoelectrochemical cell configuration

A typical electrochemical cell consists of two electrodes, an anode and a cathode, immersed in an aqueous electrolyte solution. The cell itself can have different shapes (rectangular, cylindrical…) and configurations (one or two compartments, presence of ion exchange membrane for the separation of reactive species). This part will be discussed in Chapter 8. A system of electrolyte circulation can also be implemented. One additional parameter of the PEC cell comparing to the usual electrochemical cell is the ability to let the light penetrate through the cell to reach the photoelectrodes. Moreover, a specific illumination area must be well defined to be able to compare one measurement to another. Figure 6.3 presents the three-electrode configuration of the PEC cell used in this thesis. The cell used in the thesis is based on the one developed by Lopes et al., and is composed of several parts [163]:

- A transparent acrylic body with a capacity of 100 mL (1).
- Two quartz windows ((2), at the front and back of the transparent acrylic body) of 5 x 5 cm$^2$, that defines the maximum illumination area of the samples tested. The presence of two windows allows an illumination of the photoelectrode from back and front, depending on the number of light sources used.
- Two removable metallic frames (front and back) used to press the quartz windows against an O-ring by means of twelve screws.
- Two black acrylic masks (3) placed next to the metallic frames, allowing an illumination area of 5 x 5 cm$^2$.

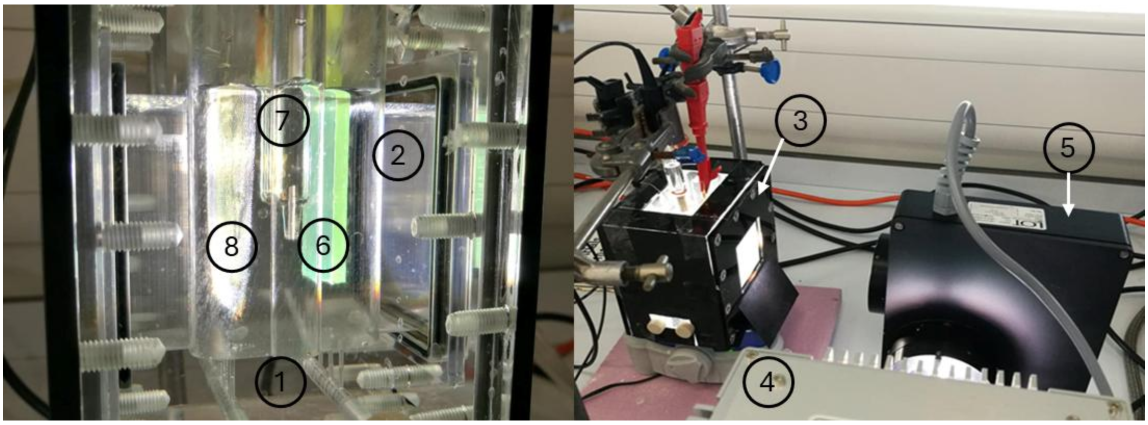

Figure 6.3: Configuration of the PEC WS cell (1) Cell acrylic body, (2) Transparent quartz window, (3) Dark acrylic mask, (4) Xe light source, (5) Electronic light shutter, (6) Working electrode, (7) Ag/AgCl reference electrode, (8) Pt mesh counter-electrode

The photoelectrochemical measurements performed in this work were done in a three-electrode configuration. As it is shown in Figure 6.3, the PEC configuration is composed several elements.

- In a three-electrode configuration, three different electrode are used: the working electrode, the counter-electrode and the reference electrode. The working electrode (WE, (6) in Fig. 6.3) is the electrode where the reactions of interest are studied. In PEC water splitting, the WE is usually made of a thin layer of photocatalyst deposited onto a transparent conductive substrate. The conductive substrate is used to ensure that the charge carriers produced by the photocatalyst properly flow from the WE to the CE to ensure the chemical reaction occurring on the other reaction site. The back contact between the substrate and the photocatalyst should be good enough to ensure an efficient charge transfer to the external circuit [165]. Usually, fluorine-doped tin oxide (FTO) and indium tin oxide (ITO) are used as conductive substrates. Also, the transparency of the substrate is an important parameter if utilising an illumination from the back face of the photoelectrode. In this work, the WE was composed of a thin layer of $BiVO_4$ (for the photoanode) or $CuBi_2O_4$ (for the photocathode) deposited by magnetron sputtering onto a FTO substrate. For the working electrode, the geometric surface area in contact with the electrolyte was defined by applying an epoxy resin mask (see Figure 6.4). Each samples was defined with a 1 $cm^2$ geometric surface area to ensure the comparison between the samples.
- The counter electrode (CE, (8) in Fig. 6.3) provides the reaction site for the other half-reaction of water splitting, which should have a large surface area and fast kinetics, so as not to limit the circuit current. The common CEs for the n-type photoanode and p-type photocathode are Pt and $RuO_2$ (or $IrO_2$), respectively [165]. In this work, the counter electrode used was a Pt mesh (5 x 5 $cm^2$, 99%, Sigma Aldrich).
- The reference electrode (RE, (7) in Fig. 6.3) in a three-electrode configuration is used to ensure that the potential of the WE are applied and measured with respect to a well-defined electrochemical potential scale. Saturated calomel electrodes (SCEs) and Ag/AgCl Res are usually used. In publications on PEC water splitting, the applied potential measured with respect to a SCE or Ag/AgCl reference electrode is normally converted into the reversible hydrogen electrode (RHE) scale for easy comparison between reported data in the literature [165]. The conversation process is based on their potential with respect to the standard hydrogen (SHE). For instance, the potential

applied on the RHE scale with a reference electrode Ag/AgCl in a 3.0 M solution of KCl can be determined with the following equation:

$$E_{RHE} = E^0{}_{Ag/AgCl} + 0.059 \times pH + E_{Ag/AgCl} \qquad (39)$$

where $E_{RHE}$ is the potential on the reservable hydrogen electrode (RHE) scale, $E^0{}_{Ag/AgCl}$ is the standard potential of the Ag/AgCl electrode (0.197 V vs RHE when using a saturated KCl solution) and $E_{Ag/AgCl}$ is the potential applied with respect to the Ag/AgCl reference electrode. In this work, the reference electrode used was a Ag/AgCl reference electrode (E0 = 0.197 $V_{RHE}$).

- To ensure the conductivity between the photoelectrodes and to complete the electrical circuit, an electrolyte with a good ionic conductivity should be used. It must be noticed that the electrolyte should not react with the photoelectrode to avoid any degradation during the measurement. For example, $BiVO_4$ is usually used with neutral electrolyte ($Na_2SO_4$, $K_2SO_4$ or $KH_2PO_4/K_2HPO_4$) because of the degradation is bismuth compounds in acidic environments [164]. For acidic electrolyte, $H_2SO_4$ is usually used (to ensure the presence of $H^+$ protons) and KOH or NaOH are usually used for alkaline electrolytes. Finally, the electrolyte should not contain any other redox couple than the one studied, to avoid any side redox reactions. In this work, the electrodes were immerged in an aqueous electrolyte (0.5M $Na_2SO_4$, prepared from anhydrous $Na_2SO_4$ powder from Sigma Aldrich, 99% purity). The three electrodes were connected to an Autolab potentiostat from Metrohm (PGSTAT302N) to perform the different photoelectrochemical measurements.

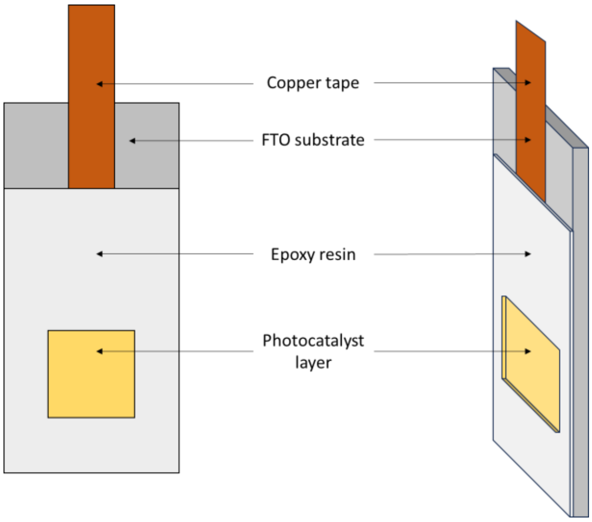

Figure 6.4: Schematic of a masked working electrode

The light source system (4) used in this thesis is composed of a Uniform Arc light source system LSU308 from Quantum Design, powered by a 150 – 300 W arc lamp system LSN354. The lamp used is a 300W Xe lamp, as it reproduces the AM 1.5G spectra (see Figure 6.5), and the optical system includes an electromechanical shutter. A series of filters is placed on the light source, a 325 nm UV filter (to protect the user from the high energy UV radiation produced by the light source) and an Air Mass filter from Newport (81094). The light source used is also equipped with an electronic shutter, to alternatively switch off and on the illumination onto the WE. The light source was placed at approximately 18 cm distance to ensure a uniform output illumination on the sample and to obtain a total power density for the light source of around 100 mW.cm$^{-2}$, measured with the use of a photodiode.

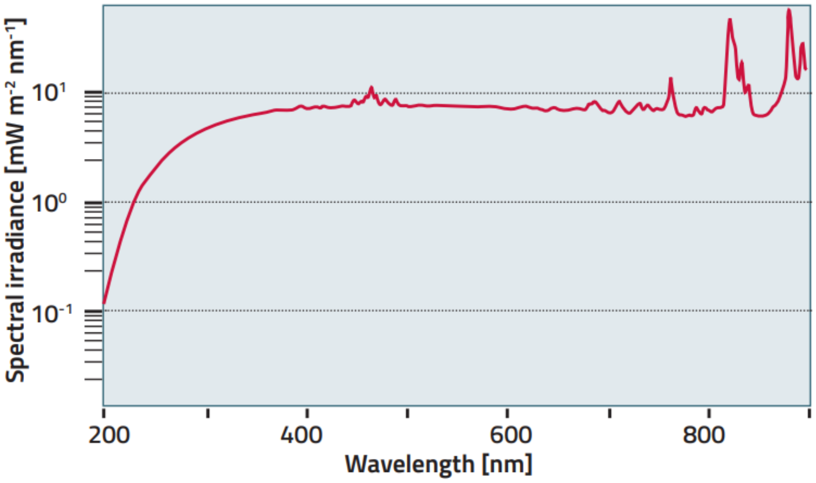

Figure 6.5: Typical Xenon spectra of ozone free lamp from Quantum Design (reproduced from technical Data sheet, product LSB530)

# 7. Analytical techniques

## 7.1. X-Ray Diffraction

X-rays are a type of electromagnetic radiation, produced by electronic transitions with the electrons releasing their energy [153]. Due to their high energy and short wavelength (in a range of $10^{-10}$ m or Ångstrom), X-rays have a better ability to penetrate matter. X-rays are largely used today in different fields, from medicine (production of radiography) to geology (phase identification of minerals). Thus, X-Ray Diffraction is a powerful analytical technique used for the identification of crystal phases in solid materials.

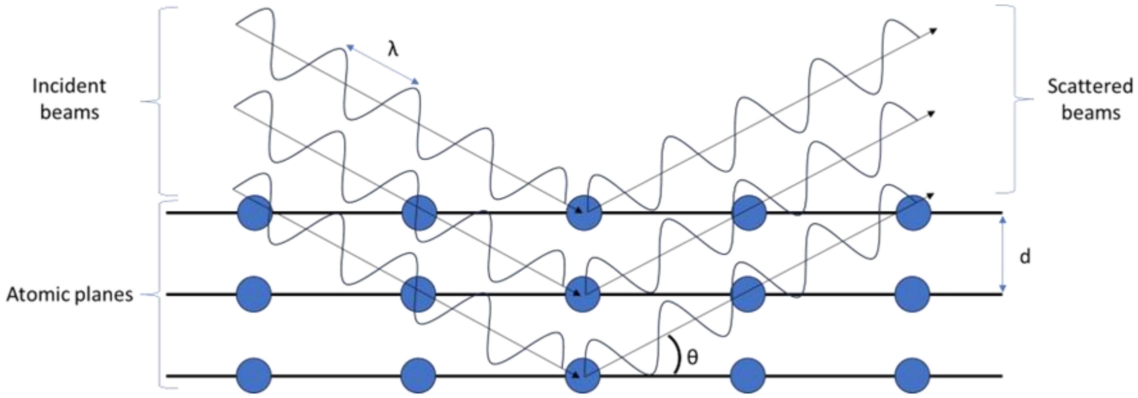

Figure 7.1: Principle of X-Ray diffraction

To produce X-Ray, a tungsten filament is heated in a vacuum environment to produce a higher energy electron beam which is directed towards a metal target (in this case copper). The electron beam causes the release of core electrons from the copper atoms, which are replaced by outer electrons that release energy equal to the transition energy between electron orbitals, thus producing an energetic and monochromatic radiation source. The wavelength of the X-rays produced depends on the nature of the anode (for example, $K_\alpha Cu = 1.54$ Å and $K_\alpha Mo = 0.71$ Å) [153]. Due to the periodic nature of a crystalline structure, and the similarity in feature size to the radiation wavelength, the X-rays produced are diffracted to produce constructive or destructive radiation and captured by an X-Ray detector, leading to diffraction patterns that are characteristic for each crystalline material (see Figure 7.1). The relation between the X-Ray beam diffraction angle and the crystal lattice is determined by the Braggs equation (Equation (31)):

$$n\lambda = 2d_{hkl}sin\theta \qquad (31)$$

where n is an integer, $\lambda$ is the wavelength of the X-ray beam, $d_{hkl}$ is the crystal lattice spacing and $\theta$ is the diffraction angle. The identification of the crystal structure of a material is crucial as a compound can exist in different crystal phases. For example, bismuth vanadate is reported to have different crystal phases with different lattice spacings (i.e. monoclinic and tetragonal), which has a significant impact on the photocatalytic performances. In this work, the photocatalysts crystallinity was assessed by X-Ray diffraction. The XRD patterns were obtained using a PANalytical Xpert system, with $CuK_\alpha$ radiation (0.154 nm) with the accelerating voltage and applied current set to 40 kV and 30 mA, respectively. The diffraction patterns were recorded in grazing incidence mode at 1°, with a $2\theta$ range of 15 to 60° in steps of 0.025° at a step time of 0.88s per step. The XRD were then identified using the International Centre for Diffraction Data (ICDD). In addition, in-situ XRD measurements were done on the $BiVO_4$ photoanodes to analyse the evolution of the XRD patterns with the temperature, starting from room temperature to 500°C with an increment of 100°C.

## 7.2 Raman Spectroscopy

Raman spectrosocpy is a non-destructive spectroscopy technique that relies on molecular vibrations to characterise the structure of a material. The Raman scattering phenomenon is based on the interaction between a monochromatic light and samples bond vibrations. When a monochromatic light source illuminates a material, the incident photons interact with the molecules, transferring their energy to the electron clouds. Those electrons are then excited for a brief moment, passing from an energy state to a virtual excited one, then relax by emitting a photon. Two types of interactions exist:

- The elastic interactions (Rayleigh scattering), where the scattered photons and the incident ones vibrate at the same frequency ν0.
- The inelastic interactions, where the scattered photons have a different frequency than the incident ones. This phenomenon is known as Raman scattering. When the frequency measured of the scattered photon is lower than the incident one (ν0-νR), this is known as Stokes Raman scattering. Anti-Stokes Raman scattering are measured for a higher frequency measured (ν0+νR). This frequency shift (νR) corresponds to the molecular vibration frequency. Hence, Raman Spectroscopy consists in measuring this molecular vibration frequency via the shift in scattered light frequency, which is specific to the composition and structure arrangement of the analysed material [154].

Raman shifts are usually measured in wavenumbers ($cm^{-1}$) and Raman spectra are plotted with count rate in ordinate and wavenumbers in in abscissa. In this work, the thin films produced were analysed by Raman Spectroscopy with a Raman Renishaw Invia with a 514 mm laser, with a power of 10mW and a long working distance microscope objective with a 50x magnification. The Raman spectra were recorded on different wavenumbers range, detailed in the results chapter for each photoanode and photocathode.

## 7.3 Scanning electron microscopy and Energy dispersive X-Ray spectroscopy

Scanning electron microscope is a powerful tool that allows the observation of a sample at a high magnification to analyse the microstructure and the morphology of a sample. Based on the interaction between a primary electron beam and the matter of the sample analysed, the information collected by the different detectors can either allow the formation of images or the collection of information about the chemical composition. A scanning electron microscope is usually composed of an electron gun, used to generate an electron beam, focused on the sample by an array of electromagnetic lenses. A vacuum is maintained in the sample chamber to avoid the collisions between primary electrons and residual gas particles, and the acceleration voltage can be up to 30 kV. A primary electron beam, generated by an electron gun, is accelerated towards the sample's surface. The primary electrons spread through the sample by inelastic and elastic collisions in a small volume, resulting in the emission of different particles (as shown in Figure 7.2):

- Secondary electrons (SE2) correspond to the electrons ejected after the inelastic collisions occurring between the primary electrons and the electrons from the sample's surface. The secondary electrons detected produce a detailed image, used to study the morphology of a sample.
- Backscattered electrons (BSE) correspond to the electrons produced by the inelastic collisions between the primary electrons and the nucleus of the sample's surface. With BSE imaging, the heavy elements appear brighter than the light ones, resulting in high resolution images produced.
- Finally, when a primary electron ejects an inner shell electron, it leaves a positively charged hole, which is then filled by an electron from a higher energy shell. This latter one releases an excess of energy in the form of X-Rays, characteristic of the atomic number (as shown in Figure 7.2). Hence, collecting those X-rays emitted can allow us to determine the elements present in the analyse sample. This technique is called the energy dispersive X-Ray spectroscopy (EDX) [155].

Scanning electron microscopy was performed to analyse the morphology of the coatings produced. A Zeiss Supra 40 VP-FEG-SEM was used to produce top surface and cross-section images with a SE detector and generated with a 2kV electron beam. As the samples studied are composed of poor conductive materials, a thin layer of gold was sputtered on top of the samples to enhance their conductivity and ensure the production of good quality images. EDX was also performed with an EDAX Trident system, performed on an imaged area of 100 µm² under an acceleration voltage of 20kV to analyse the composition of thin films. 3 different areas of each samples were analysed to obtain an average of the composition of the samples analysed.

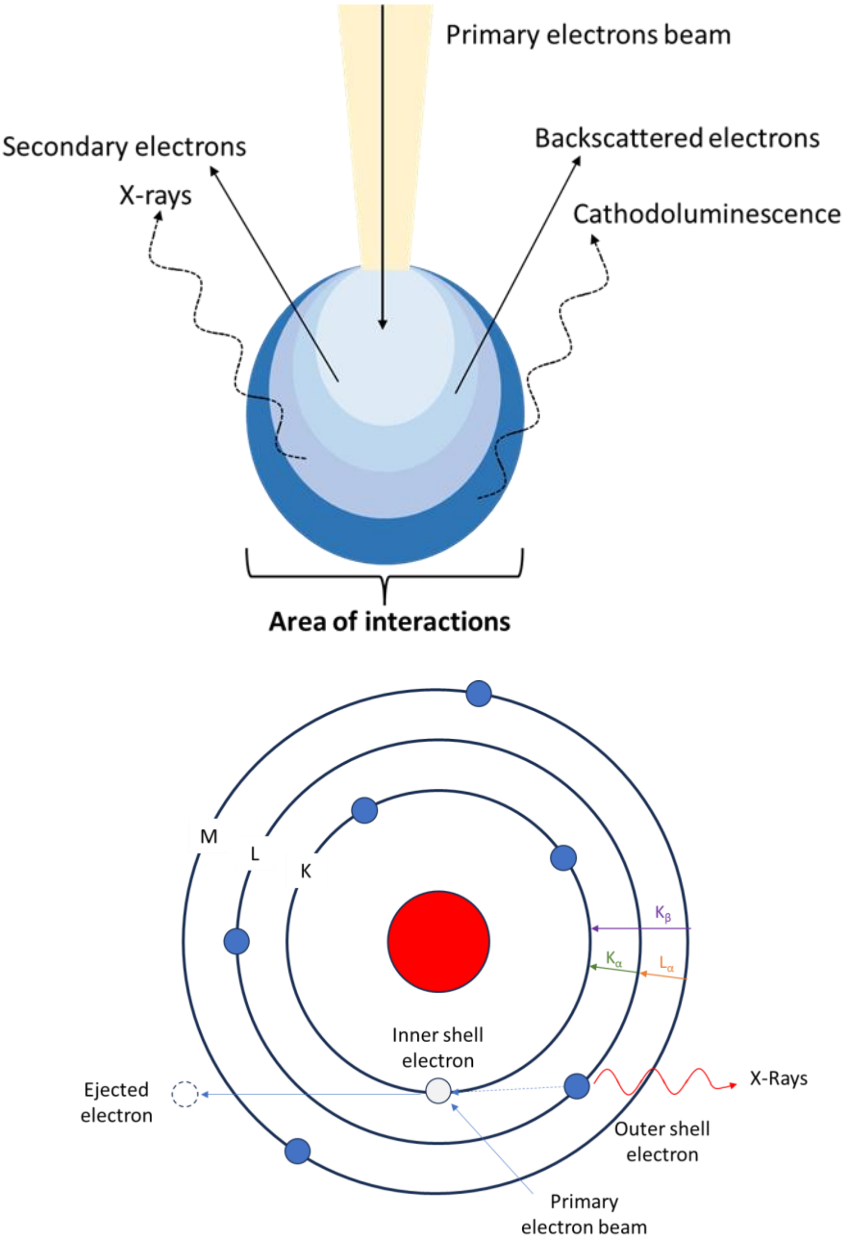

Figure 7.2: (top) Electron-Matter interactions and particles emitted; (bottom) X-Ray emission in EDX (adapted from [155])

## 7.4 Transmission Electron Microscopy

Transmission electron microscopy (TEM) is an advanced versatile characterisation technique. Contrary to SEM, the principle of TEM relies on the electrons that passed through the matter when accelerated toward a sample.  The range of information provided by TEM is quite large, with information about the crystalline structure, the morphology, or high-resolution images. The acceleration voltage is higher in TEM compared to SEM (several 200 kV) and the operation is carried out in a vacuum environment. TEM is made of similar components than the SEM (electron source, electromagnetic lenses to focus the electron beam) and a charge coupled device (CDD) for high-resolution images acquisition. As it relies on transmitted electrons, the sample's thickness should be around 100 nm [156]. Two different modes, bright-field and dark-field, are based on the transmitted and diffracted electrons, respectively:

- In the bright-field mode, the objective aperture is positioned in the back focal plane of the objective lens, allowing only the transmitted electrons to pass through the aperture. Electrons pass through different mass density within the sample, resulting in bright (light atoms) and dark (heavy atoms) areas on the screen.
- In the dark-field mode, the objective aperture is positioned in the image plane of the objective lens. The transmitted electrons are then blocked and only the diffracted electrons can pass through the aperture. A diffraction pattern is then obtained, showing series of rings with dots for polycrystalline materials (single array of dots for single crystal materials).

During this work, The TEM analysis of BiV samples produced by reactive magnetron sputtering was carried out at the Leeds EPSRC Nanoscience and Nanotechnology Facility. The thin films were prepared via FIB-SEM with a FEI Helios G4CX FIBSEM for lamellae extraction. The extracted lamellae were then analysed by HRTEM using a FEI Titan Themis FEG STEM in bright-field mode operating at 200 kV. In addition, STEM elemental mapping was performed by EDX spectroscopy.

## 7.5 Atomic force Microscopy (AFM)

Atomic force microscopy (AFM) is a scanning probe microscopy technique used to produce topographic images of a sample surface down to the atomic level. Here, the probe is a sharp tip (cantilevered force sensor) placed close to the sample surface. In the case of a repulsive force between the tip and the sample, the cantilever is deflected upward, while in the case of an attractive force, the cantilever is deflected downward. The deflexion is proportional to the force applied to the sensor, as described by Hooke's law (Equation (32)):

$$F = k.x \tag{32}$$

Where F is the force applied on the cantilever, k is the spring constant of the cantilever and x is the distance of deflection. The probe is then mechanically moved all around the sample thanks to a piezoelectric scanner controlled by a computer, to produce an image of the whole surface of the sample. Finally, a laser is reflected on the back of the cantilever to a position sensitive photodiode detector. The movements of the cantilever implied by the topographical changes in the sample are then tracked and sent to a feedback control system to produce a topographic image of the sample. A schematic of AFM instrument is shown in Figure 7.3. Different modes can be used with an AFM instrument:

- Contact mode, where the cantilevered force sensor is kept in physical contact with the sample. As the probe raster scans the surface, the deflection of the cantilever is used to record the topographic changes and then produce an image [157].
- Tapping mode (or intermittent contact), where the tip is oscillated at its resonance frequency close to the sample surface. The oscillation amplitude is firstly great and reduced when the tip comes in contact with the sample surface. This reduced amplitude is used to fix a separation distance between the tip and the sample. This reduces the tip wear and sample damaging [157].
- Finally, the non-contact mode is similar to the tapping mode, without bringing the tip into contact with the sample surface. When the topography of the surface changes, a frequency shift of the cantilever is observed, due to the attractive Van der Waals force. This frequency shift is then used to produce a topographic image [157].

In this work, a first AFM measurement was performed onto one BiV and one BiCu samples, to obtain a first idea of the roughness and confirm the morphology obtained in SEM top surface micrographs. Here, AFM measurements were done on a Horiba XPlora Plus system, in tapping mode, equipped with a polygon-based pyramid shape tip.

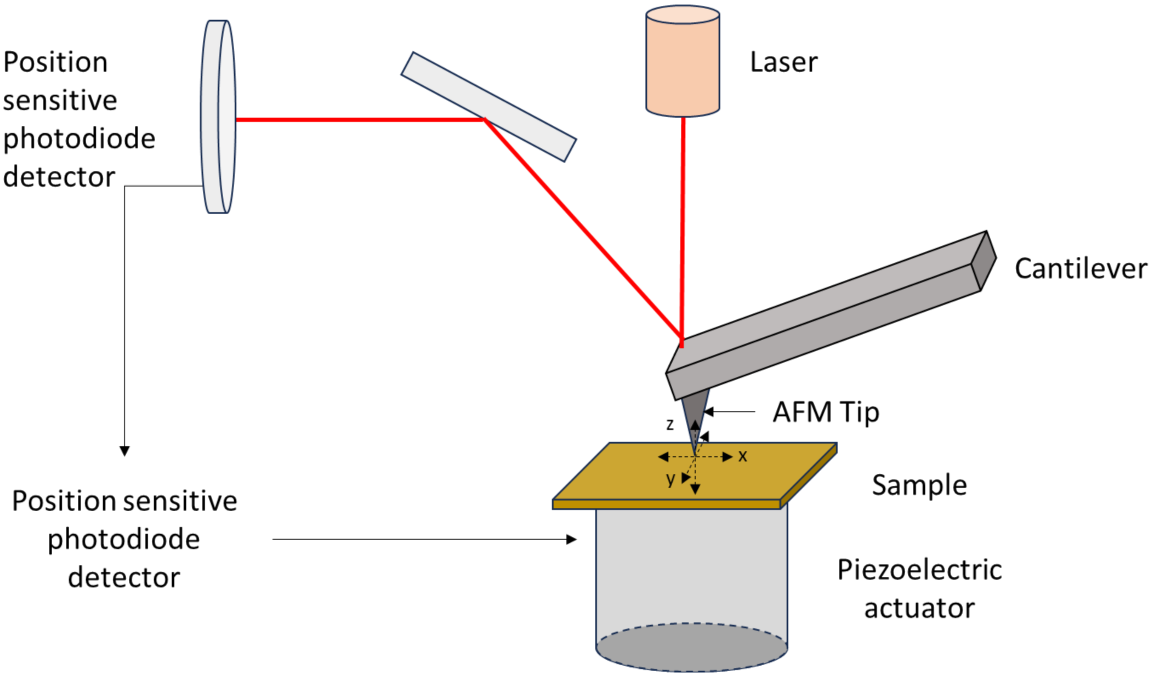

Figure 7.3: Atomic force microscopy instrument setup (adapted from [157])

## 7.6 Optical 3D Profilometry

To characterise a specimen surface (topography, morphology), optical 3D surface profilometry can be used. It is a non-contact method based on Michelson's interferometer [158]: an incident light beam (from a light source) is sent through a beam splitter and is directed to the sample (for the measurement) and to a reference surface. The two beams reflect on the different surfaces and recombine, but with two different optical paths, resulting in interferences recorded by a CCD image sensor to form a topographic image of the sample's surface. Optical 3D profilometry can be then used to image the sample's surface and determine specific characteristics (such as the average roughness Ra). It is also possible to determine a coating's thickness by creating a step on the sample with an uncoated area (by applying a mask during the thin film deposition). In this work, the surface morphology, the average roughness of the thin films produced were measured using a Profilm3D profilometer from Filmetrics with 50x magnification. In addition, the thickness of the coatings was measurement by creating a step during the deposition process. The thickness and roughness were measured on three different areas per samples, as shown in Figure 7.4., to calculate the mean and associated standard deviation. A schematic of Optical 3D profilometry is presented in Figure 7.4.

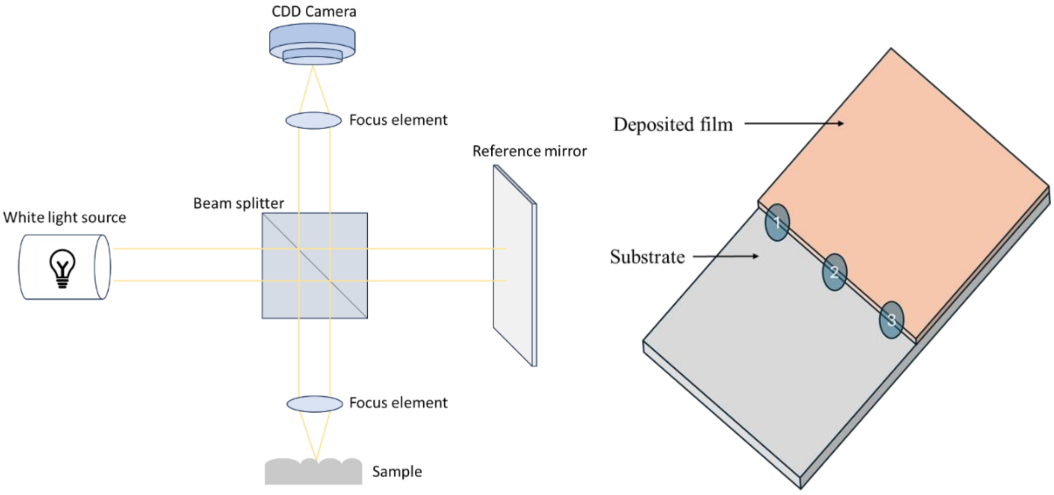

Figure 7.4: (left) Schematic of Optical 3D profilometry, (right) Schematic of the deposited films and the position for thickness measurements

## 7.7 X-Ray Photoelectron Spectroscopy (XPS)

X-Ray photoelectron spectroscopy (XPS) is a chemical state analysis technique, providing a qualitative and semi-quantitative information about a sample's surface. It must be noticed that the analysis depth in XPS does not generally go below 10 nm [159]. The principle of XPS relies on the interaction between monochromatic X-rays with a sample. The irradiation of monochromatic X-Rays causes the emission of core electrons (photoelectrons) with a specific kinetic energy ($kE$). Or, according to the Einstein's "principle of the conservation of mass", this kinetic energy is equal to the energy of the incident X-Ray ($h\nu$) minus the core electron's binding energy (BE) and the spectrometer's work function ($\Phi_S$), as described in Equation (33). By measuring the kinetic energy of the emitted photoelectrons, and as $h\nu$ and $\Phi_S$ are known, it is then possible to determine the binding energy of the core electron, which is element specific. It is then possible to identify the elements present on the sample's surface (exception for hydrogen and helium) [155]. The determination of $BE$ can also help to quanfity the chemical state of an element. Finally, it is possible to quantity the elements present in the sample as the photoelectrons produced are proportional to their concentration in the sample.

$$kE = h\nu - BE - \Phi_S \tag{33}$$

In this work, XPS was performed with a SUPRA photoelectron spectrometer from Kratos Analytical Ltd., equipped with Mg K X-Rays as the primary excitation source. The data were collected with the equipment within the Surface Engineering Group by Dr. Gary Miller.

The data were collected onto 1 x 1 $cm^2$ samples, the survey scans were collected with a pass energy of 160 eV. The region scans were collected with a pass energy of 40 eV. After that, the data were analysed using the software CasaXPS. The C 1s line at 284.8 eV was used as the reference for the calibration of the binding energy, and curve fitting was performed applying a Gaussian function with a Shirley background.

## 7.8 UV-Vis Spectroscopy

UV-Vis spectroscopy is an analytical technique based on the interaction between an incident light and an analysed sample. A UV-Vis spectrometer is composed of UV-Vis light sources, a filter monochromator, a beam splitter and a photodetector (see Figure 7.5). The light is usually produced by several light sources that generate a UV spectrum (between 180 and 400 nm) and a visible/near-infrared spectrum (from 400 to 1000 nm). A part of this incident light is absorbed by a sample, whereas the rest is divided between several phenomena such as transmission, reflection, and scattering [160]. The transmitted light is measured by a detector, where the intensity of the transmitted light is compared to the intensity of the incident light to obtain the transmittance of the sample studied (Equation 34):

$$T = \frac{I}{I_0} \tag{34}$$

$$A = -\log(T) \tag{35}$$

with I is the transmitted intensity and $I_0$ is the intensity of the light source. Then, it is possible to determine the absorption of the sample using Equation 35. By determining those two characteristics, it is then possible to determine other optical properties of a semiconductor photocatalyst. In this work, UV-Visible measurements were performed using an Ocean Optics USB4000 UV-Vis spectrometer. Hence, several characteristics of the photocatalyst thin films produced were evaluated: the optical band gap via the Tauc plot method and the light harvesting efficiency (LHE).

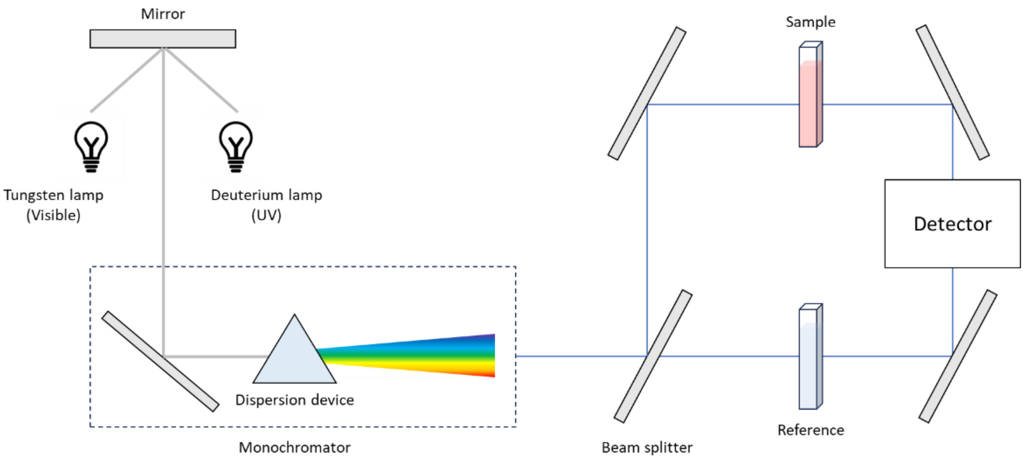

Figure 7.5 : UV – Vis spectrometer principle

### 6.8.1 Band gap calculation

The Tauc plot method was used to estimate the value of the optical band gap of the produced coatings, which is a key value in photocatalysis applications. For wide band gap semiconductors [161], the optical band gap value $E_g$ may be obtained using the following Equation (36):

$$\alpha h\nu = (h\nu - E_g)^{\frac{1}{n}} \tag{36}$$

Where α is the absorbance coefficient ($\mu m^{-1}$), h is the Plank constant (eV.s), ν is the frequency of vibration ($s^{-1}$). The coefficient n represents the nature of the band gap of the material studied. For the case of indirect bandgap material, n=1/2, and for the case of direct bandgap material, n=2. The absorbance coefficient can be determined from the transmittance (T), the reflectance (R) and the coating's thickness d (μm) from the Equation (37). The value of the bandgap energy can then be estimated by plotting $(\alpha h\nu)^{n}$ as a function of hν and extrapolating the linear region to the abscissa [161].

$$\alpha = \left(\frac{1}{d}\right) \ln\left(\frac{1-R}{T}\right) \tag{37}$$

In this work, the optical band gap of a sample was measured by determining the absorbance coefficient from the transmittance measurements, recorded thanks to the use of the Ocean Optics USB4000 UV-Vis spectrometer. The transmittance was recorded onto three different areas per sample, within a delimited range of wavelength (from 300 to 900 nm). The FTO glass substrates were used as reference.

### 6.8.2 Light harvesting efficiency (LHE)

The light absorption efficiency (or light harvesting efficiency) $\eta_{abs}$ translates the ability of the thin film photocatalyst to absorb the photons from the light source. It is defined as the percentage of incident photons that are absorbed to generate electron and hole pairs. The light harvesting efficiency can be calculated from the absorbance data A with the following Equation (38):

$$\eta_{abs} = 100\% - 10^{-A} \tag{38}$$

where $I_0(\lambda)$ is the initial light intensity (in $W.cm^{-2}$) and $I(\lambda)$ is the transmitted light intensity. The LHE can be enhanced by several methods, as illustrated in Figure 7.6.

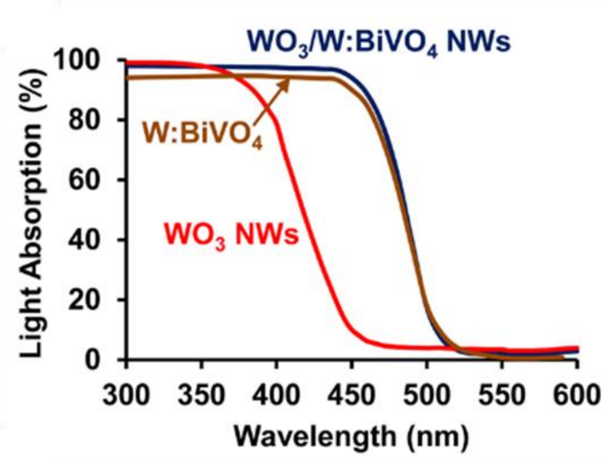

Figure 7.6: Light harvesting efficiency of WO3 nanowires, doped W:BiVO$_4$ and WO$_3$/W:BiVO$_4$ NWs heterojunction [162]

## 6.9 Photoelectrochemical (PEC) measurements

Different types of photoelectrochemical measurement were performed to assess the photoelectrochemical properties of the photoelectrodes produced. Voltammetry corresponds to the evaluation of the current passed through an electrode as a function of the potential different applied to the WE. Different studies can be done, such as linear sweep voltammetry (LSV) and cyclic voltammetry (CV). The first technique is usually done to assess the production of a photocurrent under illumination with a visible light source. In LSV, the potential applied is linearly swept between two values, with a range of value defined according to the redox reaction studied. The measurement is performed in two conditions:

- One measurement without illumination to record the “dark current”, i.e. the current produced without the photocatalytic phenomenon. For a photoelectrode, the dark current produced is usually almost zero (in a range of $10^{-1}$ μA.cm$^{-2}$), as no chemical reactions are supposed to occur in the range of voltage chosen.

- One measurement with the photoelectrode illumined by the light source, to record the photocurrent produced. It must be noticed that the nature of the photocurrent produced depends on the nature of the photocatalyst semiconductor studied. N-type semiconductors, used to perform oxygen evolution reaction, produce a positive (anodic) photocurrent. On the other hand, to study the HER, p-type semiconductors are used, producing a negative (cathodic) photocurrent.

For the study of the oxygen evolution reaction, the potentials are typically swept from a lower starting potential ($E_i$ = 0.2 $V_{RHE}$) to an upper final potential ($E_f$ = 1.8 $V_{RHE}$), whereas for the hydrogen evolution reaction, the potential is swept in the opposite direction. In this work, the LSV measurements were performed with a scan rate of 20 mV.s$^{-1}$. The upper and lower values were fixed according to the redox reaction studied : In the case of the oxygen evolution reaction, the scan was performed from 0.2 $V_{RHE}$ to 1.7 $V_{RHE}$, to observe firstly the production of anodic photocurrent when going to higher potentials. In the case of the hydrogen evolution reaction, the scan was done in the opposite direction, from 1.3 $V_{RHE}$ to 0.2 $V_{RHE}$, to observe the production of the cathodic photocurrent associated with the proton reduction reaction. From the LSV measurements, the half-cell solar-to-hydrogen efficiency (HC-STH) was calculated using Equation (40):

$$HC - STH = \frac{J(mA.cm^{-2}) \times (1.229 - |V_{app}|)(V) \times \eta_F}{P_{total}(mW.cm^{-2})} \quad (40)$$

where J is the photocurrent produced during the measurement, $V_{app}$ is the potential applied, $\eta_F$ is the Faradaic efficiency $P_{total}$ is the power density of the incident light used (estimated at 100 mW.cm$^{-2}$). Usually, the Faradaic efficiency is assumed to be 100% [169]. Between measurements, air bubbling was used to remove the gas bubbles produced during measurements.

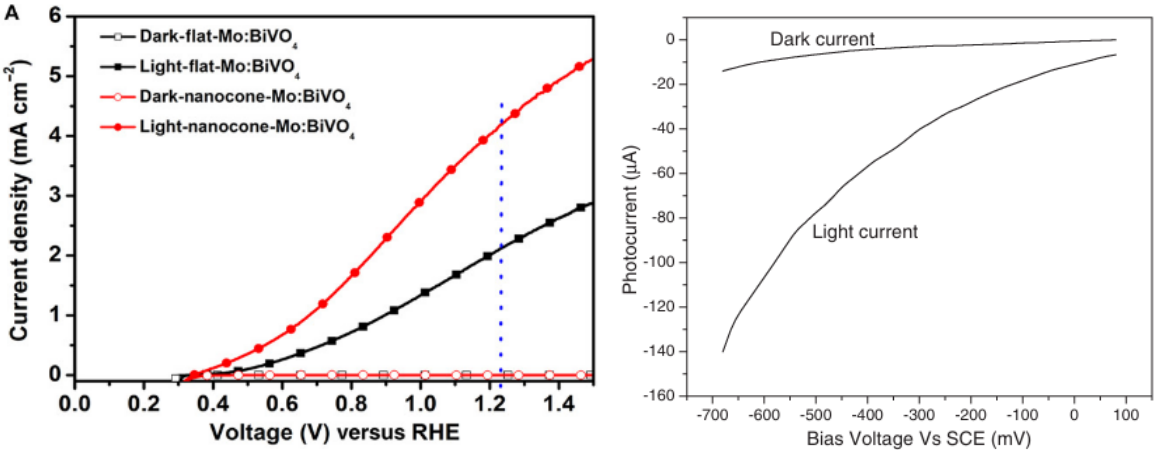

Figure 7.7: (left)) LSV for $BiVO_4$ photoanodes (dark and light) [167], (right) LSV for CuO photocathode (dark and light) [168]

In addition, cyclic voltammetry was use only in dark conditions, to estimate the electrochemical band edges of the samples produced, in order to estimate the electronic configurations of the photocatalysts semiconductor studied. For CV, the potential applied is reversed back to the starting potential $E_i$ after it reaches $E_f$, and multiple cycles are conducted. Details of the cyclic voltammetry are presented in chapter 10 for both photoanode and photocathode.

Chronoamperometry was also used to determine the stability of the samples produced. In chronoamperometry, a potential applied to the working electrode is fixed at a certain value and the current produced is record over the time. This measurement is usually performed during a long period of time, to ensure the ability of the photoelectrode to produce a high and stable photocurrent. A decay of the photocurrent after several hours of testing can be the sign of the degradation of the photocatalyst. The degradation can be caused by electrochemical interactions between the electrolyte and the thin film. For example, Cu oxides are known to degrade easily in aqueous solutions, due to low reduction potential of the $Cu/Cu^{2+}$ couple [170]. For the measurement of photoelectrode stability, chronoamperometry was parameters. Also, chronoamperometry was used to measure the transient time, which is a key characteristic of a photocatalyst. The transient time gives an estimation of the lifetime of charge carriers before recombination. As charge carriers' recombination is a limiting factor of a semiconductor photocatalyst activity, the transient time should be as long as possible. To calculate the transient time for a given photoelectrode, chopped chronoamperometry is used. When a photoelectrode is illuminated, a peak of initial photocurrent appears $I_i$, followed by a fast decay of photocurrent intensity, corresponding to the recombination of charge carriers (see Figure 50). The transient time can be then obtained from the following equations:

$$\ln D = \frac{-\tau}{t} \tag{41}$$

$$D = \frac{(I_t - I_f)}{(I_i - I_f)} \tag{42}$$

where $I_i$, $I_f$ and $I_t$ the initial photocurrent, final photocurrent, and photocurrent at time t, respectively. The transient time is obtained by plotting ln D as a function of time. By extrapolating the linear part of the curve plotted, it is possible to determine the transient time τ for ln D = -1 (see Figure 7.8).

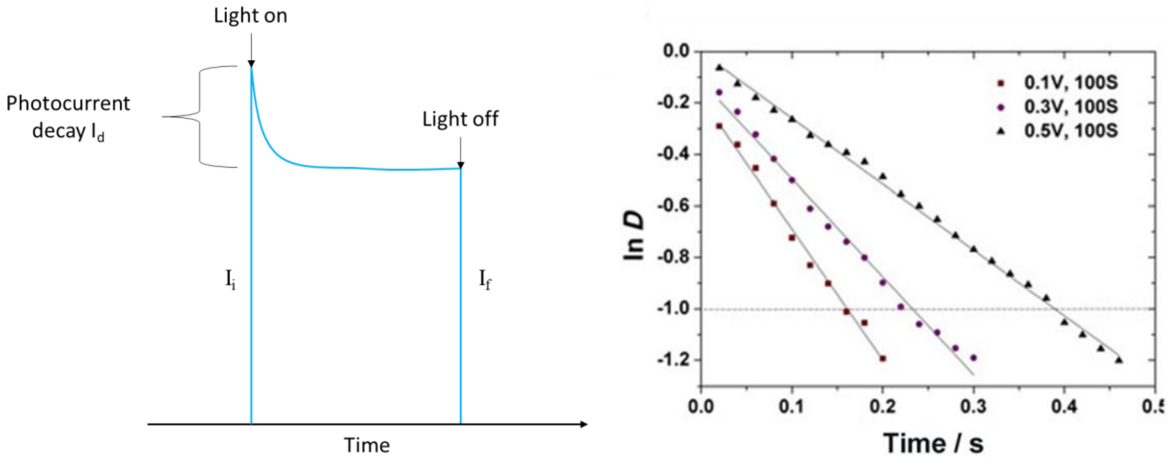

Figure 7.8: (Left) Example of photocurrent response in chronoamperometry, (Right) Plotted curves for obtaining the transient time [171]

Finally, chronoamperometry can be used to estimate the theoretical amount of gas produced during an experiment. The theoretical amount of gas produced can be determine using the following equation:

$$q_{gas} = \frac{\int_0^{\Delta t} J(t)dt}{n \times F} \tag{43}$$

with $q_{gas}$ is the number of moles produced, $\int_0^{\Delta t} J(t)dt$ is the photocurrent produced over the time of the chronoamperometry measurement, n is the number of moles of electrons used for the gas production and F the Faraday constant (96 500 $C.mol^{-1}$) [172]. Some electrochemical measurements, such as Mott-Schottky plots or impedance spectroscopy were not studied in this work, due to the potentiostat device used which was not equipped with the appropriate modules.

# III. Results

## 8. Production of photocatalytic $BiVO_4$ thin films by reactive magnetron co-sputtering for the study of oxygen evolution reaction

*This chapter presents the results obtained for the production of photocatalytic* $BiVO_4$ *thin films produced by reactive magnetron sputtering. The thin films produced are studied as photoanodes for photoelectrochemical oxygen evolution reaction. Section 1 discusses the background of* $BiVO_4$ *as a photocatalyst and photoanode material. The production parameters of the samples studied are presented in Section 2. The crystalline phase determination and morphological study are presented in Section 3 and 4 respectively. Section 5 presents the determination of the optical properties of the thin films produced. Section 6 presents the photocatalytic and photoelectrochemical activities assessment. Section 7 discusses the efficiencies of a selected range of samples and section 8 discusses the impact of film thickness onto the PEC measurements. The chapter is summarised in Section 9.*

### 8.1. Introduction

Monoclinic $BiVO_4$ photocatalyst is usually produced using wet chemical methods, such as sol-gel [184], spin coating [120] or electrodeposition [185]. However, several drawbacks can be observed with those techniques, such as excessive film thicknesses or poor adhesion to the substrate, resulting in $BiVO_4$ photoanodes with low efficiencies [186]. On the other hand, physical vapour deposition methods present some interesting advantages, such as the scalability, the lack of hazardous chemicals/precursors and enabling the production of uniform coatings in terms of morphology and composition. The production of $BiVO_4$ photoanodes by magnetron sputtering has been demonstrated several times, but mainly by using RF sputtering and from compound targets ($BiVO_4$ compound target [187] or $Bi_2O_3$ and V targets [188]). Reactive sputtering with metallic targets in oxygen/argon atmosphere offers notable advantages, such as higher deposition rates, process stability and reduction of defects. Moreover, it offers the possibility to study different production parameters (power applied on the targets), and then to optimise the sample production. Despite its clear advantages, $BiVO_4$ produced by reactive magnetron sputtering has not been characterised as a photoanode but only utilised for dye degradation [189].

## 8.2. Experimental methods

The goal of this chapter is to produce an efficient $BiVO_4$ photoanode for the study of the oxygen evolution reaction in a PEC cell. In this work, several types of $BiVO_4$ samples were produced by mid-frequency pulsed DC reactive magnetron co-sputtering, using two metallic targets (Bi and V, 99.5% purity). Various types of substrates were used for different applications (Fluorine-doped tin oxide coated glass from Pilkington®, soda-lime glass slides or Si wafer). The samples produced were characterised by different analytical techniques to determine their intrinsic properties (crystallinity, morphology, composition). Then, the initial assessment of the photocatalytic properties of the films was made with methylene blue degradation testing. Finally, the photoelectrochemical properties of the photoanodes produced were studied in a three-electrode electrolysis configuration and showed efficient photocurrent production to perform the oxygen evolution reaction.

Table 8.1 summarises the deposition conditions of the samples produced. Due to the high sputtering yield of Bi comparing to V [190], the samples were produced by fixing a relatively low power applied on Bi (50 W) and by varying the power applied on V target, from 400 to 1200 W. The samples are labelled in accordance with the power applied on the vanadium target (for example, BiV400 means that the sample was produced by applying 50 W on Bi target and 400 W on V target). Dual-channel Advanced Energy$^{TM}$ Pinnacle Plus power supply were used, with a pulse frequency of 100 kHz and a duty cycle of 60 %. Argon and oxygen flows were kept constant during the deposition, at 40 and 20 sccm, respectively. The thin films were deposited for 1h and were then annealed in air at 500°C for 1h.

Table 8-1: Sputtering parameters for the production of BiV samples

| Sample ID | $P_{Bi}$ (W) | $P_V$ (W) | $P_V/P_{Bi}$ |
|---|---|---|---|
| BiV400 | 50 | 400 | 8 |
| BiV500 | 50 | 500 | 10 |
| BiV600 | 50 | 600 | 12 |
| BiV700 | 50 | 700 | 14 |
| BiV800 | 50 | 800 | 16 |
| BiV900 | 50 | 900 | 18 |
| BiV1000 | 50 | 1000 | 20 |
| BiV1100 | 50 | 1100 | 22 |
| BiV1200 | 50 | 1200 | 24 |

After deposition, the samples were characterised with different analytical techniques. The crystal structure of the thin films produced was analysed by XRD using PANalytical X'pert X-Ray diffractometer with a Cu $K_\alpha$ source ($\lambda = 1.5406$ Å). The diffraction peaks were recorded in the range of $2\theta = 15° - 60°$, with a step size of 0.015° and a measurement time of 60 seconds per step. Then, the reference patterns were identified using the International Centre for Diffraction Data (ICCD) database. Raman spectroscopy was also performed on the coatings produced, using a Renishaw Invia, performed with a laser operating at a wavelength of 514 nm with a power of 10 mW and a long working distance microscope objective with magnification of 50x. The Raman spectra was recorded between 100 and 1000 $cm^{-1}$. Scanning electron microscopy (SEM) was used to identify the morphology of the coatings produced. Top-surface and cross section secondary electron (SE) images were recorded at a magnification of 50,000 and generated with a 2kV electron beam using a Zeiss Supra 40VP equipped with EDAX 40Vp energy dispersive X-Ray (EDX) analyser. The composition of the films was quantified on an imaged area of approximately 100 $\mu m^2$ under an acceleration voltage of 20 kV. White light interferometry (WLI) was used for thickness measurements using Profilm3D optical profilometer from Filmetrics. The measurements were done at three different positions with magnification of 50x, to determine the mean thickness and the standard deviation. High resolution transmission electron microscopy (HRTEM) imaging was performed with a FEI Titan Themis FEG STEM in bright-field mode, operating at 200 kV, onto lamellae extracted by a FIB-SEM (FEI Helios G4CX FIBSEM). In addition, STEM elemental mapping was performed by EDX spectroscopy. A first AFM measurement was performed onto one BiV sample with a Horiba XPlora Plus system, in tapping mode, onto an area of 10 x 10 $cm^2$, with 3 different areas analysed. The optical properties of the thin films produced were measured using an Ocean Optics USB4000 UV-Vis spectrometer, connected to a DH-2000-BAL UV-Vis-NIR light source. The transmission properties were recorded between 300 and 900 nm. Substrate FTO films were used as reference prior to the measurements. The oxidation state of the deposited films was determined using X-Ray photoelectron spectroscopy. The XPS analysis was performed with a Kratos Axis Supra system, equipped with a monochromated Al $K_{\alpha 1}$ X-Ray excitation source ($h\nu = 1486.6$ eV). The peak model fitting was carried out with the software CasaXPS. All spectra were charge corrected to the acquired C 1s region scan and the adventitious carbon peak (C-C) position at 284.8 eV. Curve fitting was done applying a Gaussian function with a Shirley background.

Prior to photoelectrochemical measurements, photocatalytic dye degradation tests were performed. Prior to the test, the samples were immersed in 50 mL of 2 μmol.L$^{-1}$ methylene blue (MB) solution and left in the dark for 60 min under continuous stirring, to reach adsorption-desorption equilibrium. Then, the samples were illuminated by a UV-A light source (2x15 W Sankyo Denki BLB lamps) for 1h. The evolution of the main absorption peak of MB (664 nm) was monitored with an Ocean Optics USB4000 UV-Vis spectrometer. The photoelectrochemical measurements were performed in a three-electrode configuration powered by au Autolab potentiostat from Metrohm (PGSTAT302N). In brief, the BiV$_x$/FTO samples were used as the working electrode, whereas the counter electrode was a Pt mesh (5 x 5 cm$^2$), and the reference electrode was an Ag/AgCl reference electrode. The geometric surface area was defined as 1 cm$^2$ (defined with an epoxy resin mask). A 0.5 M $Na_2SO_4$ (pH ≈ 7) solution was used as the electrolyte. To assess the photoelectrochemical activity of the films, Linear Sweep Voltammetry (SV) measurements were performed from 0.2 to 1.8 V$_{RHE}$ at a scan rate of 20 mV.s$^{-1}$. The measurements were performed in the dark and under visible light illumination to assess the photoelectrochemical activity of the samples produced. From the photocurrent produced, the half-cell solar-to-hydrogen conversion efficiency (HC-STH) of all samples were determined, using equation (36):

$$HC - STH = \frac{J_{ph}(mA.cm^{-2}) \times (E_{O_2/H_2O} - |V_{app}|)(V) \times \eta_F}{P_{total}(mW.cm^{-2})} \tag{40}$$

with J$_{ph}$ the photocurrent density at V$_{app}$, V$_{app}$ the potential applied during the measurement, Ptotal the power density of the incident light (100 mW.cm$^{-2}$) and $E_{O_2/H_2O}$ the standard potential for the oxygen evolution reaction (here 1.23 V$_{RHE}$). The three-electrode configuration was also used to perform chronoamperometry (CA). Firstly, CA was used to measure the stability of the photocurrent produced by the samples at 1.23 V$_{RHE}$ for 3 hours. CA was also performed for a shorter period of time (60 s) to determine the transient time τ for the samples produced by using equation x:

$$\ln D = \frac{-\tau}{t} \tag{41}$$

$$D = \frac{(I_t - I_f)}{(I_i - I_f)} \tag{42}$$

where I$_i$, I$_f$ and I$_t$ the initial photocurrent, final photocurrent, and photocurrent at time t, respectively. The transient time is obtained by plotting ln D as a function of time. By extrapolating the linear part of the curve plotted, it is possible to determine the transient time τ for ln D = -1.

## 8.3. Crystallinity assessment

Raman Spectroscopy was initially used for identification of crystalline phases of the BiV coatings produced. As stated earlier, the phase of interest for $BiVO_4$ photoanode is the monoclinic scheelite (m-s), which produces specific Raman bands corresponding to specific elongations within the $BiO_6$ or $VO_4$ units. Especially, 6 typical Raman bands are of interest for the m-s $BiVO_4$ compound [191]:

- The most intense band centred at 826 $cm^{-1}$ is attributed to the $A_g$ symmetric mode of the V-O bonds in the $VO_4$ tetrahedra.
- The asymmetric mode ($B_g$) can be observed by the presence of the shoulder peak at around 710 $cm^{-1}$.
- The two bands located at 367 $cm^{-1}$ and 325 $cm^{-1}$ correspond to the symmetric and asymmetric bending modes of the $VO_4$ tetrahedra, respectively.
- Finally, the last two bands (210 $cm^{-1}$ and 125 $cm^{-1}$) correspond to the two external modes for rotation and translation.

The Raman spectra of the different BiV samples produced are presented in Figure 8.1. Three different types of spectra can be observed among the different samples, allowing them to be grouped in three different categories. The first group of samples regroups the three samples with the lower power applied on the vanadium target (BiV400, BiV500 and BiV600, see Figure 6.2a). Those samples present typical Raman bands associated with the presence of $Bi_4V_2O_{11}$ compound, with two bands located at 152 $cm^{-1}$ and 930 $cm^{-1}$ [192]). This compound was previously reported in $BiVO_4$ coatings produced by magnetron sputtering, due to a too high amount of Bi in the film and leading to the formation of this crystal phase during the annealing step [193]. In addition, the different bands of $BiVO_4$ can be observed but are slightly shifted to lower wavenumbers and widely spread, indicative of the lack of crystallisation of this phase. The second group of samples (BiV700, BiV800 and BiV900, see Fig. 6.2b) all exhibit the bands attributed to m-s $BiVO_4$, whereas some additional bands appear for the samples produced with the higher power applied on the vanadium target (BiV1000, BiV1100 and BiV1200, see Fig. 6.2c). The bands located at 142 $cm^{-1}$, 280 $cm^{-1}$, 401 $cm^{-1}$, 481 $cm^{-1}$, 523 $cm^{-1}$ and 991 $cm^{-1}$ can all be attributed to the presence of $V_2O_5$ phase [194]. This compound becomes predominant in the coating for $P_V$ =1200 W, as the main bands of $BiVO_4$ are either shifted to lower wavenumbers (such as the band at 816 $cm^{-1}$) or are diminished in terms of intensity.

A correlation between the Raman Spectra and the composition of the thin films produced can be done thanks to the EDX analysis performed on the samples, where three different areas of the samples were analysed to calculate the standard deviation (the error measured is comprised within the range of typical error of EDX measured, comprised between 1 and 5 %, see Figure 8.1d and Table 8.2). As it can be observed, a higher power applied on the V target results in a higher content of V in the coating, resulting in the formation of $V_2O_5$. On other hand, if the amount of vanadium is not sufficient, it favours the formation of the $Bi_4V_2O_{11}$ phase. The sample BiV800 appears to be the closest to $BiVO_4$ in terms of stoichiometry, with an atomic ratio (Bi/V) close to 1. According to the phase diagram of the Bi2O3 – V2O5 binary system, the $BiVO_4$ compound corresponds to a solid solution containing 50% of Bi2O3 and 50% of V2O5 [282].

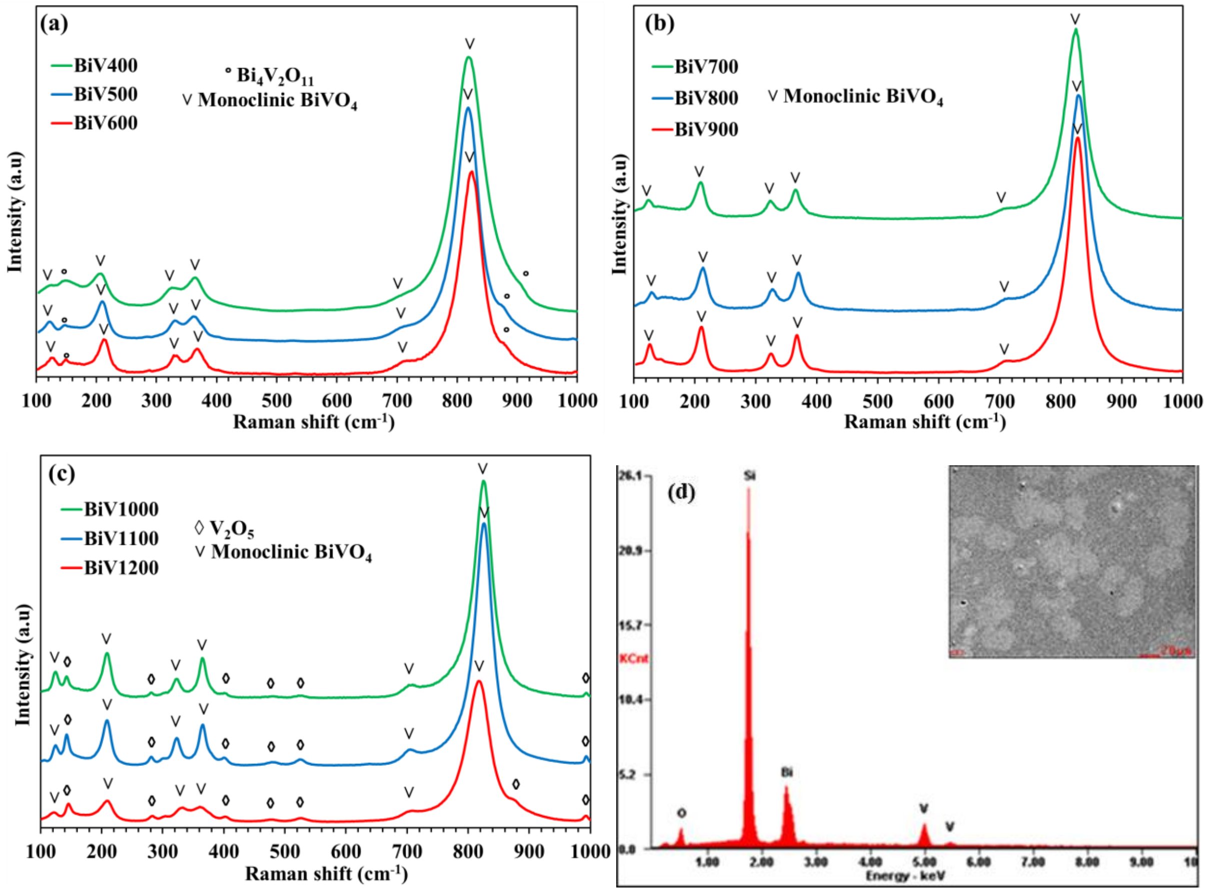

Figure 8.1: Raman spectra of the samples (a) BiV400, BiV500 and BiV600; (b) BiV700, BiV800 and BiV900 ; (c) BiV1000, BiV1100 and BiV1200 ; (d) Example of EDX spectra of BiV1100 deposited onto Si water

Table 8-2: Elemental (EDX) analysis of the BiV samples produced

| Sample | Z | Element | Atomic fraction (%) | At% V/Bi ratio |
|---|---|---|---|---|
| | 8.00 | O | 70.4 ± 1.2 | |
| BiV400 | 29.00 | V | 12.3 ± 1.2 | **1.39** |
| | 83.00 | Bi | 17.2 ± 1.1 | |
| | 8.00 | O | 69.8 ± 1.3 | |
| BiV500 | 29.00 | V | 13.2 ± 1.1 | **1.28** |
| | 83.00 | Bi | 17.0 ± 1.1 | |
| | 8.00 | O | 70.5 ± 1.4 | |
| BiV600 | 29.00 | V | 13.3 ± 1.2 | **1.22** |
| | 83.00 | Bi | 16.2 ± 1.2 | |
| | 8.00 | O | 70.6 ± 1.3 | |
| BiV700 | 29.00 | V | 13.7 ± 1.2 | **1.14** |
| | 83.00 | Bi | 15.7 ± 1.4 | |
| | 8.00 | O | 70.2 ± 1.3 | |
| BiV800 | 29.00 | V | 14.7 ± 1.3 | **1.04** |
| | 83.00 | Bi | 15.0 ± 1.2 | |
| | 8.00 | O | 69.8 ± 1.6 | |
| BiV900 | 29.00 | V | 15.5 ± 1.3 | **0.94** |
| | 83.00 | Bi | 14.7 ± 1.3 | |
| | 8.00 | O | 70.7 ± 1.5 | |
| BiV1000 | 29.00 | V | 13.4 ± 1.4 | **0.87** |
| | 83.00 | Bi | 15.9 ± 1.4 | |
| | 8.00 | O | 70.0 ± 1.5 | |
| BiV1100 | 29.00 | V | 16.5 ± 1.2 | **0.81** |
| | 83.00 | Bi | 13.4 ± 1.1 | |
| | 8.00 | O | 70.9 ± 1.3 | |
| BiV1200 | 29.00 | V | 16.8 ± 1.4 | **0.73** |
| | 83.00 | Bi | 12.3 ± 1.2 | |

X-ray diffraction was performed on the BiV samples to confirm the findings from Raman Spectroscopy. In addition, XRD was used to investigate evolution of the crystallisation process of BiV800 sample with the annealing temperature. The XRD patterns obtained can be seen in Figure 8.2, where the FTO peaks can be observed (ICDD card 041-1445). The "stoichiometric" samples (BiV700, BiV800 and BiV900) present the following peaks, attributed to m-s $BiVO_4$ (ICDD card 14-0688), as shown in figure 6.3b: 18.9° (1 1 0), 28.8° (1 2 1), 30.5° (0 4 0), 34.6° (2 0 0), 35.2° (0 0 2), 40° (2 1 1), 42.4° (1 5 0), 45.9° (1 3 2), 46.8° (2 4 0), 47.2° (0 4 2) 50.2° (2 0 2), 53.5° (1 6 1), 58.3° (1 7 0) and 59.4° (3 2 1). In addition, the findings regarding the "Bismuth-rich" samples (BiV400, BiV500 and BiV600) are confirmed, with the presence of peaks from the $Bi_4V_2O_{11}$ phase (23.1° (1 1 1), 27.5° (2 0 0), 28.2° (1 1 3), 32.1 ° (0 0 6), 48.3° (2 2 0), 55° (3 1 1) and 58.8° (2 2 2), ICDD card 42-0135). As it can be observed in figure 6.3a, the $Bi_4V_2O_{11}$ peaks are predominant and progressively diminish with the increasing amount of V, favouring the formation of $BiVO_4$ phase. For the 'Vanadium-rich samples" (BiV1000, BiV1100 and BiV1200), no noticeable peaks related to the presence of $V_2O_5$ phase can be observed, but only a short shoulder peak at 30.3°, corresponding to the (0 1 1) plane (JCPDS card 65-0131) for BiV1200 sample (see Figure 6.3c).

To investigate the crystallisation process of m-s $BiVO_4$, in situ X-Ray diffraction study was performed onto the BiV800 sample (see Figure 8.3). The sample was placed into an XRD hot stage chamber and heated from room temperature to 500°C with 100°C increments, in an air atmosphere. From room temperature to 200°C, no diffraction peaks associated with crystalline $BiVO_4$ could be seen, evidential of an amorphous structure. The only visible peaks are attributed to the FTO layer of the substrate used (26.5° (1 1 0), 33.9°(1 0 1), 37.9° (2 0 0) and 51.9° (2 1 1), ICDD card 041-1445). Crystallisation occurs from 300°C, which is in agreement with the literature, as the reversible transition between monoclinic and tetragonal scheelite starts at 255°C [195]. From 400°C, the diffraction pattern contains all the peaks that can be attributed to m-s $BiVO_4$. The monoclinic scheelite is directly observable from 300°C to 500°C, with sharpened diffraction peaks with higher temperature. Based on these results, 500°C was chosen as the preferential temperature for thermal treatment of BiV samples for the rest of this work.

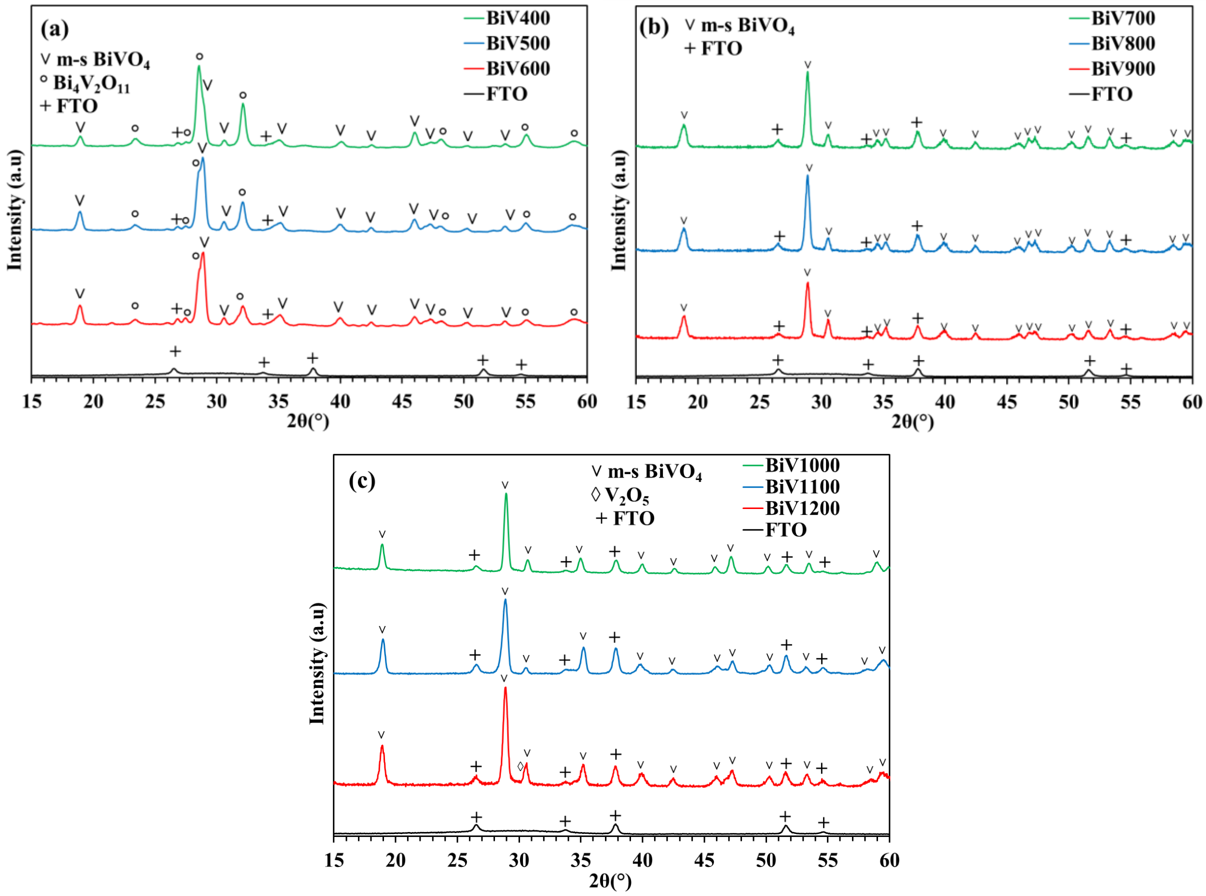

Figure 8.2: XRD patterns of the different BiV samples produced ; a) BiV400, BiV500 and BiV600, b) BiV700, BiV800 and BiV900, c) BiV1000, BiV1100 and BiV1200

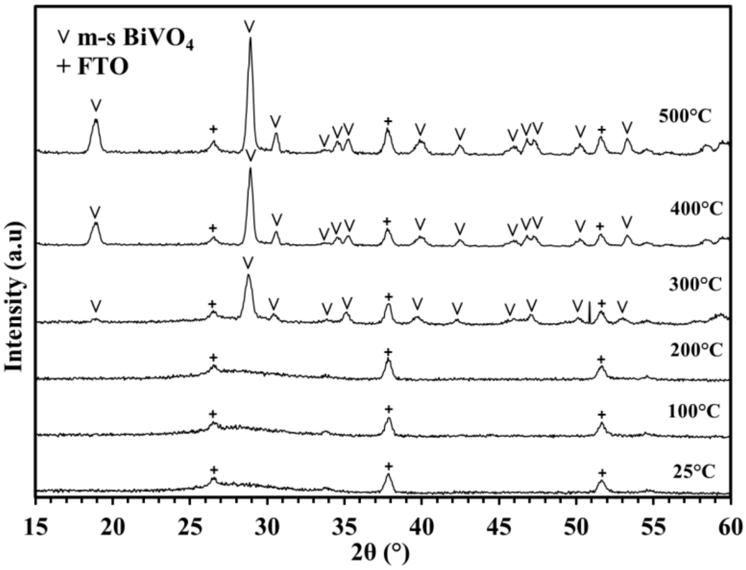

Figure 8.3: BiV800 sample heated in air from room temperature to 500°C

## 8.4. Coatings morphology

To study the morphology of the BiV samples produced, scanning electron microscopy was used. Figure 8.4 presents an example of top surface SEM image of an as-deposited BiV sample. A typical columnar structure can be observed, which corresponds to a columnar structure described in the Thornton Structure Zone Model for coatings by sputtering techniques [145]. Once annealed, the morphology observed for the samples produced changes, with different structures observed depending on the sample's composition (see Figure 8.5). The samples BiV400 and BiV500 present a highly porous structure made of small grains, with few larger grains incorporated in between. This morphology can be explained by competitive formation of $Bi_4V_2O_{11}$ phase and $BiVO_4$ phase, as observed on Raman Spectroscopy and XRD patterns. As both materials present relatively high thermal expansion coefficients, the observed porosity could result in damages occurring during the annealing step [196, 197]. A transition can be observed with the BiV600 sample, where no porosity is observed, and the coating becomes denser. From $P_V$ = 700 W, the coatings are composed of large grains of different sizes (from 200 nm to 500 nm). This morphology is the result of crystallisation occurring during the annealing process. Shi et al. produced $BiVO_4$ films by spin-coating in 2018 and reported that the samples annealed with a higher temperature (500°C and 540°C) exhibited larger grains compared to the samples annealed at lower temperatures (400°C and 450°C). They also demonstrated that this morphology was associated with a higher photoelectrochemical activity, especially regarding charge transport and charge transfer at semiconductor-electrolyte interface [198]. Moreover, Bakhtiarnia et al. obtained this morphology for $BiVO_4$ produced by reactive magnetron sputtering for water treatment purposes [189]. When the amount of vanadium in the compounds is in excess (from $P_V$ = 1000 W), nanorods and/or nanoparticles appear onto the surface of the samples. Those latter can be attributed to the formation of $V_2O_5$ phase, showing that the excess of vanadium tends to migrate to the surface of the samples to react with the oxygen of the annealing atmosphere. The formation of $V_2O_5$ crystals have been observed by Singh et al. when $BiVO_4$ is produced with an excess of vanadium. This was reported as beneficial for water cleaning application, enhancing the photocatalytic activity of $BiVO_4$ photocatalysts [199].

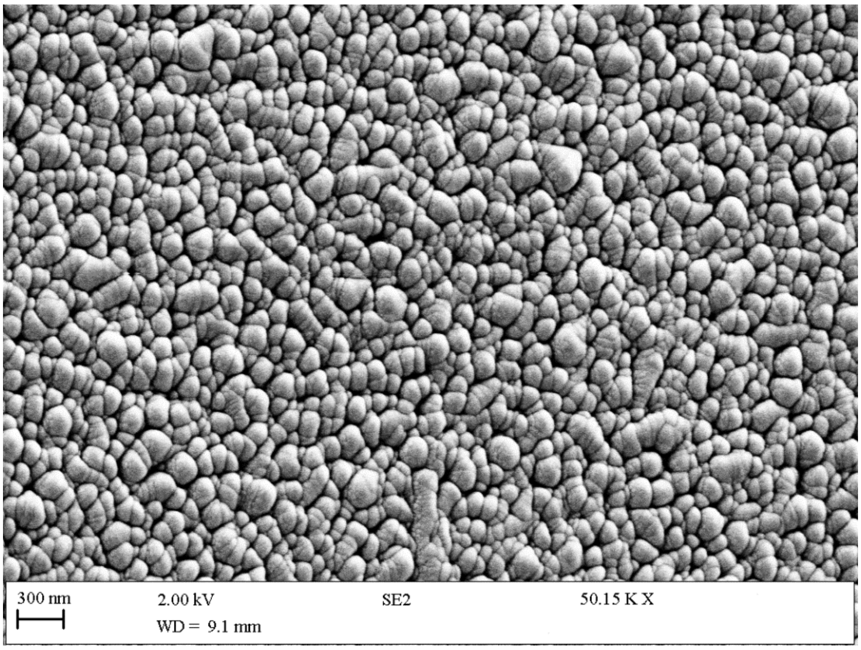

Figure 8.4: Top surface SEM micrograph of as-deposited BiV800 sample

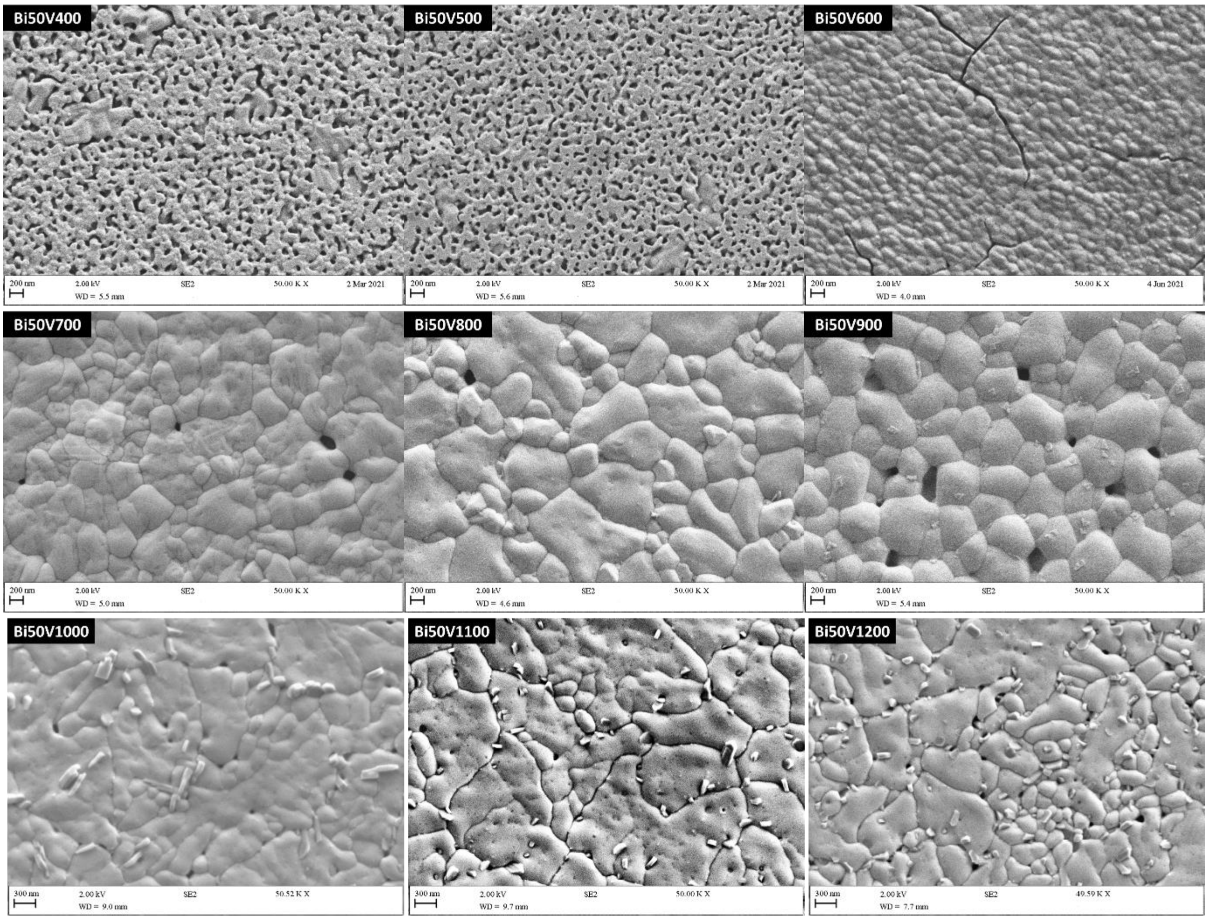

Figure 8.5: Top surface SEM micrographs of BiV samples produced, from BiV400 to BiV1200

To measure the thicknesses of the BiV samples, 3D optical profilometry was used, and all the different data recorded are listed in Table 8.3. Figure 8.6 presents the 3D images obtained for different BiV samples produced. The thicknesses of the samples produced increase with the power applied on the vanadium target, going from 303.9 nm for BiV400 to 407.7 nm for BiV1200. Some measurements of the area roughness of the different BiV samples (based on the ISO standard 27178) seem to show a relatively similar area roughness for all the samples (all around 10 nm), however the accuracy of the profilometer used is not sufficient to confirm those findings. Few first measurements were done by AFM for the BiV800 sample, showing a similar morphology than the top surface SEM image can be observed (see Figure 8.7c). This grain morphology makes the sample smooth, with a surface roughness measured of approximately 9 nm, potentially confirming the data from WLI. A more in-depth AFM analysis of the area roughness of the BiV samples could be done in additional work, to confirm the similar roughness of the BiV samples produced. Here, an approximation is made of the roughness of the samples to allow the direct comparison when performing photocatalytic and photoelectrochemical measurements.

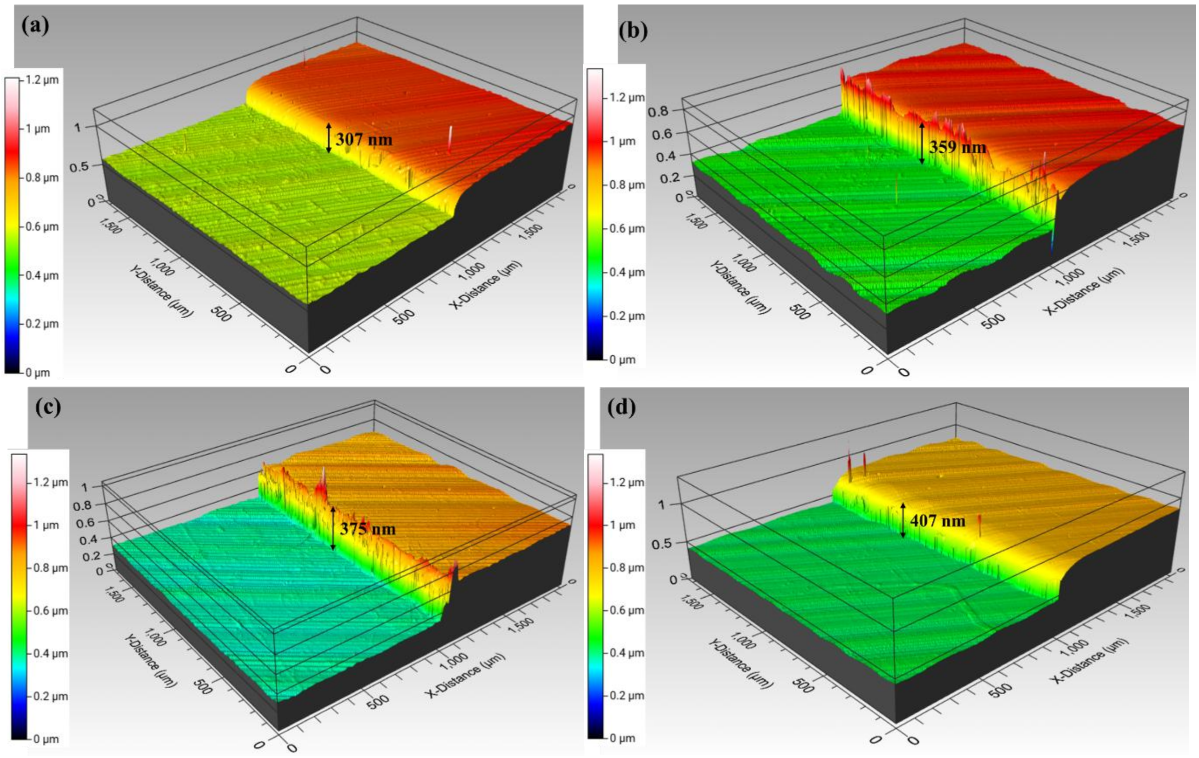

Figure 8.6: Examples of WLI 3D images of BiV coatings deposited with varying $P_V$: (a) 400 W ; (b) 800 W ; (c) 1000 W and (d) 1200 W

Table 8-3: Data recorded from 3D Optical profilometer for BiV samples

| Sample ID | Thickness measured (nm) | | | |
|---|---|---|---|---|
| | Measure 1 | Measure 2 | Measure 3 | Mean |
| BiV400 | 302 | 302 | 308 | 304 ± 12 |
| BiV500 | 318 | 322 | 327 | 322 ± 11 |
| BiV600 | 338 | 337 | 340 | 338 ± 2 |
| BiV700 | 346 | 346 | 342 | 344 ± 5 |
| BiV800 | 359 | 355 | 354 | 356 ± 7 |
| BiV900 | 365 | 364 | 367 | 365 ± 3 |
| BiV1000 | 374 | 374 | 379 | 375 ± 8 |
| BiV1100 | 392 | 394 | 389 | 391 ± 6 |
| BiV1200 | 409 | 408 | 406 | 407 ± 4 |

Finally, TEM micrograph and cross section are presented in Figure 8.7a and 8.7b. A dense structure of the coating is confirmed, with the higher presence of crystallites close to the interface with FTO. Darker and brighter areas are observed in Figure 8.7b, with further investigation that needs to be done determine what they correspond to. A d-spacing of 3.02 Å is observed, corresponding to the (1 2 1) plane of $BiVO_4$. It correlates the data obtained with the XRD patterns, where the (1 2 1) plane was the most predominant peak. EDX elemental mapping of a selected cross-section sample's revealed an homogeneous distribution of bismuth and vanadium in the $BiVO_4$ layer deposited onto FTO (see Figure 8.8). The homogeneity of the coating is of importance to ensure an effective performance of the photocatalyst and to ensure a good stability regarding the photoelectrochemical performance. Also, some gap can be observed at the interface between FTO and $BiVO_4$ layer. This might be a limiting factor for the photoelectrochemical properties, reducing the potential transfer of electron to FTO during photoelectrochemical measurements. It should be noticed that a diffusion of Na into the coating happened during the annealing step, as well as the Si from the substrate. However, no migration of Sn from the $SnO_2$ layer of the substrate can be observed in the coating.

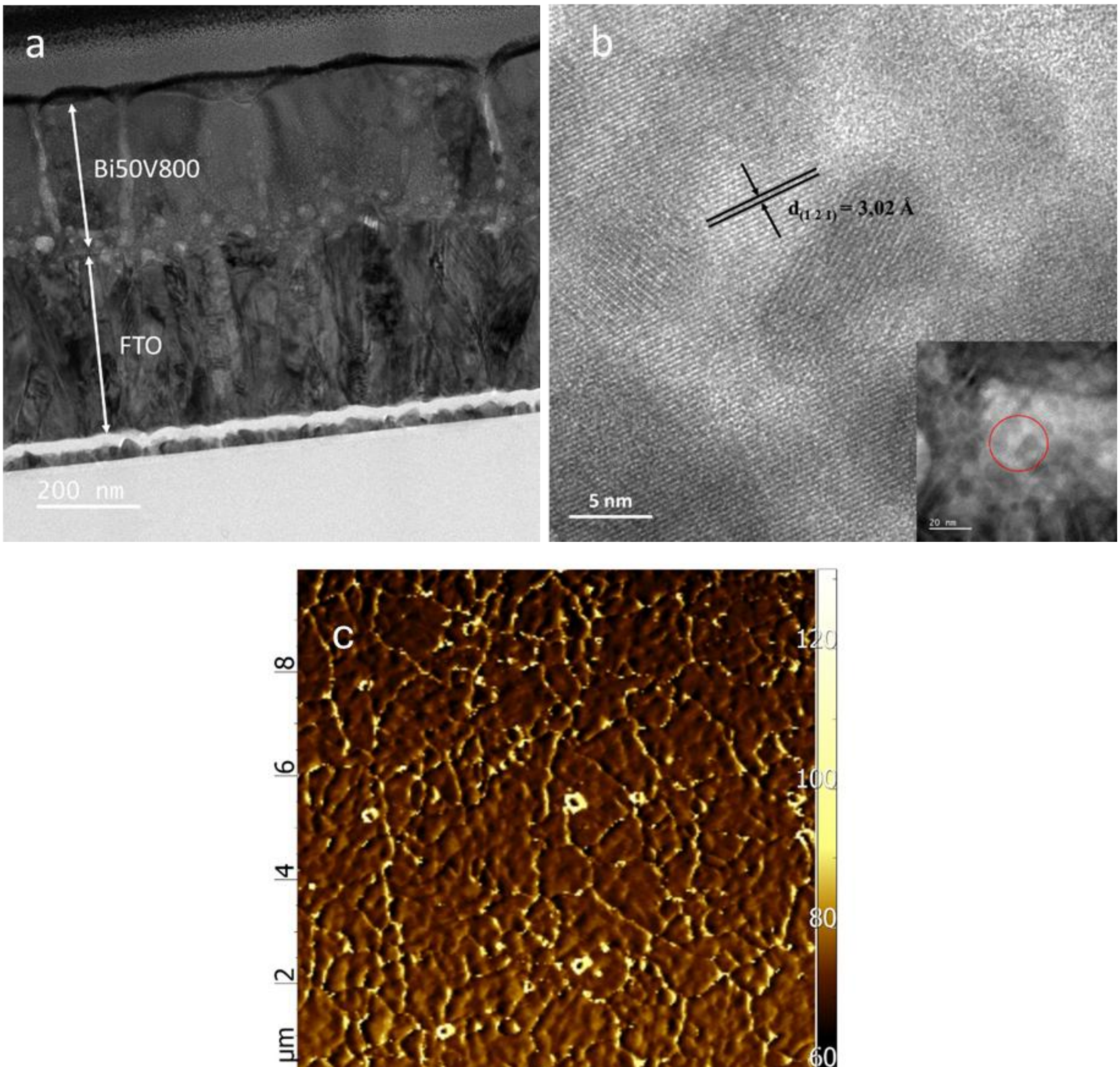

Figure 8.7: (a) Morphology of the coating at low magnification, (b) HRTEM micrograph of $BiVO_4$ (1 2 1) plane, (c) Example of AFM micrograph of BiV800 sample

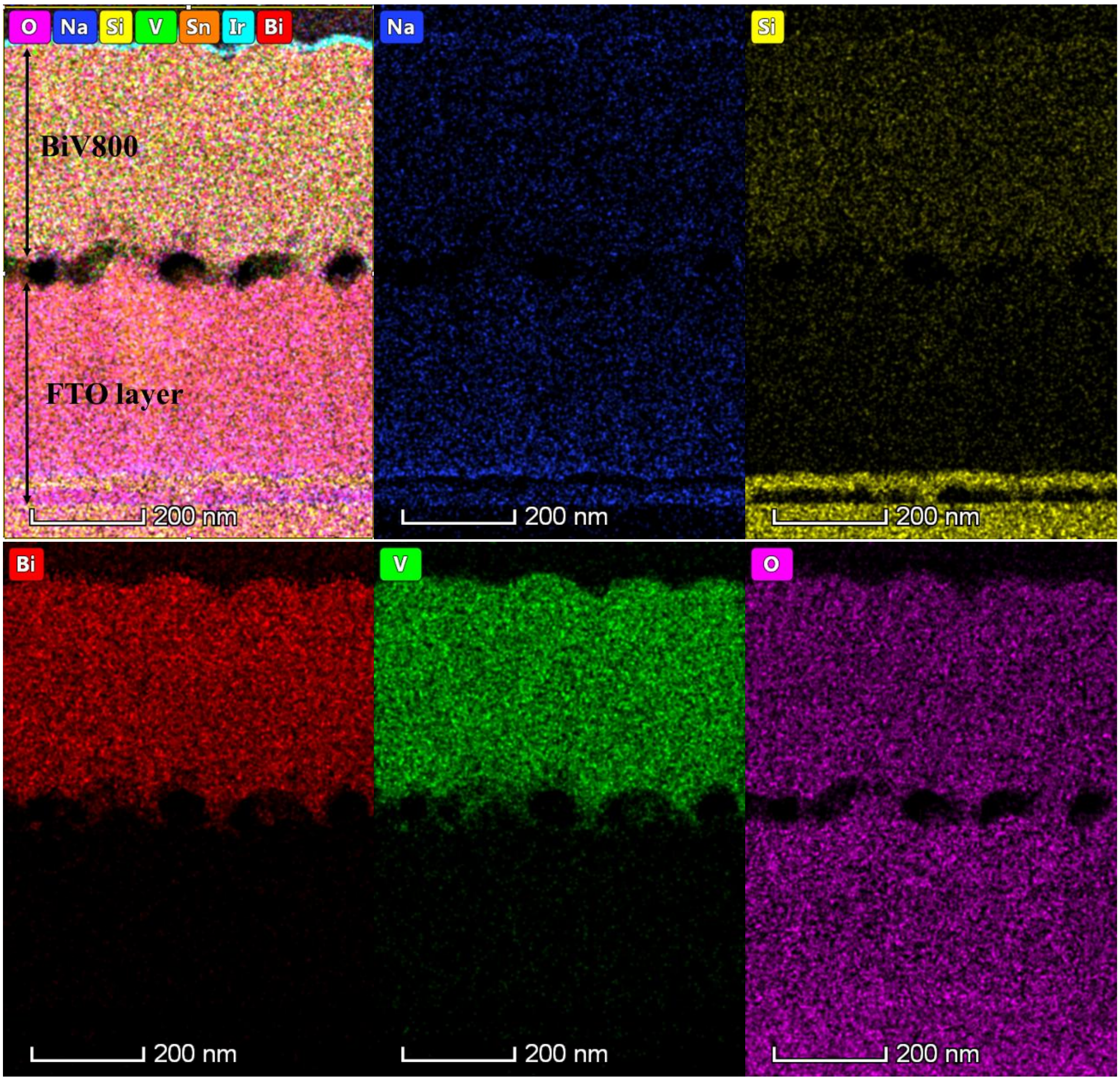

Figure 8.8: Elemental mapping of BiV800 sample with the different elements observed

## 8.5 Optical properties and band gap measurements

Figure 8.9 presents the visual aspect of BiV800 photoanode before and after annealing. It must be noticed the two samples presented are from two different runs, explaining the uncoated band in the middle of the as-deposited sample. The as-deposited sample present a transparent, yellowish colour, whereas the annealed photoanode presents an opaque yellow colour, typical from $BiVO_4$ when used as a pigment [200]. This change of transparency can be observed in the transmittance measurements, with an example given with BiV800 in Figure 8.10a. Before annealing, the transmittance is almost null until 360 nm and then increases to reach more than 90% at 500 nm, showing that visible light is easily transmitted by the sample. After annealing, the crystallisation induced has an effect on the optical properties, with a transmittance being almost null until 450 nm and reach a maximum of 80% from 650 nm. The annealed sample transmits less the incident light.

$BiVO_4$ is known for its relatively low band gap (between 2.4 and 2.6 eV) [176]. Usually, the optical band gap of a crystalline semiconductor is determined using the Tauc plot method and is obtained by plotting $(\alpha h\nu)^n$ as a function of hν and extrapolating the linear region to the abscissa (equation (36)) [157]:

$$\alpha h\nu = (h\nu - E_g)^{\frac{1}{n}} \tag{36}$$

However, the coefficient n depends on the nature of the band gap (2 for a direct band gap or 1/2 for an indirect band gap). Concerning $BiVO_4$, its band gap nature is subject to debate, with papers finding it direct [202, 203] or indirect [204, 205]. Figure 8.10b shows the Tauc plots of the $BiVO_4$ sample for both indirect and direct band gaps, where the linear part of the plots are extrapolated to the x-axis to estimate the optical bandgap. The range of bandgap for the extrapolation was chosen according to the expected bandgap for monoclinic $BiVO_4$. Indirect band gap plot shows an estimation of a 2.42 eV for the band, whereas the direct band gap exhibits an estimated band gap of 2.56 eV. Both methods show similar results and are in accordance with the findings in the literature [176]. Moreover, both values show that $BiVO_4$ sample can harvest photons from the visible light: a band gap of 2.55 eV allows the photons absorption until 477 nm, whereas a band gap of 2.42 eV allow the photons absorption until 516 nm. Wiktor et al. have found similar results [206], where density functional theory (DFT) calculations showed the difficulty to distinguish between direct and indirect band gaps in the case of $BiVO_4$. For the rest of the work, the BiV samples produced are considered as indirect band gap semiconductors. The different band gap values found for the BiV samples are listed in Table 8.4. No significant differences can be seen among the different BiV samples.

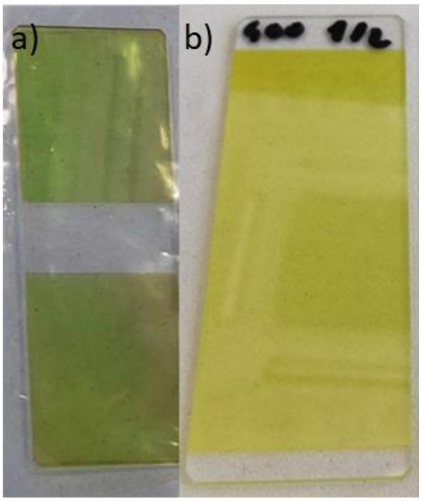

Figure 8.9: Example of BiV sample: (a) Before annealing, (b) After annealing

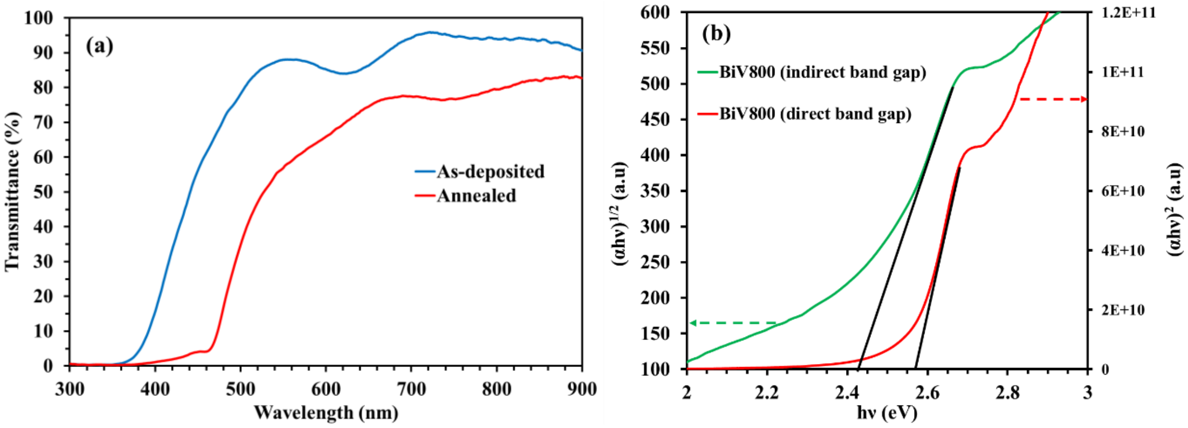

Figure 8.10: (a) Example of BiV800 transmittance measurement and (b) Tauc plot associated for direct and indirect band gap

Table 8-4: Band gap calculated for the BiV samples produced

| Sample ID | Band gap (eV) |
|---|---|
| BiV400 | 2.32 |
| BiV500 | 2.31 |
| BiV600 | 2.34 |
| BiV700 | 2.39 |
| BiV800 | 2.42 |
| BiV900 | 2.41 |
| BiV1000 | 2.38 |
| BiV1100 | 2.28 |
| BiV1200 | 2.32 |

## 8.6. Photocatalytic and photoelectrochemical activities

A first assessment of the photocatalytic activity of the BiV samples produced was done by performing methylene blue (MB) dye degradation test under UV light for 1h. The MB degradation tests were performed with all BiV samples produced and with uncoated FTO glass as a reference. Figure 8.11a presents the absorbance evolution with irradiation time, with the reference sample (referred as photolysis) showing almost no diminution of the absorbance after 1h. All BiV samples present a photocatalytic activity, showing a decreasing absorbance of the solution, but with different efficiencies. Figure 8.11b exhibits' estimations of the pseudo-first order $k_\alpha$, extracted using equation (48) (see Annexe 1). As it can be seen in Figure 8.11c, the $k_\alpha$ constant rate reach a maximum for the sample BiV800, associated with a Bi/V atomic ratio close to 1. As demonstrated earlier, this atomic ratio is associated with the production of the monoclinic phase, usually reported to be the most efficient crystal phase for $BiVO_4$. Above this ratio, corresponding to the samples BiV400 to BiV700, the $k_\alpha$ constant rate drops, showing that the presence of $Bi_4V_2O_{11}$ drastically reduces the photocatalytic activity. Samples with an atomic Bi/V ratio below 1 still exhibit a good photocatalytic activity, but the $k_\alpha$ constant rate tends to decrease when the amount of V becomes too important, as it can be observed with sample BiV1200, where the constant rate is lower than $1x10^{-5}$ $s^{-1}$ (see Figure 8.11c). This may be due to the formation of $V_2O_5$ impurities, acting as charge carriers' traps that favours the recombination of charge carriers. Finally, stability assessment of the best performing sample (BiV800) was done by removing Rhodamine B solution, a pollutant known to be more stable to photocatalytic degradation than methylene blue (with a maximum absorption of 542 nm). The sample has been tested during 10 cycles of 1h and appears to have a stable activity over the time; the results of the test are presented in the Figure 8.11d All photocatalytic data are summarised in Table 8.5.

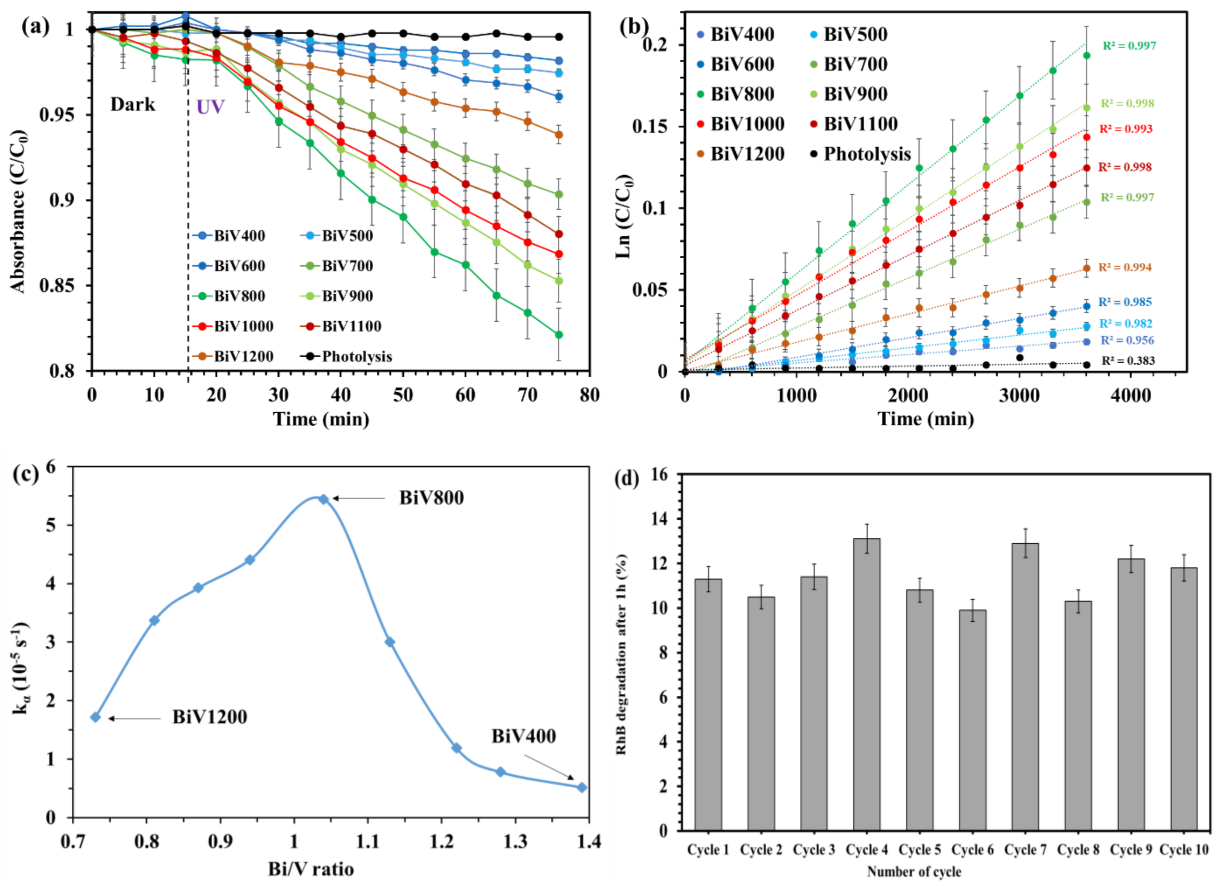

Figure 8.11: Photocatalytic activity assessment: (a) MB concentration in the dark and under UV when exposed to BiV samples and uncoated FTO ; (b) Pseudo-first order reaction rate plotted for MB removal, calculated for BiV samples and uncoated glass ; (c) evolution of k$_α$ constant rate depending on the Bi/V ratio ; (d) RhB removal percentage after 1h for 10 consecutive cycles

Table 8-5: Results of MB degradation tests under UV-A for BiV samples

| Sample No. | Pseudo first order k$_α$ (10$^{-5}$.s$^{-1}$) | R$^2$ |
|---|---|---|
| Uncoated FTO | 0.07 | 0.383 |
| BiV400 | 0.52 | 0.956 |
| BiV500 | 0.78 | 0.982 |
| BiV600 | 1.19 | 0.985 |
| BiV700 | 3.00 | 0.997 |
| BiV800 | 5.44 | 0.997 |
| BiV900 | 4.41 | 0.998 |
| BiV1000 | 3.93 | 0.993 |
| BiV1100 | 3.37 | 0.998 |
| BiV1200 | 1.72 | 0.994 |

The first photocatalytic measurements are then followed by photoelectrochemical characterisation, performed in a three-electrode configuration in a PEC cell, as described in Chapter 5. The working electrode used is the BiV sample, the counter-electrode is the Pt mesh, and the reference-electrode is the Ag/AgCl electrode. The electrolyte used is a neutral electrolyte solution, 0.5M $Na_2SO_4$, with a pH close to 7, as degradation of the coatings has been observed when an acidic electrolyte was used ($H_2SO_4$). Also, $Na_2SO_4$ is the usual electrolyte used for measurement of PEC properties of $BiVO_4$ photoanodes [180, 182]. Photocurrent production was assessed by performing linear sweep voltammetry (LSV) with a visible light source, calibrated to the AM 1.5 standard. Figure 65 presents the LSV curves recorded for each group of samples. The different PEC characterisation values are listed in Table 8.6.Two different measurements were performed, with and without the visible light source, to illustrate the ability of the samples to produce a current under illumination. For the BiV samples, the LSV measurements were not recorded under chopped illumination, except for the sample BiV1200, as shown in Figure 8.12c, to show an example of chopped illumination. All samples present a similar behaviour, with a photocurrent production starting with an onset potential between 0.5 and 0.6 $V_{RHE}$, meaning the oxygen evolution reaction starts occurring at low potentials, showing the photoelectrochemical activity of the samples. Usually, the onset potential for $BiVO_4$ photoanodes is around 0.7 V vs RHE [207]. It must be noted that the onset potentials are not even clearly distinguishable for BiV400 and BiV500, due to their low photocurrent productions. A correlation between the results of photocatalytic MB degradation tests and photocurrent production can be made. A tendency curve (see Figure 8.12e), similar to the photocatalytic activity, can provide a relation between the Bi/V ratio and the photocurrent production. For the "Bismuth-rich" samples (BiV400, BiV500 and BiV600), the photoelectrochemical activity was very low, with a photocurrent not exceeding 0.2 $mA.cm^{-2}$, likely due to the poor crystallisation of the coatings produced. The samples that present the best results are BiV800 and BiV900, with a photocurrent production of 1.95 $mA.cm^{-2}$ and 1.58 $mA.cm^{-2}$ at 1.23 V vs RHE, respectively. These high photocurrents are associated with the highest HC-STH efficiencies, determined with equation (40). The HC-STH efficiencies determined from the photocurrent densities are listed in Table 8.6. BiV1000 also present an interesting photoactivity, but then the photocurrent production drops for BiV1100 and BiV1200. The latter even presents a photocurrent divided between a cathodic part (negative photocurrent below 0.7 V vs RHE) and an anodic current, contrary to the rest of the samples. This behaviour is indicating the p-type nature of those samples and can be attributed to the high presence of $V_2O_5$, usually known as a p-type semiconductor. As mentioned earlier, $V_2O_5$ is sometimes mentioned as a way to enhance the PEC activity of $BiVO_4$ by forming heterojunctions [200]. However, in this case, the presence of $V_2O_5$ seems to reduce the photoactivity of the photoelectrode, giving to the photoanode a p-type behaviour, which is not desired in this work.

Table 8-6: Photoelectrochemical data recorded from LSV and HC-STH measurements for each BiV samples

| Sample ID | Photocurrent production (mA.cm$^2$ at 1.23 V vs RHE) | Max HC-STH (%) |
|---|---|---|
| BiV400 | 0.07 | > 0.01 |
| BiV500 | 0.13 | 0.015 |
| BiV600 | 0.18 | 0.02 |
| BiV700 | 0.42 | 0.06 |
| BiV800 | 1.95 | 0.27 |
| BiV900 | 1.58 | 0.16 |
| BiV1000 | 1.28 | 0.15 |
| BiV1100 | 0.56 | 0.05 |
| BiV1200 | 0.15 | / |

Table 8-7: Examples of $BiVO_4$ photoanodes fabricated with various sputtering techniques

| Bi and V target(s) | Electrolyte | Counter-electrode | Reference-electrode | Photocurrent density at 1.23 V (vs RHE) | Onset potential (V vs RHE) | Ref |
|---|---|---|---|---|---|---|
| V (99.95 at%)<br>$Bi_2O_3$ (99.99 at%) | 0.1M $Na_2SO_4$ | Pt | Ag/AgCl (3M) | 1.19 mA.cm$^2$ | 0.7 V vs RHE | [209] |
| V (99.99 at%)<br>$Bi_2O_3$ (99.99 at%) | 0.5M $Na_2SO_4$ + 0.1M $K_2HPO_4$ | Pt mesh | Ag/AgCl (3M) | 0.4 mA.cm2 | 0.4 V vs RHE | [193] |
| $BiVO_4$ (99.99 at%) | 0.5M phosphate buffer | Pt | Ag/AgCl (3M) | 1.86 mA.cm2 | 0.65 V vs RHE | [211] |
| Bi (99.95 at%)<br>V (99.95 at%) | 0.5M $Na_2SO_4$ | Pt mesh | Ag/AgCl (3M) | 1.2 mA.cm2 | 0.4 V vs RHE | [188] |

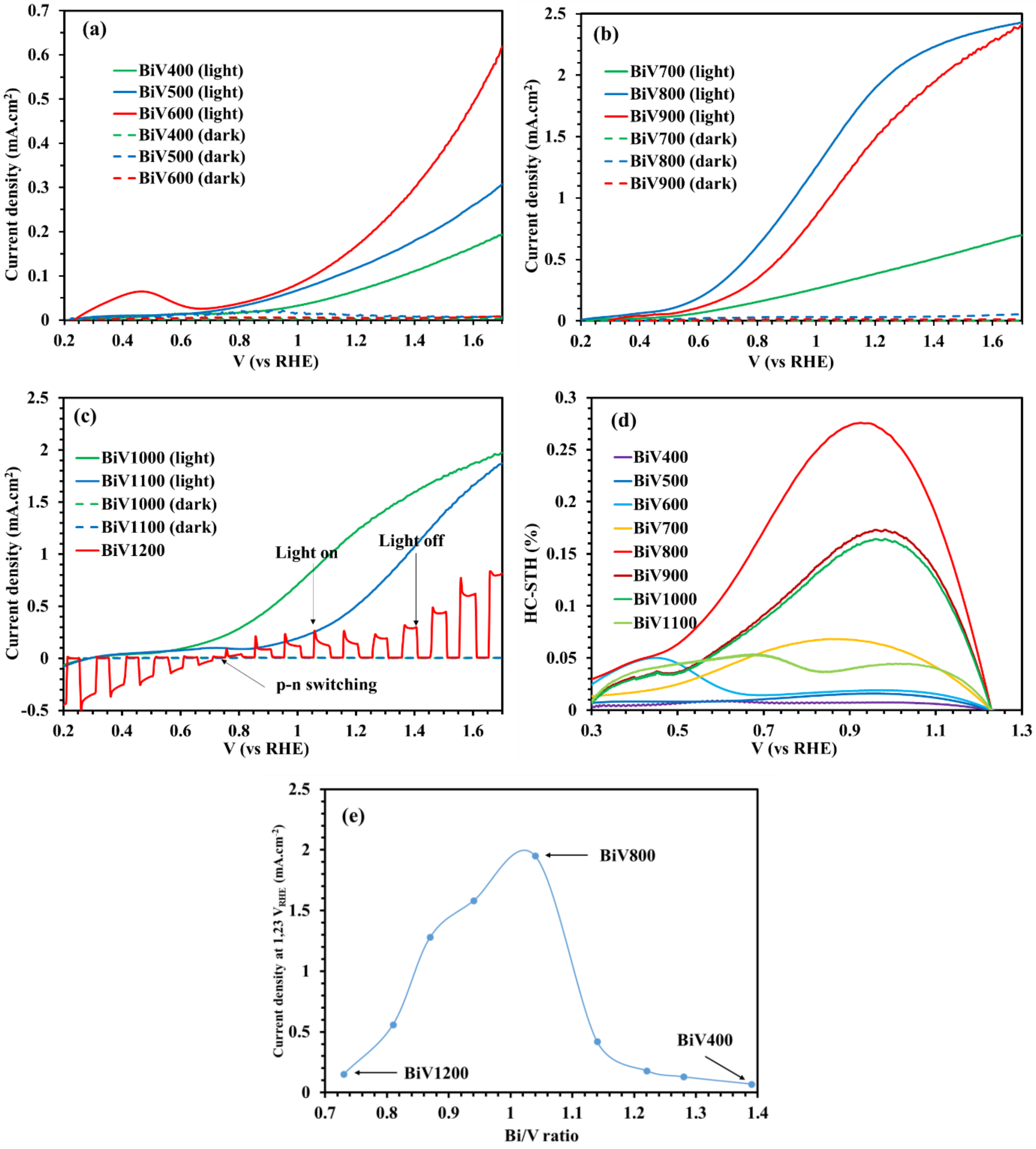

Figure 8.12: LSV measurement of the different BiV samples: (a) BiV400, BiV500 and BiV600 ; (b) BiV700, BiV800 and BiV900 ; (c) BiV1000, BiV1100, BiV1200 ; (d) HC-STH associated with the LSV measurements ; (e) Evolution of photocurrent density production at 1.23 $V_{RHE}$ with the Bi/V ratio

The BiV samples produced does not outperform some of the $BiVO_4$ photoanodes produced by wet chemical methods, where specific morphologies such as nanostructures or higher porosities are used to enhance the surface area and so their photoelectrochemical activities [208, 209]. Table 8.7 presents different photoelectrochemical data related to $BiVO_4$ photoanodes produced by sputtering techniques. The lack of standard among the different studies (type and concentration of the electrolyte) does not allow a proper comparison between the different $BiVO_4$ photoanodes. However, the results obtained for this work remain promising, allowing the production of a high photocurrent density at 1.23 $V_{RHE}$ for BiV800.

## 8.7. Charge separation and charge transport efficiencies

As seen in the previous section, the samples that present the most interesting photoelectrochemical properties are BiV800, BiV900 and BiV1000. All three were selected to measure their respective charge transfer and charge transport efficiencies ($\eta_{transfer}$ and $\eta_{transport}$), both representing key factors to understand PEC properties of the materials. Both efficiencies are determined with the following equations:

$$\eta_{transfer} = \frac{J_{H_2O}}{J_{scavenger}} \tag{44}$$

$$\eta_{transport} = \frac{J_{scavenger}}{J_{abs}} \tag{45}$$

where $J_{H_2O}$ is the photocurrent density produced without scavengers, $J_{scavenger}$ is the photocurrent density produced with scavengers and $J_{abs}$ is the theoretical maximum photocurrent produced. The scavengers used for the efficiency's measurement was 0.1M $H_2O_2$ solution added to the electrolyte. $H_2O_2$ was here used a hole scavenger and is assumed that its oxidation kinetics is very fast, with a charge transfer efficiency of 100% [211]. This scavenger is often used as hole scavenger for charge transport and charge transfer efficiencies for $BiVO_4$ photoanodes [43].

$J_{abs}$ can be deduced from the light harvesting efficiency, as described in equation (46):

$$J_{abs} = \frac{q}{hc}\int_{\lambda_1}^{\lambda_2} \lambda \times \Phi_\lambda \times LHE \times d\lambda \tag{46}$$

where $\Phi_\lambda$ is the spectral irradiance of the light source used (estimated at 100 $mW.cm^{-2}$), calibrated under the AM 1.5G standard and LHE the light harvesting efficiency (in %) [rajouter une reference]. As described in Chapter 7, it corresponds to a theoretical measure, and is used to estimate how efficiently the photons absorbed by the photocatalysts are contributing for the production of electron/hole pairs [43]. This measurement is usually calculed for the measurement of other efficiencies, such as STH. The LHE efficiencies for the BiV samples selected are presented in Figure 8.13. This value remains theoretical and does not take into account other optical phenomena, such as scattering or reflection. Charge transport and charge transfer efficiencies ($\eta_{transfer}$ and $\eta_{transport}$) for selected samples are presented in Figure 8.14a and 8.14b, respectively. The charge transfer efficiency of BiV1000 is drastically lower than the two other samples tested, not exceeding 10% at 1.23 V vs RHE. The two other samples present a higher $\eta_{transfer}$ values, with 14,5 and 17.7 % for BiV900 and BiV800, respectively. Those values remain low and can be explained by the poor kinetics of $BiVO_4$ regarding the oxygen evolution reaction, often identified as a key limitation to photoanode performance [213].

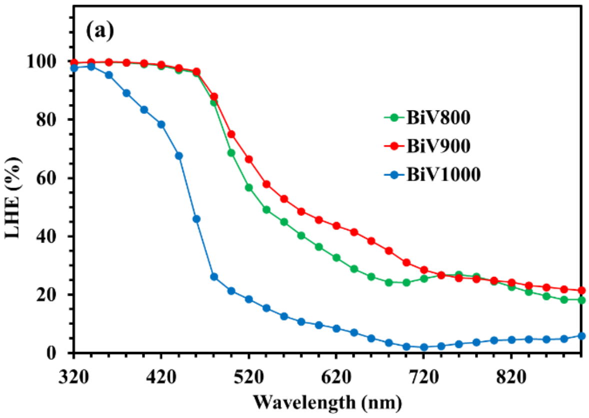

Figure 8.13: Efficiencies related to BiV800, BiV900 and BiV1000 samples : (a) Light harvesting efficiency $\eta_{harvesting}$ ; (b) Charge transfer efficiency $\eta_{transfer}$ ; (c) Charge transport efficiency $\eta_{transport}$

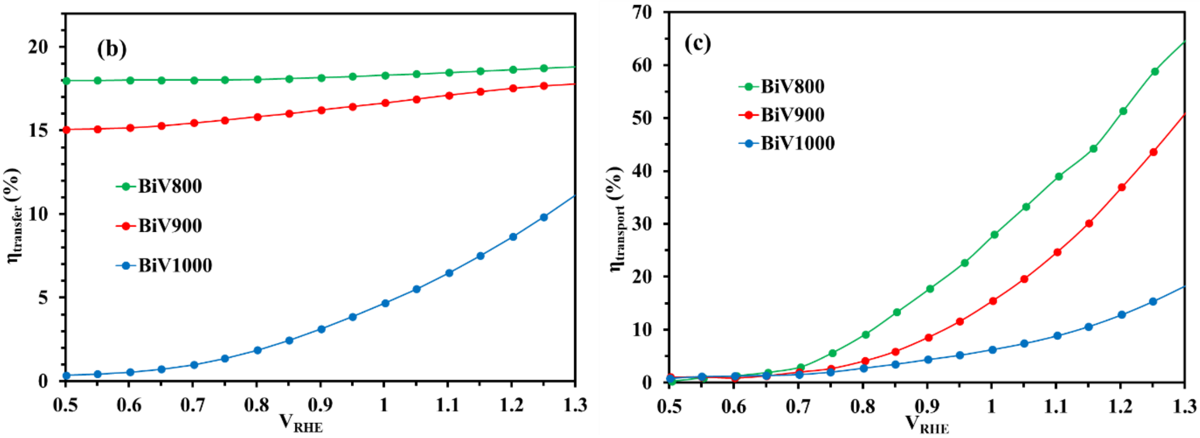

Figure 8.14: Efficiencies related to BiV800, BiV900 and BiV1000 samples : (a) Light harvesting efficiency $\eta_{harvesting}$ ; (b) Charge transfer efficiency $\eta_{transfer}$ ; (c) Charge transport efficiency $\eta_{transport}$

Contrary to the two other samples, BiV1000 presents at its surface $V_2O_5$ nanoparticles. Usually, the combination of $BiVO_4$ and $V_2O_5$ enhances the charge transfer from the semiconductor to the electrolyte, thanks to the formation of heterojunctions [200] [214]. However, here $V_2O_5$ is not produced as a thin layer on top of $BiVO_4$ but is randomly distributed as nanoparticles across the surface, as it can be seen on the SEM top surface images in Figure 8.5. In this case, $V_2O_5$ nanoparticles act more as recombination charge centre, thus lowering the transfer efficiency to the electrolyte. On the other hand, BiV800 and BiV900 exhibit the highest charge transfer efficiency. Regarding the charge transport efficiency, BiV800 exhibits the highest rate, with a charge transport efficiency of 60% at 1.23 $V_{RHE}$. To understand the different photoelectrochemical activity measured for the selected samples and the higher efficiencies of the BiV800 sample, their respective chemical and electronic states were investigated using XPS analysis.

The survey spectra for the three selected samples are shown in Figure 8.15, where the residual carbon can be observed with the C 1s peak. The bindings energies of other peaks were referenced to the C 1s peak located at 284.9 eV. Figure 8.16 shows high resolution XPS spectra of Bi 4f, V2p and O1s states. The Bi 4f spectrum reveals two peaks located at 158.9 eV and 164.2 eV, attributed to the binding energies of Bi $4f_{7/2}$ and Bi $4f_{5/2}$ states. These values are in good agreement with the literature information and are indicative of the presence of bismuth in the $Bi^{3+}$ state but slightly shifted to lower values. Li et al. attributed this shift to the break of Bi-O bonds, forming low valent Bi ions ($Bi^{(3-x)+}$), indicative of the formation of oxygen vacancies [215]. It must be noticed that no other peaks can be observed for Bi 4f. The spectrum of V 2p reveals the presence of two peaks, attributed to the V $2p_{1/2}$ and V $2p_{3/2}$ states, with binding energies of 516.3 eV and 524.1 eV, respectively. The vanadium is present in the $V^{5+}$ oxidation states, which is in agreement with the formation of $BiVO_4$ [215]. It is not possible to verify the $V_2O_5$ presence with XPS, due to the same valence of vanadium between $V_2O_5$ and $BiVO_4$. The high-resolution XPS spectra of O 1s before and after annealing is presented in Figure 68c and 68d, respectively. As observed, prior to the annealing step, the O 1s peak can be deconvoluted into two peaks located at 529.5 eV and 531.3 eV. Those peaks can be attributed to the lattice oxygen and hydroxyl species adsorbed onto oxygen vacancies. Before annealing, the O 1s L peak is greater than the O 1s V peak. Once the sample is annealed, the atomic percentage ratio between the O 1s L to O 1s V (calculated from the relative areas of the XPS peaks) changes, with an increasing amount of oxygen vacancies. This indicates a significant higher number of oxygen vacancies within the sample, which is in good agreement with the photoelectrochemical measurements.

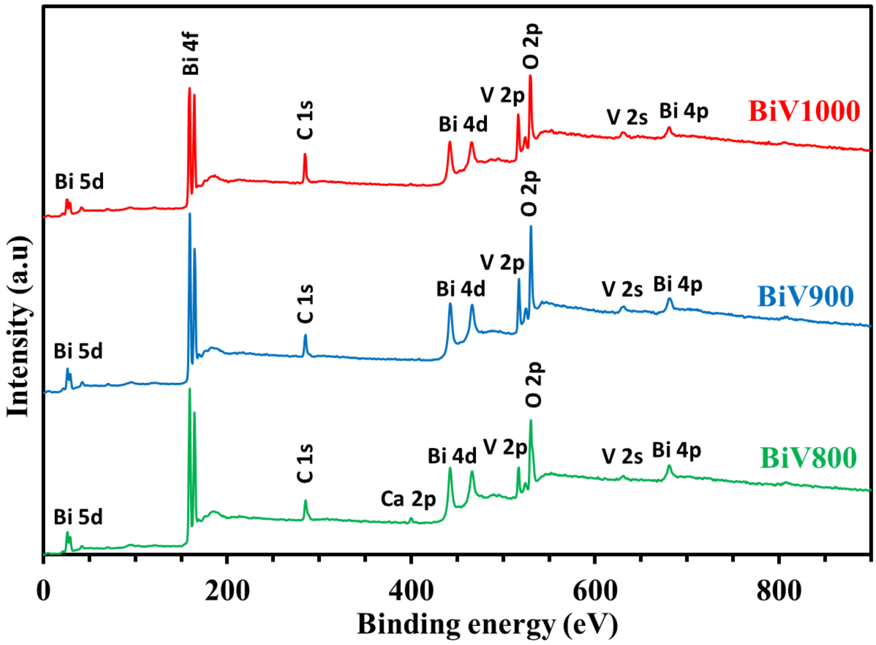

Figure 8.15: Wide XPS spectrum of BiV800, BiV900 and BiV1000 samples

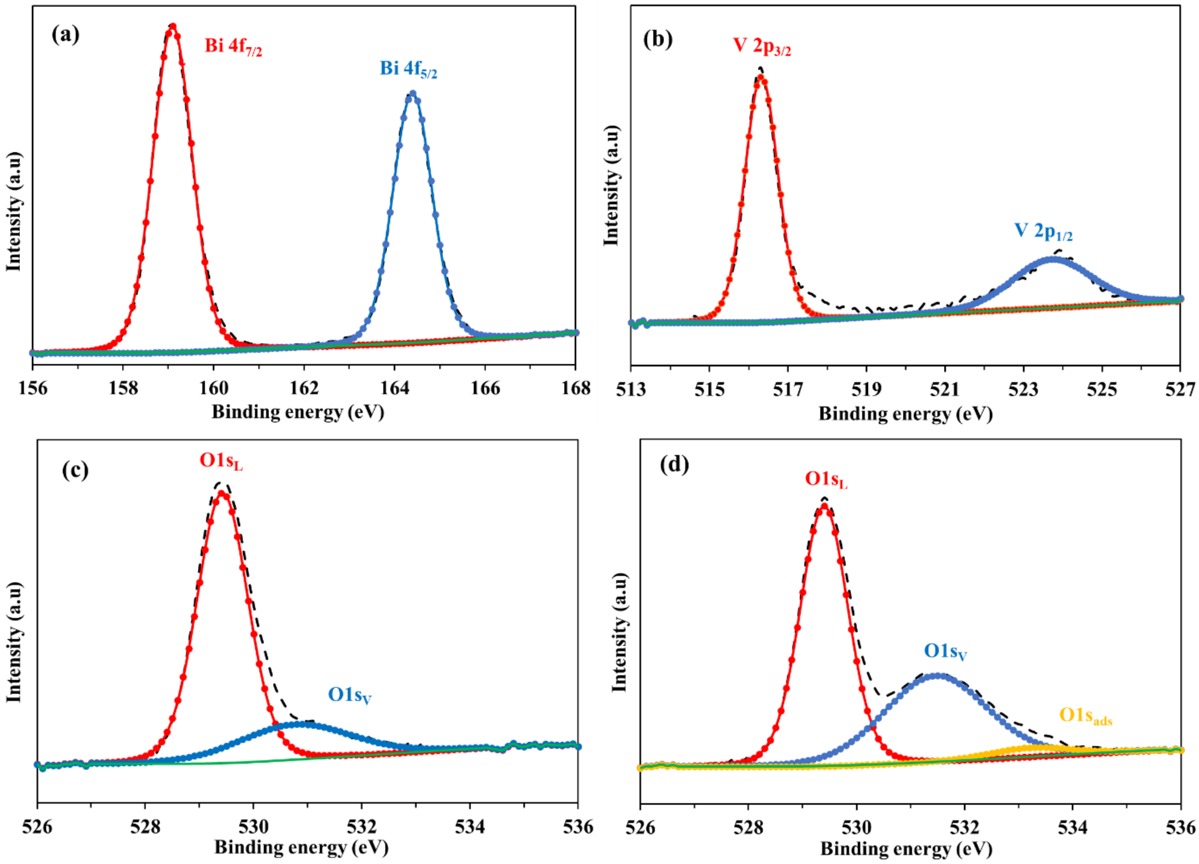

Figure 8.16: High resolution XPS analysis of BiV800 sample: (a) Bi 4f state, (b) V 2p state, (c) O 1s state before annealing , (d) O1s state after annealing

The presence of oxygen vacancies could explain the better charged transport and charge transfer efficiency measured for the BiV800 sample compared with the two others. In metal oxides, oxygen vacancies act as electron traps, thus helping to avoid the recombination within the lattice and enhancing the charge carrier's lifetime [94]. Here, it appears that BiV800 possesses the highest amount of oxygen vacancies (see Table 8.8). It is complicated to properly quantify the amount of oxygen vacancies within the bulk of the materials and at the surface of the coatings. Nonetheless, the presence of oxygen vacancies has been found to increase the charge transport efficiency in many cases of $BiVO_4$ photoanode. The increasing efficiency of charge transfer is usually done by altering the surface of the photoelectrode by diverse meaning. For example, Lu et al. deposited a $VO_x$ layer on the top of a photoanode surface boosting the charge transfer efficiency of the $BiVO_4$ photoanode produced [216]. On the other hand, Liu et al. studied the impact of Bi and oxygen vacancies within the lattice of a $BiVO_4$ photoanode and demonstrated its positive impact on the charge transport efficiency [217].

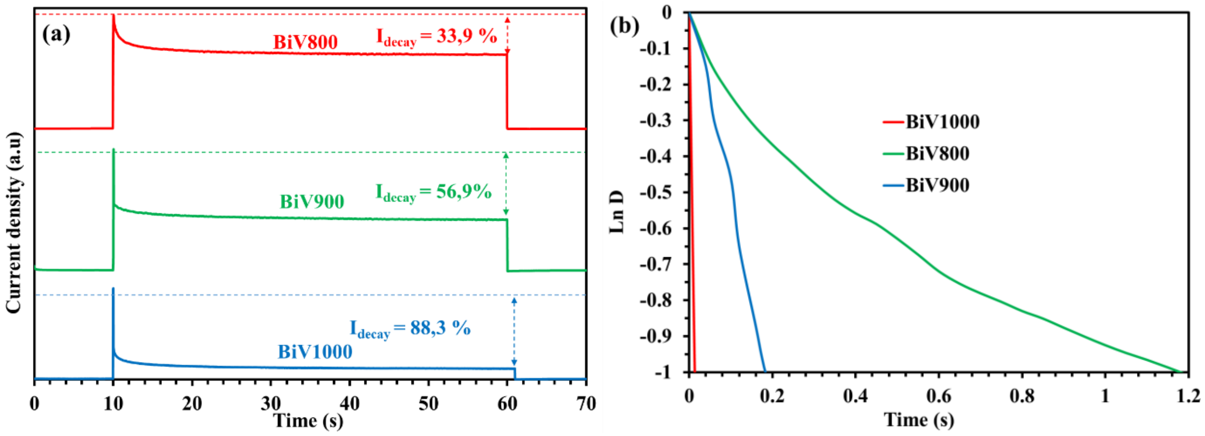

Figure 8.17: (a) Transient time photocurrent measured for BiV samples, (b) Associated calculation process for obtaining the transient time, obtained for Ln D = -1

To illustrate this extended lifetime of charge carriers induced by oxygen vacancies, transient time measurements were performed. Transient photocurrents were measured for the three-selected samples in a three-electrodes configuration and are presented in Figure 8.17a. The decay of photocurrent when the sample is illuminated can be determined using Equation (42) described in section 5.10.5. The transient time $\tau$ can be obtained with Equation (41) at the time when ln D = -1. Associated transient time plots are presented in Figure 8.17b. It can be seen from the transient photocurrents and the transient times associated that BiV800 seems to produce charge carriers with the highest lifetime. This measure can be correlated with the high oxygen vacancies amount estimated for this sample. The transient times measured with this method are more qualitative data than quantitative data, as the transient times measurement is not accurate. Abdi et al. investigated the charge carrier's lifetime and diffusion length of $BiVO_4$ photoanodes with time-resolved microwave conductivity (TRMC) [218]. It was found that the charge carriers' lifetime was about 40 ns, which is more than 10000 times less than the values found with transient time measurements. Further investigation would be then needed to precisely determine the charge carrier's lifetime within the BiV samples produced. Table 8.8 summarise the different data presented in this section.

Table 8-8: Data recorded for BiV800, BiV900 and BiV1000

| | Oxygen vacancy amount (area %) | Transient time τ (s) | $\eta_{transfer}$ at 1.23 V vs RHE (%) | $\eta_{transport}$ at 1.23 V vs RHE (%) |
|---|---|---|---|---|
| BiV800 | 40.12 | 1.19 | 17.7 | 59 |
| BiV900 | 32.18 | 0.19 | 14.5 | 38 |
| BiV1000 | 23.46 | > 0.1 | 10 | 15 |

## 8.8. Thickness dependence of the $BiVO_4$ films

Finally, the BiV800 sample was replicated with different thicknesses by varying the deposition time, to study the impact of film thickness onto the photoelectrochemical performances. Table 8.9 presents the different deposition times selected, with the different thicknesses associated. Several sources of errors can influence the thickness measurement from the cross-section images, such as the resolution of the SEM, errors of calibration or errors associated with the angle of the camera. Here, the measure was repeated 5 times and standard deviation was calculated. The cross-section SEM micrographs are shown in Figure 8.18, where the deposited layers can be observed on top of the FTO layers from the substrates.

Table 8-9: Data recorded for the BiV800 films deposited at different thicknesses

| Deposition time | Thickness measured | Photocurrent production at 1.23 V vs RHE (in $mA.cm^{-2}$) | Maximum HC-STH efficiency (%) |
|---|---|---|---|
| 15 min | 87 ± 11 nm | 0.3 | 0.02 |
| 30 min | 190 ± 16 nm | 2.6 | 0.35 |
| 1h | 340 ± 22 nm | 1.5 | 0.17 |
| 1h 30min | 445 ± 37 nm | 1.2 | 0.12 |
| 2h | 572 ± 31 nm | 0.5 | 0.05 |

All samples present a dense morphology made of large grains, which is indicative of the recrystallization zone depicted in the Thornton model [147]. Figure 8.19 presents the different PEC measurements done with the produced samples. According to the LSV scans, the photocurrent produced decreases with the thickness of the coatings. The best performance obtained is for BiV800 deposited for 30 min, resulting in a thickness of 190 nm. The photocurrent produced by this sample reaches around 2.5 mA.cm$^{-2}$ at 1.23 V vs RHE, with a maximum HC-STH efficiency of 0.35%. The performances then drastically decrease when the thickness is increased, with only 0.5 mA.cm$^{-2}$ at 1.23 V vs RHE (maximum HC-STH efficiency of 0.05%) produced for a sample deposited for 2h. A correlation between the coatings thickness and the photocurrent produced is shown in Figure x. It is interesting to notice that a too thin film (BiV800 deposited for 15 min, 87 nm thick) does not exhibit a larger photocurrent compared to the BiV800 sample deposited for 30 min.

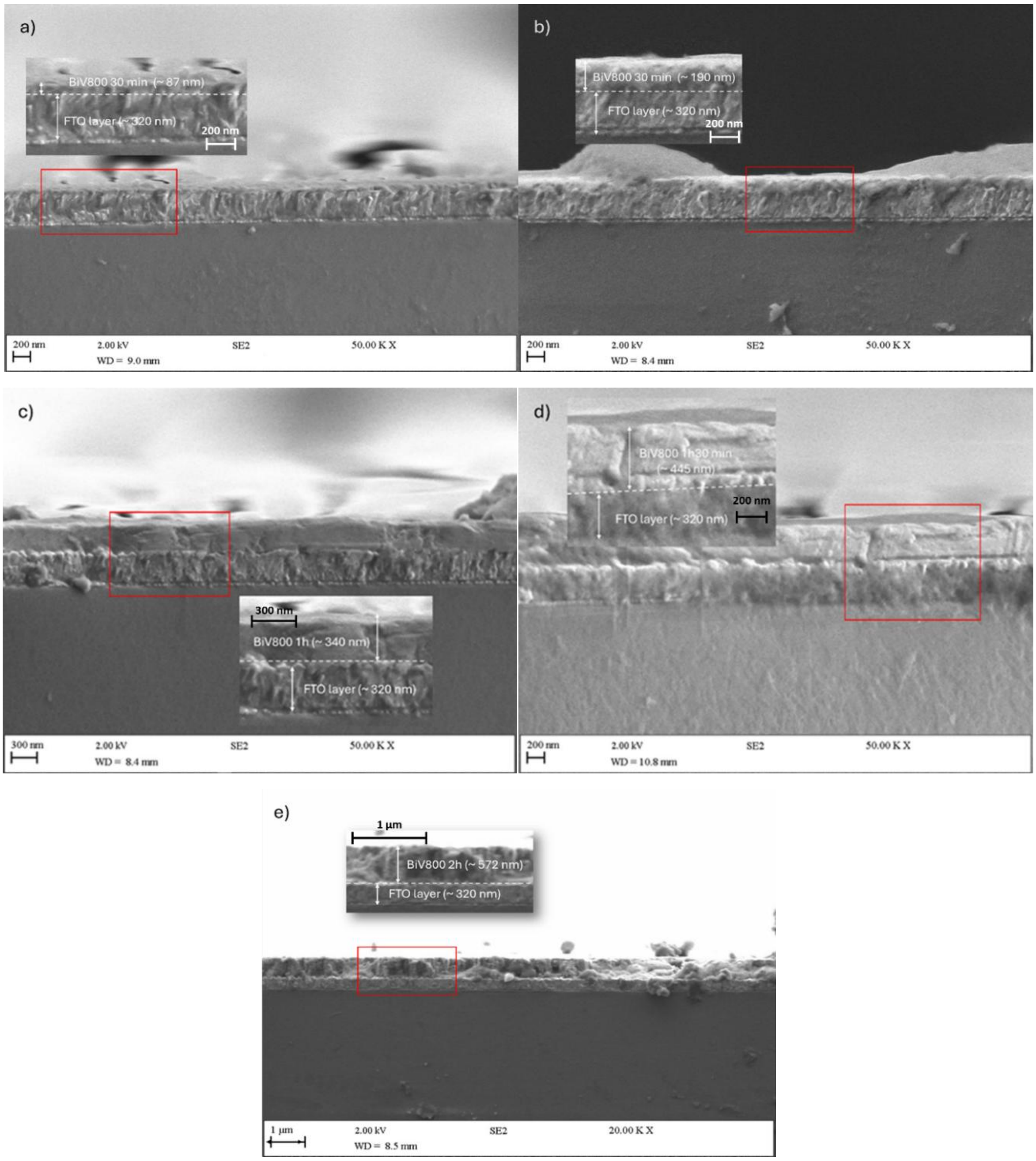

Figure 8.18: Cross-section SEM images of BiV800 sample deposited for; (a) 15 min; (b) 30 min; (c) 1h; (d) 1h 30min; (e) 2h

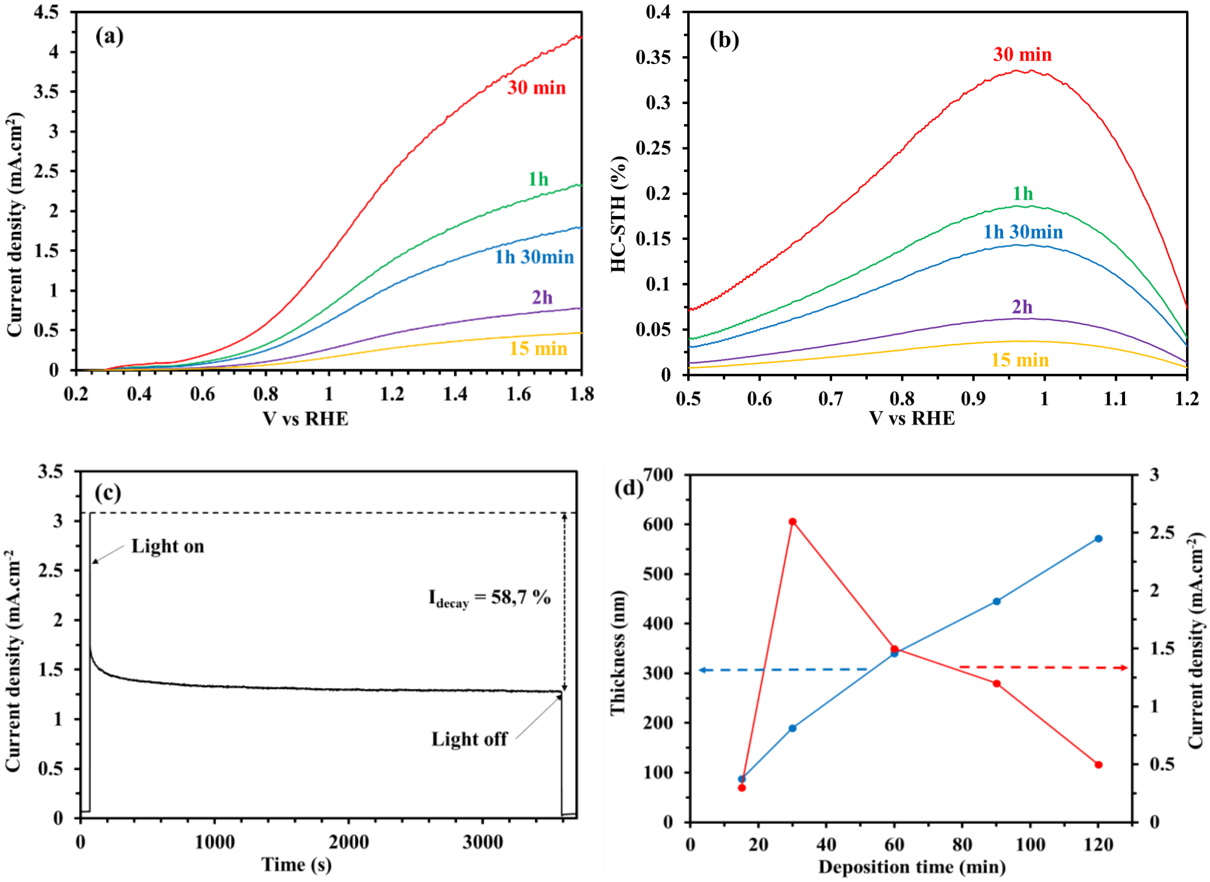

Figure 8.19: a) LSV scans for the BiV samples produced with different thicknesses, b) Associated HC-STH efficiencies, c) Stability measurement for BiV sample deposited for 30 min, (d) Correlation between thicknesses and photocurrents produced by the BiV samples deposited for several times

The impact of film's thickness can be explained by the short diffusion length of the charge carriers within $BiVO_4$ before recombination. As mentioned earlier, the short charge carriers' lifetime within $BiVO_4$ (40 ns) is associated with a short diffusion length (around 70 nm) [218]. When the charge carriers are produced in the bulk of a thick layer of photocatalyst, they need to reach the reaction sites on the photocatalyst surface to drive the chemical reactions. Despite the presence of electron traps such as oxygen vacancies, their diffusion length within the material (and then their lifetime) is limited. Hence, a thick film results in a higher recombination rate and so a lower photocurrent produced. Interestingly, the sample produced for 15 min, resulting in a thickness of 87 nm does not produce a high photocurrent, probably due to the lack of matter deposited compared to thicker coatings. An equilibrium should be then found to obtain a coating thin enough to avoid charge recombination, but thick enough to harvest the incident photons. Finally, the stability measurement photocurrent is presented in Figure 8.19c, and was recorded by performing chronoamperometry with a fixed potential at 1.23 $V_{RHE}$ on sample BiV800 deposited for 30 min. The chronoamperometry was recorded for

180 min to observe the stability of the photocurrent produced by the sample. A peak of photocurrent can be observed and then a decay of photocurrent (Idecay = 58.7%) that stabilises around 1.4 mA.cm$^{-2}$ produced. The large and quick decay of the photocurrent observed can be explained by a large number of electron-hole pairs produced, followed by a quick recombination of some of them. Compared to LSV measurements presented in Figure 8.19a, the photocurrent produced by the photoanode is less important, probably due the poor charge transfer efficiency demonstrated in the previous section. This is also associated with a decay of the photocurrent more important compared to a BiV800 sample deposited for 1h. Additional work could be then done to enhance this charge transfer efficiency, to expect a higher photocurrent produced and a lower photocurrent decay during stability measurements.

## 8.9. Summary

To summarise, $BiVO_4$ photocatalysts were produced using pDC reactive magnetron co-sputtering to be used as photoanode for the study of the oxygen evolution reaction. The first parameter studied was the variation of power applied on the Bi and V targets, due to the high sputter yield difference between the two metals. This difference of sputter yield can result in the formation of "bismuth-rich" or "vanadium-rich" compounds, with the presence of impurity phases ($Bi_4V_2O_{11}$ and $V_2O_5$), reducing the performances of the materials. The phase of interest (m-s $BiVO_4$) was obtained for the samples produced with a Bi/V ratio close to 1. Regarding the photocatalytic and photoelectrochemical performances, all samples presented a photoactive response to UV light and visible light. The BiV800 sample presented the highest degradation rate and photocurrent production, with a photocurrent produced of 1.95 $mA.cm^{-2}$ at 1.23 $V_{RHE}$, resulting in a HC-STH efficiency of 0.28% at 1.23 $V_{RHE}$. To understand this better activity, the different charge transport and charge transfer efficiencies were evaluated. In particular, a better charge transport efficiency was measure for the BiV800 sample (59% at 1.23 $V_{RHE}$). This improved efficiency can be then explained by a higher amount of oxygen vacancies produced within the coating, acting as charge carrier traps and then reducing the recombination rate within the bulk of the photocatalyst. On the other hand, all samples presented a poor charge transfer efficiency, due to the poor kinetics of $BiVO_4$ regarding the oxygen evolution reaction. The impact of the films thicknesses was also studied, showing a maximum of photocurrent produced at 1.23 $V_{RHE}$ for a 30 min deposited film, resulting in a thickness of 190 nm and a photocurrent produced of 2.6 $mA.cm^{-2}$ at 1.23 $V_{RHE}$. However, when the photocurrent stability is studied, a large photocurrent decay is observed (more than 60% of photocurrent lost after 1h), which can be explained by the low charge transfer efficiency of the material. This lack of charge transfer efficiency could be improved in future studies, with the addition of co-catalyst (such as Co-Pi), the combination with other photocatalysts to build heterojunctions or with implementation of protection layers. The findings presented in this chapter show the feasibility of producing $BiVO_4$ coatings for photoanodes by pDS reactive magnetron sputtering. In addition, several studies can be done to improve or characterise the BiV photocatalysts produced. Additional work should be done in future work to obtain more information on the photocatalysts. Firstly, the specific surface area should be measured with additional techniques, such as AFM, or by electrochemical techniques such as cyclic voltammetry. Mott-Schottky plots could obtain information about the electronic band structure. Finally, impedance spectroscopy would help to understand the electronic behaviour of the electrical circuit.

# 9. Production of $CuBi_2O_4$ photocathode by magnetron sputtering for PEC hydrogen evolution reaction

*This chapter presents the results obtained for the production of copper bismuth oxide coatings produced by reactive magnetron co-sputtering for the study of the photoelectrochemical hydrogen evolution reaction.*

*This chapter discusses the background on* $CuBi_2O_4$ *photocatalysts (Section 1), the work overview explaining the production method (Section 2), the characterization of the samples produced, with crystallinity (Section 3), morphology (Section 4), the optical measurements (section 5) and a first assessment of the photoelectrochemical activity (Section 6). Section 7 presents the measurements of charge transfer and charge transport for a selected range of samples and Section 8 discusses the impact of thicknesses onto photocurrent production. A summary of the chapter is given in section 9.*

## 9.1. Introduction

As for most of the metal oxide photocatalysts, $CuBi_2O_4$ photocathodes have been typically produced using wet chemical methods, such as spin-coating [231] or hydrothermal synthesis [232]. As with the study of $BiVO_4$, PVD methods present interesting advantages, such as the scalability, the lack of hazardous chemicals/precursors and enabling the production of uniform coatings in terms of morphology and composition. In this work, BiCu thin films were produced using mid-frequency pulsed DC reactive magnetron co-sputtering, using two metallic targets (Bi and Cu, 99.5% purity). Duployer et al. demonstrated the feasibility of producing $CuBi_2O_4$ photocathodes by RF sputtering from a ceramic compound target [233]. Otherwise, no mentions of production of $CuBi_2O_4$ photocathodes by sputtering techniques have been found to date. Contrary to RF sputtering, reactive sputtering with metallic targets in an argon/oxygen atmosphere offers several advantages, such as higher deposition rates, process stability and reduction of defects. As two targets are used, it is possible to tune the chemical composition of the thin films deposited by adjusting the power densities applied to the targets. Hence, it is possible to study the effect of the sputtering parameters on the photoelectrochemical properties of the samples produced. It must be noted that Bi and Cu have different sputtering deposition rates, with Bi being known for having a high sputtering yield [234].

## 8.2. Experimental methods

The goal of this chapter is to produce an efficient $CuBi_2O_4$ photocathode by pulsed DC magnetron sputtering using two metallic targets (Bi and Cu, 99.5% purity), for the study of the hydrogen evolution reaction in a PEC cell. BiCu samples were produced by varying the power densities applied on the targets during deposition, with the sputtering parameters summarized in Table 9.1. The power applied on Bi was fixed at 100 W and the power applied on Cu was varied, from 25 W to 200 W with a 25 W increment, to ensure a various of $P_{Bi}/P_{Cu}$ range (from 4 to 0.5). The samples are labelled in accordance with the power applied on the copper target (for example, BiCu25 means that the sample was produced by applying 100 W on Bi target and 25 W on Cu target). The films were deposited onto Si wafer (for EDX analysis) and Fluorine-doped Tin oxide (FTO) glass substrate from Pilkington. Dual-channel Advanced Energy$^{TM}$ Pinnacle Plus power supply was used, with a pulse frequency of 100kHz and a duty cycle of 60% (off time: 4 μs). Argon and oxygen flows were kept constant during the deposition, at 40 and 10 sccm respectively. The deposited samples were then annealed in air at 500°C to get a crystalline $CuBi_2O_4$ photocatalyst.

Table 9-1: Sputtering parameters for the production of CuBi samples

| Sample ID | $P_{Bi}$ (W) | $P_{Cu}$ (W) | $P_{Cu}/P_{Bi}$ |
|---|---|---|---|
| BiCu25 | 100 | 25 | 0.25 |
| BiCu50 | 100 | 50 | 0.5 |
| BiCu75 | 100 | 75 | 0.75 |
| BiCu100 | 100 | 100 | 1 |
| BiCu125 | 100 | 125 | 1.25 |
| BiCu150 | 100 | 150 | 1.5 |
| BiCu175 | 100 | 175 | 1.75 |
| BiCu200 | 100 | 200 | 2 |

Similarly to the previous chapter, the BiCu samples produced were characterised with different analytical techniques, to understand their composition, morphology or crystal structure. A first measurement was done by Raman Spectroscopy with a Renishaw Invia performed with a laser operating at a wavelength of 514 nm with a power of 10 mW and a long working distance microscope objective with magnification of 50x. The Raman spectra was recorded between 100 and 900 $cm^{-1}$. Then, XRD was performed PANalytical X'pert X-Ray diffractometer with a Cu $K_{\alpha}$ source ($\lambda = 1.5406$ Å). The diffraction peaks were recorded in the range of $2\theta = 15° - 60°$, with a step size of 0.015° and a measurement time of 0.88 seconds per step. Then, the reference patterns were identified using the International Centre for Diffraction

Data (ICCD) database. The morphology of the BiCu samples was analysed by Scanning electron microscopy (SEM), to produce top surface and cross section images. The micrographs were recorded using secondary electron emission at a magnification of 50,000 and generated with a 2kV electron beam using a Zeiss Supra 40VP equipped with EDAX 40Vp energy dispersive X-Ray (EDX) analyser. The composition of the films was quantified on an imaged area of approximately 100 $\mu m^2$ under an acceleration voltage of 20 kV, and three different areas of the samples were analysed to calculate the standard deviation. White light interferometry (WLI) was used for thickness measurements using Profilm3D optical profilometer from Filmetrics. The measurements were done at three different positions with magnification of 50x, to determine the mean thickness and the standard deviation. A first AFM measurement was performed onto one BiCu sample with a Horiba XPlora Plus system, in tapping mode, onto an area of 10 x 10 $cm^2$, with 3 different areas analysed. The optical measurements (transmission, optical band gap) were assessed by the use of an Ocean Optics USB4000 UV-Vis spectrometer, connected to a DH-2000-BAL UV-Vis-NIR light source. The transmission properties were recorded between 300 and 900 nm. Substrate FTO films were used as reference prior to the measurements. The oxidation state of the deposited films was determined using X-Ray photoelectron spectroscopy. The XPS analysis was performed with a Kratos Axis Supra system, equipped with a monochromated Al $K_{\alpha1}$ X-Ray excitation source (hν = 1486.6 eV). The peak model fitting was carried out with the software CasaXPS. All spectra were charge corrected to the acquired C 1s region scan and the adventitious carbon peak (C-C) position at 284.8 eV. Curve fitting was done applying a Gaussian function with a Shirley background.

Similarly to the previous chapter, photocatalytic dye degradation tests were performed by degradation of solution of mythelene blue (2 umol.L-1) under UV light irradiation. However, the BiCu studied did not present significant photocatalytic properties regarding MB degradation tests. The results of the photocatalytic measurements are presented in Annexe x. The photoelectrochemical measurements were performed in a three-electrode configuration powered by au Autolab potentiostat from Metrohm (PGSTAT302N). In brief, the $BiV_x$/FTO samples were used as the working electrode, whereas the counter electrode was a Pt mesh (5 x 5 $cm^2$), and the reference electrode was an Ag/AgCl reference electrode. The geometric surface area was defined as 1 $cm^2$ (defined with an epoxy resin mask). A 0.5 M $Na_2SO_4$ (pH ≈ 7) solution was used as the electrolyte. To assess the photoelectrochemical activity of the films, Linear Sweep Voltammetry (SV) measurements were performed from 1.4 to 0.2 $V_{RHE}$ at a scan rate of 20 $mV.s^{-1}$. The measurements were performed in the dark and under visible light illumination to assess the photoelectrochemical activity of the samples produced. From the photocurrent produced, the half-cell solar-to-hydrogen conversion efficiency (HC-STH) of all samples were determined, using equation (36):

$$HC - STH = \frac{J_{ph}(mA.cm^{-2}) \times (E_{O_2/H_2O} - |V_{app}|)(V) \times \eta_F}{P_{total}(mW.cm^{-2})} \tag{40}$$

with $J_{ph}$ the photocurrent density at $V_{app}$, $V_{app}$ the potential applied during the measurement, $P_{total}$ the power density of the incident light (100 mW.cm$^{-2}$) and $E_{O_2/H_2O}$ the standard potential for the hydrogen evolution reaction (here 0.0 $V_{RHE}$). The three-electrode configuration was also used to perform chronoamperometry (CA). Firstly, CA was used to measure the stability of the photocurrent produced by the samples at 1.23 $V_{RHE}$ for 3 hours. CA was also performed for a shorter period of time (60 s) to determine the transient time τ for the samples produced by using equation x:

$$\ln D = \frac{-\tau}{t} \tag{41}$$

$$D = \frac{(I_t - I_f)}{(I_i - I_f)} \tag{42}$$

where $I_i$, $I_f$ and $I_t$ the initial photocurrent, final photocurrent, and photocurrent at time t, respectively. The transient time is obtained by plotting ln D as a function of time. By extrapolating the linear part of the curve plotted, it is possible to determine the transient time τ for ln D = -1.

## 9.3. Crystallinity assessment

Firstly, the identification of the crystalline phases of the BiCu samples produced was done by Raman Spectroscopy. The phase of interest for $CuBi_2O_4$ photocathode is the tetragonal phase, which produces specific Raman bands corresponding to specific elongations within the $BiO_6$ and $CuO_4$ units. Especially, 7 distinctive Raman bands can be identified for the tetragonal $CuBi_2O_4$ compound [236]:

- A strong peak at 130 $cm^{-1}$ is associated to the A1g mode which originates from translational vibrations of the $CuO_4$ planes along the c-axis.
- The small peak at 189 $cm^{-1}$ is the Eg mode and indicates the vibrations of the Cu-Cu links
- The A1g mode at 263 $cm^{-1}$ corresponds to the rotation of two stacked $CuO_4$ squares in opposite directions. The peaks at 280 $cm^{-1}$ and 466 $cm^{-1}$, corresponding to $B_{2g}$ modes are mainly assigned to the oxygen motion.
- Finally, the band observed at 406 $cm^{-1}$ is the A1g mode of the Bi-O stretching vibration while the peak at 589 $cm^{-1}$ is an in-plane breathing of $CuO_4$ squares.

The Raman spectra of the different BiCu samples produced are presented in Figure 9.1. Similarly to the BiV samples, different types of spectra can be observed among the different BiCu samples. The samples with the lowest power applied on the Cu target (BiCu25, BiCu50 and BiCu75, see Figure 9.1a) present different bands that can be associated with the presence of the monoclinic α-$Bi_2O_3$ phase (150, 210 and 440 $cm^{-1}$), with specific bands attributed to the displacements of Bi and O atoms within the monoclinic α-$Bi_2O_3$ lattice [236]. In addition, some bands associated with $CuBi_2O_4$ are visible, but slightly shifted to lower wavenumbers, and can be interpreted as a lack of crystallinity of the samples. A transition occurs from $P_{Cu}$ = 100 W, with all the typical Raman bands appearing for BiCu100, BiCu125 and BiCu150 samples. Moreover, no additional phase can be observed on the Raman spectra (see Figure 9.1b). Finally, increasing the power applied on the coper target (BiCu175 and BiCu200) results in the appearance of two new Raman bands on the spectra (340 and 633 $cm^{-1}$, Figure 9.1c). Those bands can be attributed to the formation of CuO [237]. Those findings are in good agreement with EDX analysis performed on samples deposited onto Si wafer (see Figure 9.1d), reported in Table 9.2. As expected, increasing the power applied on Cu results in a higher proportion of copper within the coatings. The formation of α-$Bi_2O_3$ is correlated with an excess of Bi in the compound. Similarly, BiCu175 and BiCu200 exhibit a high amount of Cu comparing to Bi, this excess of Cu being oxidized during the annealing step to form CuO. Interestingly, BiCu150 also presents a slight excess of Cu compared to Bi according to EDX measurements, without presenting any bands attributed to CuO phase.The phase diagram of the CuO – Bi2O3 binary system reveals that the $CuBi_2O_4$ phase corresponds to a solid solution containing 68% of CuO and 32% of Bi2O3. This is in accordance with the findings of the EDX analysis, showing that for this configuration, a power ratio $P_{Bi}/P_V$ results in sputtering twice more copper than Bi [283].

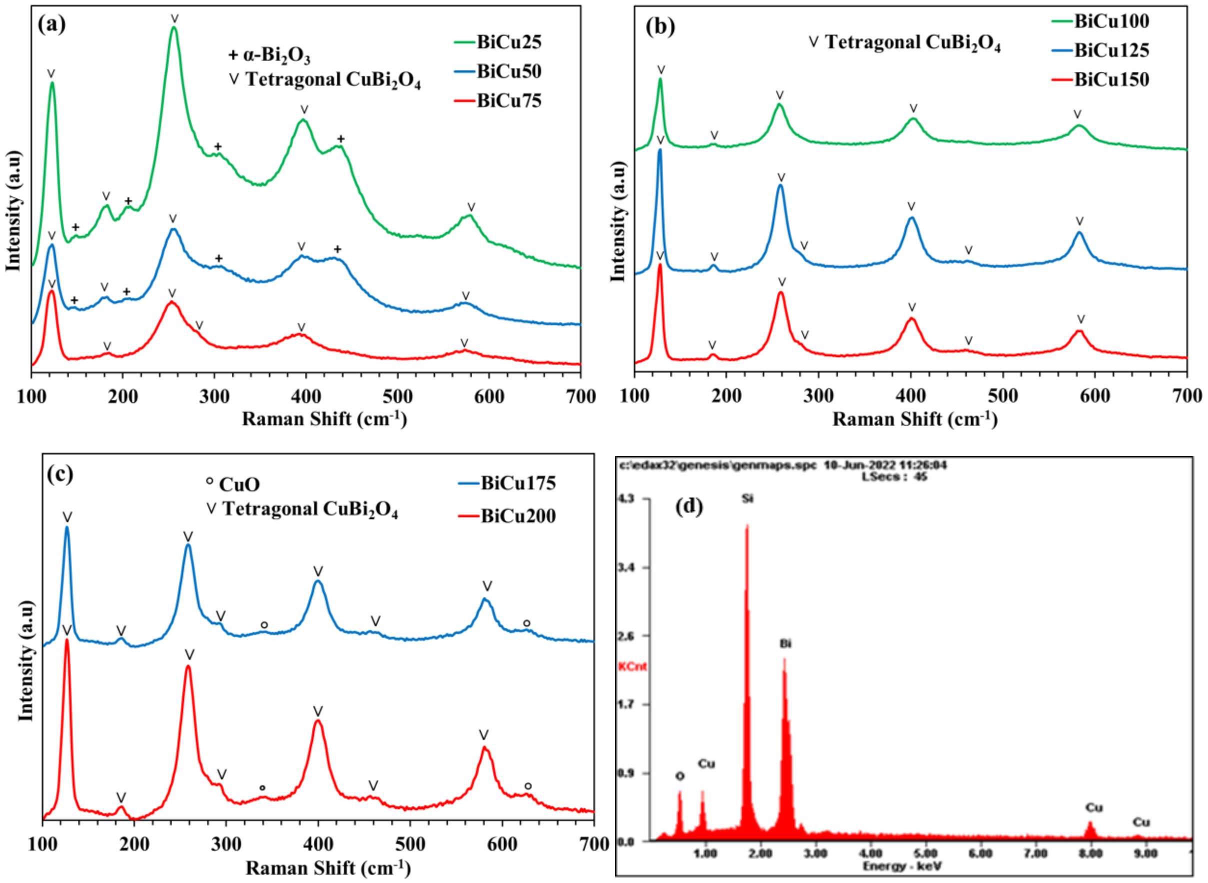

Figure 9.1: (a) Raman Spectra for the samples BiCu25, BiCu50 and BiCu75, (b) Raman Spectra for the samples BiCu100, BiCu125 and BiCu150, (c) Raman Spectra for samples BiCu175 and BiCu200, (d) Example of EDX analysis of BiCu150 deposited onto Si

Table 9-2: Elemental (EDX) analysis of the CuBi samples produced

| Sample | Z | Element | Atomic fraction (%) | At% Bi/Cu ratio |
|---|---|---|---|---|
| BiCu25 | 8.00 | O | 74.1 ± 1.2 | **2.31** |
| | 29.00 | Cu | 7.8 ± 1.1 | |
| | 83.00 | Bi | 18.1 ± 1.3 | |
| BiCu50 | 8.00 | O | 73.5 ± 1.3 | **2.23** |
| | 29.00 | Cu | 8.2 ± 1.3 | |
| | 83.00 | Bi | 18.3 ± 1.4 | |
| BiCu75 | 8.00 | O | 73.8 ± 1.1 | **2.11** |
| | 29.00 | Cu | 8.4 ± 1.2 | |
| | 83.00 | Bi | 17.8 ± 1.1 | |
| BiCu100 | 8.00 | O | 74.4 ± 1.4 | **2.05** |
| | 29.00 | Cu | 8.4 ± 1.6 | |
| | 83.00 | Bi | 17.2 ± 1.2 | |
| BiCu125 | 8.00 | O | 73.8 ± 1.4 | **1.98** |
| | 29.00 | Cu | 8.8 ± 1.4 | |
| | 83.00 | Bi | 17.4 ± 1.3 | |
| BiCu150 | 8.00 | O | 74 ± 1.5 | **1.91** |
| | 29.00 | Cu | 8.9 ± 1.4 | |
| | 83.00 | Bi | 17.1 ± 1.7 | |
| BiCu175 | 8.00 | O | 73.9 ± 1.7 | **1.83** |
| | 29.00 | Cu | 9.2 ± 1.5 | |
| | 83.00 | Bi | 16.9 ± 1.4 | |
| BiCu200 | 8.00 | O | 73.6 ± 1.3 | **1.72** |
| | 29.00 | Cu | 9.7 ± 1.5 | |
| | 83.00 | Bi | 16.7 ± 1.6 | |

To confirm the findings from Raman spectroscopy, X-Ray diffraction was used to identify the crystalline phases of the coatings produced. All XRD patterns can be seen in Figure 8.3 (a-c). The XRD peaks associated with the presence of $CuBi_2O_4$ phase were identified using the ICDD card 48-1886. The peaks are the following: 20.84° (200), 28° (211), 29.68° (220), 30.76° (002), 33.26° (310), 34.26° (112), 37.42° (202), 45.16° (330), 45.92° (312), 46.68° (411) and 47.82° (420). As already seen in analysis by Raman spectroscopy, the “bismuth-rich” samples (BiCu25, BiCu50 and BiCu75) exhibit several diffraction peaks related to the presence of $\alpha$-$Bi_2O_3$ (ICDD card 76-1730), in addition to the peaks associated with the $CuBi_2O_4$ crystal phase, meaning the presence of a mixture of both materials. It should be noticed that the diffraction peaks of $CuBi_2O_4$ are slightly shifted, with a lower intensity, showing the lack of crystallinity compared to bismuth oxide. The rest of the samples strongly exhibit $CuBi_2O_4$ diffraction peaks. In addition, samples with the higher amount of Cu (BiCu175 and BiCu200) presents 2 additional peaks associated with the presence of CuO (35.5° (-1 1 1), 38.6° (1 1 1), ICDD card 48-1548), without altering the $CuBi_2O_4$ phase.

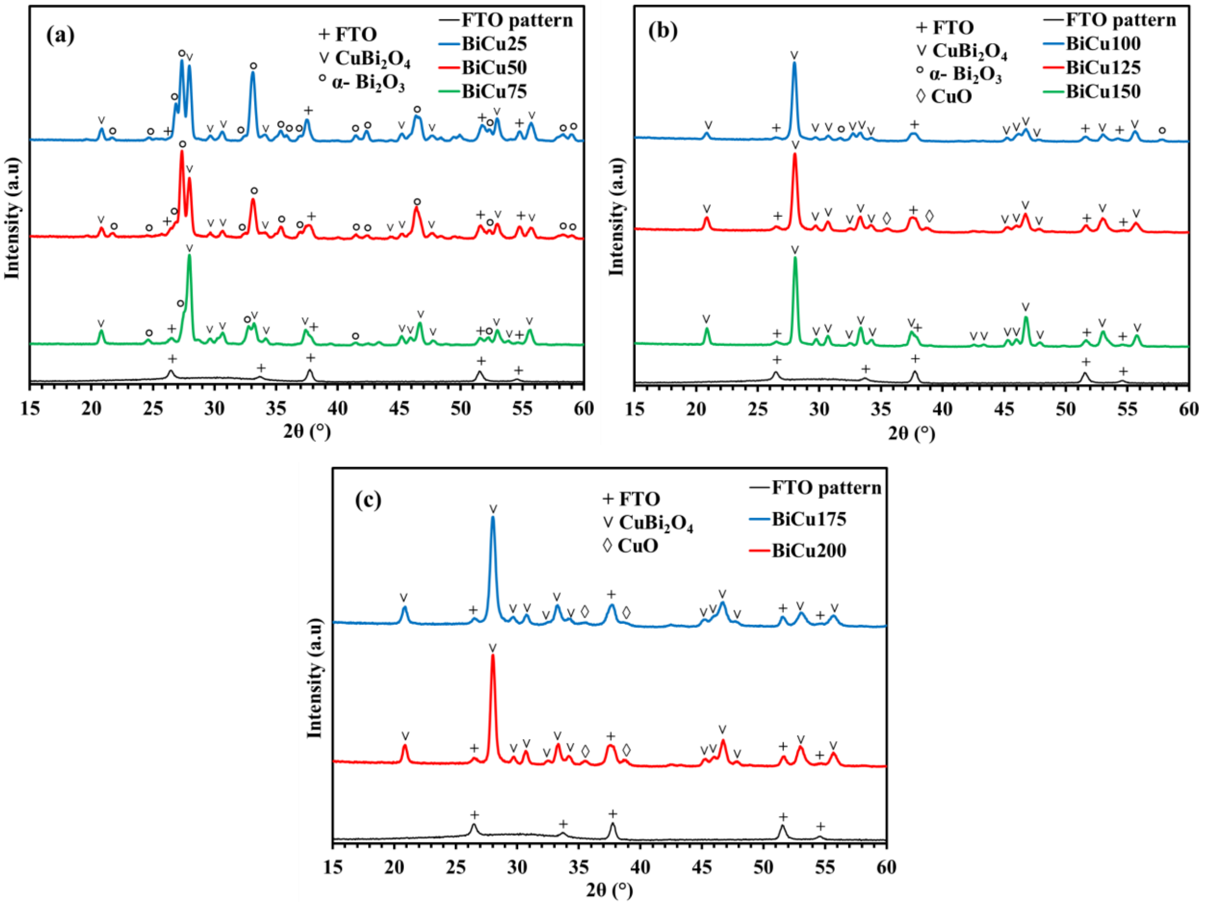

Figure 9.2: XRD patterns of the different BiCu samples produced ; (a) BiCu25, BiCu50 and BiCu75 ; (b) BiCu100, BiCu125 and BiCu150 ; (c) BiCu175 and BiCu200

## 9.4. Coatings morphology

The top surface morphology of the CuBi samples produced was studied by SEM. A first observation can be made when the coatings are observed with SEM before and after annealing, as it can be seen in Figure 9.3. Before annealing, all samples produced in this work present a columnar structure, typical from samples produced by sputtering techniques and related to the porous columnar structure described in the Thornton Structure Zone Model [146]. After annealing, a change in the morphology can be observed and differs from one sample to another, depending on the sputtering parameters. As it can be observed on the SEM micrographs (Figure 9.4 and Figure 9.5), the variation of sputtering parameters influenced the morphology obtained. The samples with the lowest amount of Cu (BiCu25 and BiCu50) present a morphology made of small grains (around 100 nm) and with a lot of cavities in between. The presence of these cavities can be interpreted as damage due to the difference of thermal expansion between $Bi_2O_3$ and $CuBi_2O_4$, respectively [236, 237]. When the amount of Cu is increased to reach the composition close to $CuBi_2O_4$, a transition in the morphology occurs, with the formation of larger grains, as it can be observed with samples BiCu75 and BiCu100. BiCu125 and BiCu150 exhibit a morphology with large, smooth, and well-defined grains. This type of morphology was already reported from the production of $CuBi_2O_4$ photocathodes by PVD techniques, such as PLD by Gottesman et al. [240]. Finally, the “Copper-rich” samples exhibit another type of morphology, with the formation of a denser granular structure. This morphology is correlated with the appearance of CuO phase on Raman spectroscopy and XRD patterns. This morphology has been observed with the deposition of CuO thin films from a CuO target by RF sputtering [241, 242]. The importance of grain size was studied by Wang et al. in 2022, where $CuBi_2O_4$ photocathodes were produced by TSA method and annealing in two steps [243]. It was shown that the formation of a dense coating composed of large grains (between 500 nm to 1μm) was associated with a higher photocurrent density, due to the improvement of charge carrier lifetime and increasing charge carrier transport within the coating.

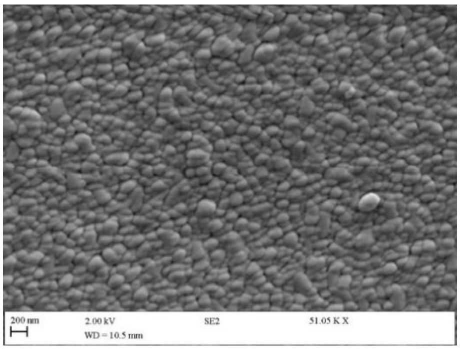

Figure 9.3: Example of CuBi sample before annealing

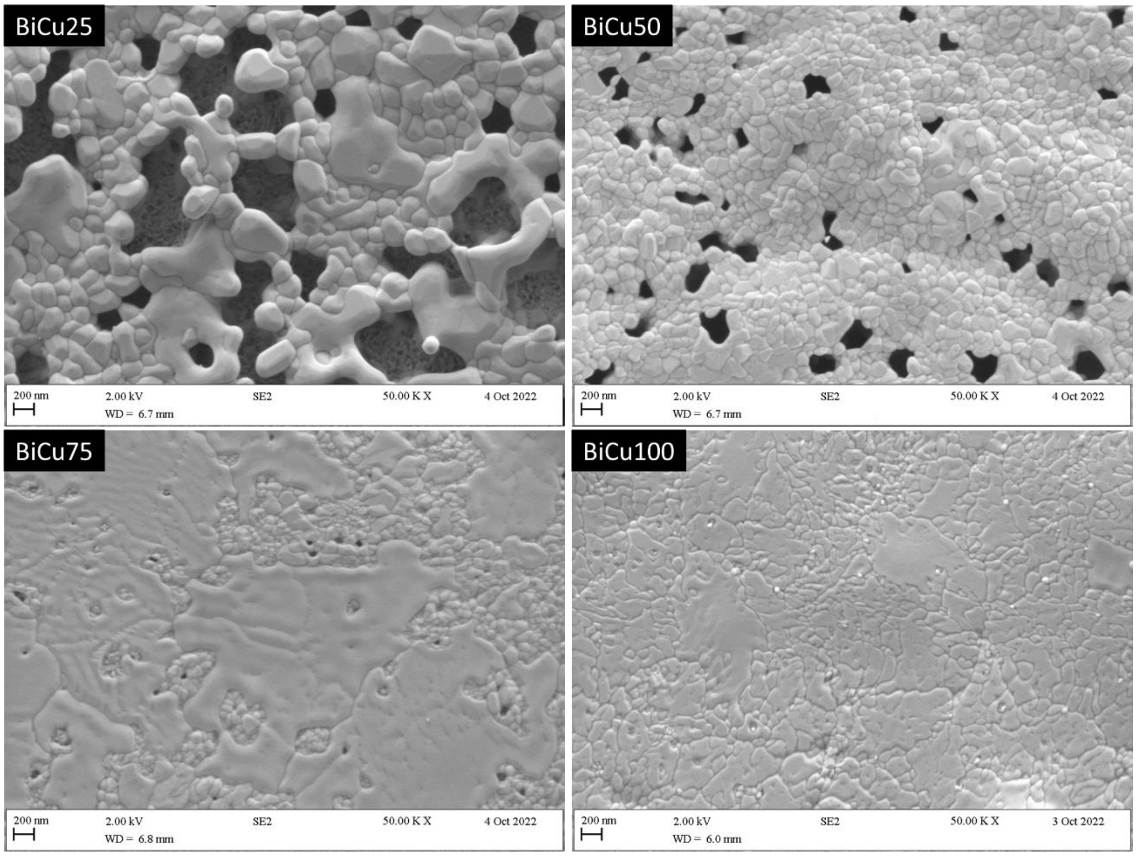

Figure 9.4: SEM images of CuBi samples produced, from BiCu25 to BiCu100

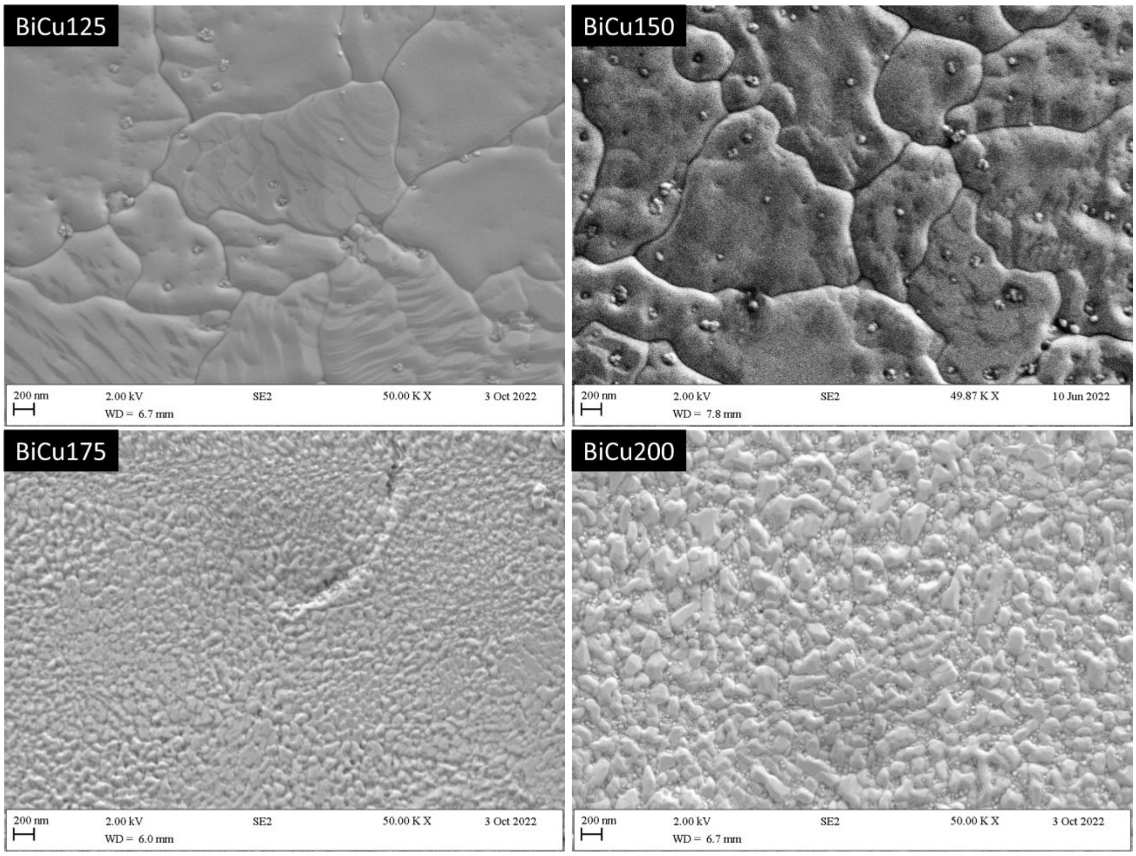

Figure 9.5: SEM images of CuBi samples produced, from BiCu125 to BiCu200

The importance of grain size was studied by Wang et al. in 2022, where $CuBi_2O_4$ photocathodes were produced by TSA method and annealing in two steps [243]. It was shown that the formation of a dense coating composed of large grains (between 500 nm to 1μm) was associated with a higher photocurrent density, due to the improvement of charge carrier lifetime and increasing charge carrier transport within the coating. 3D Optical profilometry was used for thickness measurements of the samples produced. The data recorded are listed in Table 9.3. Figure 9.6 presents the 3D images obtained for each CuBi samples produced. As expected, increasing the power applied to copper target results in thicker coatings, with thicknesses varying from 341 nm for BiCu25 to 426 nm for BiCu200. As an indication, the area roughness of the samples was measured, based on the ISO standard 27178. Similarly to the BiV samples, the area roughness appears very low for each sample (around 10 nm for each sample). AFM image is presented in annexes, but were not usable to compare the roughness obtained, due to the poor image quality obtained. Nonetheless, as all samples present a similar area roughness with 3D Optical profilometry, it allows the direct comparison when performing photocatalytic and photoelectrochemical measurements.

Table 9-3: Data recorded from 3D Optical profilometer for CuBi samples

| Sample ID | Thickness measured (nm) | | | |
|---|---|---|---|---|
| | Measure 1 | Measure 2 | Measure 3 | Mean |
| BiCu25 | 315 | 313 | 318 | 315 ± 6 |
| BiCu50 | 337 | 332 | 332 | 333 ± 8 |
| BiCu75 | 347 | 345 | 343 | 345 ± 9 |
| BiCu100 | 363 | 365 | 368 | 365 ± 6 |
| BiCu125 | 378 | 377 | 372 | 375 ± 10 |
| BiCu150 | 393 | 391 | 396 | 393 ± 6 |
| BiCu175 | 407 | 414 | 414 | 411 ± 16 |
| BiCu200 | 421 | 423 | 428 | 424 ± 13 |

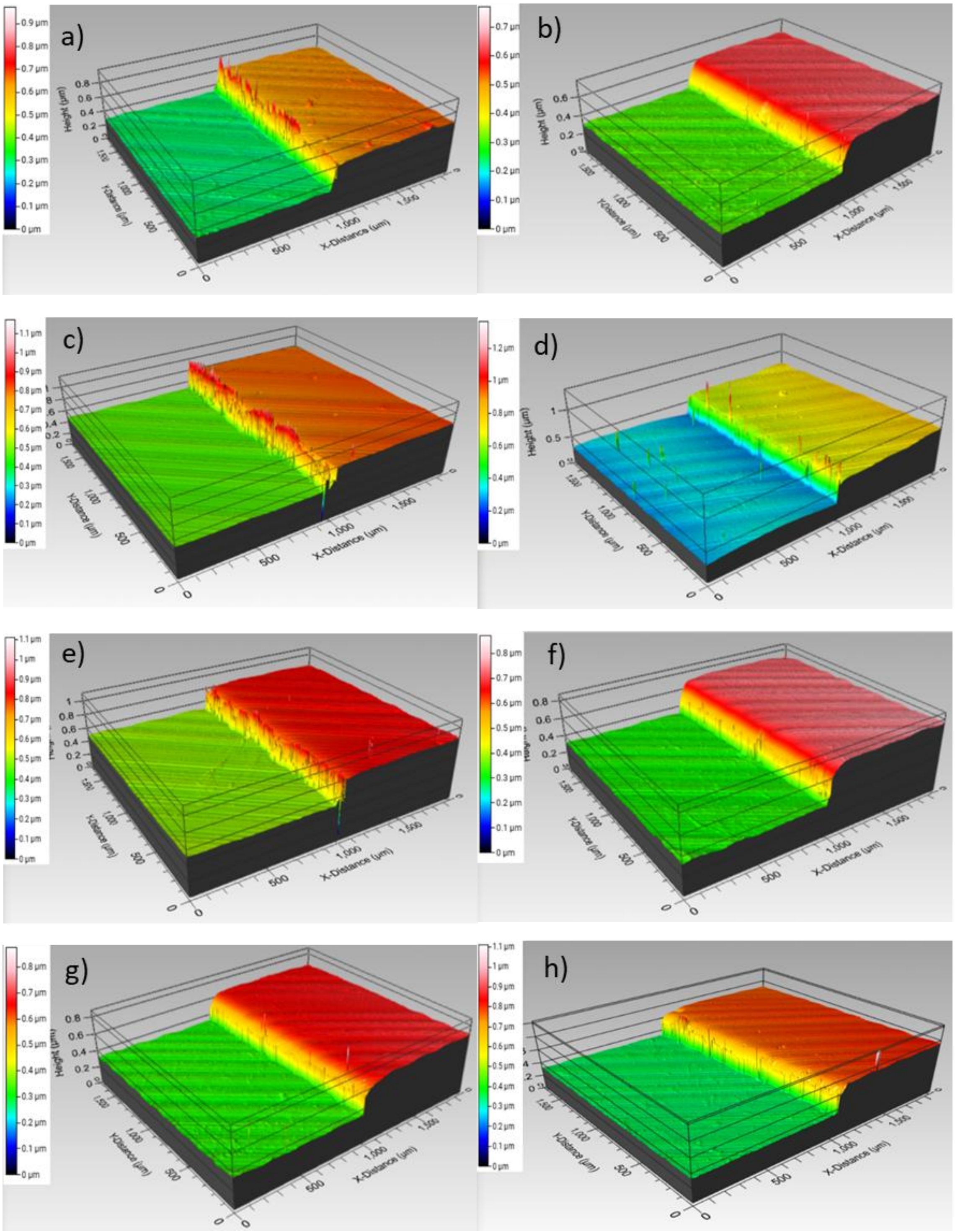

Figure 9.6: WLI images of BiCu samples produced, from a) BiCu25 to h) BiCu200

## 9.5. Optical properties and band gap measurements

The optical measurements were performed using an Ocean Optics USB4000 UV-Vis spectrometer. Interestingly, once annealed the BiCu samples for not become opaquer, but more transparent, as it can be seen in Figure 9.6. The as-deposited sample presents a dark brown colour whereas the annealed sample presents a pale brownish colour. This behaviour was already observed by Hahn et al. for $CuBi_2O_4$ photocathode produced by electrochemical synthesis and was attributed to a higher light scattering within the materials after crystallisation [244]. As a result, the transmittance of the annealed sample is higher, starting to increase from 360 nm to reach around 80% for longer wavelengths (see Figure 9.8a). As mentioned in Section 7.1., the bandgap of $CuBi_2O_4$ photocatalyst varies between 1.6 and 1.9 eV [226].As with $BiVO_4$ earlier, several studies show both types of behaviour the band gap of $CuBi_2O_4$ (direct [244], 245] or indirect [246, 247]). Figure 9.8b shows the Tauc plot obtained for both indirect and direct band gaps, with a value of 1.71 for an indirect band gap and a value of 1.93 for a direct band gap. Both methods appear to be close in values, and are both below 2 eV, meaning the samples are theoretically able to harvest a large portion of photons from visible light. For the rest of the work, the BiCu samples produced are considered as direct band gap semiconductors. The different band gap values found for the BiCu samples are listed in Table 9.4.

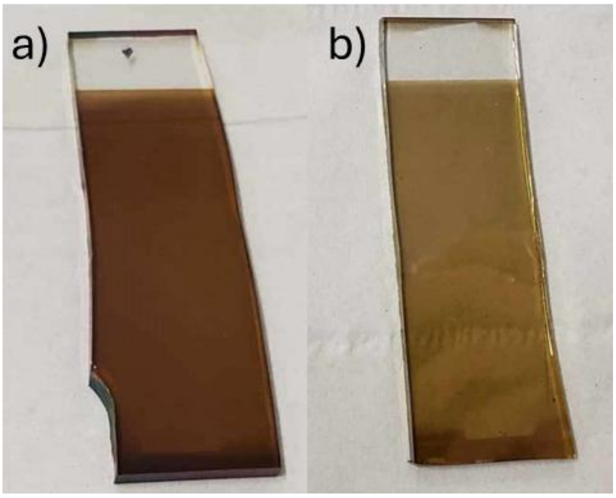

Figure 9.7: Examples of BiCu samples deposited onto FTO a) Before annealing, b) After annealing

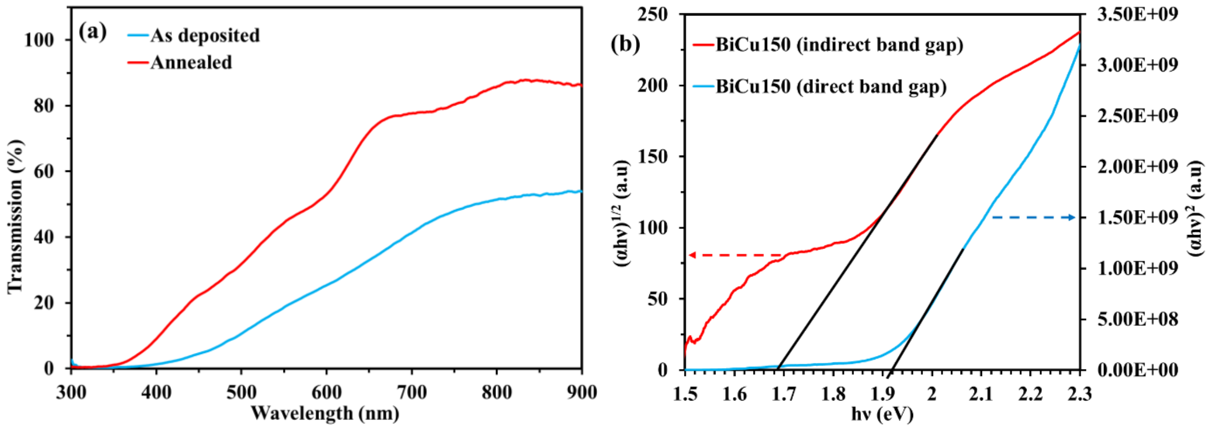

Figure 9.8: (a) Example of BiCu150 transmittance measurement before (blue line) and after (green line) annealing and (b) Tauc plots associated for direct and indirect band gap

Table 9-4: Band gap calculated for BiCu samples produced

| Sample ID | Band gap (eV) |
|---|---|
| BiCu25 | 1.84 ± 0.01 |
| BiCu50 | 1.85 ± 0.01 |
| BiCu75 | 1.83 ±0.04 |
| BiCu100 | 1.86 ± 0.03 |
| BiCu125 | 1.87 ± 0.05 |
| BiCu150 | 1.93 ± 0.02 |
| BiCu175 | 1.91 ± 0.08 |
| BiCu200 | 1.79 ± 0.07 |

## 9.6. First assessment of photoelectrochemical properties

A first evaluation of the photocatalytic activity of the coatings was done by performing MB degradation tests under UV light. Contrary to the BiV samples, BiCu samples did not exhibit a significant photocatalytic activity, with 3.2% of methylene blue removed after 1h of UV irradiation as the highest degradation rate (see annexes). Usually, $CuBi_2O_4$ is reported to be a promising photocatalyst for dye degradation when it is combined with several semiconductors to form heterojunctions to ensure a higher activity [248, 250]. The photoelectrochemical activity of the samples produced was assessed by the measurement of photocurrent production under visible light in a three-electrode configuration PEC water splitting cell. The electrolyte used was a 0.5M $Na_2SO_4$ neutral solution (pH ≈ 7), the working electrode used was the BiCu/FTO photoelectrode, the counter-electrode was a Pt mesh, and the reference electrode was an Ag/AgCl. The linear sweep voltammetry (LSV) technique was used, with a range of voltage between 1.4 and 0.2 $V_{RHE}$. Figure 9.9 (a-c) presents the LSV curves recorded for each sample. Figure 9.9a presents the LSV curves for the “Bismuth-rich” samples (Cu25, Cu50 and Cu75). All samples produce a cathodic photocurrent, indicating the p-type nature of the photocatalysts produced. However, the photocurrents remain very low, with -0.175 mA.cm$^{-2}$ produced as the highest photocurrent. This poor activity of the “Bismuth-rich” samples can be explained by the presence of α-$Bi_2O_3$ , known to be not an efficient photocathode. When the amount of Cu in the coating is increased to form a stoichiometric compound (BiCu100, BiCu125 and BiCu150), the photocurrent production is improved, reaching a value of -1.13 mA.cm$^2$ for BiCu150. The “Copper-rich” (BiCu175 and BiCu200) samples present a good photocurrent production ,which, however, is still lower than the one of stoichiometric samples.The photocurrent measurements were used to evaluate two additional characteristics of the photoelectrodes produced. The half-cell solar-to-hydrogen (HC-STH) efficiencies are presented in Figure 9.9d. Due to their high photocurrent production, the stoichiometric samples present the highest HC-STH efficiencies, reaching a value of 0.42 % at 0.5 V vs RHE for BiCu150 sample, whereas the maximum HC-STH for the “Rich-Bi” and “Rich-Cu” samples are 0.05% at 0.3 V vs RHE and 0.17% at 0.45 V vs RHE, respectively. All photocurrent values and maximum HC-STH efficiencies are reported in Table 9.5.

Table 9-5: Photoelectrochemical data recorded from LSV and HC-STH measurements for each BiCu samples

| Sample ID | Photocurrent production (mA.cm$^2$ at 0.3 V vs RHE) | Max HC-STH (%) |
|---|---|---|
| BiCu25 | -0.08 | 0.02 |
| BiCu50 | -0.11 | 0.03 |
| BiCu75 | -0.18 | 0.05 |
| BiCu100 | -0.88 | 0.32 |
| BiCu125 | -1.02 | 0.38 |
| BiCu150 | -1.13 | 0.42 |
| BiCu175 | -0.53 | 0.18 |
| BiCu200 | -0.38 | 0.14 |

$CuBi_2O_4$ photocathodes are usually not produced by PVD techniques, which makes the comparison with the CuBi samples produced by reactive magnetron co-sputtering difficult. Cooper et al. produced $CuBi_2O_4$ photocathodes in 2021 by reactive sputtering and obtained similar results in terms of photocurrent production, with a photocurrent density of -1.18 mA.cm$^2$ produced at 0.3 V vs RHE [36]. It must be noticed that to date, it appears to be the best performances of $CuBi_2O_4$ produced by a PVD technique. Examples of $CuBi_2O_4$ photocathode produced by pulsed laser deposition (PLD) are listed in Table 9.6, showing a photocurrent produced approximately half as much as the photocathode produced by sputtering. Similarly to

BiV photoanodes, the lack of consistency between the different configurations used (electrolyte, counter-electrode, reference electrode …) makes difficult a proper comparison. However, the results obtained with sputtering remains quite encouraging, as the photocurrent produced appears high compared to the literature.

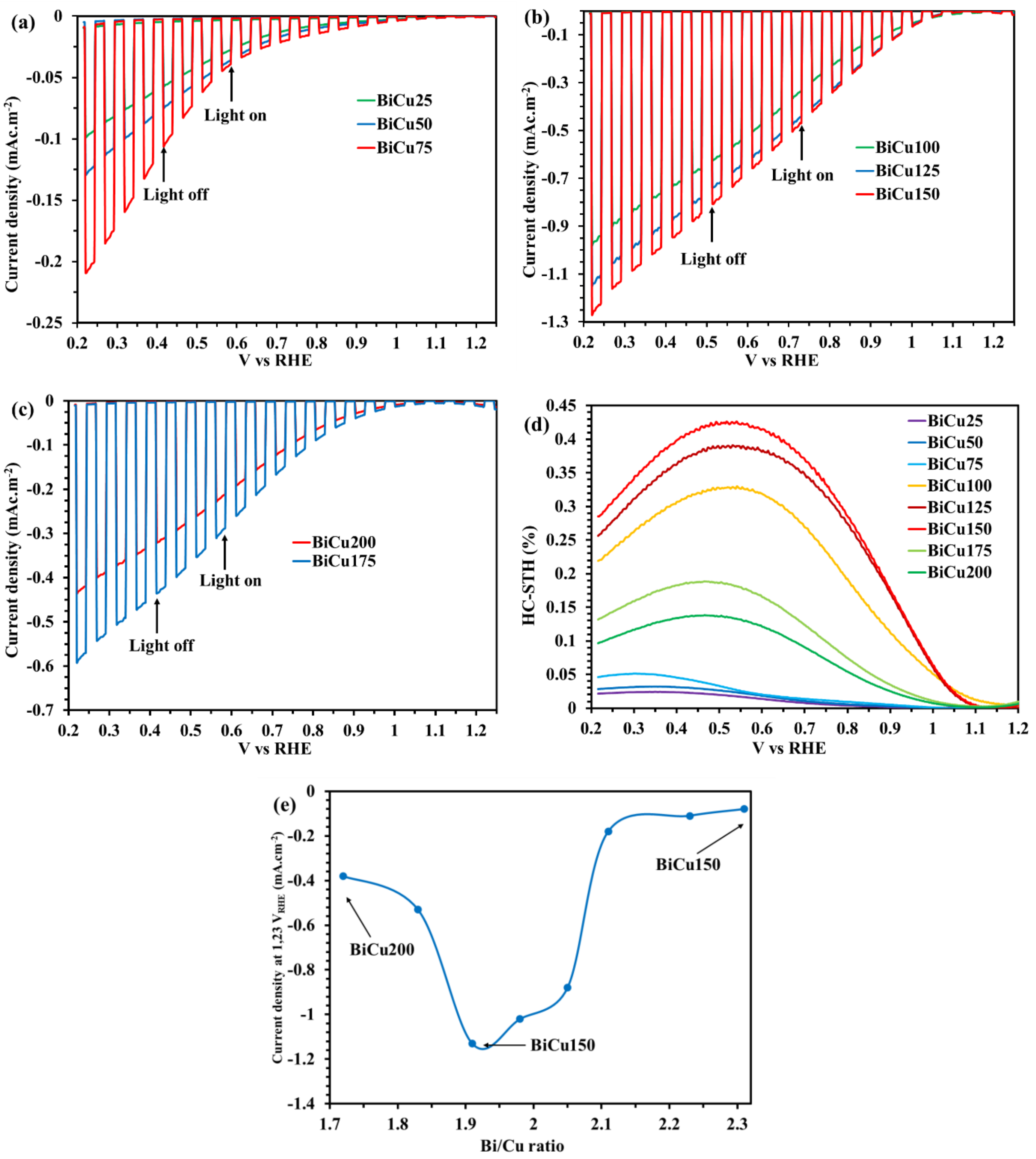

Figure 9.9: Chopped LSV of CuBiO samples: (a) samples (BiCu25, BiCu50, BiCu75), (b) samples (BiCu100, BiCu125, BiCu150), (c) samples (BiCu175, BiCu200) and (d) HC-STH for the corresponding samples, (e) Correlation between composition and photocurrent produced for each sample

Table 9-6: Examples of $CuBi_2O_4$ photocathode produced by PVD techniques and their respective photocurrent densities values

| $CuBi_2O_4$ production method | Electrolyte | Counter-electrode | Reference-electrode | Photocurrent density at 0.3 V vs RHE | Onset potential (V vs RHE) | Ref |
|---|---|---|---|---|---|---|
| Reactive magnetron sputtering | 0.5 M $Na_2S_2O_8$ | Pt wire | Ag/AgCl 3M KCl | $-1.1$ mA.cm$^{-2}$ | 1.1 V vs RHE | [226] |
| PLD | 0.1 Potassium phosphate | Pt wire | Ag/AgCl 1M KCL | $-0.5$ mA.cm$^{-2}$ | 1.0 V vs RHE | [239] |
| PLD | 0.3M $K_2SO_4$/0.2 Phosphate buffer | Pt wire | Ag/AgCl | $-0.06$ mA.cm$^{-2}$ | 1.1 V vs RHE | [251] |
| TSA | 0.3M $K_2SO_4$/ 0.2M phosphate buffer | Pt | Ag/AgCl | $-0.4$ mA.cm$^{-2}$ | 1.08 V vs RHE | [242] |

## 9.7. Charge separation and charge transport efficiencies

Based on the previous findings, three BiCu samples (CuBi100, CuBi125, CuBi150) were selected to estimate their respective charge transport and charge transfer efficiencies. Similarly to the measurements done with the BiV samples, 0.1M $H_2O_2$ solution was added to the electrolyte as it can act as an electron scavenger with fast kinetics [253]. The same equations used in Chapter 8 can be used to calculate $\eta_{transfer}$ and $\eta_{transport}$, with an example of LHE measurement for BiCu150 presented in Figure 9.10a, impacted by the transparency of the samples produced. As depicted in Figure 9.10b, no significant differences can be observed with the charge transfer efficiency between the samples, with a $\eta_{transfer}$ ranging from 10 to 11.8% at 0.3 V vs RHE. All samples present relatively low $\eta_{transfer}$, as $CuBi_2O_4$ is also subject to poor kinetics for the proton reduction reaction [254].

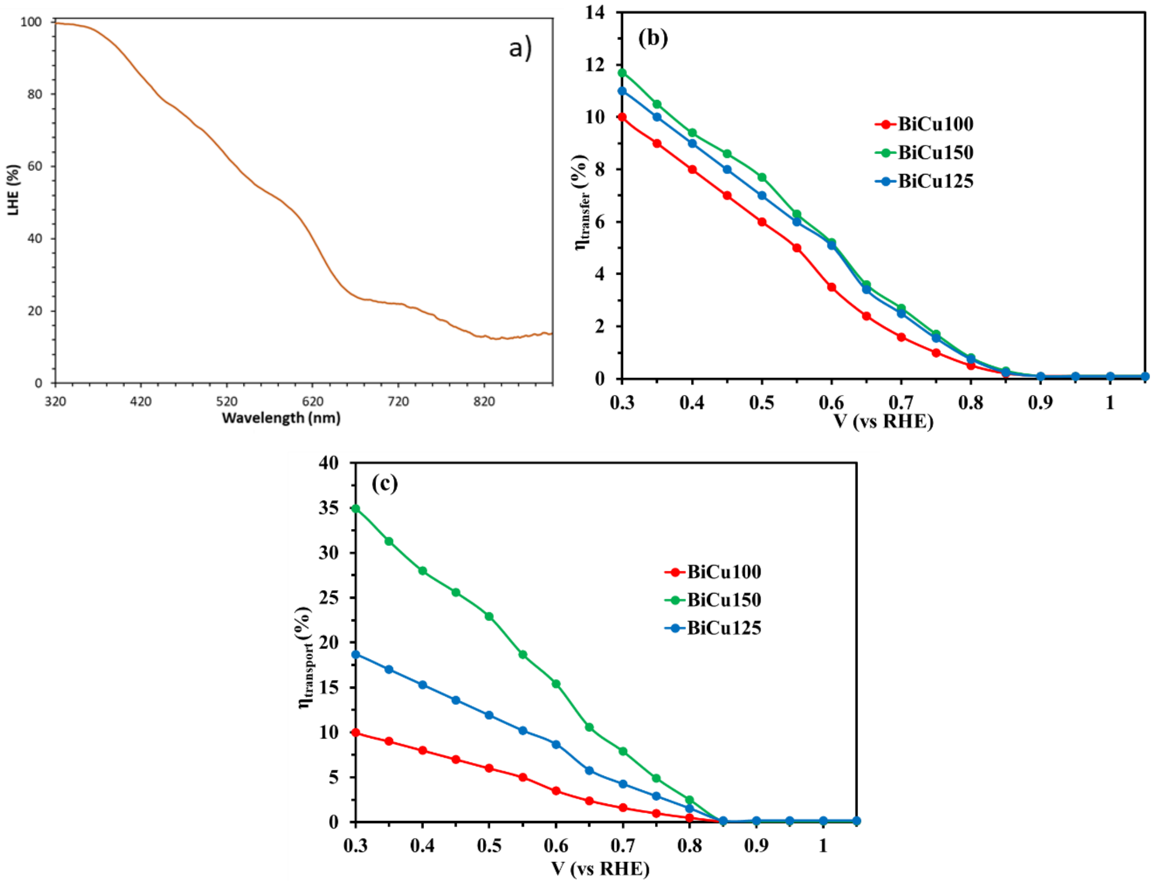

Figure 9.10: (a) LHE efficiency for BiCu150, (b) Charge transfer efficiencies of the selected samples, (c) Charge transport efficiencies of the selected samples

As depicted in Figure 9.10c, BiCu150 presents the best efficiency with 35% at 0.3 V vs RHE, whereas the BiCu125 and BiCu100 exhibit lower $\eta_{transport}$ , with 18% and 10.3%, respectively. This charge transfer efficiency appears to be lower than the on measured for the BiV samples, which can be a limiting factor when running a PEC tandem cell. All efficiencies are listed in Table 9.7. Also, the efficiencies shown here are significantly slower than BiV samples. This might be due to the use of $H_2O_2$ as an electron scavenger, often referred as good electron scavenger but some other scavengers can be used [284]. This can be discussed in further studies. XPS analysis was used to investigate the chemical and electronic states of the CuBi samples produced. The survey spectra for the three selected samples are presented are shown in Figure 9.11. The residual carbon C 1s peak, located at 284.9 eV, was used as a reference to identify the binding energies of other peaks. Figure 9.12 shows the high resolution XPS spectra of Bi 4f, Cu 2p and O 1s states. Contrary to the BiV samples, the Bi 4f states (see Figure 86c) are not shifted to lower binding energies, with peaks located at 159.6 and 165.3, attributed to the binding energies of Bi $4f_{7/2}$ and Bi $4f_{5/2}$, respectively [255]. No other peaks can be observed for Bi 4f state. For the Cu 2p states (see Figure 9.13b), several peaks can be observed. Two satellite peaks can be observed (between 941 – 944 eV and at 962.3 eV) can be attributed to the presence of $Cu^{2+,}$ corresponding to the valence of Cu in $CuBi_2O_4$ [256]. Moreover, two peaks are located at 933.2 and 953.8 eV, corresponding to the Cu $2p_{3/2}$ and Cu $2p_{1/2}$ states, respectively. Similarly to $BiVO_4$, a difference in the high-resolution O 1s XPS spectra can be observed before and after annealing. As seen in Figure 9.13c, O 1s peak can be deconvoluted into three peaks, located at 529.6 eV, 531.2 eV and 532.5 eV. These peaks can be attributed to the presence of lattice oxygen (O 1s L), oxygen vacancies (O 1s V) and adsorbed/chemisorbed oxygen (O 1s Ads), respectively [93]. After annealing, the area of the O 1s V peak drastically increases, indicating an increasing number of oxygen vacancies within the sample. When comparing the atomic percentage ratio between the O 1s L to O 1s V (calculated from the relative areas of the XPS peaks) after annealing, BiCu150 appears to have the highest amount of oxygen vacancies, which could explain its improved charge transport efficiency. This behaviour has already been reported in this work for $BiVO_4$ produced by reactive magnetron sputtering, but also previously by Grao et al. who produced a $Bi_{12}TiO_{20}/Bi_4Ti_3O_{12}$ composite by reactive magnetron sputtering, which contained a high number of oxygen vacancies and lead to an increasing photocatalytic activity [257]. Similarly to $BiVO_4$, the presence of oxygen vacancies at the surface or within the bulk of $CuB_{i2}O_4$ was shown to be an effective way to improve the photocatalytic activity of the material [271]. Further investigation about the production of oxygen vacancies in bismuth ternary compounds produced by reactive magnetron sputtering could lead to the production of highly efficient photoelectrodes.

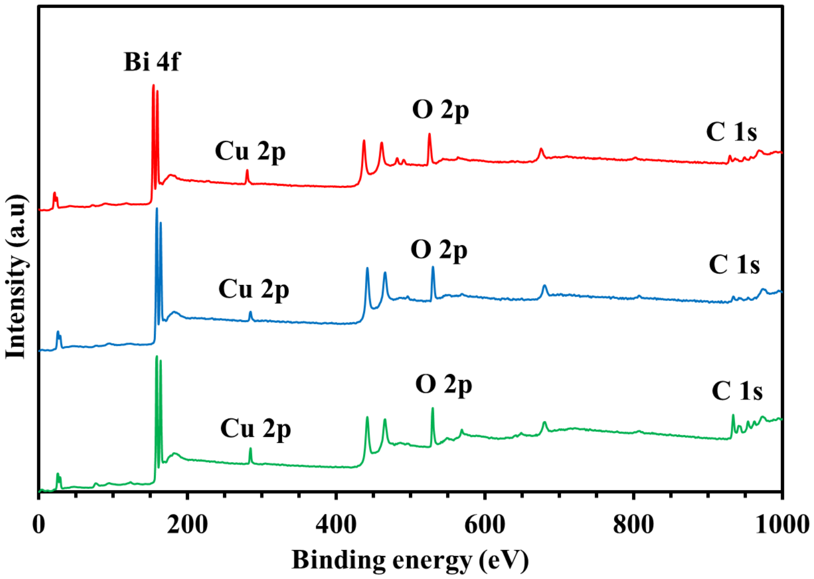

Figure 9.11: Wide spectrum of BiCu100, BiCu125 and BiCu150 samples

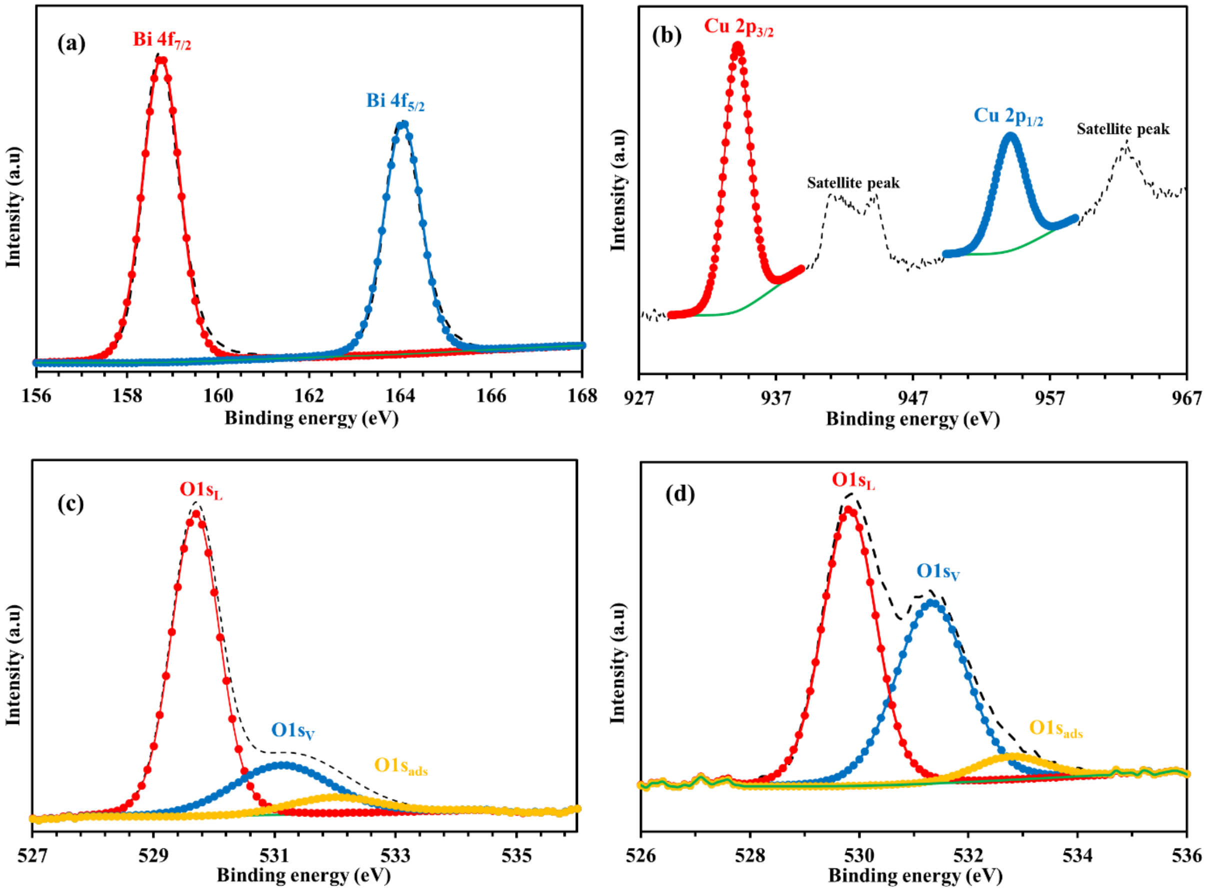

Figure 9.12: High resolution XPS analysis of BiCu150 sample: a) O 1s before annealing , b) after annealing, c) Bi 4f state, d) Cu 2p state

Finally, the transient time of the produced samples was estimated using the same method than $BiVO_4$, confirming a longer lifetime for the charge carriers produced by BiCu150, correlated with the high amount of oxygen vacancies. It must be noted that the measured transient times are shorter than the transient times measured for $BiVO_4$.

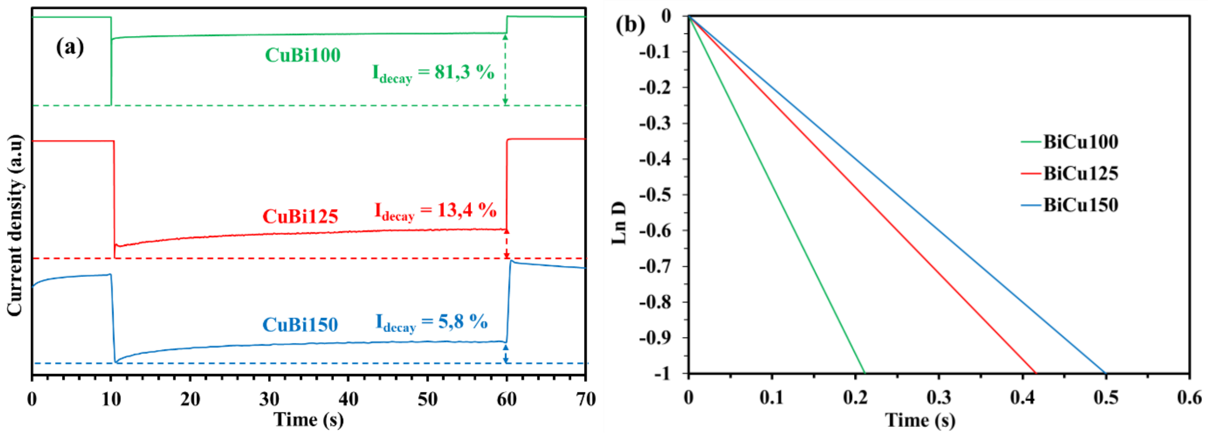

Figure 9.13: Transient time photocurrent measured for CuBi samples, Associated calculation process for obtaining the transient time

Such as $BiVO_4$, Abdi et al. studied the charge carriers' lifetime and diffusion length associated within $CuBi_2O_4$ using TRMC [228]. Several values were found for the charge carriers' lifetime, ranging from 32 ns to 819 ns. It means the photogenerated charge carriers produced within $CuBi_2O_4$ can either recombine quickly or have a significant longer lifetime [287]. Table 9.7 summarises the different data presented in this section.

Table 9-7: Data recorded for BiCu100, BiCu125, BiCu150

| | Oxygen vacancy amount (area %) | Transient time τ (s) | $\eta_{transfer}$ at 0.3 V vs RHE (%) | $\eta_{transport}$ at 0.3 V vs RHE (%) |
|---|---|---|---|---|
| BiCu100 | 31.49 | 0.22 | 10 | 10.5 |
| BiCu125 | 39.76 | 0.43 | 11.6 | 19 |
| BiCu150 | 42.21 | 0.5 | 11.8 | 35 |

## 9.8 Thickness dependence of the $CuBi_2O_4$ films

Due its better performances, BiCu150 samples was replicated with different thicknesses by changing the deposition times during the sputtering process, to identify the optimal thickness for the best photocathode performances. Table 9.8 presents the different deposition times with the thicknesses measured for each sample. Several sources of errors can influence the thickness measurement from the cross-section images, such as the resolution of the SEM, errors of calibration or errors associated with the angle of the camera. Here, the measure was repeated 5 times and standard deviation was calculated. Cross-section SEM micrographs are presented in Figure 9.15, where all the different layers can be observed. Such as $BiVO_4$ coatings, the layers present a dense morphology made of large grains. The PEC measurements done with the produced samples are presented in Figure 9.14, with the impact on photocurrent production can be seen in Figure 9.14a: the thinnest coatings produce the highest cathodic photocurrent, reaching a value of -1.6 $mA.cm^{-2}$ at 0.3 V vs RHE. The corresponding HC-STH efficiencies are presented in Figure 88b, showing a maximum HC-STH efficiency of 0.58%. As expected, the performances decrease with the thickness of the coatings, with the BiCu150 sample deposited for 2h being the lass active sample. All PEC data are listed in Table 9.8.

Table 9-8: Data recorded for the CuBi fims deposited at different thicknesses

| Deposition time | Thickness measured | Photocurrent production at 0.3 V vs RHE (in mA.cm$^{-2}$) | Maximum HC-STH efficiency (%) |
|---|---|---|---|
| 15 min | 110 ± 10 nm | 1.38 | 0.49 |
| 30 min | 205 ± 11 nm | 1.62 | 0.58 |
| 1h | 388 ± 16 nm | 1.16 | 0.39 |
| 1h 30min | 549 ± 25 nm | 0.61 | 0.19 |
| 2h | 735 ± 20 nm | 0.22 | 0.07 |

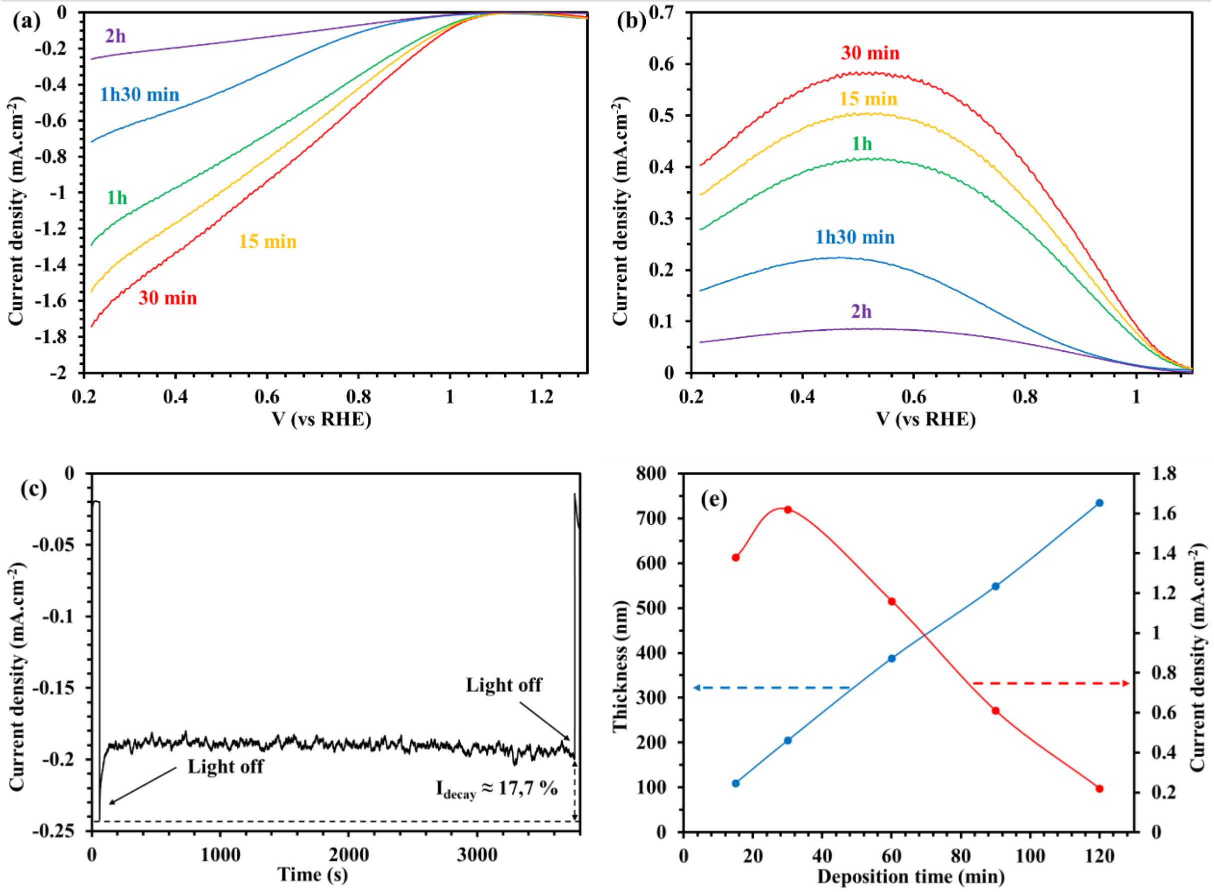

Figure 9.14: a) LSV scans for the CuBi150 samples produced with different thicknesses, b) Associated HC-STH efficiencies, c) Stability measurement for CuBi150 sample deposited for 30 min, d) H2 and O2 evolution rate associated with the stability measurement

Such as $BiVO_4$, the investigation of charge carriers' lifetime by Abdi et al. resulted in the determination of a short diffusion length for the charge carriers, measured at around 52 nm [228]. These behaviours appear to be relatively similar among metal oxides semiconductors and can explain the poor conductivity reported for $BiVO_4$ or $CuBi_2O_4$. By optimizing the thickness obtained, the charge carriers produced in the bulk are closer to the surface reactions sites and then can migrate to the surface with less chances to recombine. Here, a thickness of 200 nm appears to give the most efficient photocathode. The stability measurement of the CuBi150 sample tested (see Figure 9.14c) exhibits a lot of tiny photocurrent peaks during the measurement and might a sign of a possible degradation of the material during the measurement. $CuBi_2O_4$ is known to be sensitive to photo-corrosion, which could impact the performances if the photocathode is used in a PEC tandem cell.

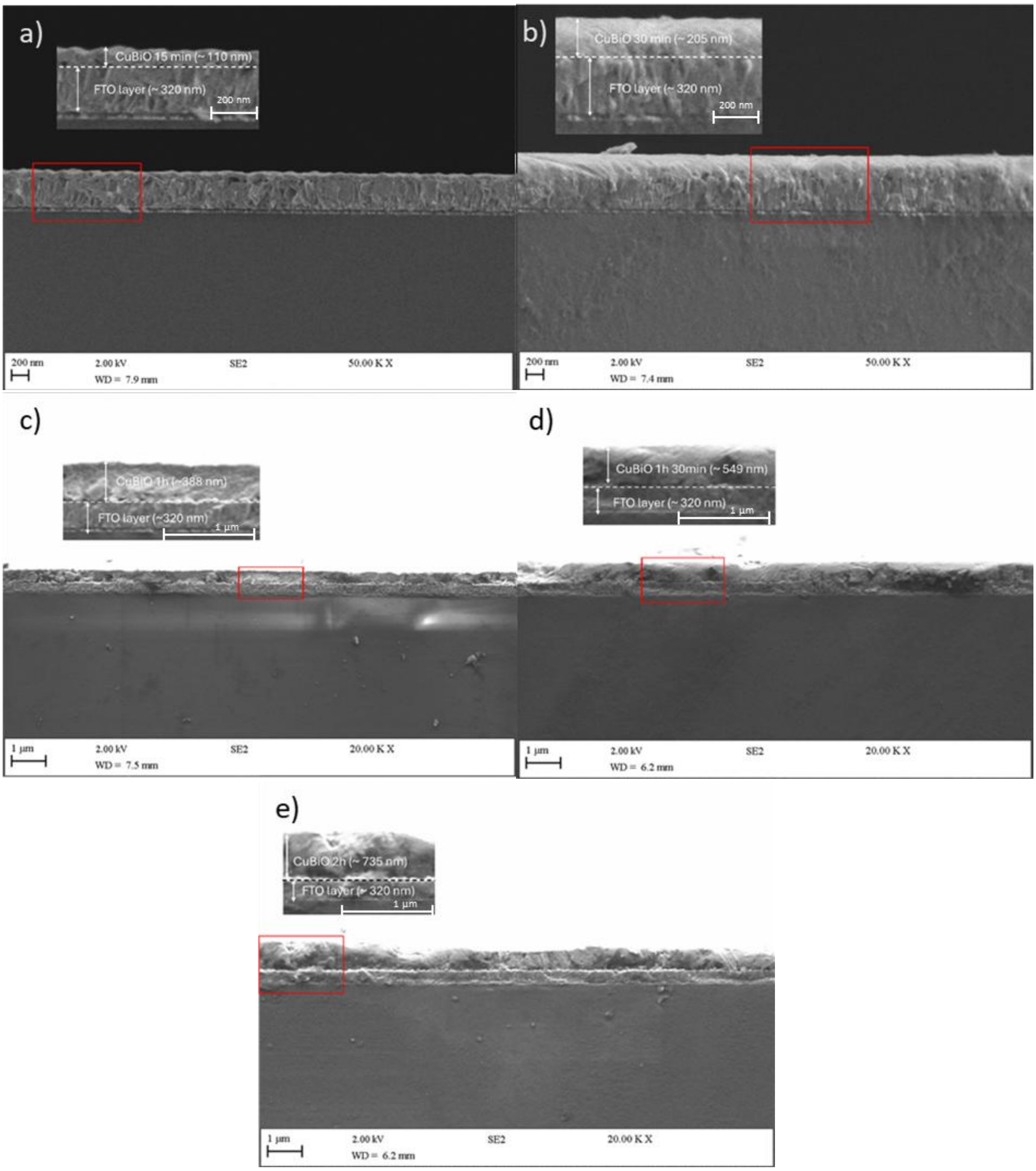

Figure 9.15: Cross-section SEM images of BiCu150 sample deposited for; (a) 15 min; (b) 30 min; (c) 1h; (d) 1h 30min; (e) 2h

## 9.9. Summary

In this work, $CuBi_2O_4$ photocatalysts were successfully synthetized by pDC reactive magnetron co-sputtering from two Cu and Bi metallic targets, to be used as photocathodes for the study of the hydrogen evolution reaction. Similarly to the BiV samples produced, the first parameter studied was the power ratio applied between the Cu and Bi targets. This resulted in the production of different impurity crystal phases ($Bi_2O_3$in "bismuth-rich" samples, CuO in "copper-rich" samples) when the Bi/Cu ratio obtained for the samples differs from 2. The samples that presented the tetragonal $CuBi_2O_4$ phase exhibited the best photoelectrochemical performances, with the BiCu150 sample presenting the highest photocurrent production, with a photocurrent produced of -1.13 $mA.cm^{-2}$ at 0.3 $V_{RHE}$, resulting in a HC-STH efficiency of x% at 0.3 $V_{RHE}$. The charge transfer efficiency of the BiCu samples studied were all measured around the same value (around 11% at 0.3 $V_{RHE}$). On the other hand, the BiCu150 sample exhibited the highest charge transport efficiency compared to the other samples (35% at 0.3 $V_{RHE}$), explained by the large amount of oxygen vacancies measured by XPS analysis. Those findings present similarities with the BiV samples, and future studies could be done on the understanding of the presence of oxygen vacancies is Bismuth based photocatalysts produced by reactive magnetron co-sputtering.

Finally, the influence of the film thicknesses was studied by varying the deposition time, producing samples with thicknesses from 100 to 750 nm. The optimum thickness was found around 200 nm, producing a photocurrent of -1.62 $mA.cm^{-2}$ at 0.3 $V_{RHE}$. If the photocurrent decay was less important for the BiCu150 photocathode compared to the BiV800 photoanode, the photocurrent produced during stability measurement was drastically lower, with a possible degradation of the coating during the measurement. Further study needs to be done to improve the stability of the photocathode. Improvements can be done regarding the scavenger used, here both for photoanode and photocathode. However, precedent studies showed the difficulty to replace H2O2 as an electron scavenger, due to the unintended side reactions that can occur with the photocatalysts. For example, Berglund et al. tested several compounds as electron scavengers ($K_3[Fe(CN)_6]$, $I_2$/Kl and $FeCl_3$), without the obtention of satisfying results [228].

# 10. PEC tandem cell with $BiVO_4$ photoanode and $CuBi_2O_4$ photocathode: first PEC measurements, limitations and solutions

*This chapter presents the first results obtained for the study of a tandem PEC cell based on a bismuth vanadate photoanode and a copper bismuth oxide photocathode. This tandem PEC cell was based on the findings from Chapter 6 and Chapter 7. This chapter discusses such aspects as description of the proposed PEC tandem cell (Section I), a characterization of the photoelectrodes with the determination of their respective electronic structure (Section II), firsts PEC measurements for the tandem PEC cell (Section III) and then a discussion of the results in Section IV.*

## 10.1. PEC water splitting cell design

As presented in chapter 2, there are several configurations possible to achieve PEC water splitting: p-n tandem PEC cell, PEC-PV cell and buried junction device. On the previous chapters, the photoelectrodes were tested in a single-photoelectrode configuration. The main drawback of a single-photoelectrode cell is the necessity of applying a potential to start the overall water splitting reaction. The addition of another photoelectrode can help to achieve an unbiased PEC tandem cell, as explained in Chapter 2. In the following parts, the only configuration considered would be the p-n PEC cell, as it was the configuration of interest for this work. Several characteristics can be measured to assess the performance of p-n PEC tandem cell. Firstly, both materials exhibit intrinsic properties, such as the onset potential $E_{onset}$ corresponding to the applied potential where the reaction of interest occurs, or the photogenerated current $J_{ph}$, corresponding to the difference between the current produced in the dark $J_{dark}$ and the current produced with illumination $J_{light}$ [285]. When two photoelectrodes are used in a PEC tandem cell, other efficiencies can be measured, such as the Faradaic Efficiency (FE), defined as the ratio of the amount of gas produced by the theoretical amount of gas produced according to the photocurrent measured, and that can be expressed with equation (x):

$$FE = \frac{\alpha \times n\ (mol) \times F\left(C.mol^{-1}\right)}{J_{photo}\ (mA.cm-2) \times t\ (s)} \tag{49}$$

with α the electron transfer number (with the production of $H_2$, $\alpha = 2$; with the production of $O_2$, $\alpha = 4$), n the number of moles of the gas product, F the Faraday constant

(96485 C.mol$^{-1}$), $J_{photo}$ the generated photocurrent and t the reaction time. The FE can then be used to estimate the solar-to-hydrogen efficiency mentioned in chapter 7 (equation 36):

$$STH\ (\%) = \frac{J_{op}\ (mA.cm-2)\times 1.23\ (V_{RHE})\times FE\ (\%)}{P_{light}\ (mW.cm^{-2})} \tag{36}$$

with Jop is the photocurrent at which the PEC cell is operating, 1.23 $V_{RHE}$ corresponds to the theoretical standard potential of the overall water splitting reaction, FE the faradaic efficiency and $P_{light}$ the power of the incident light (usually 100 mW.cm$^{-2}$). However, to determine the FE, it is necessary to determine the number of mol produced during a measurement. This measurement can be theoretically calculated thanks to equation (43) seen in chapter 7, or experimentally by GCMS. It is then necessary for the PEC tandem cell to fit into the GCMS device, which is not always the case. When it is not possible to use GCMS, the FE is usually approximated to 100% [43, 92]. In practical, the FE is always less than 100%, due to side reactions occurring at the photoelectrodes and inhibiting the OER and the HER [286 – 288]. Other efficiencies can be measured, such as the APCE efficiency, which is the photocurrent generated per photon absorbed (equation 50). Finally, when an applied bias is required to run the PEC tandem cell, due to limitations of the materials or the cell itself, the STH can not be measured and is replaced by the Applied bias photon-to-current conversion efficiency (ABPE), calculated with equation (51):

$$APCE\ (\%) = \frac{IPCE\ (\%)}{A} = \frac{IPCE\ (\%)}{1-R-T} = \frac{J_{mono}(mA.cm^{-2})\times 1239.8\ (eV.nm)}{P_{mono}(mW.cm^{-2})\times\lambda(nm)\times(1-R-T)} \tag{50}$$

$$ABPE\ (\%) = \frac{J_{phono}(mA.cm^{-2})\times(1.23-V_{bias})(V_{RHE})}{P_{light}(mW.cm^{-2})} \tag{51}$$

with $V_{bias}$ the bias applied to measure $J_{photo}$. All those efficiencies and their parameters are mainly influenced by the geometry and design of the PEC tandem cell. The design of a PEC cell must take into account three main points: efficiency, cost and stability [285]. In this part, only the possible photocell design for a p-n PEC tandem cell would be discussed. A PEC consists of a vessel containing an electrolyte where photoelectrodes are immerged. The simplest configuration for a vessel is a transparent open vessel to allow the illumination of the photoelectrodes (see Figure 10.1a). This vessel would contain the electrolyte where the photoelectrodes are be immerged. However, to ensure that the visible light from a solar simulator is completely transmitted to the photoelectrodes, quartz vessels should be required. As quartz vessels are expensive devices, the body of a PEC is usually made of more robust material (Perspex or Teflon) and are equipped with an optical quartz window, which allows a good illumination of the photoelectrodes without being too expensive (as shown in Figure 10.1b). The body of the cell can also be equipped with separate ports to ensure a consistency in the distance between the electrodes, avoiding a change of electrical parameters in the electrical circuit of the cell and then the efficiency of the PEC tandem cell [289]. It must be noticed that, in a single vessel PEC cell, the photoanode and the photocathode are positioned in the same compartment and are immerged in the same electrolyte. The separation of the reactive sites prevents the recombination surface reaction of $H_2$ and $O_2$ to form $H_2O$. However, for potential upscaled applications, it is important to separate the production of $H_2$ and $O_2$, to avoid the mixture of the two gases that can be potentially dangerous [285, 289]. Then, the photoelectrodes need to be separated in two different compartments. This can be done with the use of H-type vessels, where two vertical glass tubes are connected by a smaller horizontal tube. As the gases produced flow upward, they are naturally separated, avoiding the risk of mixing them. Finally, different electrolytes can be used to perform the OER or the HER, but not all photocatalysts can be immerged in every electrolyte. For example, $BiVO_4$ can be degraded within acidic environments [290]. The use of physical separators, such as glass frit or proton exchange membranes can be added to a two vessels configuration to allow the use of two different electrolytes. Proton exchange membranes such as Nafion are commonly used in fuel cells and does not allow $H_2$ or $O_2$ gas to pass through but only $H^+$ ions to ensure the conductivity between the two vessels. It must be noticed that Nafion membrane can not be used with electrolytes containing cations (such as $Na^+$), as they will take the place of $H^+$ ions and reduce the production of $H_2$ at the photocathode side.

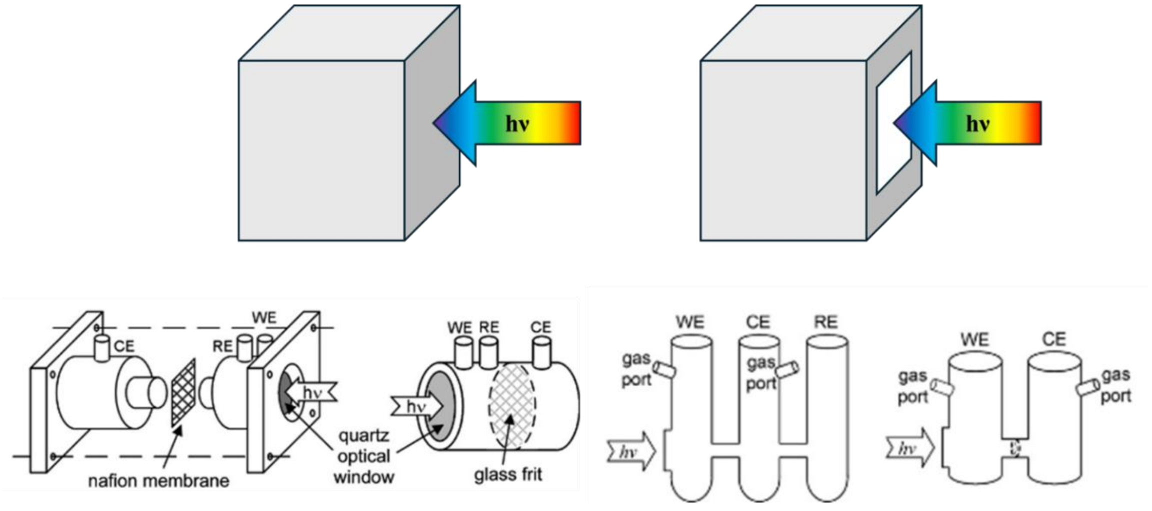

Figure 10.1: Examples of photocell designs: (a) single vessel, (b) single vessel equipped with optical windows, (c) Two compartments vessel with physical separator, (d) H-type vessel (adapted and reproduced from [289])

Table 10-1: Examples of $BiVO_4/CuBi_2O_4$ PEC tandem cell proposed in the literature

| Photoanode | Photocathode | Electrolyte | Max photocurrent | Max STH (if measured) | Ref |
|---|---|---|---|---|---|
| Mo-doped $BiVO_4$ | MgO-passivated $CuBi_2O_4$ | 0.2 M KOH;<br>0.4 M $H_3BO_3$ | 0.33 mA.cm$^{-2}$ at 0.4 $V_{RHE}$ | 0.41% (measured for the tandem PEC cell) | [294] |
| $BiVO_4$ | $CuBi_2O_4$ | 0.1 M $Na_2SO_4$ | 0.81 mA.cm$^{-2}$ at 0.45 $V_{RHE}$ | 0.61% (only measured for the photocathode) | [250] |
| Nano-$BiVO_4$ | Micro-$CuBi_2O_4$ | 0.5 M $Na_2SO_4$ | 0.036 mA.cm$^{-2}$ at 0 $V_{RHE}$ | 0.04 % (measured for the tandem PEC cell) | [259] |
| W:$BiVO_4$ | $TiO_2$:$CuBi_2O_4$ | 0.3 M $K_2SO_4$; 0.2 M phosphate buffer | 0.05 mA 0.6 $V_{RHE}$ | / | [295] |
| $ZnIn_2S_4$ | $CuBi_2O_4$ | 0.1 $Na_2SO_4$ | 0.03 mA.cm$^{-2}$ at 0 $V_{RHE}$ | / | [258] |
| $BiVO_4$ | $CuBi_2O_4$ | 0.5 M $Na_2SO_4$ | 2 mA.cm$^{-2}$ at 0.45 $V_{RHE}$ | / | [296] |

As the geometry and the design are important parameters regarding the efficiency of the PEC tandem cell, the p-n photoelectrodes used remain the limiting factor regarding the photoelectrochemical properties. Table 10.1 presents several examples of p-n PEC tandem cell composed of a $BiVO_4$ photoanode and a $CuBi_2O_4$ photocathode. An example of a tandem PEC cell can be presented with the work of Lai et al. In their work, they presented a p-n tandem cell composed of a $BiVO_4$ photoanode produced from a single $Bi_4O_5I_2$ nanosheet template, and of a $CuBi_2O_4$ photocathode [260] . The cell was made of 2 separate chamber (H-type vessel) and was equipped with quartz windows and a 117 Nafion proton exchange membrane. The tandem exhibited a high photovoltage (2.0 V), technically enough to perform water splitting without external bias. The bias-free photocurrent produced by the cell was around 36 µA.cm$^{-2}$, corresponding to a 0.04% STH efficiency. The main limitations reported were the low charge transport and charge transfer efficiencies reported for both photoelectrodes. It is usually considered to be economically viable that a PEC tandem cell should exhibit a STH efficiency above 10% [47]. As reported in 10.1, the STH efficiency reported for $BiVO_4/CuBi_2O_4$ PEC tandem cells does not exceed 1%. Several limitations have been reported by the different studies. As the PEC tandem cell are still not extremely efficient compared to electrolysers, the main efficiency (STH efficiency) is not systematically measured in the studies, as shown in Table 10.1.

## 10.2 Methods for the proposed BiV/BiCu PEC tandem cell

As explained in Chapter 2, several strategies can be employed to build an unbiased water splitting cell for hydrogen production. The use of photocatalysts to build a n-type/p-type tandem device offers several advantages, such as a low-cost of the material used, especially with metal oxides photocatalysts [257]. In this configuration, a photoanode and a photocathode are connected to each other and immersed in an aqueous electrolyte containing the reactive species to perform the overall water splitting reaction. However, several requirements should be met to reach a hydrogen production efficiency commercially viable. In particular, it is estimated that a PEC/PEC tandem cell should reach a solar-to-hydrogen efficiency larger than 10 % [46]. In practical, this STH efficiency is never reached and can be limited by several factors, such as the low reaction kinetics at the surface of the photoelectrodes or the complex interactions involving sunlight, semiconductors and liquid solutions. Among the different photocatalysts combination possible, $BiVO_4$ photoanode and $CuBi_2O_4$ photocathode has been tested into PEC tandem cells with various types of photocatalysts, but only to achieve very poor conversion efficiencies. As an example, Xu et al. produced an unassisted water splitting cell using $BiVO_4$ photoanode and Si photocathode, only to reach a STH efficiency of 0.57% [278].

It must be noted that several studies demonstrated the feasibility of coupling BiVO4 photoanode and $CuBi_2O_4$ photocathode to obtain an unassisted PEC water splitting cell [251, 258, 259]. The efficiencies associated with these cells are respectively. Both materials meet the requirements to perform both half-reactions associated with water splitting, as demonstrated in the previous chapters. It must be noticed that no PEC tandem cells with photoelectrodes produced by reactive magnetron co-sputtering have been reported yet.

In this work, the PEC tandem cell proposed was based on the PEC cell developed by Tania Lopes et al. and was supplied by an external company [160]. It is composed of several parts: an acrylic body with a capacity of a 100 mL. two quartz windows equipped with metallic and black acrylic frames, to allow the illumination of the photoelectrodes (with a maximum illumination area of 5 x 5 $cm^2$), as shown in Figure 10.2. The light source used was a Uniform Arc light source system LSU308 from Quantum Design, powered by a 150 – 300 W arc lamp system LSN354. The lamp used is a 300W Xe lamp, equipped with filters from Newport to better reproduce the AM 1.5G spectra (an Air Mass Filter 81094 and a 325 nm UV filter).

The $BiVO_4$ photoanode and $CuBi_2O_4$ photocathode were chosen based on the findings from Chapter 8 and Chapter 9, respectively. The two materials were produced by reactive magnetron co-sputtering, by applying 50 and 800 W of power to the bismuth and vanadium targets for $BiVO_4$, and 100 and 150 W of power to the bismuth and copper targets for $CuBi_2O_4$, respectively. The materials were deposited onto fluorine-doped tin oxide coated glass from Pilkington® for 30 minutes, to get the optimum thicknesses. After deposition, the samples were annealed in air at 500°C for 1h, to obtain crystalline coatings. Those parameters correspond to the parameters used for the production of BiV800 sample and CuBi150 sample in Chapters 8 and 9, respectively. The samples were then characterized to ensure the formation of the desired materials (SEM, Raman, XRD, EDX), based on the previous methods described. In addition, the electronic band diagrams of each photocatalysts were investigated, to determine the overall band diagram of the proposed PEC tandem cell. Different extrapolation techniques (Valence band XPS, Tauc plot method, Cyclic voltammetry) were used. Cyclic voltammetry was performed for both materials to determine their electrochemical electronic structure. Cyclic voltammetry was performed in dark conditions, to make sure that the electrons were driven out of the conduction and valence band. The cyclic voltammetry was performed from -0.5 to 2.3 $V_{RHE}$ for the BiV photoanode and was performed from -1.5 to 1.5 $V_{RHE}$ for the BiCu photocathode. The photoelectrodes were analysed for 10 cycles at a scan rate of 10 $mV.^{-1}$. The electrolyte used was a 0.5M $Na_2SO_4$, as it was used for the previous chapter for both materials. A schematic of the theoretical $BiVO_4/CuBi_2O_4$ PEC tandem cell is presented in Figure 10.2. The first assessment of the photoelectrochemical activity of the proposed PEC cell was done by measuring the photocurrent production and the associated hydrogen production rate under illumination with AM 1.5G simulated visible light source. The valence band measurement was performed by XPS analysis performed by a SUPRA photoelectron spectrometer from Kratos Analytical Ltd, by performing a region scan at very low binding energy, with a pass energy of 40 eV.

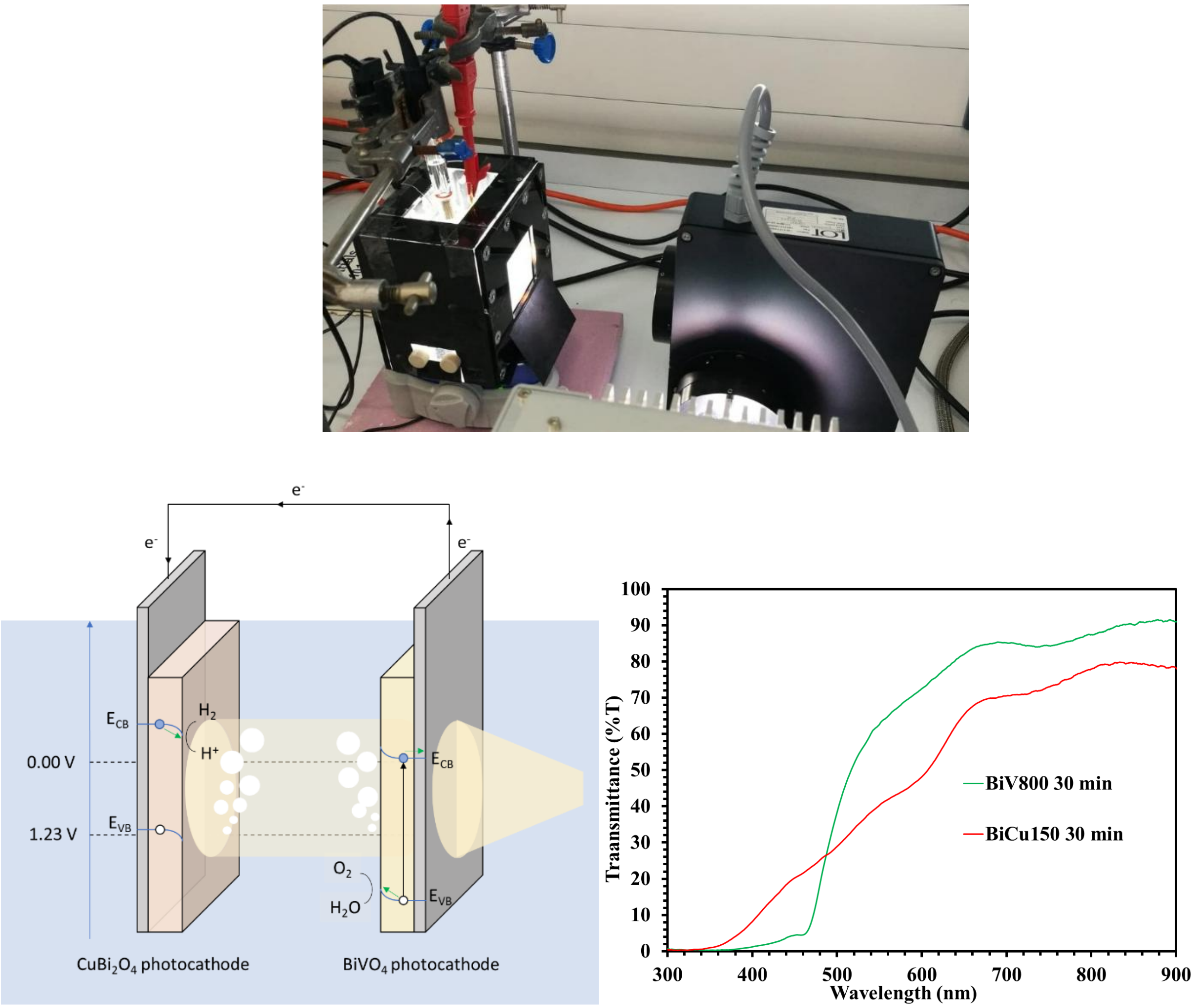

Figure 10.2: (top) Photograph of the PEC water splitting used with the visible light source; (bottom left) Schematic of the PEC tandem cell formed by the $BiVO_4$ photoanode and the $CuBi_2O_4$ photocathode; (bottom right) Comparison of transmittance spectra for both photoelectrode

## 10.3 Characterisation of $BiVO_4$ photoanode and $CuBi_2O_4$ photocathode

To ensure the formation of the desired materials (m-s $BiVO_4$ and tetragonal $CuBi_2O_4$), Raman spectroscopy and XRD were used. Figure 10.3a exhibits the Raman spectra and XRD patterns for both materials. In addition to the FTO peaks (ICDD card 041-1445), the different peaks attributed to the presence of m-s $BiVO_4$ and tetragonal $CuBi_2O_4$ can be observed on the XRD patterns (Figure 10.3b):

- JCPDS card 14-0688 (m-s $BiVO_4$): 18.9° (1 1 0), 28.8° (1 2 1), 30.5° (0 4 0), 34.6° (2 0 0), 35.2° (0 0 2), 40° (2 1 1), 42.4° (1 5 0), 45.9° (1 3 2), 46.8° (2 4 0), 47.2° (0 4 2) 50.2° (2 0 2), 53.5° (1 6 1), 58.3° (1 7 0) and 59.4° (3 2 1).
- JCPDS card 48-1886 (tetragonal $CuBi_2O_4$): 20.84° (200), 28° (211), 29.68° (220), 30.76° (002), 33.26° (310), 34.26° (112), 37.42° (202), 45.16° (330), 45.92° (312), 46.68° (411) and 47.82° (420).

Moreover, the Raman spectra exhibit the bands associated with m-s $BiVO_4$ and tetragonal $CuBi_2O_4$. It is interesting to note the similarities between the morphologies obtained on SEM micrographs (Figure 10.4) for those two bismuth-based photocatalysts produced by reactive magnetron co-sputtering, and that corresponds to the recrystallization process predicted by the Thornton model [146]. Both samples depict the appropriate stoichiometry found earlier in Chapter 8 and Chapter 9.

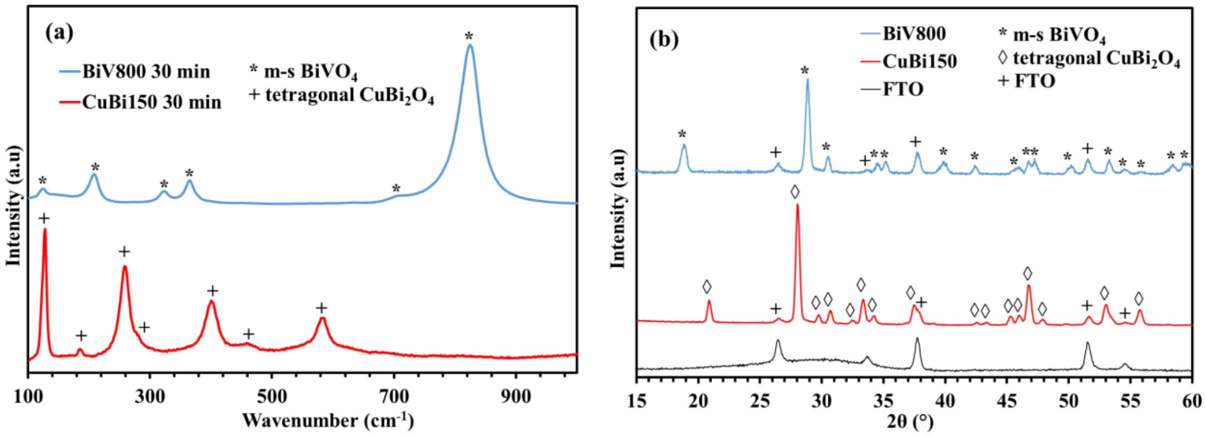

Figure 10.3: (a) Raman spectra of BiV800 and CuBi150; (b) XRD patterns of BiV800 and CuBi150

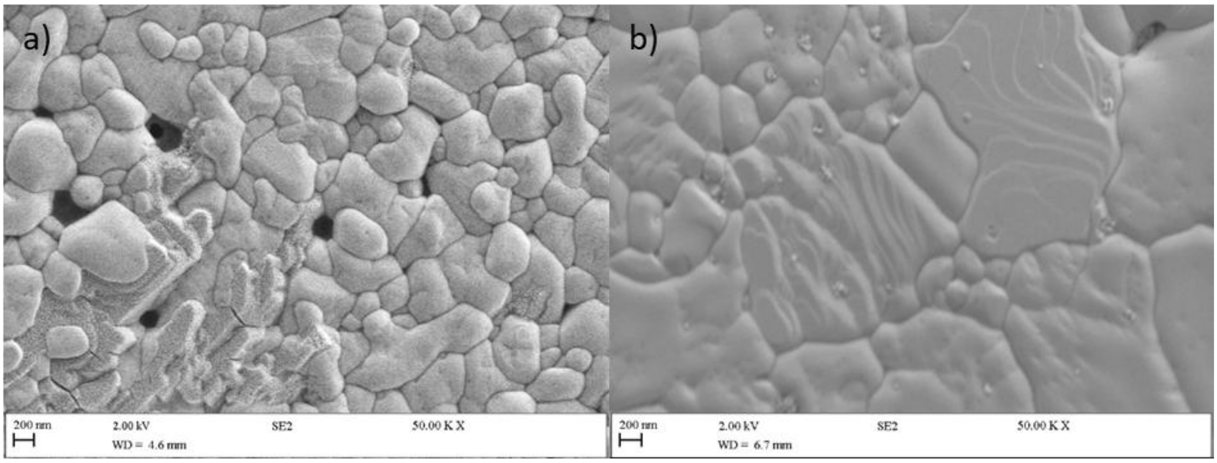

Figure 10.4: SEM micrographs of (a) $BiVO_4$ photoanode; (b) $CuBi_2O_4$ photocathode

As mentioned in Chapter 2, the electronic band structure of a photoelectrode should meet the energetic requirements to perform the reaction of interest. In the case of a photoanode, the valence band should be more positive than the standard potential for oxidation reaction, whereas the conduction band should be more negative than the standard potential for proton reduction for a photocathode. To determine the values of the CB and VB of the photocatalysts, different extrapolation techniques can be used [107]. In this work, the band diagrams of the produced photoelectrodes were determined using valence band XPS analysis coupled with the optical band gap determined by the Tauc plot method [159] and using cyclic voltammetry.

The valence band maximum can be determined by performing XPS analysis at very low binding energies. By extrapolating the straight tangent line of the plot, the intersection with the x-axis is defined as the VB maximum. This method has been used several times with different photocatalysts [262, 263]. The VB XPS analysis of the samples can be observed in Figure 10.6a. Based on the extrapolation, both valence band maximum can be estimated at 2.17 and 1.26 eV for $BiVO_4$ and $CuBi_2O_4$, respectively. Those values are in accordance with the data found in literature [10, 265]. The value of the conduction band CB can be then calculated according to equation (47):

$$E_{CB} = E_{VB} - E_g \tag{47}$$

where $E_g$ is the optical band obtained with the Tauc plot method, $E_{CB}$ is the value of the conduction band (in eV) and $E_{VB}$ is the value of the valence band (in eV). As seen in Chapter and Chapter 9, the Tauc plot method is usually used to estimate the value of the optical band gap. Figure 10.6b shows the Tauc plot method used for the determination of optical band gap for $BiVO_4$ and $CuBi_2O_4$. The type of band gap chosen for $BiVO_4$ was indirect (as seen in chapter 6) and direct for $CuBi_2O_4$ (as seen in chapter 7). Band gap energy values were estimated at 2.42

and 1.91 eV for $BiVO_4$ and $CuBi_2O_4$, respectively. The respective conduction band values can be then evaluated at -0.25 and -0.65 eV, respectively.

Another technique used to assess the electronic band structure of a semiconductor is cyclic voltammetry in dark conditions. During cyclic voltammetry, both samples exhibit an oxidation peak and a reduction peak. Those peaks are attributed to the electron transfer mediated through the VB and CB edges, respectively. This technique has been reported several times to estimate the value of the band edges of a semiconductor [266, 267]. The voltammograms of $BiVO_4$ and $CuBi_2O_4$, performed in a three-electrode configuration with a 0.5M $Na_2SO_4$ aqueous electrolyte are presented in Figure 10.6c and 10.6d. Both exhibit oxidation and reduction peaks at different potentials. The measured band edges are presented in Table 10.2. It must be noticed that the values slightly differ from the previous technique, due to the presence of overpotentials at the photoelectrodes. The energy band diagram deduced from those two techniques are presented in Figure 10.5. Thanks to these findings, it confirms that $BiVO_4$ and $CuBi_2O_4$ are both suitable to be used as photoanode and photocathode, respectively. Moreover, the n-type nature of $BiVO_4$ favours the production of anodic photocurrent used for oxygen evolution reaction, whereas the p-type nature of $CuBi_2O_4$ favours the production of cathodic photocurrent used for proton reduction reaction.

Table 10-2. Values of CB edge, Eg and VB edge (in eV) determined by Valence band XPS, Tauc plot method and Cyclic voltammetry

| Sample | XPS $E_{VB}$ | Optical $E_g$ | $E_{CB} = (E_{VB} - E_g)$ | CV $E_{CB}$ | CV $E_{VB}$ | CV $E_g$ |
|---|---|---|---|---|---|---|
| BiV photoanode | 2.17 | 2.42 | -0.25 | -0.21 | 2.12 | 2.33 |
| CBO photocathode | 1.26 | 1.91 | -0.65 | -0.7 | 1.24 | 1.94 |

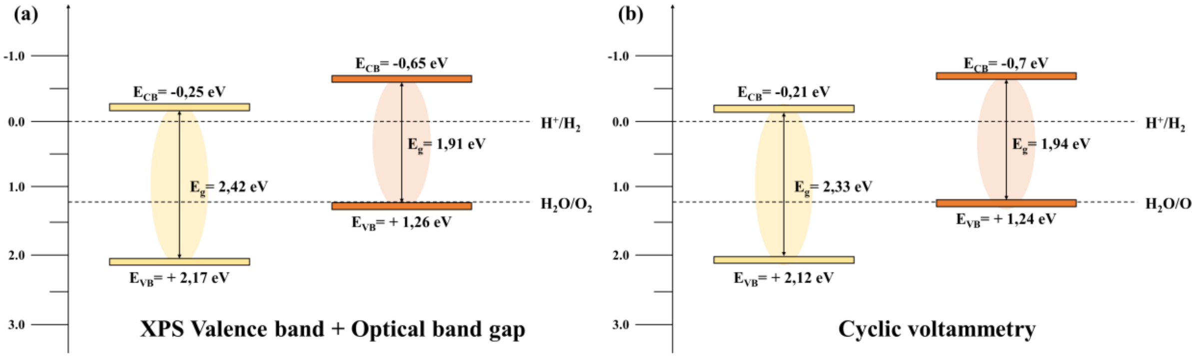

Figure 10.5: Schematic illustration of the band structure of $CuBi_2O_4$ and $BiVO_4$ samples a) Using XPS + Bandgap and b) Cyclic Voltammetry

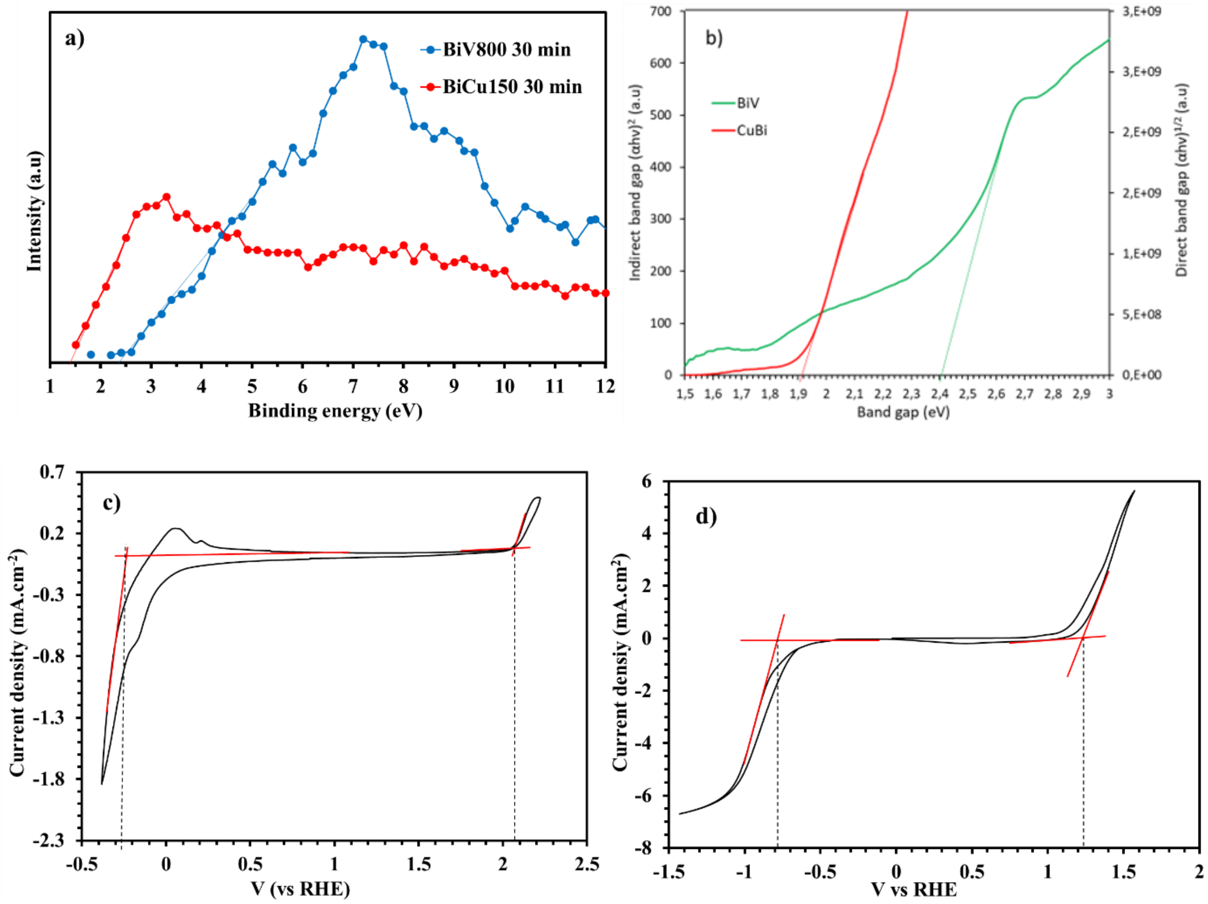

Figure 10.6: (a) Valence band XPS spectra of $BiVO_4$ photoanode and $CuBi_2O_4$ photocathode; b) Tauc plots for $BiVO_4$ photoanode and $CuBi_2O_4$ photocathode; c) Cyclic voltammogram of $BiVO_4$ photoanode; d) Cyclic voltammogram of $CuBi_2O_4$ photocathode

## 10.4 First PEC measurements

Prior to the overall performance of the PEC tandem water splitting cell, the performances of the $BiVO_4$ photoanode and the $CuBi_2O_4$ photocathode were assessed in a three-electrode configuration, with a Pt mesh as a counter-electrode and an Ag/AgCl reference electrode, all immerged in a 0.5M $Na_2SO_4$ solution. As displayed in Figure 10.7a, the LSV scans for confirm the good photoactivity under visible light illumination for both photoelectrodes when used in a single-photoelectrode configuration. The photocurrent recorded for the BiV photoanode was 3.22 mA.cm$^{-2}$ at 1.23 $V_{RHE}$, whereas the photocurrent produced by the BiCu photocathode was around -1.57 mA.cm$^{-2}$ at 0.4 $V_{RHE}$. Due to the configuration of the PEC cell, both photoelectrodes are illuminated in the same axis, meaning that one photoelectrode acts as a top absorber for the other one. The impact of the BiV photoanode as top absorber on the photocurrent produced by the BiCu photocathode can be observed in Figure 10.7a, where the photocurrent drops from -1.57 to -0.16 mA.cm$^{-2}$ at 0.4 V$_{RHE}$. This represents an intrinsic limitation of the cell design, as the photocathode losses 90% of the photocurrent produced.

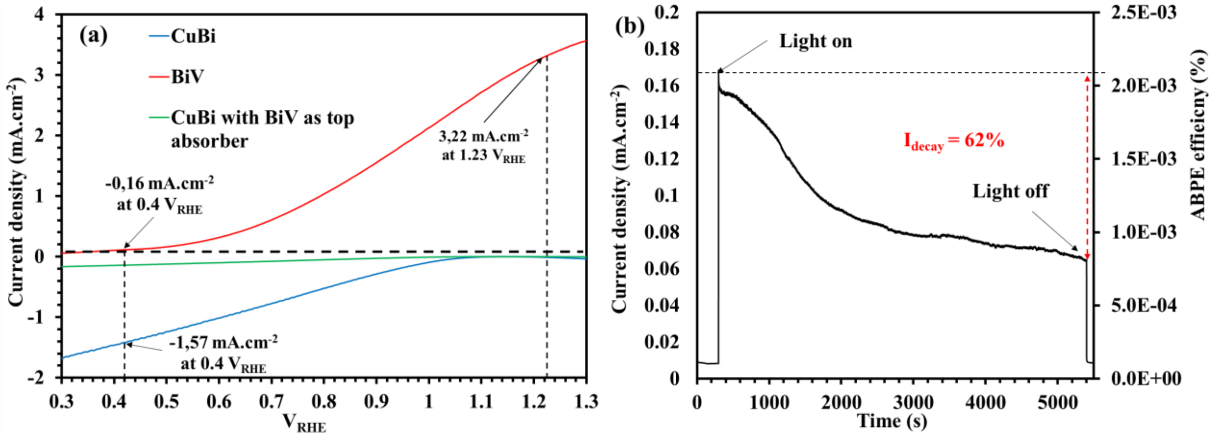

Figure 10.7: (a) LSV scans for BiVO$_4$ photoanode, CuBi$_2$O$_4$ photocathode and CuBi$_2$O$_4$ photocathode used with BiVO$_4$ as top absorber in a three-electrode configuration, (b) Photocurrent produced by the proposed PEC tandem cell in a two-photoelectrode configuration at 1.12 V$_{RHE}$

This intrinsic limitation was also observed when the p-n PEC tandem cell was tested without applying any bias and connecting both photoelectrodes in a two-electrodes configuration. No photocurrent production was detected, meaning that no water splitting reaction was occurring. It means that an applied bias is still necessary to run the proposed PEC tandem cell. Both photoelectrodes were then used at the same time in a three-electrode configuration, with the BiV photoanode used as the working electrode. The applied bias was 0.73 V$_{RHE}$, as it appears, from the single-photoelectrode measurements, that we can obtain the optimum photocurrent production for both photoelectrodes. In practical, the photocurrent produced under this bias was recorded for 90 min and is shown in Figure 10.7b. The observation is the poor photocurrent produced by the working electrode, where around 1 mA.cm-2 was expected. The peak of photocurrent produced does not exceed 0.17 mA.cm-2 and drops after several minutes, with an observed photocurrent decay of 62% after 90 min. The associated ABPE conversion efficiency is shown in Figure 10.7b, exhibiting very low efficiency (< 0.1% after 1h). This value is far from the 10 % recommended for a PEC tandem cell.

## 10.5 Discussions

Figures 10.9a and 10.9b presents the LSV scans of $BiVO_4$ and $CuBi_2O_4$ photoelectrodes when illuminated from the back and the front, respectively. It can be observed, for both photoelectrodes, that the photocurrent produced with a front illumination is drastically lower than the one produced with a back illumination. One of the reasons for this behaviour was proposed by Lin et al., who studied the effect of the porosity of a $BiVO_4$ photoanode onto its photocurrent production under back and front illumination [267]. A dense coating presented better results with a back illumination, whereas a porous structure exhibits a drastically higher photocurrent under front illumination. This was attributed in a change of charge transfer efficiency, with a higher surface area in contact with the electrolyte in the case of a porous photoanode. As the photoelectrodes proposed in this work are made of dense coatings and did not exhibit good charge transfer efficiencies, one of the photoelectrode will then automatically produce a low photocurrent when used in tandem. Moreover, the top absorber photoanode inevitably absorbs a part of the incident photons from the visible light, limiting the illumination of the photocathode and then reducing again the photocurrent produced. A schematic of the two photoelectrodes used in tandem is shown in Figure 10.8.

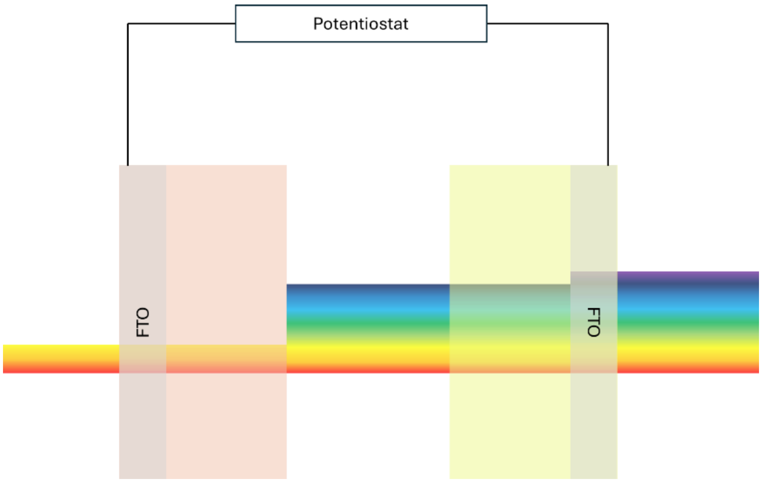

Figure 10.8: Schematic of the absorption of light by the tandem PEC cell

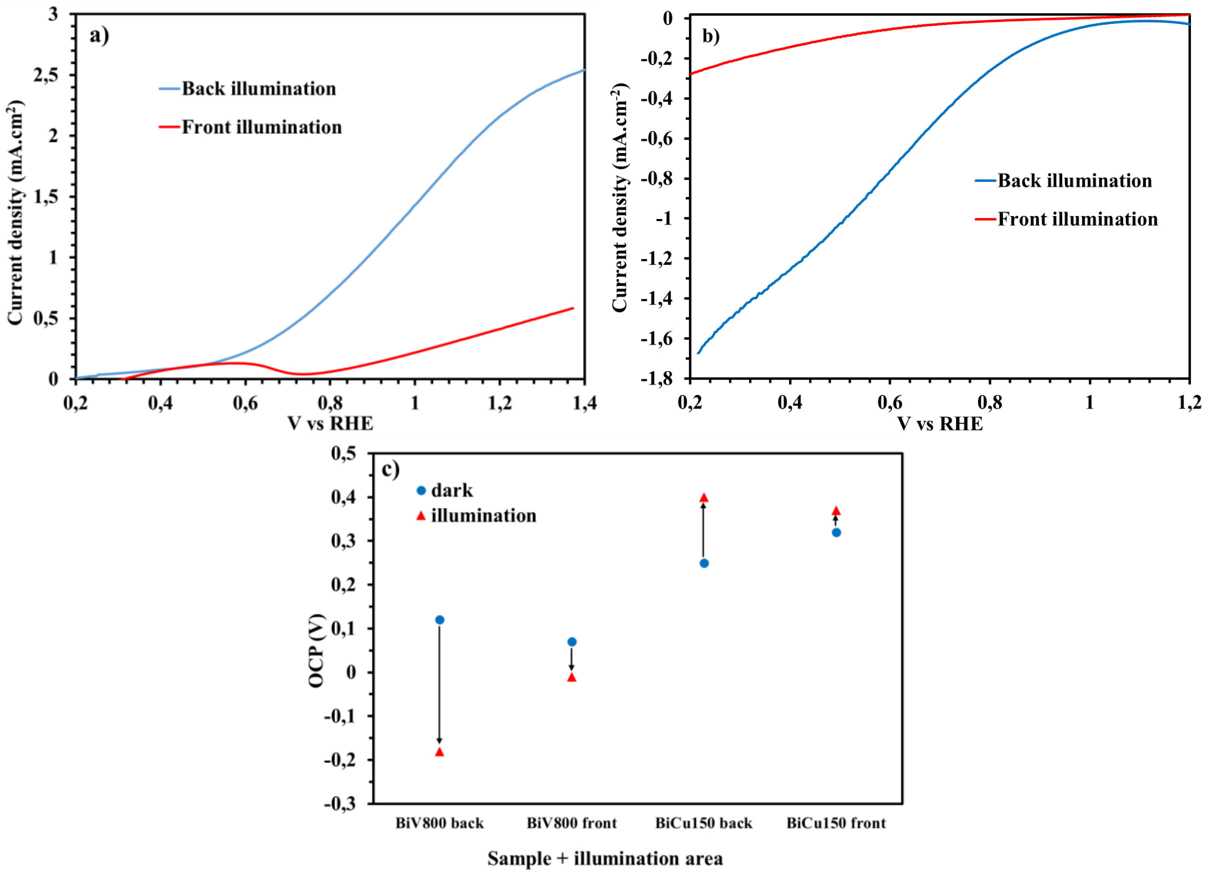

Figure 10.9: (a) Back and front illumination for $BiVO_4$ photoanode, b) Back and front illumination for $CuBi_2O_4$ photocathode, c) OCPs associated

The photovoltages produced from the photoelectrodes, determined by open-circuit potential measurements, as shown in Figure 10.9c. The photovoltage produced by the different photoelectrodes was measured by recording the open circuit potential of the electrochemical cell (Pt mesh | 0.5M $Na_2SO_4$ | photocatalyst/FTO), in dark condition and under visible light illumination. It is confirmed that the photoanode and photocathode act as a n-type and a p-type semiconductors, respectively. However, when the samples are illuminated from the front, the photovoltages are drastically reduced, and is even divided by 4 in the case of the photocathode. These back and front measurements explain the poor photocurrent produced by the PEC cell and the low STH efficiency associated. Several changes could be done then to enhance the overall efficiency of the PEC tandem cell proposed. One of the issues of the current configuration is the position of the photoelectrodes regarding the light source, that prevents one electrode to be directly illuminated. A first solution would be the use of an additional light source, directly illuminating the back of the second photoelectrode. However, it would not be possible to characterise the PEC tandem cell according to the AM 1.5G standard used. Lopes et al. proposed the implementation of a mirror system to the PEC cell, as illustrated in Figure

10.10 [159]. The use of reflective surfaces is often used in photocatalytic systems, to avoid the loss of light intensity. For example, Grao et al. used interior reflective surfaces in a photocatalytic water treatment reactor [267]. This would then allow the back illumination of the photocathode, enhancing the overall efficiency of the tandem cell.

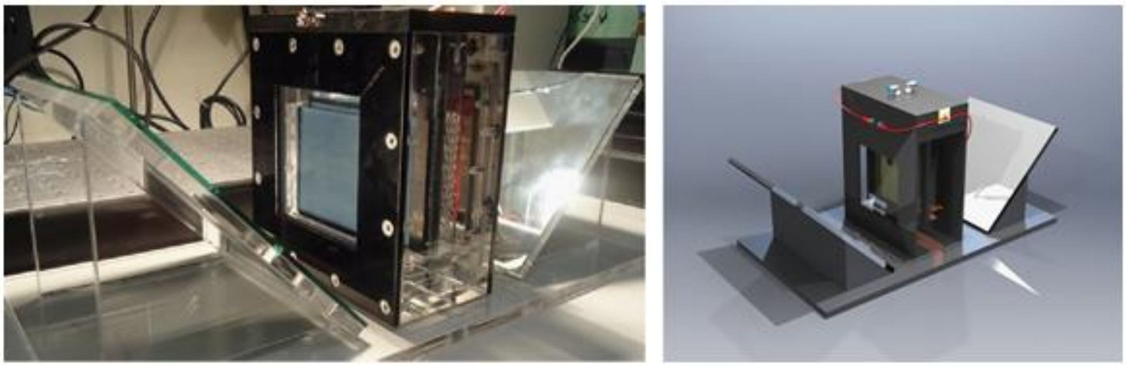

Figure 10.10: Photoelectrochemical cell with a mirror system to redirect the light beam (reproduced from [159])

The choice of $Na_2SO_4$ also has an impact onto the tandem cell performances, as this neutral electrolyte contains less reactive species than other electrolytes, $H_2SO_4$ for example. As seen before, bismuth compounds tend to degrade in acidic or neutral electrolytes [160], and even the $CuBi_2O_4$ produced is not completely stable in the proposed electrolyte. To solve this issue, protective layers can be added on the top of the photoelectrodes. Several materials have been tested as protective layers, with both $BiVO_4$ and $CuBi_2O_4$ [269, 270]. Interestingly, $TiO_2$, known as one of the most studied photocatalyst, appears to be a more interesting materials to be used as protective layers [271]. Other materials, such as $Al_2O_3$ or $SnO_2$ have also been tested [272, 273]. Those materials can be produced by reactive magnetron sputtering, which would then an interesting continuation of the work started in this thesis. Finally, additional elements could be added to the PEC tandem cell to improve its overall efficiency. A porous membrane (Nafion® or Teflon®) could be implemented to avoid the recombination of $H_2$ and $O_2$ gases produced, due to their tendency to recombine easily as mentioned in Chapter 2. The choice of membrane depends also on the electrolyte used, to avoid any degradation during the measurement [274]. As seen with the OCP measurements, the photovoltages produced by the photoelectrodes remains poor, not exceeding 0.25 V for the $BiVO_4$ photoanode. Then, the addition of a PV cell, to build a PV-PEC tandem cell, would provide additional photocurrent and photovoltage to enhance overall efficiency of the proposed PEC cell. PV-PEC tandem cell are usually considered as the upgraded version of the PEC tandem cell and are more and more investigated in the field of research [275-277].

## 10.6 Summary

In this chapter, the findings from the previous result chapters were used to perform first measurement of a PEC tandem cell composed of a $BiVO_4$ photoanode and a $CuBi_2O_4$ photocathode. Different techniques were used to determine the band gap and band edge positions of the photoelectrodes produced. XPS valence band combined with Tauc plot method exhibited similar results compared to Cyclic voltammetry, with valence band being more positive than the OER standard potential for the BiV photoanode (between 2.17 and 2.12 eV), whereas the conduction of the BiCu photocathode was found to be more negative than the HER standard potential (between -0.65 and -0.7 eV). Both photoelectrodes exhibited good photoelectrochemical properties in a single-photoelectrode configuration, with a photocurrent production of 3.22 $mA.cm^{-2}$ and -1.57 $mA.cm^{-2}$ for the BiV photoanode and BiCu photocathode, respectively. This association of $BiVO_4$ and $CuBi_2O_4$ has already been demonstrated several times and appears to be a serious alternative as a PEC tandem cell [259, 260].

However, when tested in a two-photoelectrodes configuration, the activity of the photoelectrodes decreases, with a low photocurrent and ABPE efficiency associated during photoelectrochemical tests. This lack of activity can be explained by several reasons, either by the photoelectrodes properties (poor charge transfer efficiencies measured in the previous chapters) or the configuration of the cell. Especially, an alternative to the current illumination system should be done to get an effective illumination of both photoelectrodes at the same time. The first upgrade that can be done is the addition of a proton exchange membrane between the photoanode and the photocathode. It would help to separate reactive species (especially the H+ ions that could migrate to the photocathode side) and would allow the use of two different electrolytes, one to provide the reactive species for the OER and one to provide the H+ ions for the HER. The separation in two different compartments would make the PEC tandem more suitable for potential upscaling for industrial applications, as the gases would produce in separated environments. The illumination of the photoelectrodes is also an issue, as with the current configuration, one acts as a light absorber to the other. The addition of a supplementary light or the implementation of reflective surfaces around the PEC cell would help a better illumination for the second photoelectrode. Finally, the measurements of the OCP showed that the photovoltage produced by the samples is too low to enable to run the PEC tandem cell without bias. Th addition of a PV cell to form a PV-PEC tandem cell appears to be an interesting upgrade for the proposed cell, as it can reach STH efficiencies close to the target for the commercial applications [277].

# IV. Synopsis

## 10. Conclusion and future work

*This chapter provides a summary of the main results presented in this thesis and discusses how the objectives laid out in the Introduction section (Chapter I) were achieved. In light of the presented findings, unexplored areas of interest for future research projects are suggested. The main findings and achievements of the project are summarized in Section 9.1. The issues that require additional work and directions of further research in this area are discussed in Section 9.2.*

### 10.1. Overall Conclusion

The aim of this thesis was to produce novel and efficient photocatalytic materials by magnetron sputtering used as photoelectrodes for the study of photoelectrochemical hydrogen production via solar activated water splitting. The first objective of this work was to produce an efficient $BiVO_4$ photoanode by magnetron co-sputtering in a reactive atmosphere. The study of the deposition parameters demonstrated the importance of the power applied on the Bi and V targets to ensure the production of monoclinic scheelite $BiVO_4$ films. By tuning the power ratio between Bi and V targets, it was possible to produce $BiVO_4$ coatings with a stoichiometry close to 1, resulting in the formation of m-s $BiVO_4$ without the presence of additional phases, such as $Bi_4V_2O_{11}$ or $V_2O_5$. Especially, the samples with the stoichiometry close to 1 demonstrated the best photocatalytic properties and photoelectrochemical performances regarding the oxygen evolution reaction, achieving a photocurrent of 1.95 $mA.cm^{-2}$ produced at 1.23 $V_{RHE}$ for the BiV800 sample. The second objective of this work was to produce a novel copper bismuth oxide ($CuBi_2O_4$) photocathode by reactive magnetron co-sputtering for the study of the hydrogen evolution reaction. As for the $BiVO_4$ photoanode, it was demonstrated that the power applied to the magnetron (Bi and Cu targets) was crucial to produce the tetragonal $CuBi_2O_4$ material, with a less important difference between the powers, due to the higher sputter yield of copper compared to vanadium. Stoichiometric samples, which did not present impurities such as $Bi_2O_3$ phase, exhibited the best photoelectrochemical performances, with a cathodic photocurrent of -1.13 mA.cm-2 produced at 0.3 $V_{RHE}$ for the BiCu150 sample. The understanding of the photoelectrodes performances was assessed by measuring different types of efficiencies related to the photocatalytic process. As no particular work was done to improve the surface of the photoelectrodes produced, both BiV photoanodes and BiCu photocathodes presented low charge transfer efficiencies, respectively 17.7% and 11.8% for the maximum $\eta_{transfer}$ measured. On the other hand, higher charge transport efficiencies were measured for the BiV800 photoanode and BiCu150 photocathode, with $\eta_{transport}$ measured of 59% and 35%, respectively. These behaviours were explained by the higher amount of oxygen vacancies measured in theses samples, favouring the separation of charge carriers within the bulk of the material and then improving the transport within the coatings. This high amount of oxygen vacancy was already reported for Bismuth based photocatalysts produced by reactive magnetron co-sputtering and it might then represent an interesting area of study in order to improve the efficiencies of Bismuth-based photoanodes deposited by sputtering []. Then, the thicknesses of the photoelectrodes were optimised by adjusting the deposition time, in order to improve the photoelectrochemical performances of the photocatalysts. It was shown that optimum thicknesses of around 200 nm allowed to improve the photocurrent production for both photoelectrodes, with maximum photocurrents recorded of -1.62 mA.cm-2 at 0.3 $V_{RHE}$ for the BiCu150 sample and 2.61 mA.cm-2 at 1.23 $V_{RHE}$ for the BiV800 sample. Finally, both photoanode and photocathode produced were tested for the in a PEC tandem cell for a first assessment of the photoelectrochemical properties of the proposed tandem cell. The electronic band diagrams were estimated for both materials, showing the good position of the valence band for the BiV photoanode (between 2.17 and 2.42 eV) and the good position for the conduction band of the BiCu photocathode (between -0.21 and -0.7 eV). Despite their efficient photocurrent production in a single photoelectrode configuration, when used at the same time, no photocurrent production was observed. The necessity of applied a potential and the lack of stability during CA measurements demonstrated the limitations of the proposed PEC cell and several upgrades were then proposed to enhance the PEC activity of the cell. This work demonstrated the importance of sputtering parameters on the production of bismuth-based photocatalyst by reactive magnetron sputtering. As bismuth possesses a high sputter yield compared to many metals, the sputtering parameters are of importance to ensure the formation of stoichiometric compounds and the production of efficient photocatalysts. This work shown the feasibility of producing bismuth-based photocatalyst by reactive magnetron co-sputtering to be used as photoelectrodes for hydrogen production via solar assisted water splitting. It was shown that both materials are produced with oxygen vacancies, defects known to enhance the photocatalytic power of semiconductors. Nonetheless, additional work is necessary to increase get most efficient materials for hydrogen production via solar activated water splitting.

## 10.2. Future work

Based on the findings of this thesis, the following suggestions are proposed for future research work.

**Additional characterisations for the proposed photoelectrodes**

Additional in-depths characterisations would allow a better understanding of the behaviour of the photoelectrodes produced. The roughness of the Bi-based coatings produced by pDC magnetorn sputtering could be determined in a systematic AFM study. This could add an additional explanation of the lack of efficiency, or the good efficiency of the samples studied. For the lifetime of the charge carriers produced within the Bi-based photoelectrodes, photoluminescence spectroscopy or time-resolved microwave conductivity measurements can be performed, allowing a proper quantification of the charge carriers lifetime. Mott-Schottky plots would be an additional method for the determination of electronic band diagram. Moreover, it would give information of the doping density $N_D$ and then would give information on the conductivity of the photoelectrodes. The different resistances involved in the PEC tandem cell could be determined using electrochemical impedance spectroscopy (EIS), to determine the Nyquist plots [280]. These measurements would provide information such as the flat-band potential, the resistances at the different interfaces or the charge-carrier density within the materials.

**Optimisation of the photoelectrode deposition process**

As reactive magnetron sputtering appears to be an appropriate process to produce efficient photoelectrodes, an optimisation of the deposition parameters could be done for each material to obtain the most efficient photocatalysts possible. Several parameters were not studied in this work, such as the influence of gas flows or the influence of electrical parameters (off-time, frequency of the power applied). Some parameters could directly influence the morphology or the crystallinity of the coating, such as the use of a substrate heater or the use of substrate bias, to provide more energy to the adatoms to form the crystalline films. As the crystallinity appears to be a crucial parameter for the activity of the Bi-based photoelectrodes produced, HiPIMS technique could be then employed in the continuation of the pDC magnetron sputtering process. It would allow to produce highly crystalline coatings without the necessity of an annealing step. Moreover, an understanding of the appearance of oxygen vacancies after annealing could allow a better control of these defects, to optimise their effect as electron traps.

### Improvements of the photoelectrodes

The photoelectrodes produced could still be improved to enhance their charge transfer efficiencies or their resistance to degradation in aqueous electrolyte. Protective layers could be deposited on top of each photoelectrodes, such as $TiO_2$, $Al_2O_3$ or ZnO. As shown in chapter 10, examples of MgO-passivated $CuBi_2O_4$ exhibited better stability in aqueous electrolytes and a better change transfer efficiency [294]. Heterojunctions could be produced by depositing an additional photocatalyst semiconductors on top of the $BiVO_4$ or $CuBi_2O_4$ layers. This could lead to an improvement of charge separation, leading to higher photocurrent production. Dopants can be implemented in the lattice to reduce the band gaps and enhance the photocatalytic activity of the photoelectrodes. Finally, the addition of co-catalyst at the surface of photoelectrodes could lead to higher charge transfer efficiencies such as Co-Pi, or noble metal nanoparticles to take advantage of the plasmonic effect, for example with Au or Ag nanoparticles [291 – 293].

### Upgrade of the PEC tandem cell

As seen in Chapter 10, the configuration used was appropriate for a single-photoelectrode cell, but the BiV/BiCu PEC tandem cell proposed was not the most optimal configuration. One of the main improvements that could be done would be the implementation of a Nafion proton exchange membrane. Several studies can be done, such as the influence of the thickness of the membrane on the PEC performances of the cell. An additional light source could be added to take advantage of the two quartz optical windows and to allow the illumination of both photoelectrodes from the back. However, to be able to compare the PEC measurements, the total illumination should correspond to the AM 1.5G standard. Then, a system of mirror could be experienced to reflect the light to the back of the BiCu photocathode. The physical separation of the photoelectrodes in two different vessels could help to enhance the production of $H_2$ and $O_2$ and would allow to test different electrolytes that would correspond better to the half-reactions of interest. Finally, the integration of a PV cell would enhance the photocurrent and photovoltage produced to form an efficient PV-PEC tandem water splitting cell.

# References

[1] United Nations Framework Convention on Climate Change (2024, Jan. 04), *The Paris Agreement*, https://unfccc.int/process-and-meetings/the-paris-agreement

[2] International Energy Agency (2024, Jan. 09), Global Energy Review: $CO_2$ Emissions in 2021, https://www.iea.org/reports/global-energy-review-co2-emissions-in-2021-2

[3] A. Hassan, S.Z. Ilyas, A. Jalil and Z. Ullah, ‘Monetization of the environmental damage caused by fossil fuels’, *Environmental Science and Pollution Research,* vol. 28, p. 21204 – 21211, Jan. 2021, doi: 10.1007/s11356-020-12205-w

[4] J. Jiang, L. Cao, X. Jin, Z. Yu, H. Zhang, J. Fu and G. Jiang, ‘Response of ocean acidification to atmospheric carbon dioxide removal’, *Journal of Environmental Sciences*, Volume 140, p. 79-90, June 2024, doi: 10.1016/j.jes.2023.04.029

[5] J.A. Duro, C. Lauk, T. Kastner, K. Erb and H. Haberl, ‘Global inequalities in food consumption, cropland demand and land-use efficiency: A decomposition analysis’, *Global Environmental Change*, vol. 64, p. 102124, Sept. 2020, doi: 10.1016/j.gloenvcha.2020.102124

[6] Our World in Data (2024, Jan. 09), *Energy Production and Consumption*, https://ourworldindata.org/energy-production-consumption

[7] U.S. Energy Information Administration (2024, Jan. 09), *International Energy Outlook 2021*, https://www.eia.gov/outlooks/ieo/consumption/sub-topic-03.php

[8] Our World in Data (2024, Jan. 09), *Fossil fuels*, https://ourworldindata.org/fossil-fuels

[9] A. Rahman, O. Farrok and MM. Haque, ‘Environmental impact of renewable energy source based electrical power plants: Solar, wind, hydroelectric, biomass, geothermal, tidal, ocean, and osmotic’, *Renewable and Sustainable Energy Reviews*, vol. 161, p. 112279, June 2022, doi: 10.1016/j.rser.2022.112279

[10] International Energy Agency (2024, Jan. 09), *Renewable electricity*, https://www.iea.org/reports/renewables-2022/renewable-electricity

[11] Hren R, Vujanovi´ c A, Van Fan Y, Kleme˘ s JJ, Krajnc D, ˘ Cu˘ cek L. ‘Hydrogen production, storage and transport for renewable energy and chemicals: An

environmental footprint assessment', *Renewable and Sustainable Energy Reviews,* vol. 173, p. 113113, Mar. 2023, doi: 10.1016/j.rser.2022.113113

[12] WHA International (2024, Jan. 09), *Top Industrial Uses of Hydrogen, and the Need for the Industrial Hydrogen Safety*, https://wha-international.com/hydrogen-in-industry

[13] M.A. Aminudin, S.K. Kamarudin, B.H. Lim, E.H. Majilan, M.S. Masdar and N.Shaari, 'An overview: Current progress on hydrogen fuel cell vehicles', *International Journal of Hydrogen Energy,* vol. 48, p. 4371 – 4388, doi: 10.1016/j.ijhydene.2022.10.156

[14] U.S. Department of Energy (2024, Jan. 09), Hydrogen Strategy Enabling A Low-Carbon Economy,https://www.energy.gov/sites/prod/files/2020/07/f76/USDOE_FE_Hydrogen _Strategy_Jul y2020.pdf

[15] A. Kusoglu, 'The many colours of hydrogen', *The Electrochemical Society Interface*, vol. 30, p. 30-44, 2021, doi: 10.1149/2.F12214IF

[16] A. Kusoglu, '(Re)Defining Clean Hydrogen: From Colors to Emissions', *The Electrochemical Society Interface* 2022, vol. 31, p. 31-47, 2022, doi: 10.1149/2.F08224IF

[17] B. Zainal, P. Ker, H. Mohamed, H. Ong, I.M.R. Fattah, S.M. Rahman, L. Nghiem and T.M. Mahlia, 'Recent advancement and assessment of green hydrogen production technologies', *Renewable and Sustainable Energy Reviews*, vol. 189, p. 113941, Jan. 2024, doi: 10.1016/j.rser.2023.113941

[18] J. Brauns and T. Turek, 'Alkaline Water Electrolysis Powered by Renewable Energy: A Review', *Processes*, vol. 8, p. 248, Feb. 2020, doi: 10.3390/pr8020248

[19] Ember (2024, Jan. 09), Yearly Electricity Data, https://ember-energy.org/data/yearly-electricity-data/

[20] Hannah Ritchie, Pablo Rosado and Max Roser (2020) - "Energy Production and Consumption" Published online at OurWorldInData.org. Retrieved from: 'https://ourworldindata.org/energy-production-consumption'

[21] R. de Levie, 'The electrolysis of water', *Journal of Electroanalytical Chemistry*, vol. 476, p. 92-93, Oct. 1999, doi: 10.1016/S0022-0728(99)00365-4.

[22] B. Parigrahy, K. Narayan and B. Rao, ‘Green hydrogen production by water electrolysis: A renewable energy perspective’, *Materials Today: Proceedings*, vol. 67, p. 1310-1314, 2022, doi: 10.1016/j.matpr.2022.09.254.

[23] J.E. Funk, ‘Thermochemical hydrogen production: past and present’, *International Journal of Hydrogen Energy*, vol. 26, p. 185-190, Mar. 2001, doi: 10.1016/S0360-3199(00)00062-8.

[24] J. Wang, X. Yue, Y. Yang, S. Sirisomboonchai, P. Wang, X. Ma, A. Abudula and G. Guan, ‘Earth-abundant transition-metal-based bifunctional catalysts for overall electrochemical water splitting: A review’, *Journal of Alloys and Compounds*, vol. 819, p. 153346, Apr.2020, doi: 10.1016/j.jallcom.2019.153346.

[25] S. Anantharaj and S. Noda, ‘Amorphous Catalysts and Electrochemical Water Splitting: An Untold Story of Harmony’, Small, vol. 16, p. 1905779, Jan. 2020, doi: 10.1002/smll.201905779

[26] N. A. Kelly, ‘Hydrogen production by water electrolysis’, in *Advances in Hydrogen Production, Storage and Distribution*, A. Basile and A. Iulianelli, Eds., Woodhead Publishing, 2014, pp. 159-185, doi: 10.1016/C2013-0-16359-3.

[27] S. S. Kumar and H. Lim, ‘An overview of water electrolysis technologies for green hydrogen production’, *Energy Reports*, vol. 8, p. 13793 – 13813, Nov. 2022, doi: 10.1016/j.egyr.2022.10.127.

[28] J. Wang, Y. Gao, H. Kong, J. Kim, S. Choi, F. Ciucci, Y. Hao, S. Yang, Z. Shao and J. Lim, ‘Non-precious-metal catalysts for alkaline water electrolysis: operando characterizations, theoretical calculations, and recent advances’, *Chemical Society Reviews*, vol. 49, p. 9154-9196, Nov. 2020, doi: 10.1039/D0CS00575D.

[29] S. S. Kumar and V. Himabindu, ‘Hydrogen production by PEM water electrolysis – A review’, *Materials Science for Energy Technologies*, vol. 2, p. 442 – 454, Dec. 2019, doi: 10.1016/j.mset.2019.03.002.

[30] A. Fujishima and K. Honda, ‘Electrochemical photolysis of water at a semiconductor electrode’, *Nature*, vol. 238, p.37 – 38, Jul. 1972, doi: 10.1038/238037a0.

[31] Z. Wei, J. Liu and W. Shangguan, ‘A review on photocatalysis in antibiotic wastewater: Pollutant degradation and hydrogen production’, *Chinese Journal of Catalysis*, vol. 41, p. 1440 – 1450, Oct. 2020, doi: 10.1016/S1872-2067(19)63448-0.

[32] G. Liu, T. Zhao, H. Fei, F. Li, W. Guo, Z. Yao and Z. Feng, ‘A review of various self-cleaning surfaces, durability and functional applications on building exteriors’, *Construction and Building Materials*, vol. 409, p. 134084, Dec. 2023, doi: 10.1016/j.conbuildmat.2023.134084.

[33] O. Baaloudj, I. Assadi, N. Nasrallah, A. El Jery, L. Khezami and A. A. Assadi, ‘Simultaneous removal of antibiotics and inactivation of antibiotic-resistance bacteria by photocatalysis: A review’, *Journal of Water Process Engineering*, vol. 42, p. 102089, Aug. 2021, doi: 10.1016/j.jwpe.2021.102089.

[34] X. Yang and D. Wang, ‘Photocatalysis: From Fundamental Principles to Materials and Applications’, *ACS Applied Energy Materials*, vol. 1, p. 6657 – 6693, Dec. 2018, doi: 10.1021/acsaem.8b01345.

[35] M. Wang, W. Zhen, B. Tian, J. Ma and G. Lu, ‘The inhibition of hydrogen and oxygen recombination reaction by halogen atom on overall water splitting over Pt-$TiO_2$ photocatalyst’, *Applied Catalysis B: Environment and Energy*, vol. 236, p. 240 – 252, Nov. 2018, doi: 10.1016/j.apcatb.2018.05.031.

[36] A. Kudo and Y. Miseki, ‘Heterogeneous photocatalyst materials for water splitting’, *Chemical Society Reviews*, vol. 38, p. 253 – 278, Nov. 2008, doi: 10.1039/b800489g.

[37] H. Wang, X. Li, X. Zhao, C. Li, X. Song, P. Zhang, P. Huo and X. Li, ‘A review on heterogeneous photocatalysis for environmental remediation: from semiconductors to modification strategies’, *Chinese Journal of Catalysis*, vol. 43, p. 178 – 214, Feb. 2022, doi: 10.1016/S1872-2067(21)63910-4.

[38] F. E. Osterloh, ‘Photocatalysis versus Photosynthesis: A Sensitivity Analysis of Devices for Solar Energy Conversion and Chemical Transformations’, *ACS Energy Letters*, vol. 2, p. 445−453, Jan. 2017, doi: 10.1021/acsenergylett.6b00665.

[39] R. Min, E. S. Aldeen, A. Alhebshi and M. Tahir, ‘Recent advancements in strategies to improve performance of tungsten-based semiconductors for photocatalytic hydrogen production: A review’, *Journal of Physics D: Applied Physics*, vol. 54, p. 503001, Sept. 2021, doi: 10.1088/1361-6463/ac21fc

[40] C. Jiang, S. Moniz, A. Wang, T. Zhang and J. Tang, “Photoelectrochemical devices for solar water splitting – materials and challenges”, Chemical Society Reviews, vol. 46, p. 4645-4660, Jun. 2017, doi: 10.1039/C6CS00306K.

[41] C. Ampelli, G. Centi, R. Passalacqua and S. Perathoner, ‘Synthesis of solar fuels by a novel photoelectrocatalytic approach’, *Energy & Environmental Science*, vol. 3, p. 292-301, Feb. 2010, doi: 10.1039/B925470F.

[42] B. Liu, S. Wang, G. Zhang, Z. Gong, B. Wu, T. Wang and J. Gong, ‘Tandem cells for unbiased photoelectrochemical water splitting’, Chemical Society Reviews, vol. 52, p. 4644-4671, Jun. 2023, doi: 10.1039/D3CS00145H.

[43] X. Shi, L. Cai, M. Ma, X. Zheng and J. Park, ‘General Characterization Methods for Photoelectrochemical Cells for Solar Water Splitting’, *ChemSusChem*, vol. 8, p. 3192 – 3203, Sep. 2015, doi: 10.1002/cssc.201500075.

[44] O. Zandi, B. Klahr and T. Hamann, “Highly photoactive Ti-doped α-$Fe_2O_3$ thin film electrodes: resurrection of the dead layer”, *Energy & Environmental Science*, vol. 6, p. 634 – 642. Dec. 2013, doi: 10.1039/C2EE23620F.

[45] Z. Chen, T. Jaramillo, T. Deutsch, A. Kleiman-Schwarsctein, A. Forman, N. Gaillard, R. Garland, K. Takanabe, C. Heske, M. Sunkara, E. McFarland, K. Domen, E. Miller, J. Turner and H. Dinh, ‘Accelerating materials development for photoelectrochemical hydrogen production: Standards for methods, definitions, and reporting protocols’, *Journal of Materials Research*, vol. 25, p. 3 – 16, Jan. 2010, doi: 10.1557/JMR.2010.0020.

[46] H. Yoneyama, H. Sakamoto and H. Tamura, ‘A photoelectrochemical cell with production of hydrogen and oxygen by a cell reaction’, *Electrochemica Acta*, vol. 20, p. 341 – 345, May 1975, doi: 10.1016/0013-4686(75)90016-X.

[47] J. H. Kim, D. Hansora, P. Sharma, J. Jang and J. S. Lee, ‘Toward practical solar hydrogen production – an artificial photosynthetic leaf-to-farm challenge’, *Chemical Society Reviews*, vol. 48, p. 1908-1971, Mar. 2019, doi: 10.1039/C8CS00699G.

[48] Li, M. Griep, Y. Choi and D. Chu, ‘Photoelectrochemical overall water splitting with textured $CuBi_2O_4$ as a photocathode”, *Chemical Communications*, vol. 54, p. 3331-3334, Feb. 2018, doi: 10.1039/C7CC09041B.

[49] C. Du, J. Yang, J. Yang, Y. Zhao, R. Chen and B. Shan, ‘An iron oxide - copper bismuth oxide photoelectrochemical cell for spontaneous water splitting’, *International Journal of Hydrogen Energy*, vol. 43, p. 22807 – 22814, Dec. 2018, doi: 10.1016/j.ijhydene.2018.10.170.

[50] J. Brillet, J. Yum, M. Cornuz, T. Hisatomi, R. Solarska, J. Augustynski, M. Graetzel and K. Sivula, ‘Highly efficient water splitting by a dual-absorber’, *Nature Photonics*, vol. 6, p. 824 – 828, Nov. 2012, doi: 10.1038/nphoton.2012.265.

[51] P. Dias, M. Schreier, S. Tilley, J. Luo, J. Azevedo, L. Andrade, D. Bi, A. Hagfeldt, A. Mendes, M. Grätzel and M. Mayer, ‘Transparent Cuprous Oxide Photocathode Enabling a Stacked Tandem Cell for Unbiased Water Splitting’, *Advanced Energy Materials*, vol. 5, p. 150537- 150546, Dec. 2015, doi: 10.1002/aenm.201501537.

[52] A.E. Delahoy, S.C. Gau, O.J. Murphy, M. Kapur and J.O’M. Bockris, ‘A one-unit photovoltaic electrolysis system based on a triple stack of amorphous silicon (pin) cells’, *International Journal of Hydrogen Energy*, vol. 10, p. 113-116, 1985, doi: 10.1016/0360-3199(85)90043-6.

[53] J. Wu, Y. Li, J. Kubota, K. Domen, M. Aagesen, T. Ward, A. Sanchez, R. Beanland, Y. Zhang, M. Tang, S. Hatch, A. Seeds and H. Liu, ‘Wafer-Scale Fabrication of Self-Catalyzed 1.7 eV GaAsP Core-Shell Nanowire Photocathode on Silicon Substrates, *Nano Letters*, vol. 14, p. 2013–2018, Apr. 2014, doi: 10.1021/nl500170m.

[54] J. W. Jang, C. Du, Y. Ye, Y. Lin, X. Yao, J. Thorne, E. Liu, G. McMahon, J. Zhu, A. Javey, J. Guo and D. Wang, ‘Enabling unassisted solar water splitting by iron oxide and silicon’, *Nature Communications*, vol. 6, p. 7447-7452, Jun. 2015, doi: 10.1038/ncomms8447.

[55] E. L. Miller, D. Paluselli, B. Marsen and R. E. Rocheleau, ‘Development of reactively sputtered metal oxide films for hydrogen-producing hybrid multijunction photoelectrodes’, Solar Energy Materials and Solar Cells, vol. 88, p. 131–144, Jul. 2005, doi: 10.1016/j.solmat.2004.07.058

[56] W.-H. Cheng, M. H. Richter, M. M. May, J. Ohlmann, D. Lackner, F. Dimroth, T. Hannappel, H. A. Atwater and H.-J. Lewerenz, ‘Monolithic Photoelectrochemical Device for Direct Water Splitting with 19% Efficiency’, *ACS Energy Letters*, vol. 3, p. 1781-2020, Aug. 2018, doi: 10.1021/acsenergylett.8b00920.

[57] S. Y. Reece, J. A. Hamel, K. Sung, T. D. Jarvi, A. J. Esswein, J. Pijpers and D. G. Nocera, ‘Wireless Solar Water Splitting Using Silicon-Based Semiconductors and Earth-Abundant Catalysts’, *SCIENCE,* vol. 334, p. 645-648, Sep. 2011, doi: 10.1126/science.1209816.

[58] J. Long, M. Xiao, X. Huang, Z. Xing, X. Li, P. Dai, M. Tan, Y. Wu, M. Song and S. Lu, ‘High efficiency thin film GaInP/GaAs/InGaAs inverted metamorphic (IMM) solar cells based on electroplating process’, *Journal of Crystal Growth*, vol. 513, p. 38-42, May 2019, doi: 10.1016/j.jcrysgro.2019.02.057.

[59] S. A. Holgate, *Understanding Solid State Physics*, CRC Press, 2021, pp. 177–178, doi: 10.1201/9780429288234.

[60] A. Kahn, ‘Fermi level, work function and vacuum level’, *Materials Horizons*, vol. 3, p. 7-10, Oct. 2016, doi: 10.1039/C5MH00160A.

[61] A. M. Smith and S. Nie, ‘Semiconductor Nanocrystals: Structure, Properties, and Band Gap Engineering’, *Accounts of Chemical Research*, vol. 43, p. 190 – 200, Oct. 2009, doi: 10.1021/ar9001069.

[62] A. W. Bott, “Electrochemistry of Semiconductors”, Current Separations, vol. 17, 1998, p. 87 – 91.

[63] W. Schmickler and E. Santos, ‘The semiconductor-electrolyte interface’, in *Interfacial Electrochemistry*, Springer Berlin Heidelberg, 2010, pp. 117 – 131, doi: 10.1007/978-3-642-04937-8_11.

[64] Y. Zhao, L. Bouffier, G. Xu, G. Loget, and N. Sojic, ‘Electrochemiluminescence with semiconductor (nano)materials’, *Chemical Science*, vol. 13, p. 2528 – 2550, Jan. 2022, doi: 10.1039/D1SC06987J.

[65] M. T. Mayer, ‘Photovoltage at semiconductor-electrolyte junctions’, Current Opinion in Electrochemistry, vol. 2, Issue 1, April 2017, p. 104-110.

[66] T. F. Kuech, ‘III-V compound semiconductors: Growth and structures’, *Progress in Crystal Growth and Characterization of Materials*, vol. 62, p. 352 – 370, Jun. 2016, doi: 10.1016/j.pcrysgrow.2016.04.019.

[67] M. Afzaal and P. O'Brien, 'Recent developments in II-VI and III-VI semiconductors and their applications in solar cells', *Journal of Materials Chemistry*, vol. 16, p. 1597 – 1602, Nov. 2005, doi: 10.1039/B512182E.

[68] Q. Huang, Z. Ye and X. Xiao, 'Recent progress in photocathodes for hydrogen evolution', Journal of Materials Chemistry A, vol. 3, p. 15824-15837, Jun. 2015, doi: 10.1039/C5TA03594E.

[69] J. Sun, L. Gao, and Q. Zhang, 'Synthesizing and Comparing the Photocatalytic Properties of High Surface Area Rutile and Anatase Titania Nanoparticles', *Journal of the American Ceramic Society*, vol. 86, p. 1677–1682, Oct. 2003, doi: 10.1111/j.1151-2916.2003.tb03539.x.

[70] Y. Du, X. Ai, Z. Li, T. Sun, Y. Huang, X. Zeng, X. Chen, F. Rao and F. Wang, 'Visible-to-Ultraviolet Light Conversion: Materials and Applications', *Advanced Photonics Research*, vol. 2, p. 2000213-2000233, Jun. 2021, doi: 10.1002/adpr.202000213.

[71] T. Imrich, H. Krysova, M. Neumann-Spallart and J. Krysa, '$Fe_2O_3$ photoanodes: Photocorrosion protection by thin $SnO_2$ and $TiO_2$ films', *Journal of Electroanalytical Chemistry*, vol. 892, p. 115282, Jul. 2021, doi: 10.1016/j.jelechem.2021.115282.

[72] C. Y. Toe, J. Scott, R. Amal and Y. H. Ng, 'Recent advances in suppressing the photocorrosion of cuprous oxide for photocatalytic and photoelectrochemical energy conversion', *Journal of Photochemistry and Photobiology C: Photochemistry Reviews*, vol. 40, p. 191 – 211, Sep. 2019, doi: 10.1016/j.jphotochemrev.2018.10.001.

[73] D. K. Sharma, S. Shukla, K. K. Sharma and V. Kumar, 'A review on ZnO: Fundamental properties and applications', *Materials Today: Proceedings*, vol. 49, p.3028 – 3035, 2022, doi: 10.1016/j.matpr.2020.10.238.

[74] Y. Yao, D. Sang, L. Zou, Q. Wang and C. Liu, 'A Review on the Properties and Applications of $WO_3$ Nanostructure-Based Optical and Electronic Devices', *Nanomaterials*, vol. 11, p. 2136, Aug. 2021, doi: 10.3390/nano11082136.

[75] K. Bouras, J.L. Rehspringer, G. Schmerber, H. Rinnert, S. Colis, G. Ferblantier, M. Balestrieri, D. Ihiawakrim, A. Dinia and A. Slaoui, 'Optical and structural properties of Nd doped $SnO_-$ powder fabricated by the sol–gel method', *Journal of Materials Chemistry C*, vol. 2, p. 8235–8243, Aug. 2014, doi: 10.1039/C4TC01202J.

[76] M.F. Al-Kuhaili, M. Saleem and S.M.A. Durrani, ‘Optical properties of iron oxide (α-$Fe_2O_3$) thin films deposited by the reactive evaporation of iron’, *Journal of Aloys and Compounds*, vol. 521, p. 178 – 182, Apr. 2012, doi: 10.1016/j.jallcom.2012.01.115.

[77] M. Mallik, S. Monia, M. Gupta, A. Ghosh, M. P. Toppo and H. Roy, ‘Synthesis and characterization of $Cu_2O$ nanoparticles’, *Journal of Alloys and Compounds*, vol. 829, p. 154623 – 154629, Jul. 2020, doi: 10.1016/j.jallcom.2020.154623.

[78] L. Xu, G. Zheng, S. Pei and J. Wang, ‘Investigation of optical bandgap variation and photoluminescence behaviour in nanocrystalline CuO thin films’, *Optik*, vol. 158, p. 382 – 390, Apr. 2018, doi: 10.1016/j.ijleo.2017.12.138.

[79] R. Wang and J. Wu, ‘Structure and Basic Properties of Ternary Metal Oxides and Their Prospects for Application in Supercapacitors’, in *Metal Oxides in Supercapacitors*, D.P. Dubal and P. Gomez-Romero, Eds., Elsevier, 2017, pp. 99-132, doi: 10.1016/B978-0-12-810464-4.00005-X.

[80] M. I. Diez-Garcia and R. Gomez, ‘Progress in Ternary Metal Oxides as Photocathodes for Water Splitting Cells: Optimization Strategies’, *Solar RRL*, vol. 6, p. 2100871-2100295, Apr. 2022, doi: 10.1002/solr.202100871.

[81] H. He, A. Liao, W. Guo, W. Luo, Y. Zhou and Z. Zou, ‘State-of-the-art progress in the use of ternary metal oxides as photoelectrode materials for water splitting and organic synthesis’, *Nanotoday*, vol. 28, p. 100763, Oct. 2019, doi: 10.1016/j.nantod.2019.100763.

[82] A. H. Zahid and Q. Han, “A review on the preparation, microstructure, and photocatalytic performance of $Bi_2O_3$ in polymorphs”, *Nanoscale*, vol. 42, p. 17687-17724, Aug. 2021, doi: 10.1039/D1NR03187B.

[83] S. Kamimura, M. Higashi, R. Abe and T. Ohno, ‘Fabrication of a porous $ZnRh_2O_4$ photocathode for photoelectrochemical water splitting under visible light irradiation and a significant effect of surface modification by ZnO necking treatment’, *Journal of Materials Chemistry A*, vol. 4, p. 6116-6123, Mar. 2016, doi: 10.1039/C6TA01567K.

[84] S. Ida, K. Yamada, T. Matsunaga, H. Hagiwara, Y. Matsumoto and T. Ishihara, ‘Preparation of p-type $CaFe_2O_4$ Photocathodes for Producing Hydrogen from Water’, *Journal of the American Chemical Society*, vol. 132, p. 17343 – 17345, Dec. 2015, doi: 10.1021/ja106930f.

[85] S.Maitra, S. Pal, T. Maitra, S. Halder and S. Roy, ‘Solvothermal Etching-Assisted Phase and Morphology Tailoring in Highly Porous $CuFe_2O_4$ Nanoflake Photocathodes for Solar Water’, *Energy Fuels*, vol. 35, p. 14087 – 14100, Sep. 2021, doi: 10.1021/acs.energyfuels.1c02090.

[86] C.G. Read, Y. Park and K. Choi, ‘Electrochemical synthesis of p-type $CuFeO_2$ electrodes for use in a photoelectrochemical cell’, The Journal of Physical Chemistry Letters, vol. 19, p. 1872 – 1878, Jul. 2012, doi: 10.1021/jz300709t.

[87] A.Diaz-Garcia, T. Lana-Villareal and R. Gomez, ‘Sol-gel copper chromium delafossite thin films as stable oxide photocathodes for water splitting’, *Journal of Materials Chemistry A*, vol. 3, p. 19683-19687, Sep. 2015, doi: 10.1039/C5TA05227K.

[88] J. Gu, Y. Yan, J. W. Krizan, Q. D. Gibson, Z. M. Detweiler, R. J. Cava and A. B. Bocarsly, ‘p-type $CuRhO_2$ as a self-healing photoelectrode for water reduction under visible light’, Journal of the American Chemical Society, vol 136, p. 821-833, Jan. 2014, doi: 10.1021/ja408876k.

[89] U. A. Joshi, A. Palasyuk, D. Arney and P. A. Maggard, ‘Semiconducting Oxides to Facilitate the Conversion of Solar Energy to Chemical Fuels’, The Journal of Physical Letters, vol. 1, p. 2719 – 2726, Sep. 2010, doi: 10.1021/jz100961d.

[90] S. Gu, X. Zhou, F. Zheng, L. Fang, W. Dong and M. Shen, ‘Improved photocathodic performance in Pt catalysed ferroelectric $BiFeO_3$ films sandwiched by a porous carbon layer’, *Chemical Communications*, vol. 53, p. 7052-7055, Jun. 2017, doi: 10.1039/C7CC03222F.

[91] M. Diez-Garcia and R. Gomez, ‘Metal Doping to Enhance the Photoelectrochemical Behaviour of $LaFeO_3$ Photocathodes’, *ChemSusChem*, vol. 10, p. 2457 – 2463, Jun. 2017, doi: 10.1002/cssc.201700166.

[92] T. Kim and K. Choi, ‘Nanoporous $BiVO_4$ Photoanodes with Dual-Layer Oxygen Evolution Catalysts for Solar Water Splitting’, *Science*, vol. 343, p. 990 – 994, Feb. 2014, doi: 10.1126/science.1246913.

[93] J. Song, M. Seo, T. Lee, Y. Jo et al., ‘Tailoring Crystallographic Orientations to Substantially Enhance Charge Separation Efficiency in Anisotropic $BiVO_4$ Photoanodes’, ACS Catalysis, vol. 8, p. 5952 – 5962, Jul. 2018, doi: 10.1021/acscatal.8b00877.

[94] G. Zhuang, Y. Chen, Z. Zhuang, Y. Yu and J. Yu, ‘Oxygen vacancies in metal oxides: recent progress towards advances catalyst design’, *Science China Materials*, vol. 63, p. 2089 – 2118, May 2020, doi: 10.1007/s40843-020-1305-6.

[95] F. C. Tompkins, ‘Superficial Chemistry and Solid Imperfections’, *Nature*, vol. 186, p. 3 – 6, 1960, doi: 10.1038/186003a0.

[96] J. Wu, X. Li, W. Shi P. Ling et al., ‘Efficient visible light drive $CO_2$ reduction mediated by defect engineered BiOBr atomic layers’, Angewandte Chemie International Edition, vol. 57, p. 8719-8723, Jul. 2018, doi: 10.1002/anie.201803514.

[97] X. Sun, J. Wu, Q. Li, Q. Liu, Y. Qi, L. You, Z. Ji, P. He, P. Sheng, J. Ren, W. Zhang, J. Lu and J. Zhang, ‘Fabrication of $BiOIO_3$ with induced oxygen vacancies for efficient separation of the electron-hole pairs’, vol. 218, p. 80-90, Dec. 2017, doi: 10.1016/j.apcatb.2017.06.041.

[98] J. Gan, X. Lu, J. Wu, S. Xie, T. Zhai, M. Yu, Z. Zhang, Y. Mao, S. Wang, Y. Shen and Y. Tong, ‘Oxygen vacancies promoting photoelectrochemical performance of $In_2O_3$ nanocubes’, *Scientific Reports*, vol. 3, p. 1 – 7, Jan. 2013, doi: 10.1038/srep01021.

[99] HY. Xu, YH. Huang, S. Liu, K.W. Xu, F. Ma and P.K. Chu, ‘Effects of annealing ambient on oxygen vacancies and phase transition temperature of $VO_2$ thin films’, *RSC Advances*, vol. 6, p. 79383 – 79388, Aug. 2016, doi: 10.1039/C6RA13189A.

[100] L. Hou, M. Zhang, Z. Guan, Q. Li and J. Yang, ‘Effect of annealing ambience on the formation of surface/bulk oxygen vacancies in $TiO_2$ for photocatalytic hydrogen evolution’, Applied Surface Science, vol. 428, p. 640 – 647, Jan. 2018, doi: 10.1016/j.apsusc.2017.09.144.

[101] Q. Liang, Y. Guo, N. Zhang, Q. Qian, Y. Hu, J. Hu, Z. Li and Z. Zou, ‘Improved water-splitting performances of $CuW_{1-x}Mo_xO_4$ photoanodes synthesized by spray pyrolysis’, *Science China Materials*, vol. 61, p. 1297 – 1304, May 2018, doi: 10.1007/s40843-018-9287-5.

[102] P. Schlexer, D. Widmann, RJ. Behm et G. Pacchioni, ‘CO oxidation on a Au/$TiO_2$ nanoparticle catalyst via the Au-assisted Mars–van Krevelen mechanism’’ ACS Catalysis, vol. 8, p. 6513 – 6525, Jun. 2018, doi: 10.1021/acscatal.8b01751.

[103] L. Ma, S. Chen, Z. Pei, H. Li, Z. Wang, Z. Liu, Z. Tang, J. Zapien and C. Zhi, ‘Flexible waterproof rechargeable hybrid zinc batteries initiated by multifunctional oxygen vacancies rich cobalt oxide’, *ACS Nano*, 1vol. 2, p. 8597 – 8605, Aug. 2018, doi: 10.1021/acsnano.8b04317.

[104] A. Deml, V. Stavanovic, C. L. Muhich, C. B. Musgrave and R. O’Hayre, ‘Oxide enthalpy of formation and band gap energy as accurate descriptors of oxygen vacancy formation energetics’, *Energy & Environmental Science*, vol. 6, p. 1996 – 2004, Mar. 2014, doi: 10.1039/C3EE43874K.

[105] K. Ye, K. Li, Y. Lu, Z. Guo, N. Ni, H. Liu, Y. Huang, H. Ji and P. Wang, ‘An overview of advanced methods for the characterization of oxygen vacancies in materials’ *TrAc Trends in Analytical Chemistry*, vol. 116, p. 102 – 108, Jul. 2019, doi: 10.1016/j.trac.2019.05.002.

[106] H. Idriss, ‘On the wrong assignment of the XPS O1s signal at 531-532 eV attributed to oxygen vacancies in photo- and electro-catalysts for water splitting and other materials applications’, *Surface Science*, vol. 712, p. 121894, Oct. 2021, doi: 10.1016/j.susc.2021.121894.

[107] S. Nasir, N. Mohamed, M. Tukimon, M. Noh, N. Arzaee and M. Teridi, ‘Direct extrapolation techniques on the energy band diagram of $BiVO_4$ thin films’, *Physica B: Condensed Matter*, vol. 604, p. 412719, Mar. 2021, doi: 10.1016/j.physb.2020.412719.

[108] R. Asahi, T. Morikawa, T. Ohwaki, K. Aoki and Y. Taga, ‘Visible-Light Photocatalysis in Nitrogen-Doped Titanium Oxides’, *Science*,vol. 293, p. 269 – 271, Jul. 2001, doi: 10.1126/science.1061051.

[109] J. Wang, T. Hasegawa, Y. Asakura and S. Yin, ‘Recent Advances in Ternary Metal Oxides Modified by N Atom Photocatalysis’, *Catalysts*, vol. 12, p. 1568 – 1587, Dec. 2022, doi: 10.3390/catal12121568.

[110] M. T. Naing, J. B. Hwang, J. Lee, Y. Kim, Y. Jung and S. Lee, ‘Synergistic effect of Co doping and borate impregnation on $BiVO_4$ photoanode for efficient photoelectrochemical water splitting’, *International Journal of Hydrogen Energy*, vol. 55, p. 234 – 242, Feb. 2024, doi: 10.1016/j.ijhydene.2023.11.155.

[111] S. Bakhtiarna, S. Sheibani, A. Nadi, E. Aubry, H. Sun, P. Briois and M. Yazdi, 'Preparation of sputter-deposited Cu-doped $BiVO_4$ nanoporous thin films comprised of amorphous/crystalline heterostructure as enhanced visible-light photocatalyst' *Applied Surface Science*, vol. 608p. 155248, Jan. 2023, doi: 10.1016/j.apsusc.2022.155248.

[112] J. Liu, N. Ma, W. Wu and Q. He, 'Recent progress on photocatalytic heterostructures with full solar spectral responses', *Chemical Engineering Journal*, vol. 393, p. 124719, Aug. 2020, doi: 10.1016/j.cej.2020.124719.

[113] K. Yin, Z. Yan, N. Fang, W. Yu, Y. Chu, S. Shu and M. Xu, 'The synergistic effect of surface vacancies and heterojunctions for efficient photocatalysis: A review', *Separation and Purification Technology*, vol. 325, p. 124636, Nov. 2023, doi: 10.1016/j.seppur.2023.124636.

[114] D. Onwudiwe, O. Olatunde, V. Nkme, O. Oyewo, A. Muliwa, H. Ferjani and T. Yousef, 'Synthesis of p-n GCN/$CuBi_2O_4$ heterostructures for enhanced visible light photocatalysis', *Inorganic Chemistry Communications*, vol. 162, p. 112193, Apr. 2024, doi: 10.1016/j.inoche.2024.112193.

[115] Y. Liu, G. Li, R. Mi, C. Deng and P. Gao, 'An environment-benign method for the synthesis of p-NiO/n-ZnO heterostructure with excellent performance for gas sensing and photocatalysis', *Sensors and Actuators B: Chemical*, vol. 191, p. 537-544, Feb. 2014, doi: 10.1016/j.snb.2013.10.068.

[116] C. Zhou, S. Wang, Z. Zhao, Z. Shi, S. Yan and Z. Zou, 'A facet-dependent Schottky junction electron shuttle in a $BiVO_4${010}–Au–$Cu_2O$ Z-scheme photocatalyst for efficient charge separation', *Advanced Functional Materials*, vol. 28, p. 1801214, Aug. 2018, doi: 10.1002/adfm.201801214.

[117] K. Iwashina, A. Iwase, Y.H. Ng, R. Amal and A. Kudo, 'Z-schematic water splitting into $H_2$ and $O_2$ using metal sulfide as a hydrogen-evolving photocatalyst and reduced graphene oxide as a solid-state electron mediator', *Journal of the American Chemical Society*, vol. 137, p. 604–607, Jan. 2015, doi: 10.1021/ja511615s.

[118] P. Wei, Y. Wen, K. Lin and X. Li, ‘2D/3D $WO_3/BiVO_4$ heterostructures for efficient photoelectrocatalytic water splitting’, *International Journal of Hydrogen Energy*, vol. 46, p. 27506 – 27515, Aug. 2021, doi: 10.1016/j.ijhydene.2021.06.007.

[119] Q. Zhang, B. Zhai, Z. Lin, X. Zhao and P. Diao, ‘$CuO/CuBi_2O_4$ bilayered heterojunction as an efficient photocathode for photoelectrochemical hydrogen evolution reaction’, *International Journal of Hydrogen Energy*, vol. 46, p. 11607 – 11620, Mar. 2021, doi: 10.1016/j.ijhydene.2021.01.050.

[120] W. Mbiombi, B. Mathe, D. Wamwangi, R. Erasmus, A. Every and D. G. Billing, ‘Optoelectronic and mechanical properties of PVD diamond-like carbon films’, *Materials Today: Proceedings*, vol. 5, p. 27307-27315, 2018, doi: 10.1016/j.matpr.2018.08.156.

[121] P. Zamani, Z. Valefi and K. Jafarzadeh, ‘Comprehensive study on corrosion protection properties of $Al_2O_3$, $Cr_2O_3$ and $Al_2O_3$-$Cr_2O_3$ ceramic coatings deposited by plasma spraying on carbon steel’, *Ceramic International*, vol. 48, p. 1574-1588, Jan. 2022, doi: 10.1016/j.ceramint.2021.09.237.

[122] V.O. Smilyk, S.S. Fomanyuk, G.Ya. Kolbasov, I.A. Rusetskyi and V.S. Vorobets, ‘Electrodeposition, optical and photoelectrochemical properties of $BiVO_4$ and $BiVO_4/WO_3$ films’, *Research on Chemical Intermediates*, vol. 45, p. 4149-4161, Jun. 2019, doi: 10.1007/s11164-019-03897-y.

[123] S. Hernandez, G. Gerardi, K. Bejtka, A. Fina and N. Russo, ‘Evaluation of the charge transfer kinetics of spin-coated $BiVO_4$ thin films for sun-driven water photoelectrolysis’, *Applied Catalysis B: Environmental*, vol. 190, p. 66-74, Aug. 2016, doi: 10.1016/j.apcatb.2016.02.059.

[124] S. Obregon, A. Caballero and G. Colon, ‘Hydrothermal synthesis of $BiVO_4$: Structural and morphological influence on the photocatalytic activity’, *Applied Catalysis B: Environmental*, , vol. 117-1178, p. 59-66, May 2012, doi: 10.1016/j.apcatb.2011.12.037.

[125] N.Y. Abu-Thabit and A.S.H. Makhlouf, ‘Chapter 1 - Fundamental of smart coatings and thin films: synthesis, deposition methods, and industrial applications’, in *Advances in Smart Coatings and Thin Films for Future Industrial and Biomedical Engineering Applications*, N.Y. Abu-Thabit and A.S.H. Makhlouf, Eds. Elsevier, 2020, pp. 3-35, doi: 10.1016/B978-0-12-849870-5.00001-X.

[126] D. M. Mattox, ‘Physical vapor deposition (PVD) processes’, *Metal Finishing*, vol. 99, p. 409-423, Jan. 2001, doi: 10.1016/S0026-0576(02)82043-8.

[127] H. Angus Macleod, ‘Chapter 1 – Recent developments in deposition techniques for optical thin films and coatings’, in *Optical Thin films and Coatings (Second Edition)*, Angela PiegarI and Francois Flory, Eds. Woodhead Publishing, 2018, pp. 3-23, doi: 10.1016/B978-0-08-102073-9.00001-1.

[128] D. H. Hoffman, B. Singh and J. H. Thomas ‘Chapter 1.1 – Vacuum Nomenclature and Definitions’, in *Handbook of Vacuum Science and Technology*, D. H. Hoffman, B. Singh and J. H. Thomas, Eds. Elsevier, 1998, pp. 3-7.

[129] Charles A. Bishop, ‘Pumping’, in *Vacuum Deposition onto Webs, Films, and Foils*, Charles A. Bishop Eds., William Andrew Publishing, 2011, pp. 63-80.

[130] N. Yoshimura, ‘Vacuum Pumps’, in *Vacuum Technology*, Springer Berlin, Heidelberg, 2008, pp. 35-76.

[131] D. R. Poirier and G. H. Geiger, ‘Flow and Vacuum Production’, in *Transport Phenomena in Materials Processing*, Springer, Cham, 2016, p. 145-183.

[132] S. G. Walton and J. E. Greene, ‘Chapter 2 - Plasma in deposition processes’, in *Handbook of Deposition Technologies for Films and Coatings*, P. M. Martin, Eds., William Andrew Publishing, 2010, pp. 32-92, doi: 10.1016/B978-0-8155-2031-3.00002-8.

[133] J. E. Harry, ‘1.1 Plasma, an Overview’, in *Introduction to Plasma Technology: Science, Engineering and Applications*, J.E. Harry, Eds., 2010, pp. 1-13, doi: 10.1002/9783527632169.ch1.

[134] M. Keidar and I. I. Beilis, ‘Chapter 1 - Plasma concepts’, in *Plasma Engineering*, M. Keidar and I. I. Beilis, Eds., Academic Press, 2013, pp. 1 – 81, doi: 10.1016/B978-0-12-385977-8.00001-9.

[135] W. R. Grove, ‘On the electro-chemical polarity of gases’, *Philosophical Transactions of the Royal Society of London*, vol. 142, p. 87-101, 1852, https://www.jstor.org/stable/108536

[136] H. Adachi and K. Wasa, ‘1 - Thin Films and Nanomaterials’, in *Handbook of Sputtering Technology (Second Edition),* K. Wasa, I. Kanno, and H. Kotera, Eds. Oxford: William Andrew Publishing, 2012, pp. 3–39, doi: 10.1016/B978-1-4377-3483-6.00001-2.

[137] A. W. Hull, ‘The Effect of a uniform magnetic field on the motion of electrons between coaxial cylinders’, *Physical Review*, vol. 18, 1921, doi: 10.1103/PhysRev.18.31.

[138] S. M. Rossnagel, ‘Magnetron sputtering’, *Journal of Vacuum Science & Technology A*, vol. 38, p. 060805, Dec. 2020, doi: 10.1116/6.0000594.

[139] P.J. Kelly and R.D. Arnell, ‘Magnetron sputtering: a review of recent developments and applications’, *Vacuum*, vol. 56, p. 159-172, Mar. 2000, doi: 10.1016/S0042-207X(99)00189-X.

[140] N. Savvides and B. Window, ‘Unbalanced magnetron ion-assisted deposition and property modification of thin films’, *Journal of Vacuum Science & Technology A*, vol. 4, p. 504-508, May 1986, doi: 10.1116/1.573869.

[141] P.J. Kelly and R.D. Arnell, ‘Recent advances in magnetron sputtering’, *Surface and Coatings Technology*, vol. 112, p. 170-176, Feb. 1999, doi: 10.1016/S0257-8972(98)00749-X.

[142] A. H. Simon, ‘Chapter 4 – Sputter Processing’, in *Handbook of Thin Film Deposition*, K. Seshan, Eds., William Andrew Publishing, 2012, pp. 55-88, doi: 10.1016/B978-1-4377-7873-1.00004-8.

[143] A. Belkind A. Freilich, J. Lopez, Z. Zhao, W. Zhu and K. Becker, ‘Characterization of pulsed DC magnetron sputtering plasmas’, New Journal of Physics, vol. 7, Jan 2005, doi: 10.1088/1367-2630/7/1/090.

[144] J.E. Greene, ‘Chapter 12 - Thin film nucleation, growth, and microstructural evolution: an atomic scale view’, in *Handbook of Deposition Technologies for Films and Coatings*, P.M. Martin, Eds., William Andrew Publishing, 2010, pp. 554 – 620, doi: 10.1016/B978-0-8155-2031-3.00012-0.

[145] L. Aissani, A. Alhussein, A.W. Zia, G. Mamba and S. Rtimi, ‘Magnetron sputtering of transition metal nitride thin films for environmental remediation’, *Coatings*, vol. 12, p. 1746-1775, Nov. 2022, doi: 10.3390/coatings12111746.

[146] N. Kaiser, ‘Review of the fundamentals of thin-film growth’, *Appl Opt.*, vol. 41, p. 3053-3060, Jun. 2002, doi: 10.1364/ao.41.003053.

[147] B. A. Movchan and A. V. Demchishin, ‘STRUCTURE AND PROPERTIES OF THICK CONDENSATES OF NICKEL, TITANIUM, TUNGSTEN, ALUMINUM OXIDES, AND ZIRCONIUM DIOXIDE IN VACUUM.’, *Fiz. Metal. Metalloved.*, vol. 28, p. 653-60, Jan. 1969, [Online]. Available: https://www.osti.gov/biblio/4181669 (Accessed Jun. 02, 2023)

[148] A. Kameneva, ‘Evolution of the film structure in the various evaporation processes’, *Research Journal of Pharmaceutical, Biological and Chemical Sciences*, vol. 6, p. 951-960, Sep. 2015.

[149] J. A. Thornton, ‘Influence of apparatus geometry and deposition conditions on the structure and topography of thick sputtered coatings’, *Journal of Vacuum Science & Technology*, vol. 11, p. 666-670, 1974, doi: 10.1116/1.1312732.

[150] J. A. Thornton, ‘High-rate thick film growth’, *Annual Review of Materials Science*, vol. 7, p. 239–260, Aug. 1977, doi: 10.1146/annurev.ms.07.080177.001323.

[151] P.J. Kelly and R.D. Arnell, ‘Characterization studies of the structure of Al, Zr, and W coatings deposited by closed-field unbalanced magnetron sputtering’, *Surface and Coatings Technology*, vol. 97, , p. 595-602, Dec. 1997, doi: 10.1016/S0257-8972(97)00328-9.

[152] P.J. Kelly and R.D. Arnell, ‘Development of a novel structure zone model relating to the closed field unbalanced magnetron sputtering system’, Journal of Vacuum Science & Technology A, vol. 16, p. 2858 – 2869, Sep. 1998, doi: 10.1116/1.581432.

[153] J.Epp, ‘4 – X-Ray diffraction (XRD) techniques for materials characterization’, in *Materials Characterization Using Non-Destructive (NDE) Methods*, G. Hübschen, I. Altpeter, R. Tschuncky and H-G. Herrman, Eds. Woodhead Publishing, 2016, pp. 81-124, doi: 10.1016/B978-0-08-100040-3.00004-3

[154] Peter J. Larkin, ‘Chapter 2 – Basic Principles’, in *Infrared and Raman Spectroscopy (Second Edition),* P.J. Larkin, Ed. Elsevier, 2018, pp. 7 – 28, doi: 10.1016/B978-0-12-804162-8.00002

[155] M. Pereira-da-Silva and F. A. Ferri, ‘1 – Scanning Electron Microscopy’, in *Nanocharacterization Techniques*, A.L. da Roz, M. Ferreira, F. Leite and O.N. Oliveira Jr., Eds. William Andrew, 2017, pp. 1 – 35, doi: 10.1016/B978-0-323-49778-7.00001-1.

[156] C. Y. Tang and Z. Yang, ‘Chapter 8 – Transmission Electron Microscopy (TEM)’, in *Membrane Characterization*, N. Hilal, A.F. Ismail, T. Matsuura, D. Oatley Radcliffe, 2017, pp. 145 – 159, doi: 10.1016/B978-0-444-63776-5.00008-5.

[157] D. Johnson, N. Hilal and W.R. Bowen, ‘Basic Principles of Atomic Force Microscopy’, in *Atomic Force Microscopy in Process Engineering*, Elsevier Ltd., 2009, pp. 1 – 30, doi: 10.1016/B978-1-85617-517-3.00001-8.

[158] P. de Groot, ‘Principles of interference microscopy for the measurement of surface topography’, *Advances in Optics and Photonics*, vol. 7, p.1 – 65, 2015, doi: 10.1364/AOP.7.000001.

[159] H. Bluhm, ‘4 – X-Ray photoelectron spectroscopy (XPS) for *in situ* characterization of thin film growth’, in *In Situ Characterization of Thin Film Growth*, G. Koster and G. Rijnders, Eds. Woodhead Publishing, 2011, pp. 75 – 98, doi: 10.1533/9780857094957.2.75

[160] C. De Caro and C. Haller, “UV/VIS Spectrophotometry – Fundamentals and Applications”, 2015

[161] J. Tauc, ‘Optical properties and electronic structure of amorphous Ge and Si’, *Materials Research Bulletin,* vol. 3, p. 37 – 46, Jan. 1968, doi: 10.1016/0025-5408(68)90023-8.

[162] P.M. Rao, L. Cai, C. Liu, I.S. Cho, C.H. Lee, J.M. Weisse, P. Yang and X. Zheng, ‘Simultaneously Efficient Light Absorption and Charge Separation in $WO_3$/$BiVO_4$ Core/Shell Nanowire Photoanode for Photoelectrochemical Water Oxidation’, *Nano Letters*, vol. 14, p. 1099-1105, Jan. 2014, doi: 10.1021/nl500022z

[163] T. Lopes, P. Dias, L. Andrade and A. Mendes, ‘An innovative photoelectrochemical lab device for solar water splitting’, *Solar Energy Materials and Solar Cells*, vol.128, p. 399 – 410, Sep. 2014, doi: 10.1016/j.solmat.2014.05.051.

[164] X. Yao, X. Zhao, J. Hu, H. Xie, D. Wang, X. Cao, Z. Zhang, Y. Huang, Z. Chen and T. Sritharan, ‘The Self-Passivation Mechanism in Degradation of $BiVO_4$ Photoanode’, *iScience*, vol. 19, p. 976-985, Sep 2019, doi: 10.1016/j.isci.2019.08.037.

[165] X. Shi, L. Cai, M. Ma, X. Zheng and J.H. Park, ‘General Characterization Methods for Photoelectrochemical Cells for Solar Water Splitting’, *ChemSusChem*, vol. 8, p. 3192 – 3203, Sep. 2015, doi: 10.1002/cssc.201500075.

[166] https://www.astm.org/g0173-03r20.html (consulted on the 01/11/2023)

[167] Y. Qiu, W. Liu, W. Chen, G. Zhou, P-C. Hsu, R. Zhang, Z. Liang, S. Fan, Y. Zhang and Y. Cui, ‘Efficient solar-drive water splitting by nanocone $BiVO_4$-perovskite tandem cells’, *ScienceAdvances,* vol. 2, p. , Jun. 2016, doi: 10.1126/sciadv.1501764.

[168] R.P. Wijesundera, ‘Fabrication of the CuO/Cu2O heterojunction using an electrodeposition technique for solar cell applications’, Semiconductor Science and Technology, vol. 25, 2010, doi: 10.1088/0268-1242/25/4/045015.

[169] J. Park, J. Lee, H. Lee, H. Im, S. Moon, C. Jeong, W. Yang and J. Moor, ‘Hybrid Perovskite-Based Wireles Integrated Device Exceeding a Solar to Hydrogen Conversion Efficiency of 11%’, *Small,* vol. 19, p. 2300147-2300185, Jul. 2023, doi: 10.1002/smll.202300174.

[170] G. Liu, F. Zheng, J. Li, G. Zeng, Y. Ye, D.M. Larson, J. Yano, E.J. Crumlin, J.W. Ager, L. Wang and F.M. Toma, ‘Investigation and mitigation of degradation mechanisms in $Cu_2O$ photoelectrodes for $CO_2$ reduction to ethylene’, *Nature Energy*, vol. 6, p. 1124 – 1132, Nov. 2021, doi: 10.1038/s41560-021-00927-1.

[171] X. Shi, I.Y. Choi, K. Zhang, J. Kwon, D. Y. Kim, J. K. Lee, S. H. Oh, J. K. Kim and J. H. Park, ‘Efficient photoelectrochemical hydrogen production from bismuth vanadate – decorated tungsten trioxide helix nanostructured’, *Nature Communications*, vol. 5, p. 4775, Sep. 2014, doi: 10.1038/ncomms5775.

[172] K. T. Fontaine, H. J. Lewerenz and H.A. Atwater, ‘Efficiency limits for photoelectrochemical water-splitting’, Nature Communications, vol.7, p. 13706, Dec. 2016, doi: 10.1038/ncomms13706.

[173] S. Limwichean, N. Kasayapanand, C. Ponchio, H. Nakajima, V. Patthanasettakul, P. Eiamchai, G. Meng and M. Horprathum, ‘Morphology-controlled fabrication of nanostructured $WO_3$ thin films by magnetron sputtering with glancing angle deposition for enhanced efficiency photo-electrochemical water splitting’, *Ceramics international*, vol. 47, p. 34455-34462, Dec. 2021, doi: 10.1016/j.ceramint.2021.08.359.

[174] M. M, Y. Huang, J. Liu, K. Liu, Z. Wang, C. Zhao, S. Qu and Z. Wang, ‘Engineering the photoelectrochemical behaviours of ZnO for efficient solar water splitting’, *Journal of Semiconductors*, vol. 41, 2020, doi: 10.1088/1674-4926/41/9/091702.

[175] P. Sharma, J-W. Jang and J.S. Lee, ‘Key Strategies to Advance the Photoelectrochemical Water Splitting Performance of $\alpha$-$Fe_2O_3$ Photoanode’, *ChemCatChem*, vol. 11, p. 157-179, Jan. 2019, doi: 10.1002/cctc.201801187.

[176] S. Bhat and H. W. Jang, ‘Recent Advances in Bismuth-Based Nanomaterials for Photoelectrochemical Water Splitting’, *ChemSusChem*, vol. 10,p. 3001 – 3018, Jun 2017, doi: 10.1002/cssc.201700633.

[177] A. Kudo, K. Ueda, H. Kato and I. Mikami, ‘Photocatalytic $O_2$ evolution under visible light irradiation on $BiVO_4$ in aqueous $AgNO_3$ solution’, *Catalysis Letters*, vol. 53, p. 229-230, Aug. 1998, doi: 10.1023/A:1019034728816.

[178] S. Lotfi, M. El Ouardi, H. Ait Ahsaine and A. Assani, ‘Recent progress on the synthesis, morphology and photocatalytic dye degradation of $BiVO_4$ photocatalysts: A review’, *Catalysis Reviews,* vol. 66, Apr. 2022, doi: 10.1080/01614940.2022.2057044.

[179] M. Rodrigues, K. Borges, A. Tello, R. Roca, R. Gonçalves, A. da Silva, E. Longo and M. Godinho, ‘Effect of pH on the synthesis of $BiVO_4$ to improve photocatalysis and antimicrobial properties’, *Materials Chemistry and Physics*, vol. 296, p. 127198, Feb. 2023, doi: 10.1016/j.matchemphys.2022.127198.

[180] Y. Park, K. Mcdonald, and K-S. Choi, ‘Progress in bismuth vanadate photoanodes for use in solar water oxidation’, Chemical Society Reviews, vol. 42, p. 2321-2337, Feb. 2013, doi: 10.1039/c2cs35260e.

[181] H. Shi, H. Guo, S. Wang, G. Zhang, Y. Hu, W. Jiang and G. Liu, ‘Visible Light Photoanode Material for Photoelectrochemical Water Splitting: A Review of Bismuth Vanadate’, *Energy Fuels*, vol. 36, p. 11404-11427, Apr. 2022, doi: 10.1021/acs.energyfuels.2c00994.

[182] B. Kalanoor, H. Seo and S.S. Kalanur, ‘Recent developments in photoelectrochemical water-splitting using $WO_3$/$BiVO_4$ heterojunction photoanode: A review’, *Materials Science for Energy Technologies*, vol. 1, p. 49-62, Jun. 2018, 10.1016/j.mset.2018.03.004

[183] Y. Gao, W. Fan, K. Qu, F. Wang, P. Guan, D. Xu, H. Bai and W. Shi, ‘Confined growth of Co-Pi co-catalyst by organic semiconductor polymer for boosting the photoelectrochemical performance of $BiVO_4$’, New Journal of Chemistry, vol. 43, p. 8160-8167, Apr. 219, doi: 10.1039/C9NJ01336A.

[184] S. Wang, T. He, P. Chen, A. Du, K. Ostrikov, W. Huang and L. Wang, ‘In Situ Formation of Oxygen Vacancies Achieving Near-Complete Charge Separation in Planar $BiVO_4$ Photoanodes’, *Advanced Materials*, vol. 32, p. 2001385, Jul. 2020, doi: 10.1002/adma.202001385.

[185] J.P. Deebasre, V. Maheskumar and B. Vidhya, ‘Investigation of the visible light photocatalytic activity of $BiVO_4$ prepared by sol gel method assisted by ultrasonication’, *Ultrasonics Sonochemistry*, vol. 45, p. 123-132, Jul. 2018, doi: 10.1016/j.ultsonch.2018.02.002

[186] K. Tolod, S. Hernandez, M. Castellino, F. Deorsola, E. Davarpanah and N. Russo, ‘Optimization of $BiVO_4$ photoelectrodes made by electrodeposition for sun-driven water

oxidation', *International Journal of Hydrogen Energy*, vol. 45, p. 605-618, Jan. 2020, doi: 10.1016/j.ijhydene.2019.10.236.

[187] N. Yang, S. Zhang, Y. Xiao, Y. Qi, Y. Bao, P. Xu, S. Jin and F. Zhang, 'Insight into the key restriction of $BiVO_4$ photoanodes prepared by pyrolysis method for scalable preparation', *Angewandte Chemie International Edition*, vol. 62, 2023, doi: 10.1002/anie.202308729

[188] R. Venkatesan, S. Velumani, K. Ordon, M. Makowska-Janusik, G. Corbel and A. Kassiba, 'Nanostructured bismuth vanadate ($BiVO_4$) thin films for efficient visible light photocatalysis', *Materials Chemistry and Physics*, vol. 205, p. 325-333, Feb. 2018, doi: 10.1016/j.matchemphys.2017.11.004.

[189] S. Thalluri, R. Rojas, O. Rivera, S. Hernandez, N. Russo and S. Rodil, 'Chemically induced porosity on $BiVO_4$ films produced by double magnetron sputtering to enhance the photo-electrochemical response', Physical Chemistry Chemical Physics, vol. 17, p.17821, Jun. 2015, doi: 10.1039/C5CP01561H.

[190] S. Bakhtiarnia, S. Sheibani, A. Billard, E. Aubry and M. Yazdi, 'Deposition of nanoporous $BiVO_4$ thin-films photocatalyst by reactive magnetron sputtering: Effect of total pressure and substrate', *Transactions of Nonferrous Metals Society of China*, vol. 32, p. 957-971, Mar. 2022, doi: 10.1016/S1003-6326(22)65846-1.

[191] R. Schelfhout, K. Strijckmans and D. Depla, 'Sputter yield measurements to evaluate the target state during reactive magnetron sputtering', *Surface & Coatings Technology*, vol. 399, p. 126097, Oct. 2020, doi: 10.1016/j.surfcoat.2020.126097.

[192] Y. Kshetri, B. Chaudhary, T. Kamiyama, T-H. Kim, F. Rosei and S.W. Lee, 'Determination of ferroelastic phase transition temperature in $BiVO_4$ by Raman spectroscopy,'*Materials Letters*, vol. 291, p. 129519, May 2021, doi: 10.1016/j.matlet.2021.129519

[193] S. Kumar, P.D. Sahare, 'Photocatalytic activity of bismuth vanadate for the degradation of organic compounds', *NANO: Brief Reports and Reviews,* vol. 8, p. 1350007, 2013, doi: 10.1142/S1793292013500070.

[194] H. Gong, N. Freudenberg, M. Nie, R. van de Krol and K. Ellmer, '$BiVO_4$ photoanodes for water splitting with high injection efficiency, deposited by reactive magnetron co-sputtering', *AIP Advances*, vol. 6, p. 045108, Apr. 2016, doi: 10.1063/1.4947121.

[195] R. Baddour-Hadjean, M.B. Smirnov, K.S. Smirnov, V. Kazimirov, J.M. Gallardo-Amores, U. Amador, M.E. Arroyo-de Dompablo and J.P. Pereira-Ramos, 'Lattice Dynamics of $\beta$-$V_2O_5$: Raman Spectroscopic Insight into the Atomistic Structure of a High-Pressure Vanadium Pentoxide Polymorph', *Inorganic Chemistry*, vol. 51, p. 2719-3342, Mar. 2012, doi: 10.1021/ic202651b.

[196] S. Tokunaga, H. Kato and A. Kudo, 'Selective Preparation of Monoclinic and Tetragonal $BiVO_4$ with Scheelite Structure and Their Photocatalytic Properties', *Chemistry of Materials*, vol. 13, p. 4624-4628, Dec. 2001, doi: 10.1021/cm0103390.

[197] V.V. Kharton, F.M.B. Marques and A. Atkinson, ‘Transport properties of solid oxide electrolyte ceramics: a brief review’, *Solid State Ionics*, vol. 174, p. 135 – 149, Oct. 2004, doi: 10.1016/j.ssi.2004.06.015.

[198] X. He, C. Zhang and D. Tian, ‘The Structure, Vibrational Spectra, and Thermal Expansion Study of $AVO_4$ (A = Bi, Fe, Cr) and $Co_2V_2O_7$’, *Materials*, vol. 13, p. 1628 – 1636, Apr. 2020, doi: 10.3390/ma13071628.

[199] L. Shi, S. Zhuo, M. Abulikemu, G. Mettela, T. Palaniselvam, S. Rasul, B. Tang, B. Yan, N. B. Saleh and P. Wang, ‘Annealing temperature effects on photoelectrochemical performance of bismuth vanadate thin film photoelectrodes’, RSC Advances, vol. 8, p. 29179 – 29188, Aug. 2018, doi: 10.1039/C8RA04887H.

[200] G. Singh, M. Kumar and R. Vaish, ‘Promising multicatalytic and adsorption capabilities in $V_2O_5/BiVO_4$ composite pellets for water-cleaning application’, *Surfaces and Interfaces*, vol. 23, p. 100924 – 100934, Apr. 2021, doi: 10.1016/j.surfin.2021.100924.

[201] L. Guan, J. Fan, Y. Zhang, Y. Guo, H. Duan, Y. Chen, H. Li and H. Liu, ‘Facile preparation of highly cost-effective $BaSO_4$@$BiVO_4$ core-shell structured brilliant yellow pigment’, *Dyes and Pigments*, vol. 128, p. 49-53, May 2016, doi: 10.1016/j.dyepig.2016.01.013.

[202] A. Walsh, Y. Yan, M. Huda, M. Al-Jassim and S-H. Wei, ‘Band Edge Electronic Structure of $BiVO_4$: Elucidating the Role of the Bi s and V d Orbitals’, *Chemistry Materials*, vol. 21, p. 547-551, 2009, doi: 10.1021/cm802894z.

[203] S.Sarkar and K.K. Chattopadhyay, ‘Size-dependent optical and dielectric properties of $BiVO_4$ nanocrystals’, *Physica E: Low-dimensional Systems and Nanostructures,* vol. 44, p. 1742-1746, Apr. 2012, doi: 10.1016/j.physe.2011.11.019.

[204] J.K. Cooper, S. Gul, F.M. Toma, Y-S. Liu, J. Guo, J.W. Ager, J. Yano and I.D. Sharp, ‘Indirect Bandgap and Optical Properties of Monoclinic Bismuth Vanadate’, *The Journal of Physical Chemistry C*, vol. 119, p. 2925-3446, Feb. 2015, doi: 10.1021/jp512169w.

[205] Y. Yuan, Y. Huang, F. Ma, Z. Zhang, X. Wei and G. Zhu, ‘Structural stability, band structure and optical properties of different $BiVO_4$ phases under pressure’, *Journal of Materials Science*, vol. 51, p. 6662 – 6673, Apr. 2016, doi: 10.1007/s10853-016-9951-2.

[206] J. Witkor, I. Reshetnyak, F. Ambrosio and A. Pasquarello, ‘Comprehensive modelling of the band gap and absorption spectrum of $BiVO_4$’, *Physical Review Materials*, vol. 1, Jul. 2017, doi: 10.1103/PhysRevMaterials.1.022401.

[206] W. Qiu, Y. Zhang, Y. Liu and X. Yin, ‘Creation of oxygen vacancies to activate 2D $BiVO_4$ photoanode by photoassisted self-reduction for enhanced solar-driven water splitting’,

*Electrochemica Acta*, vol. 399, p. 139428, Dec 2021, doi: 10.1016/j.electacta.2021.139428.

[207] H. Q. Alijani, S. Iravani and R. S. Varma, 'Bismuth Vanadate ($BiVO_4$) Nanostructures: Eco-Friendly Synthesis and Their Photocatalytic Applications', vol. 13, p. 59, 2023, doi: 10.3390/catal13010059.

[208] X. Yin, W. Qiu, W. Li, C. Li, K. Wang, X. Yang, L. Du, Y. Liu and J. Li, 'High porosity Mo-doped $BiVO_4$ film by vanadium re-substitution for efficient photoelectrochemical water splitting', *Chemical Engineering Journal,* vol. 389, p. 124365, Jun. 2020, doi: 10.1016/j.cej.2020.124365.

[209] S. Ju, J. Jun, S. Son, J. Park, H. Lim, W. Kim, D. Chae and H. Lee, 'Structured $BiVO_4$ photoanode Fabricated via Sputtering for Large Areas and Enhanced Photoelectrochemical Performance', *ACS Sustainable Chemistry & Engineering*, vol. 8, p. 17923 – 17932, Dec. 2020, doi: 10.1021/acssuschemeng.0c05225.

[210] D. Zhong, S. Choi and D. Gamelin, 'Near-Complete Suppression of Surface Recombination in Solar Photoelectrolysis by "Co-Pi" Catalyst-Modified W:$BiVO_4$', *Journal of the American Chemical Society*, vol. 133, p. 18370 – 18377, Sep. 2011, doi: 10.1021/ja207348x.

[211] L. Chen, E. Alarcon-Llado, M. Hettick, I. D. Sharp, Y. Lin, A. Javey and J. W. Ager, 'Reactive Sputtering of Bismuth Vanadate Photoanodes for Solar Water Splitting', *The Journal of Physical Chemistry C*, vol. 117, p. 21635 – 21642, Sep. 2013, doi: 10.1021/jp406019r.

[212] Y. Ma, C.A. Mesa, E. Pastor, A. Kafizas, L. Francas, F. Le Formal, S.R. Pendlebury and J.R. Durrant, 'Rate Law Analysis of Water Oxidation and Hole Scavenging on a $BiVO_4$ Photoanode', *ACS Energy Letters*, vol. 1, p. 618-623, Aug. 23, doi: 10.1021/acsenergylett.6b00263.

[213] J. Su, X-X. Zou, G-D. Li, X. Wei, C. Yan, Y-N. Wang, J. Zhao, L-J. Zhou and J-S. Chen, 'Macroporous $V_2O_5$-$BiVO_4$ Composites: Effect of Heterojunction on the Behavior of Photogenerated Charges', *The Journal of Physical Chemistry C*, vol. 115, p. 8064-8071, Apr. 2011, doi: 10.1021/jp200274k.

[214] J. Li, L. Guo, N. Lei, Q. Song and Z. Liang, 'Metallic Bi Nanocrystal-Modified Defective $BiVO_4$ Photoanodes with Exposed (040) Facets for Photoelectrochemical Water Splitting', *ChemElectroChem,* vol. 4, p. 2722-3026, Nov. 2017, doi: 10.1002/celc.201700680.

[215] Y. Lu, Y. Yang, X. Fan, Y. Li, D. Zhou, B. Cai, L. Wang, K. Fan and K. Zhang, 'Boosting Charge Transport in $BiVO_4$ Photoanode for Solar Water Oxidation', Advanced Materials, vol. 32, Feb. 2022, doi: 10.1002/adma.202108178.

[216] B. Liu, X. Wang, Y. Zhang, L. Xu, T. Wang, X. Xiao, S. Wang, L. Wang and W. Huang, 'A $BiVO_4$ Photoanode with a $VO_x$ Layer Bearing Oxygen Vacancies Offers Improved

Charge Transfer and Oxygen Evolution Kinetics in Photoelectrochemical Water Splitting', *Angewandte Chemie*, vol. 135, Mar. 2023, doi: 10.1002/ange.202217346.

[217] F.F. Abdi, T.J. Savenije, M.M. May, B. Dam and R. van de Krol, 'The Origin of Slow Carrier Transport in $BiVO_4$ Thin Film Photoanodes: A Time-Resolved Microwave Conductivity Study', *The Journal of Physical Chemistry Letters*, vol.4, p. 2599-2788, Aug. 2013, doi: 10.1021/jz4013257.

[218] I. Lorenzo, E. Gonzaga, and C. C. Mercado, 'Copper ternary oxides as photocathodes for solar-driven $CO_2$ reduction', *Reviews on Advanced Materials Science*, vol. 61, p. 430 – 457, Jul. 2022, doi: 10.1515/rams-2022-0043.

[219] Q. Zhang, K. Zhang, D. Xu, G. Yang, H. Huang, F. Nie, C. Liu and S. Yang, 'CuO nanostructures: Synthesis, characterization, growth mechanisms, fundamental properties, and applications', *Progress in Materials Science*, vol. 60, p. 208 – 337, Mar. 2014, doi: 10.1016/j.pmatsci.2013.09.003.

[220] R. Wick and S.D. Tilley, 'Photovoltaic and Photoelectrochemical Solar Energy Conversion with $Cu_2O$', *The Journal of Physical Chemistry C*, vol. 119, p. 26243 - 26257, Nov. 2015, doi: 10.1021/acs.jpcc.5b08397.

[221] C. Li, J. He, Y. Xiao, Y. Li and J.J. Delaunay, 'Earth-abundant Cu-based metal oxide photocathodes for photoelectrochemical water', *Energy Environmental & Science*, vol. 13, p. 3269 – 3306, Sep. 2020, doi: 10.1039/D0EE02397C.

[222] T. Arai, Y. Konishi, Y. Iwasaki, H. Sugihara and K. Sayama, 'High-throughput screening using porous photoelectrode for the development of visible-light-responsive semiconductors', *Journal of Combinatorial Chemistry*, vol. 9, p. 574-584, Jul. 2007, doi: https://doi.org/10.1021/cc0700142

[223] Z. Zhang, S. Hao, X. Duan, T. Wang, H. Li, G. Fan, Y. Zhao and J. Li, 'Photocatalytic activity of $CuBi_2O_4/WO_3$ p-n heterojunction photocatalysts in benzyl alcohol oxidation to benzaldehyde', *Journal of Alloys and Compounds*, vol. 968, p. 172209, Dec. 2023, doi: 10.1016/j.jallcom.2023.172209.

[224] M. Sun, B. Liu, W. Han, Z. Zhang and M. Xie, '$CuBi_2O_4$ photocathode with integrated electric field for enhanced H2O2 production', *Applied Catalysis B: Environmental*, vol. 304, p. 120980, May 2022, doi: 10.1016/j.apcatb.2021.120980.

[225] L. S. Ribeiro, I. M. Pinatti, J. A. Torres, A. S. Giroto, F. Lesse, E. Longo, C. Ribeiro and A. E. Nogueira, 'Rapid microwave-assisted hydrothermal synthesis of $CuBi_2O_4$ and its application for the artificial photosynthesis', *Materials Letters*, vol. 275, p. 128165, Sep. 2020, doi: 10.1016/j.matlet.2020.128165.

[226] J. Cooper, Z. Zhang, S. Roychoudhury, C. Jiang, S. Gul, Y. Liu, R. Dhall, A. Ceballos, J. Yano, D. Prendergast and S. Reyes-Lillo, '$CuBi_2O_4$: Electronic Structure, Optical Properties, and Photoelectrochemical Performance Limitations of the Photocathodes', *Chemistry of Materials*, vol. 33, p. 934 – 945, Feb. 2021, doi: 10.1021/acs.chemmater.0c03930.

[227] S. Berglund, F. Abdi, P. Bogdanoff, A. Chemseddine, D. Friedrich and R. van de Krol, ‘Comprehensive Evaluation of $CuBi_2O_4$ as a photocathode material for photoelectrochemical water splitting’, *Chemistry of Materials*, vol. 28, p. 4231 – 4242, Jun. 2016, doi: 10.1021/acs.chemmater.6b00830.

[228] S. Pulipaka, N. Boni, G. Ummethala and P. Meduri, ‘CuO/$CuBi_2O_4$ heterojunction photocathode: high stability and current densities for solar water splitting’, *Journal of Catalysis*, vol. 387, p. 17 – 27, Jul. 2020, doi: 10.1016/j.jcat.2020.04.001.

[229] S. Liu, J. Zhou, Y. Lu and J. Su, ‘Pulsed laser/electrodeposited $CuBi_2O_4$/$BiVO_4$ p-n heterojunction for solar water splitting’, *Solar Energy Materials and Solar Cells*, vol. 180, p. 123 – 129, Jun. 2018, doi: 10.1016/j.solmat.2018.02.031.

[230] L. Qu, R. Tan, A. Sivanantham, M. Kang, Y. Jeong, D. Seo, S. Kim and I. Cho, ‘Point-defect engineering of nanoporous $CuBi_2O_4$ photocathode via rapid thermal processing for enhanced photoelectrochemical activity’, *Journal of Energy Chemistry*, vol. 71, p. 201 – 209, 2022, doi:.1016/j.jechem.2022.03.013.

[231] L. Zhu, P. Basnet, S. Larson, L. Jones, J. Howe, R. Tripp and Y. Zhao, ‘Visible light-induced photoelectrochemical and antimicrobial properties of hierarchical $CuBi_2O_4$ by facile hydrothermal synthesis’, *Chemistry Select*, vol. 1, p. 1518 – 1524, Jun. 2016, doi: 10.1002/slct.201600164.

[232] B. Duployer, C. Tenailleau, Y. Thimont, P. Lenormand, A. Barnabé and L. Presmanes, ‘Preparation and study of $CuBi_2O_4$ thin films by RF magnetron sputtering’, *Materials Research Bulletin*, vol. 130, p. 110940, Oct. 2020, doi: 10.1016/j.materresbull.2020.110940.

[233] M.P. Seah, C.A. Clifford, F.M. Green and I.S. Gilmore, ‘An accurate semi-empirical equation for sputtering yields I: for argon ions’, Surface and Interface Analysis, vol. 37, p. 444-458, May 2005, doi: 10.1002/sia.2032.

[234] Z.V. Popovic, G. Kliche, M. Cardona and R. Liu, ‘Vibrational properties for $Bi_2CuO_4$’, *Physical review. B, Condensed matter*, vol. 41, p.3824-3828, Mar. 1990, doi: 10.1103/PhysRevB.41.3824

[235] C. Ho, C. Chan, Y. Huang, L. Tien and L. Chao, ‘The study of optical band edge property of bismuth oxide nanowires α-$Bi_2O_3$’, *Optics Express*, vol. 21, p. 11965 – 11972, 2013, doi: 10.1364/OE.21.011965

[236] Y. Deng, A. Handoko, Y. Du, S. Xi and B. Yeo, ‘In Situ Raman Spectroscopy of Copper and Copper Oxide Surface during Electrochemical Evolution Reaction: Identification of $Cu^{III}$ Oxides as Catalytically Active Species’, *ACS Catalysis*, vol. 6, p. 2473 – 2481, doi: 10.1021/acscatal.6b00205

[237] P. Li, G. Yuan, Z. Lu, Q. Li and Q. Wu, ‘Network Structures and Thermal Characteristics of $Bi_2O_3$-$SiO_2$-$B_2O_3$ Glass Powder by Sol-Gel’, in *Physics and Techniques of Ceramic and Polymeric Materials*, Y. Han, Eds. Springer, 2019, doi: 10.1007/978-981-13-5947-7_24

[238] A.I. Kyndyuk, G.S. Petrov, L.A. Bashkirov, A.I. Akimov and A.F. Poluyan, 'Thermal Stability and Phase Transformations in $CuBi_2O_4$', Russian Journal of Inorganic Chemistry, vol. 44, p. 1-4, 1999, doi: 10.1002/chin.199927026.

[239] R. Gottesman, A. Song, I. Levine, M. Krause, A. T. M. Islam, D. Abou-Ras, T. Dittrich, R. van de Krol and A. Chemseddine, 'Pure $CuBi_2O_4$ Photoelectrodes with Increased Stability by Rapid Thermal Processing of $Bi_2O_3$/CuO Grown by Pulsed Laser Deposition', *Advanced Functional Materials*, vol. 30, p. 1910832, May 2020, doi: 10.1002/adfm.201910832.

[240] A. A. Al-Ghamdi, M.H. Khedr, M. S. Ansari, P.M.Z. Hasan, M. Sh. Abdel-Wahad and A.A. Farghali, 'RF sputtered CuO thin films: Structural, Optical and photo-catalytic behavior', *Physica E: Low-dimensional Systems and Nanostructures*, vol. 81, p. 83-90, Jul. 2016, doi: 10.1016/j.physe.2016.03.004.

[241] W. Peng, Y. Zhou, J. Li, Y. Liu, J. Zhang, G. Xiang, X. Zhu, R. Li, H. Wang and Y. Zhao, 'Annealing temperature induced physical characteristics of CuO films grown by magnetron sputtering', *Materials Science in Semiconductor Processing*, vol. 131, p. 105883, Aug. 2021, doi: 10.1016/j.mssp.2021.105883.

[242] Y. Wang, J. Hu, S. Liu, D. Zhu, Z. Li and A. Song, 'Influence of grain size on photoelectrocatalytic performance of $CuBi_2O_4$ photocathodes', *International Journal of Hydrogen Energy*, vol. 47, p. 37774-37782, Nov. 2022, doi: 10.1016/j.ijhydene.2022.08.270.

[243] N. Hahn, V. Holmberg, B. Korgel and C. Mullins, 'Electrochemical Synthesis and Characterization of p-$CuBi_2O_4$ thin film photocathodes', *The Journal of Physical Chemistry C*, vol. 116, p. 6459 – 6466, Mar. 2012, doi: 10.1021/jp210130v.

[244] G. Sharma, Z. Zhao, P. Sarker, B.A. Nail, J. Wang, M.N. Huda and F.E. Osterloh, 'Electronic structure, photovoltage, and photocatalytic hydrogen evolution with p-$CuBi_2O_4$ nanocrystals', *Journal of Materials Chemistry A*, vol. 4, p. 2936-2942, Dec. 2015, doi: 10.1039/C5TA07040F.

[245] Y. Choi, K.D. Yang, D-H. Kim, K.T. Nam and S-H. Hong, 'p-type $CuBi_2O_4$ thin films prepared by flux-mediated one-pot solution process with improved structural and photoelectrochemical characteristics', *Materials Letters*, vol. 188, p. 192-196, Feb. 2017, doi: 10.1016/j.matlet.2016.10.124.

[246] D. Roy, G.F. Samu, M.K. Hossain, C. Janaky and K. Rajeshwar, 'On the measured optical bandgap values of inorganic oxide semiconductors for solar fuels generation', *Catalysis Today*, vol. 300, p. 136-144, Feb. 2018, doi: 10.1016/j.cattod.2017.03.016.

[247] X. Zhang, S. Wang, C. Pan and Y. Zeng, 'Construction of Ag/$CuB_{i2}O_4$/$Ag_2MoO_4$ composites for enhanced degradation of methylene blue and the proposed possible photocatalytic mechanisms', *Materials Letters*, vol. 288, p. 129388, Apr. 2021, doi: 10.1016/j.matlet.2021.129388.

[248] A.C. Nogueira, L. Gomes, J. Ferencz, J. Rodriges, R. Gonçalves and H. Wender, 'Improved visible light photoactivity of $CuBi_2O_4/CuO$ heterojunctions for photodegradation of methylene blue and metronidazole', *The Journal of Physical Chemistry C,* vol. 123, p. 25680 – 25690, Oct. 2019, doi: 10.1021/acs.jpcc.9b06907.

[249] X. Zhang, S. Wang, L. Lin, X. Tan and Y. Zeng, 'Design of novel $CuBi_2O4/CdMoO_4$ heterojunctions with nano-microsphere structure: synthesis and photocatalytic degradation mechanism', *Colloids and Surfaces A*, vol. 614, p. 126008, Apr. 2021, doi: 10.1016/j.colsurfa.2020.126008.

[250] G. Meena, M. Kumar, R. K. Hocking, S. Juodkazis, V. Biju, P. Subramanyan and C. Subrahmanyam, "Exploring $CuBi_2O_4$ as a Promising Photocathode Material for PEC water Splitting", *Energy Fuels*, 37, 2023, 14280 – 14289.

[251] J. Lee et al., "Long-term stabilized high-density $CuBi_2O_4/NiO$ heterostructure thin film photocathode grown by pulsed deposition", *Chem. Commun.*, 2019, 55, 12447.

[252] M. Samsudin, L. Siang, S. Sufian, R. Bashiri, N. Mohamed and R. Ramli, 'Exploring the role of electron-hole scavengers on optimizing the photocatalytic performance of $BiVO_4$', *Materials Today: Proceedings*, vol. 5, p. 21703-21709, 2018, doi: 10.1016/j.matpr.2018.07.022.

[253] I. Rodriguz-Gutierrez, R. Garcia-Rodriguez, M. Rodriguez-Perez, A. Vega-Poot, G. Rodriguez Gattorno, B. A. Parkinson and G. Oskam, 'Charge Transfer and Recombination Dynamics at Inkjet-Printed $CuBi_2O_4$ Electrodes for Photoelectrochemical Water splitting', *The Journal of Physical Chemistry C*, vol. 122, p. 27169 – 27179, Nov. 2018, doi: 10.1021/acs.jpcc.8b07936.

[254] M. Lv et al., 'Bismuth and chromium co-doped strontium titanates and their photocatalytic properties under visible light irradiation', *Phys. Chem. Chem. Phys.,* vol. 17, no. 39, pp. 26320 26329, Sep. 2015, doi: 10.1039/C5CP03889H.

[255] C.G.O. Bruziquesi, M. Stolzemburg, R. de Souza, M. Rodriguez, M. Rocco, P. Salomao, A. Nogueira, Z. Lopez-Cabana, M. Pereira and A. Silva, 'Cobalt as a sacrificial metal to increase the photoelectrochemical stability of $CuBi_2O_4$ films for water splitting', *International Journal of Hydrogen Energy*, vol. 48, p. 3456-3465, Jan. 2023, doi: 10.1016/j.ijhydene.2022.10.195.

[256] M. Grao, J. Redfern, P.J. Kelly and M. Ratova, 'Magnetron co-sputtered $Bi_{12}TiO_{20}/Bi_4Ti_3O_{12}$ composite – An efficient photocatalytic material with photoinduced oxygen vacancies for water treatment application', *Applied Surface Science*, vol. 552, p. 149486, Jun. 2021, doi: 10.1016/j.apsusc.2021.149486.

[257] R. van de Krol, 'Principles of Photoelectrochemical Cells', in *Photoelectrochemical Hydrogen Production. Electronic Materials: Science & Technology*, R. van de Krol and M. Grätzel, Eds., Springer, Boston, MA, 2012, pp. 13-67, doi: 10.1007/978-1-4614-1380-6_2.

[258] A. Song, P. Bogdanoff, A. Esau, I.Y. Ahmet, I. Levine, T. Dittrich, T. Unold, R. van de Krol and S.P. Berglund, ‘Assessment of a W:$BiVO_4$–$CuBi_2O_4$ Tandem Photoelectrochemical Cell for Overall Solar Water Splitting’, *ACS Applied Materials & Interfaces*, vol. 12, p. 13587-14628, Mar. 2020, doi: 10.1021/acsami.0c00696.

[259] Y-H. Lai, K-C. Lin, C-Y. Yen and B-J. Jiang, ‘A tandem photoelectrochemical water splitting cell consisting of $CuBi_2O_4$ and $BiVO_4$ synthetized from a single $Bi_4O_5I_2$ nanosheet template’, *Faraday Discussions,* vol. 215, Dec. 2018, doi: 10.1039/C8FD00183A.

[260] Z. Mo, X. She, Y. Li, L. Liu, L. Huang, Z. Chen, Q. Zhang, H. Xu and H. Li, ‘Synthesis of g-$C_3N_4$ at different temperatures for superior visible/UV photocatalytic performance and photoelectrochemical sensing of MB solution’, *RSC Advances*, vol.5, p. 101552–101562, Nov. 2015, doi: 10.1039/C5RA19586A.

[261] F. Dong, Z. Zhao, T. Xiong, Z. Ni, W. Zhang, Y. Sun and W.K. Ho, ‘In situ construction of g-$C_3N_4$/g-$CN_4$ metal-free heterojunction for enhanced visible-light photocatalysis’, *ACS Applied Materials & Interfaces*, vol. 5, p. 10397-11488, Nov. 2013, doi: 10.1021/am403653a.

[262] A.G. Joshi, S. Sahai, N. Gandhi, Y.G.R. Krishna and D. Haranath, ‘Valence band and core-level analysis of highly luminescent ZnO nanocrystals for designing ultrafast optical sensors’, *Appl. Phys. Lett.*, vol. 96, p. 1–15, 2010, doi: 10.1063/1.3354025.

[263] W. Shi, M. Li, X. Huang, H. Ren, F. Guo, Y. Tang and C. Lu, ‘Construction of $CuBi_2O_4$/$Bi_2MoO_6$ p-n heterojunction with nanosheets-on-microrods structure for improved photocatalytic activity towards broad-spectrum antibiotics degradation’, *Chemical Engineering Journal*, vol. 394, p. 125009, Aug. 2020, doi: 10.1016/j.cej.2020.125009.

[264] Y. A. Jadhav, P. R. Thakur and S.K. Haram, ‘Voltammetry investigation on copper zinc tin sulphide /selenide ($CZTS_xSe_{1-x}$) alloy nanocrystals: Estimation of composition dependent band edge parameters’, *Solar Energy Materials & Solar Cells*, vol. 155, p. 273-279, Oct. 2016, doi: 10.1016/j.solmat.2016.06.030.

[265] S.N. Inamdar, P.P. Ingole and S.K. Haram, ‘Determination of Band Structure Parameters and the Quasi-Particle Gap of CdSe Quantum Dots by Cyclic Voltammetry’, *ChemPhysChem*, vol. 9, p. 2425-2630, Dec. 2008, Dec. 2008, doi: 10.1002/cphc.200800482.

[266] Z. Lin, J. Hu, B. Zhang, L. Wu and J. Wang, ‘Illuminated from back or front? Insight into factors affecting the efficiency of $BiVO_4$’, *Applied Catalysis A: General*, vol. 652, p.119024, Feb. 2023, doi: 10.1016/j.apcata.2023.119024.

[267] M. Grao, M. Ratova and P. Kelly, ‘Design and optimisation of a low-cost titanium dioxide-coated stainless steel mesh photocatalytic water treatment reactor’, *Journal of*

*Cleaner Production*, vol. 297, p. 126641, May 2021, doi: 10.1016/j.jclepro.2021.126641.

[268] M. Beetz, S. Häringer, P. Elsasser, J. Kampmann, L. Sauerland, F. Wolf. M. Günther, A. Fischer and T. Bein, 'Ultra-Thin Protective Coatings for Sustained Photoelectrochemical Water Oxidation with Mo:$BiVO_4$', *Advanced Functional Materials*, vol. 31, p. 2011210, Nov. 2021, doi: 10.1002/adfm.202011210.

[269] K. Varumkumar and R. Sellappan, 'Role of carbon protective layer on the photoelectrochemical performance of drop-casted $CuBi_2O_4$ photocathodes for water s plitting', *Diamond & Related Materials*, vol. 130, p. 109547, Dec. 2022, doi: 10.1016/j.diamond.2022.109547

[270] X. Zhong, Y. Cai, H. Bai, W. Huang and B. Zhou, 'Visible Light Driven Spherical $CuBi_2O_4$ with Surface Oxygen Vacancy Enhanced Photocatalytic Activity: Catalyst Fabrication, Performance, and Reaction Mechanism', *Catalysts*, vol. 10, p. 945, Aug. 2020, doi: 10.3390/catal10080945

[271] Y. Zhang, X. Zhang, D. Wang, F. Wan and Y. Liu, 'Protecting hydrogenation-generated oxygen vacancies in $BiVO_4$ photoanode for enhanced water oxidation with conformal ultrathin amorphous $TiO_2$ layer', *Applied Surface Science*, vol. 403, p. 389-395, May 2017, doi: 10.1016/j.apsusc.2017.01.195.

[272] J. Azevedo, S.D. Tilley, M. Schreier, M. Stefik, C. Sousa, J.P. Araujo, A. Mendes, M. Grätzel and M.T. Mayer, 'Tin oxide as stable protective layer for composite cuprous oxide water-splitting photocathodes', *Nano Energy*, vol. 24, p. 10-16, Jun. 2016, doi: 10.1016/j.nanoen.2016.03.022

[273] J. Wang, L. Zuo, Z. Guo, C. Yang, Y. Jiang, X. Huang, L. Wu and Z. Tang, '$Al_2O_3$-coated $BiVO_4$ photoanodes for photoelectrocatalytic regioselective C-H activation of aromatic amines' *Angewandte Chemie*, vol. 62, Dec. 2023, doi: 10.1002/anie.202315478.

[274] A. Berger, R.A. Segalman and J. Newman, 'Material requirements for membrane separators in a water splitting photoelectrochemical cell', *Energy & Environmental Science*, vol. 7, p. 1468, Feb. 2014, doi: 10.1039/C3EE43807D.

[275] I.Y. Ahmet, Y. Ma, J-W. Jang, T. Henschel, B. Stannonwki, T. Lopes, A. Vilanova, A. Mendes, F.F. Abdi and R. van de Krol, 'Demonstration of a 50 $cm^2$ $BiVO_4$ tandem photoelectrochemical-photovoltaic water splitting device', *Sustainable Energy & Fuels*, vol. 3, p. 2366-2379, Jul. 2019, doi: 10.1039/C9SE00246D.

[276] A. Rothschild and H. Dotan, 'Beating the Efficiency of Photovoltaics-Powered Electrolysis with Tandem Cell Photoelectrolysis', *ACS Energy Letters*, vol. 2, p. 1-287, Jan. 2017, doi: 10.1021/acsenergylett.6b00610.

[277] X. Shi, H. Jeong, S.J. Oh, M. Ma, K. Zhang, J. Kwon, I.T. Choi, I.Y. Choi, H.K. Kim, J.K. Kim and J.H. Park, 'Unassisted photoelectrochemical water splitting exceeding 7% solar-to-hydrogen conversion efficiency using photon recycling', *Nature Communications*, vol. 7, p. 11943, Jun. 2016, doi: 10.1038/ncomms11943.

[278] P. Xu, J. Feng, T. Fang, X. Zhao, Z. Li and Z. Zou, ‘Photoelectrochemical cell for unassisted overall solar water splitting using a $BiVO_4$ photoanode and Si nanoarray photocathode’, *RCS Advances,* vol. 6, p. 9905-9910, Jan. 2016, doi: 10.1039/C5RA20115B

[279] M. Grao, M. Ratova, C.C. Amorim, R.B.P. Marcelino and P. Kelly, ‘Crystalline $TiO_2$ supported on stainless steel mesh deposited in a one step process via pulsed DC magnetron sputtering for wastewater treatment applications’, *Journal of Materials Research and Technology,* vol. 9, p. 5761-5773, Jun. 2020, doi: 10.1016/j.jmrt.2020.03.101.

[280] W.J. Albery, G.J.O’Shea and A.L. Smith, ‘Interpretation and use of Mott-Schottky plots at the semiconductor/electrolyte interface’ *Journal of the Chemical Society, Faraday Transactions,* vol. 92, p. 4083-4085, 1996, doi: 10.1039/FT9969204083

[282] P. Lv, M. Zheng, X. Wang, and F. Huang, ‘Subsolidus phase relationships and photocatalytic properties in the ternary system $TiO_2$–$Bi_2O_3$–$V_2O_5$’, Journal of alloys and compounds, 2014, Vol.583, p.285-290, doi: 10.1016/j.jallcom.2013.07.156.

[283] M.P. Chon, K.B. Tan, C.C. Khaw, Z. Zainal, Y.H. Taufiq-Yap, S.K. Chen and P.Y. Tan, ‘Subsolidus phase equilibria and electrical properties of pyrochlores in the $Bi_2O_3$–CuO–$Ta_2O_5$ ternary system’,Journal of alloys and compounds, 2016-08, Vol.675, p.116-127, doi: 10.1016/j.jallcom.2016.03.089

[284] M. Zohreh, M. Tayebi, S. A. Masoumi Lari, B. Seo, C. Lim, H. Kim, D. Kyung and M. Tayebi, ‘Photoelectrochemical Performance of a CuBi2O4 Photocathode with $H_2O_2$ as a scavenger’, Inorganics, Vol. 11, issue 4, doi: https://doi.org/10.3390/inorganics11040147.

[285] L. Ding, Y. Zhang, T. Wang, P. Li and K. Chang, ‘Fabrication strategies for high-performance unbiased PEC water splitting cells’, Catalysis Science & Technology, 2024, 14, 1730, doi: 10.1039/d3cy01703f

[286] X. Shi, I. Y. Choi, K. Zhang, J. Kwon,D.Y.Kim, J. K. Lee, S. H. Oh, J. K. Kim, J. H. Park, Nat. Commun. 2014, 5,4775, doi: 10.1038/ncomms5775.

[287] T. Singh, R. Müller, J. Singh and S. Mathur, ‘Tailoring surface states in WO3 photoanodes for efficient photoelectrochemical water splitting”, Applied surface science, vol. 347, 2015, p. 448-453, doi: 10.1016/j.apsusc.2015.04.126.

[288] F. G. Will, ‘Hydrogen + oxygen recombination and related heat generation in undivided electrolysis cells’, Journal of Electroanalytical Chemistry, vol. 426, issue 1-2, 1997, p. 177-184.

[289] L. J. Minggu, W. R. W. Daud and M. B. Kassim, ‘An overview of photocells and photoreactors for photoelectrochemical water splitting’, International Journal of Hydrogen Energy, vol. 35, 2010, p. 5233-5244, doi: 10.1016/j.ijhydene.2010.02.133.

[290] T.D. Nguyen, VH. Nguyen, S. Nanda et al., ‘$BiVO_4$ photocatalysts design and applications to oxygen production and degradation of organic compounds: a review’, Environmental Chemistry letters, vol. 18, 2020, p. 1779-1801, doi: 10.1007/s10311-020-01039-0.

[291] H. Huynh et al., ‘Enhancing visible-light-driven water splitting of ZnO nanorods by dual synergistic effects of plasmonic Au nanoparticles and Cu dopants’, Journal of photochemistry and photobiology. A, Chemistry., 2020-08, Vol.399, p.112639, Article 11263, doi: 10.1016/j.jphotochem.2020.112639

[292] Ch. Reddy et al., ‘Investigation of dopant and Ag plasmonic effect on $\alpha$-$Fe_2O_3$ photoelectrode for photoelectrochemical water splitting activity’, Applied surface science, 2019-09, Vol.488, p.629-638, doi : 10.1016/j.apsusc.2019.05.316

[293] G. Fang et al, ‘Enhancing the PEC water splitting performance of BiVO4 co-modifying with NiFeOOH and Co-Pi double layer cocatalysts’, Applied surface science, 2020-06, Vol.515, p.146095, Article 146095, doi: 10.1016/j.apsusc.2020.146095.

[294] H. Guan, ‘In situ surface-trap passivation of CuBi2O4 photocathode for unbiased solar water splitting’, Journal of materials chemistry A, vol. 11, 2023, p. 149-157, DOI: 10.1039/d2ta07117g

[295] J. Choi et al., ‘High-density CuBi2O4 photocathode using Well-textured buffer lyers and their unassisted solar hydrogen production performances’, Small, 2025, p. 2411800, doi: 10.1002/smll.202411800.

# Annexes

# A. Dye degradation test

The photocatalytic degradation of a dye follows a pseudo-first order kinetic reaction, as described by the following model:

$$c_t = c_0 e^{-k_\alpha t} \qquad (48)$$

where c is the solution concentration at time t, c0 is the initial concentration and $k_\alpha$ is the pseudo-first order reaction constant. This constant can be determined by plotting $\ln \frac{c_t}{c_0}$ against the time.The constant rate is usually expressed in $s^{-1}$. The photocatalytic activity of the samples produced was assessed using a testing bench described in Figure 98. The samples (2.5 cm x 2.5 cm) are placed in a quartz cuvette filled with 50 mL of a 2µmol.$L^{-1}$ MB solution. The samples are left in the dark for 60 minutes under continuous stirring, to reach adsorption-desorption equilibrium. After that, the samples are illuminated by a UV-A light source (2x15 W Sankyo Denki BLB lamps) for 1h. The methylene blue main absorption peak is located at 664 nm and its evolution with irradiation time was monitored with an Ocean Optics USB4000 UV-Vis spectrometer.

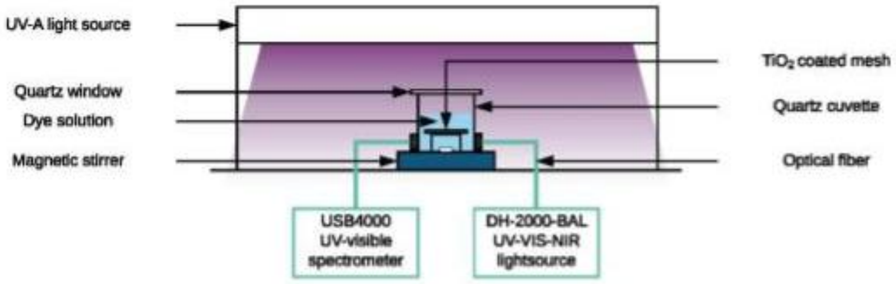

Figure 11. Schematic representation of the photocatalytic activity test set-up []

# B. MB dye degradation results for CuBi samples

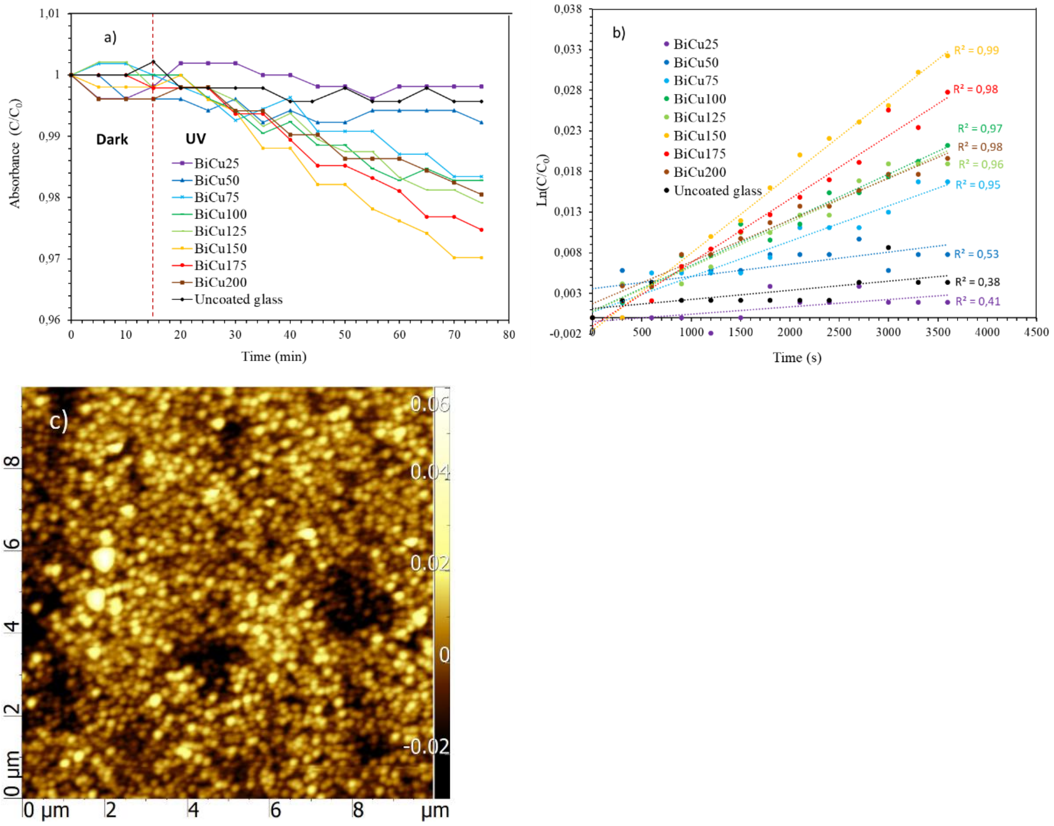

Figure 12. MB dye degradation tests for CuBi samples b) associated linear regression c) Example of AFM image for BiCu150

Table 3. Results of MB dye degradation tests for CuBi samples under UV-A

| Sample No. | MB degradation after 1h (%) | Pseudo first order $k_\alpha$ ($10^{-6}.s^{-1}$) | $R^2$ |
|---|---|---|---|
| Photolysis | 0.4 | 0.79 | 0.46 |
| Cu25 | 0.2 | 0.913 | 0.4 |
| Cu50 | 0.8 | 1.5 | 0.53 |
| Cu75 | 1.7 | 4.36 | 0.95 |
| Cu100 | 2.1 | 5.62 | 0.97 |
| Cu125 | 2.1 | 5.92 | 0.97 |
| Cu150 | 3.2 | 9.52 | 0.99 |
| Cu175 | 2.8 | 7.82 | 0.98 |
| Cu200 | 1.95 | 5.15 | 0.97 |